An experimental study of beam-columns subjected to combined torsion, bending and axial actions

by

Arne Aalberg

Department of Structural Engineering
The Norwegian Institute of Technology
N-7034 Trondheim

July 14, 1995

Contents

Abstract

This report presents an investigation on the inelastic behaviour of steel I-section beam-columns under combinations of axial load, bending and torsion. The study is motivated by the lack of information on the ultimate capacity of such members, and the lack of design procedures and design provisions.

A test facility is built for the testing of the beam-columns, with the primary objective to obtain reliable experimental data for the response for specimens tested at well controlled load- and support-conditions. Tests are carried out for two different Class1 I-sections, the wide flange section HEB 140 and the beam section IPE 160.

The behaviour in both uniform and nonuniform torsion is investigated, as well as combinations of bending and torsion at various levels of axial load. Results are given in terms of response histories.

Typical beam-column experiments are simulated by means of the general purpose finite element program ABAQUS, using shell elements to model the specimens. The objective is to verify to what extent numerical simulations may replace physical models in studies of beam-columns under similar load combinations.

Methods for calculating the full plastic nonuniform torsional moment are discussed. Second order effects are discussed for the combination of axial load and torsion, and simple design interaction equations are proposed. For the interaction between bending and torsion, the applicability of a commonly used quadratic interaction equation is investigated. For the capacity definition, a deformation norm is introduced. An interaction equation on the component level is proposed for the full load combination of axial load, bending and torsion.

Acknowledgements

I would like to express my deepest gratitude to my supervisor, Professor Per K. Larsen, for initiating this study, and for his motivating support and guidance throughout the work.

I would also like to express my appreciation to my colleagues in the ”steel group” at the department for many valuable discussions, in particular Professor Bernt Skjeggestad for his valuable criticism.

The study has involved long hours in the laboratory, and thanks are due to the laboratory staff for their efforts and assistance.

The generous financial support from the ”Stål i bygg”-project, organized by the Norwegian Steel Association, is gratefully acknowledged.

Notation

Notations and symbols used in this report are defined in the text when they occur. The axis system, the displacements and the forces are defined in Figure 5.1.

Symbol	Explanation
A, A_0	cross-sectional area, original cross-sectional area
E, G	modulus of elasticity, shear modulus of elasticity ($G=E/2(1+\nu)$)
H	transverse midspan load on beam-column
H_p	value of H giving full plastification in bending ($H_p=4M_p/l$)
I_T, I_w	section torsional constant, section warping constant
L	length
L_C	reduced parallel length of tensile test coupon
L_0	original gauge length ($=5.65\sqrt{A_0}$) for proportional test coupon
M	bending moment or bending moment at beam-column midspan
M_f	bending moment in flange about strong axis of flange plate
M_{fp}	plastic bending moment in flange
M_p	plastic bending moment about strong axis (y) of cross-section
M_Y	yield bending moment (initial yield) about strong axis
N	axial force, axial load
N_E, N_{ET}	elastic flexural buckling load, elastic torsional buckling load
N_Y	yield axial load (=squash load of cross section)
N_0	axial load applied to beam-column
N_d	design capacity for N ($=N_Y/\gamma_M$)
NMT	load combination with N, M and T
T	torsional moment (torque)
T_Y	yield torsional moment (initial yield)
T_0	torsional moment applied to end of beam-column
$T_{0,alt}$	alternative torsional capacity
T_d, T_{pd}	design capacity for T, plastic design capacity ($=T_p/\gamma_M$)
T_p	plastic torsional moment
T_r,T^*	amplified value, reduced value for torsional capacity
T_u, T_{up}	uniform torsional moment, plastic value of T_u
T_w, T_{wp}	warping torsional moment, plastic value of T_w
V, V_f	shear force, shear force in flange (y-direction)
$\overline{H}_p$	normalized value of H ($\overline{H}_p=H/H_p$)
$\overline{M}$	normalized value of M ($\overline{M}=M/M_Y$)
$\overline{M}_p$	normalized value of M ($\overline{M}_p=M/M_p$)
$\overline{N}$	normalized value of N ($\overline{N}=N/N_Y$)

$\overline{\mathrm{T}}$	normalized value of T ($\overline{\mathrm{T}}$=T/T$_Y$)
$\overline{\mathrm{T}}_p$	normalized value of T ($\overline{\mathrm{T}}_p$=T/T$_p$)
a	deformation norm
b	width of flange
f	amplification factor
f_y	yield strength (yield stress)
f_u	ultimate tensile strength
h	depth of cross-section
h_t	distance between flange centroids
l	length of beam, length of beam-column
s	thickness of web
t	thickness or thickness of flange
u	axial shortening of beam-column
u_Y	value of u due to N_Y
w	transverse displacement of beam-column at midspan
w_Y	value of w at initial yield due to transverse loading H
$\delta_{5.65}$	elongation (%) after rupture, measured over L_0
ε_{yp}	yield point elongation
ε_u	strain when f_u is reached
γ_M	partial safety factor for the resistance
ϕ	twist rotation of beam-column end
ϕ_T	twist rotation due to external torsional loading
ϕ_Y	value of ϕ at initial yield due to torsional loading T_0
ϕ_r	amplified value of ϕ due to presence of N
$\overline{u}$	normalized u ($\overline{u}$=u/u_Y)
$\overline{w}$	normalized value of w ($\overline{w}$=w/w_Y)
$\overline{\phi}$	normalized value of ϕ ($\overline{\phi}=\phi/\phi_Y$)

Chapter 1

Introduction

1.1 Background

Over the last ten years an extensive effort has been made in Europe in order to write a complete set of design specifications for the most commonly used materials in civil engineering structures. The work on these Eurocodes was initiated by the Commission of the European Union, and continued under the auspices of the European Standardisation Organisation (CEN). The codes are based on the concept of partial coefficients of structural reliability, and a major objective was to arrive at a uniform level of reliability all through the structures. As a basis for the development of Eurocode 3 - Design of Steel Structures - data bases were established containing all available data, experimental or numerical, regarding the behaviour of structures, structural components and joints and connectors.

At the ultimate limit state the provisions of the codes aim at predicting the real load carrying capacity of the structure, taking advantage of second order effects and inelastic material behaviour. For linearly elastic behaviour the theory of elasticity provides solutions both for beams in torsion, torsional buckling and lateral torsional buckling, but the interaction of bending, torsion and axial force is not well documented. When writing the specifications for beam-columns it became clear that very little information was available regarding the ultimate capacity of components subjected to combined actions that included torsion. As a consequence, the design formulas for beam-columns subjected to bending and axial force are quite advanced and accurate, while the problem of torsion is almost completely neglected.

In most civil engineering steel structures torsion is a secondary action, and is commonly avoided through good structural design. Even though the transfer of external loads by means of torsion is generally considered an inefficient way of resisting the external actions, there are cases were the torsional behaviour can not be avoided and where the torsional resistance may be of great importance. This is the case for instance in slender bridges, and for building structures under accidental situations such as fire and earthquakes. Traditionally, the torsion effects have in many cases simply been neglected in the structural analysis of building structures. However, in today's structural analysis programs it is frequently easier to include torsion in the computational model than to avoid it.

By means of the commercially available general purpose finite element codes that incorporate both geometrical and material nonlinearities structural design by analysis is now feasible. This means that the traditional design procedure of first carrying out a structural analysis followed by a separate (independent) check of member capacity in the form of a code check, can in principle be replaced by a one-step procedure in which the load carrying capacity of the structure can be determined through a nonlinear finite element analysis. The new Australian Standard (AS 4100) states certain requirements for the use of such a procedure, and Eurocode 3 also contains some general information for its use. In general, if design by analysis is to be used, the safety level specified by the appropriate building authorities and ensured by today's design specifications, has to be maintained. This means that all effects such as initial deformations, residual stresses, spatial variation of material properties such as yield and ultimate stress must be represented in the numerical model.

For the analysis of steel framed structures beam elements are available that include warping deformations of the cross section and models based on concentrated plasticity to describe the inelastic material behaviour. All the previously mentioned effects can in principle be included here, and for steel frames where the components are subjected primarily to axial and bending actions such elements predict the response with good accuracy. However, when also torsion is present the existing models for concentrated plasticity are inadequate, as the commonly available yield or bounding surfaces in force space do not include torsion.

Further research is hence needed both to provide experimental data on the structural behaviour of beam-columns subjected combinations of axial force, bending and torsion actions and on possible plastic failure or bounding surfaces for cross sections subjected to the same actions.

1.2 Objectives

The present investigation has two primary objectives. Firstly, to obtain reliable experimental data on the behaviour of beam-columns of I-shaped cross sections subjected to combinations of axial, bending and torsion actions that take the member into the inelastic range. This data is to serve as a basis both for the development of interaction formulas on the same format as the current design specifications, and may also be used for verification of plastic failure surfaces for use in concentrated plasticity models. Secondly, to use this data to evaluate the accuracy of numerical models established by means of existing general purpose finite element programs for this type of problems.

The main tasks of the present investigation are :

1. To develop and construct a test facility for testing of I-section beam-columns under various combinations of axial load, bending moment and torsional moment. The primary objectives of the tests are to provide high precision experimental data for the response of the beam-columns, tested at well controlled load- and support-conditions which can be properly modelled in a finite element analysis.

2. To carry out tests on beam-columns of two different I-shaped sections, at various load combinations, to obtain data both for member behaviour and for cross-sectional resistance. The load combination will be restricted to the case of compressive axial force, torsional moment and strong axis bending only at the critical section.

3. To simulate some typical experiments by means of an existing finite element program, using shell elements to model the test specimens. The objective here is to verify to which extent numerical simulations can replace physical models in a further study of beam-column behaviour under similar load combinations.

4. To discuss the existing design provisions for torsion in view of the experience gained in the present study.

1.3 Previous studies

Not many studies have been made of the nonlinear behaviour of structural members subjected to torsion, and especially not when torsion is combined with bending and axial force. Torsional problems related to elastic instability, such as lateral-torsional buckling of beams and torsional buckling of columns are considered to lie outside the scope of the present study, and are not included here. An extensive summary of the most relevant remaining literature is provided by Pi and Trahair (1994c).

The linear theories for elastic bending of beams and torsion of elastic beams and bars are well established (Timoshenko 1936, Timoshenko and Goodier 1951, Vlasov 1961 and others) and give quite accurate predictions for the member behaviour in the case of small deformations. The basic theories for the prediction of the plastic bending capacity of beams and plastic torsional strength of members are given by Nadai (1950), Hodge (1959) and Neal (1977).

Experimental investigations of the effects of inelastic torsion on structural members have been carried out only by few authors. Boulton (1962) tested four rolled steel I-section beams, two of which were restrained against warping deformation at both ends and two which were free to warp. Dinno and Gill (1964) tested nineteen small I-section specimens with warping restraints at the ends subjected to a centrally applied torsional moment. Dinno and Merchant (1965) tested six similar specimens in combined bending and torsion, while Farwell and Galambos (1969) tested five wide-flange beams subjected to both one and two concentrated torsional moments. For square and rectangular section specimens Gill and Boucher (1964) carried out eighteen tests with bending and torsion. Tests on cantilever I-section beams under bending and torsion are given by Driver and Kennedy (1989), and tests with combined torsion, bending and axial loading of box stub columns are presented by Kitada and Nakai (1989).

Approximate methods for calculation of plastic cross-sectional capacity in bending and torsion are available for various sections. Hill and Siebel (1953) and Steele (1954) studied the combined bending and torsion of respectively solid circular sections and solid square sections, while Imegwu (1960) studied square, triangular and circular sections. Approximate solutions in terms of lower and upper bounds for the bending and torsion interaction were presented by Hill and Siebel (1953), Steele (1954) and Gaydon and Nuttall (1957), while a lower bound solution was presented by Hodge (1959) for various sections. In all cases the bending and the torsional moment were assumed uniform along the length of the member.

For I-beam sections with warping restraints Boulton (1962) obtained an approximate lower bound solution for the fully plastic capacity for combined strong axis bending and torsion, while Dinno and Merchant (1965) proposed an empirical "upper bound" for the plastic capacity of a cantilevered beam subjected to a torsional moment at the free end. In addition, they used the lower bound interaction equation obtained by Hodge (1959) in their study of I-section beams with warping restraints. Augusti (1966) used an upper bound approach to the case of torsion of a cantilevered I-section beam, based on linear geometry and rigid plastic behaviour, and evaluated the results of Boulton (1962) and Dinno and Merchant (1965). These studies all focus on the effects of material yielding.

The effects of geometrical nonlinearity for beams and beam-columns, included the effects of torsion, have been analysed by Chen and Atsuta (1977), Attard (1986), Yang and McGuire (1986) and others. In recent years, several finite element formulations for beam elements have been presented, where both the geometrical and material nonlinearities are accounted for. Both El-Khenfas and Nethercot (1989) and Pi and Trahair (1994a) presented beam element formulations for analysis of problems with large deflections and twist rotations.

Finite element analyses have been used to study some problems which included torsion. Baba and Kajita (1982) studied torsion of a prismatic beam using a specially developed element. Bathe and Wiener (1983) studied two approaches to model an I-section cantilever in bending and warping torsion, one model built up with 1-D beam elements and one model with shell elements. May and Al-Shaarbaf (1988) used brick elements to model uniform and warping torsion on beams of various sections, included the I-section. Chen and Trahair (1992) presented a finite element model for analysing elastic-plastic torsion on I-section beams, where the effect of the transverse uniform torsion shear stresses on material yielding were specially accounted for, and used this to study two examples of nonuniform torsion.

Using their general nonlinear beam element with warping degrees of freedom, El-Khenfas and Nethercot (1989) analysed a simply supported beam with axial compression, end moments and constant torsional moment applied at the mid-span. Here, they numerically investigated the effect of the higher order terms in the nonlinear strain-displacement relationship for the element. This effect was also studied by Pi and Trahair (1994b), who used a similar element to study combined torsion and bending of a simply supported beam, torsion of a compression member and nonuniform torsion of an I-beam. Further, Pi and Trahair (1994c) investigated the inelastic combined bending and torsion of I-section beams for three cases of laterally bracing. They carried out several numerical simulations for these beams with initial stresses and geometrical imperfections, looking at the interaction effects between strong axis bending, flexural-torsional buckling and torsion. In a recent paper (Pi and Trahair 1995) they studied the behaviour of beams in nonuniform torsion only.

In the field of yield surfaces for steel sections based on force resultants, one of the most useful compendiums is the work of Chen and Atsuta (1977). They constructed three-dimensional yield surfaces for the combination of axial force and biaxial moments for a number of cross-sectional shapes, and derived analytical expressions that approximate the surfaces for some typical I-sections. For the case when uniform torsion is included, a reduced yield stress is established assuming that the torsional stresses in the section are uniformly distributed. This reduced yield stress is subsequently used when computing the capacities for bending and axial force. For interaction between axial force and bending, Orbison et al. (1982) developed a single equation approximating the Chen-Atsuta yield surface for a wide flange section. Duan and Chen (1990) extended the work to other sections. Daddazio et al. (1983) described a procedure for deriving yield surface equations for thin-walled bars with warping restraints, subjected to the combination of axial force, biaxial bending moments and warping moments. A four-dimensional, multi-faceted surface was derived for a Z-section. For I-sections with nonuniform torsion Yang and Fan (1988) derived the yield surface for the full five-dimensional action; axial force, bending moments about two axes, a bimoment (flange warping) and the uniform torsional moment. Their approach is based on a parametric expression of a five-dimensional surface with three component yield surfaces, one for each of the plates constituting the section.

For bending and torsion on simply supported laterally braced and unbraced beams, the elastical interaction effects were studied by Chu and Johnson (1974), Pastor and DeWolf (1978), Razzaq and Galambos (1979) and Nethercot et al. (1989). Simple suggestions for calculation and amplification of elastic stresses and torsional rotation due to second order effects are given.

Chapter 2

Test setup

2.1 Introductory remarks

The reported tests are a part of an investigation dealing with the behaviour and ultimate resistance of beam-columns subjected to combined axial load, bending and torsion. The primary objective of the tests is to obtain reliable experimental data on beam-column behaviour and on cross-sectional resistance of typical I-beam sections when subjected to various combinations of axial force, strong axis bending and torsional moment.

The experimental investigation is carried out for two hot-rolled I-sections, the beam section IPE 160 and the wide flange section HEB 140. The laboratory facilities and the forces needed to fail the test specimens restricted the size of the sections. The length of the beam-column to be tested was for many reasons chosen to about two meters. A special test rig was designed and built for this testing. Existing loading frames and standard hydraulic actuators and equipment in the laboratory were used as far as possible, but loading and control devices for torsional loading had to be designed and manufactured for the tests. The experiments described in this report were all carried out in the structural engineering laboratory at the Civil Engineering Department, the Norwegian Institute of Technology.

This chapter describes all parts of the test rig and discusses the support and loading of the test specimens.

2.2 Test rig

The test rig is based on a standard vertical loading frame consisting of two supporting columns and a hydraulic actuator. The test specimen is mounted in a vertical position between two end supports and is braced at the mid-height. Figures 2.1 and 2.2 illustrate the test arrangements. The test setup uses a centrally applied transverse point load for bending, while the torsional loading is applied at the ends of the test specimen. As shown in Figure 2.2, the specimen is free to rotate about its length-axis at the end supports, while the rotation is restrained at midspan.

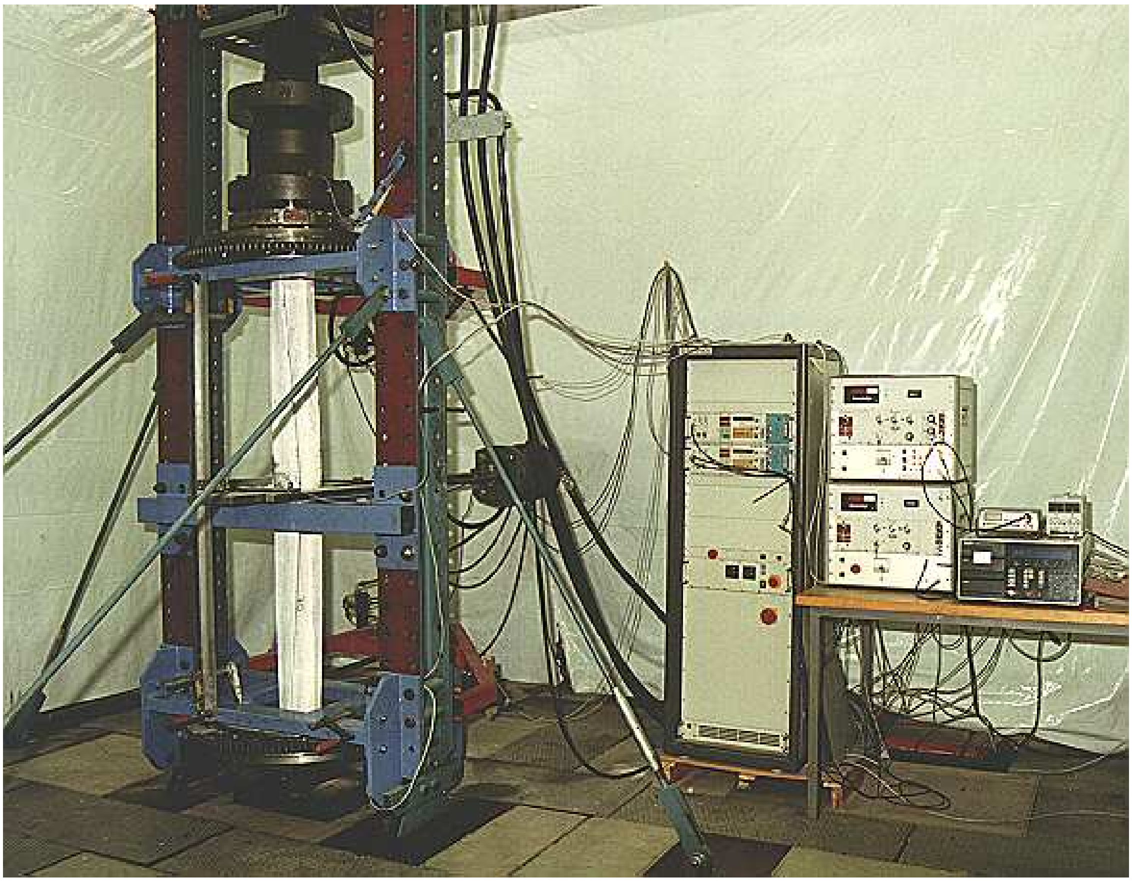

Figure 2.1: General view of the test rig. The test specimen is white-washed, the horizontal actuator is located behind the curtain.

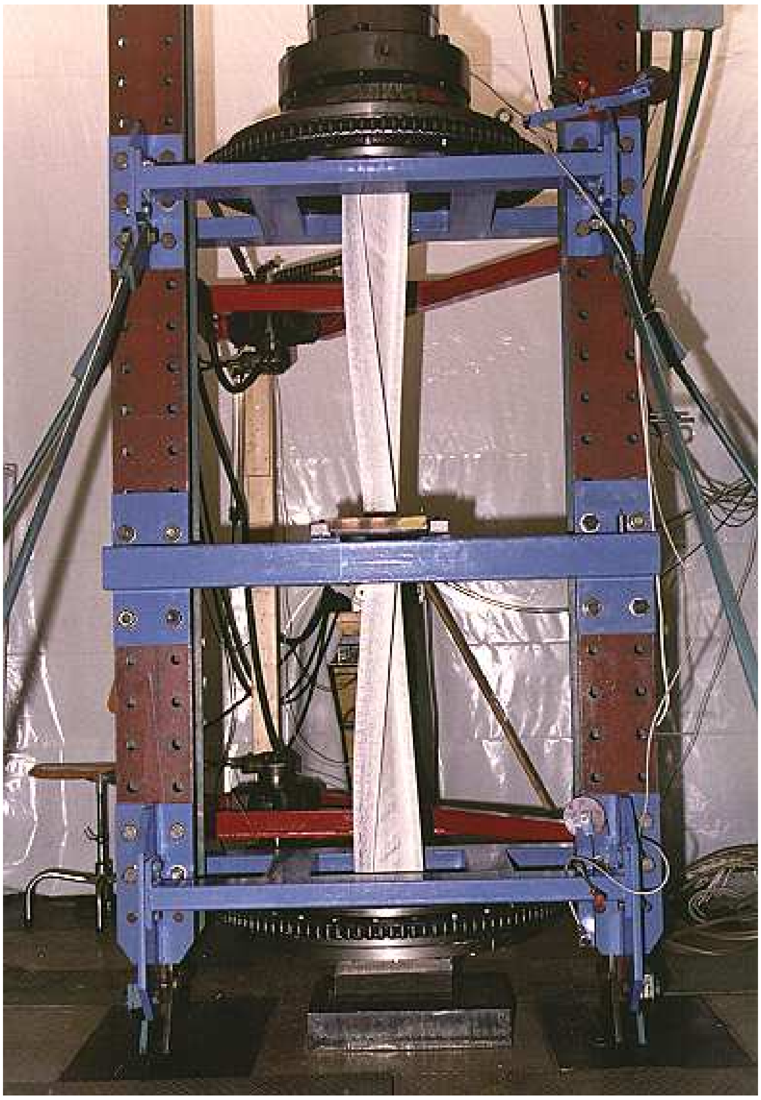

Figure 2.2: Test specimen IPE 160 mounted in the test rig.

The test rig involves three main loading devices and the necessary bearings and bracings:

- A vertically mounted hydraulic actuator in the main vertical loading frame applies axial load at the upper end of the test specimen, and the reaction force is carried by the ground support. Both ends of the specimen are equipped with base plates and spherical thrust bearings, and are laterally supported.
- A hydraulic actuator is mounted horizontally in a separate supporting frame, and applies a transverse load to the test specimen at midspan. The load is applied by means of a tension rod and a loading plate. The end supports have circular end fixture plates supported in large roller bearings.
- Two hydraulic motors applies torsional moments to the ends of the test specimen, by means of a chain driven loading arrangement. The torsional moments are transmitted to the specimen from the end fixture plates in the end supports.

Photographs of the fixture plates at the supports and the loading plate at midspan are given in Appendix B, while all loading and support arrangements are shown in detail in the following.

The fixture plates at the specimen ends acts as "hinged" supports for the beam-column specimens with respect to the transversal loading. The loading plate at midspan encloses the test specimen, transmits the transverse load, and serves as a restraint with respect to nonuniform torsional loading. At the ends, the test specimen is given a special design (Figures 2.6 and 3.1) to allow for the warping of the flanges. In addition, both ends of the specimen are provided with torsional "hinges" to allow the rotation about the longitudinal axis. As shown in Figures 2.3 to 2.6, the loading and bearing arrangements provide practically symmetrical end conditions to the test specimen.

The test specimen may hence be subjected to the following loading combination; a constant axial force in compression, a bending moment acting about an axis normal to the specimen length-axis, with the largest intensity at the loading point, and a nonuniform torsional moment. As a result of the three-point transversal load system there is also a shear force present in the specimen. A schematic and simplified view of the test arrangement and the resulting force- and moment-diagrams are shown in Figures 2.7 and 5.1.

The torsion loading device is double-acting and the torsional moment applied at the specimen ends can hence be reversed, allowing both nonuniform torsion (Figure 2.2) and uniform torsion (Figure 4.3) to be applied to the test specimen.

The test rig is designed to minimize the chances of unintentional constraints when the test specimens undergo large deformations. Furthermore, care has been taken not to assume any ideal fixed or free boundary conditions, but to measure all restraining forces and all displacements.

All loading devices have separate controllers and act separately, allowing any prescribed combination of the three force systems. The tests can be run in displacement or force control. The maximum force resultants the test rig can apply to a test specimen are: Axial force 1200 kN, bending moment 240 kNm and torsional moment 9 kNm.

2.2.1 Axial loading

The test specimen extends 30 mm beyond the end fixture plates as shown in Figure 2.6. The vertical actuator applies the load to the upper end of the test specimen through a spherical thrust bearing and a circular base plate, with an equal arrangement at the lower end. The base plates are fitted to the cross-section of the particular test specimen and to the thrust bearing as shown in Figures 2.3 and 2.8. This is done in order to prevent any end eccentricities caused by inaccurate mounting of the test specimen.

The spherical thrust bearings are needed to provide a centric load transfer, and are intended to allow end rotations of the test specimen induced by flexural deformations. Since the resisting bending moment in the bearings is negligible, the test specimen can be considered "hinged" or "simply supported" at the ends. A measurement of the friction moments at various axial load levels is presented in Section 2.3.

The thrust bearings consist of a spherical cap attached to the base plate, a sliding surface and a fixed casing (Figure 2.6). The center of rotation of the specimen end with respect to flexure-induced end-rotations is located in the plane of the end fixture plates, at the cross-sectional centroid. The thickness of the base plates is adjusted to make the rotation-center of the thrust bearing coincide with the rotation center of the specimen.

The load applied through the thrust bearings, i.e. the load applied by the actuator and the reaction force from the ground support, is enforced to point through these rotation-centers no matter how large the end-rotations become. The direction of the applied load coincide with the specimens length-axis in the initial, unloaded state, and the result is a pure axial force in the test specimen.

The shortening of the test specimen due to an axial load, or flexural or torsional deformations, causes a deflection of the circular fixture plate at the upper end support. Due to a large diameter to thickness ratio (Figures 2.3 and 2.8) the bending stiffness of the plate is so small that it can sustain the deflection without developing significant load.

2.2.2 Transverse loading

The transversal loading arrangement is shown in Figure 2.5. The horizontal actuator applies load to the test specimen through a tension rod bolted to a loading plate. The reaction forces due to the transversal load are balanced by forces in

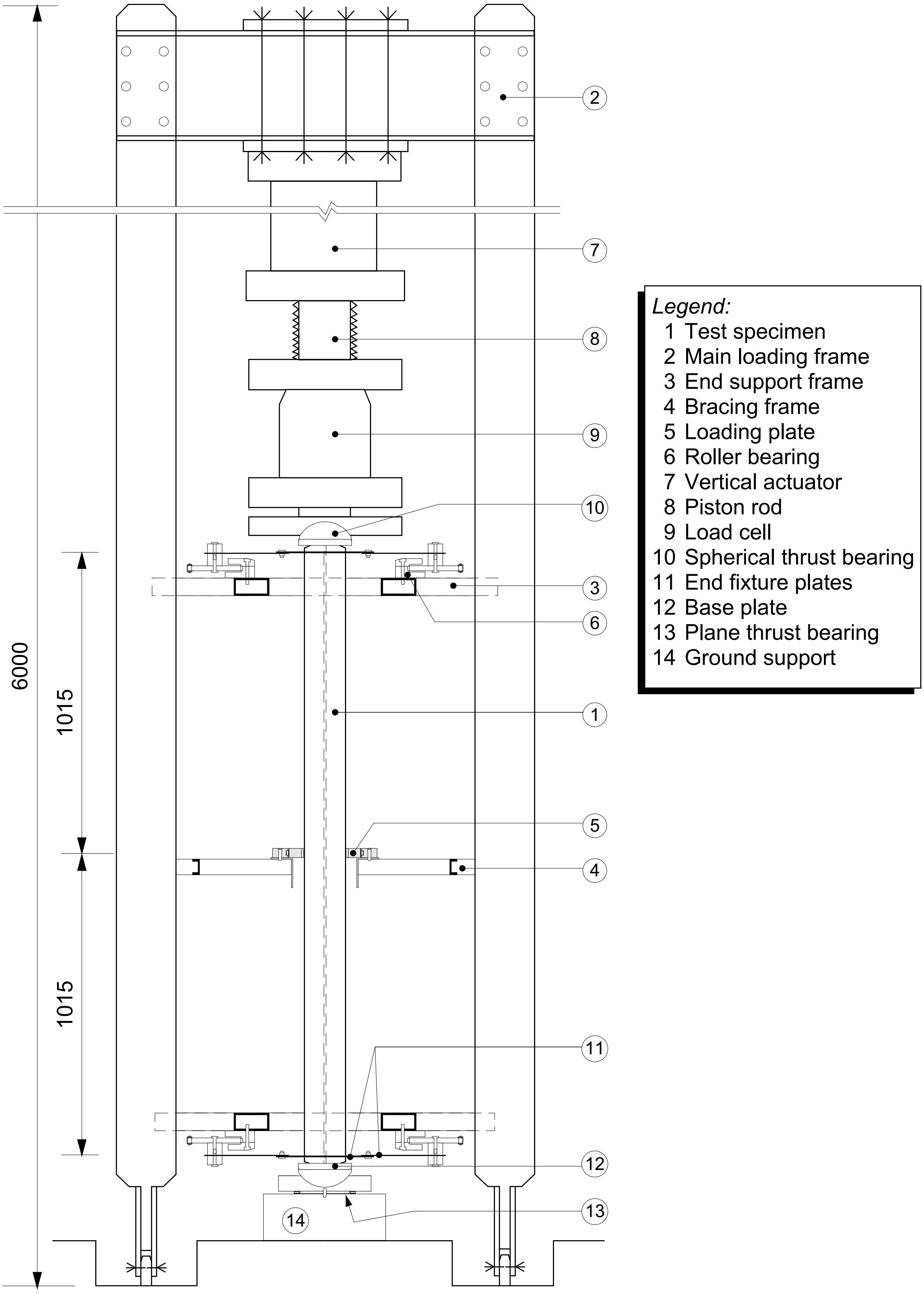

Figure 2.3: Part of the test rig, test specimen in vertical loading frame.

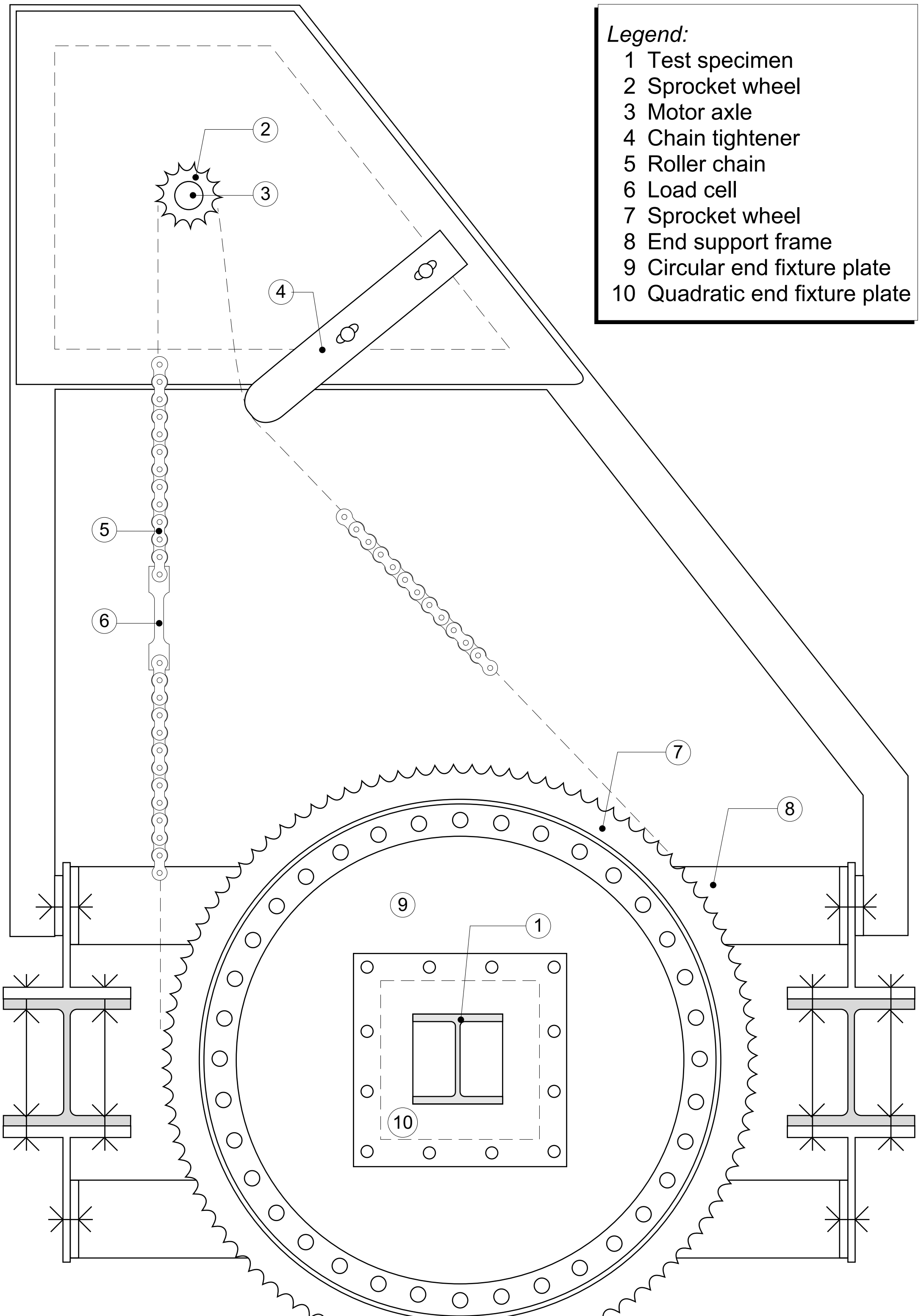

Figure 2.4: Torsional loading device and end support.

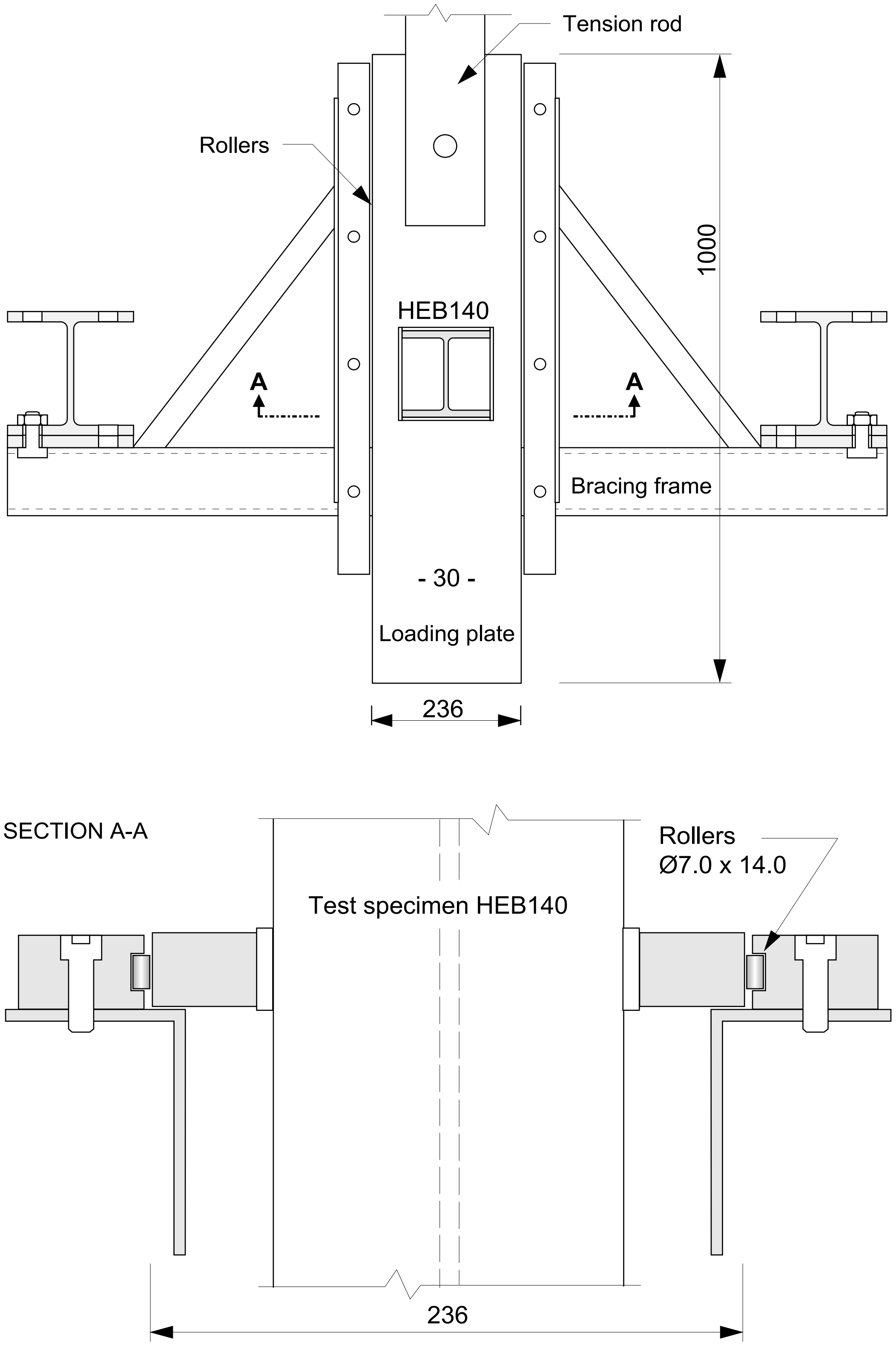

Figure 2.5: Bracing frame and loading plate.

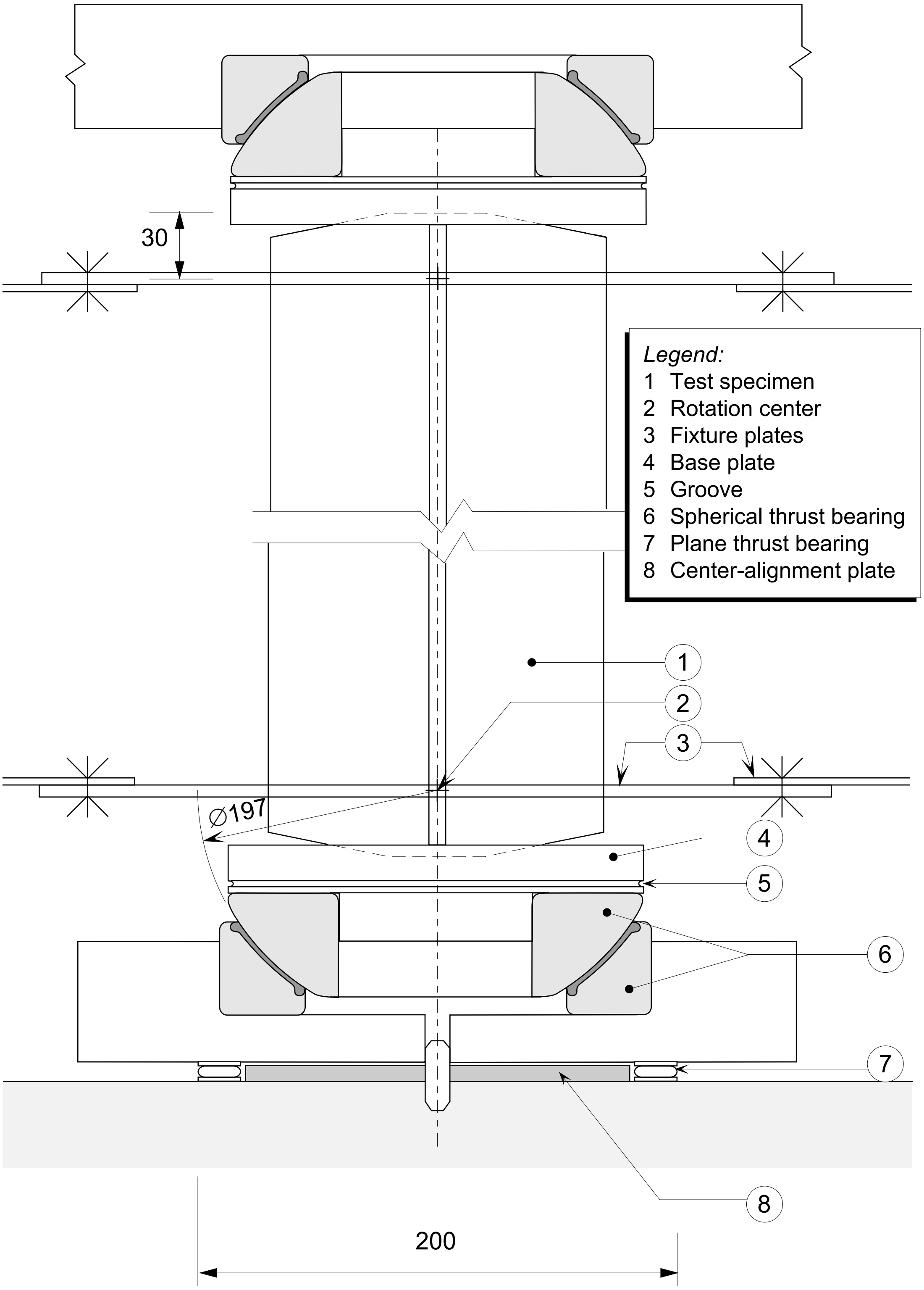

Figure 2.6: Part drawing of test specimen ends.

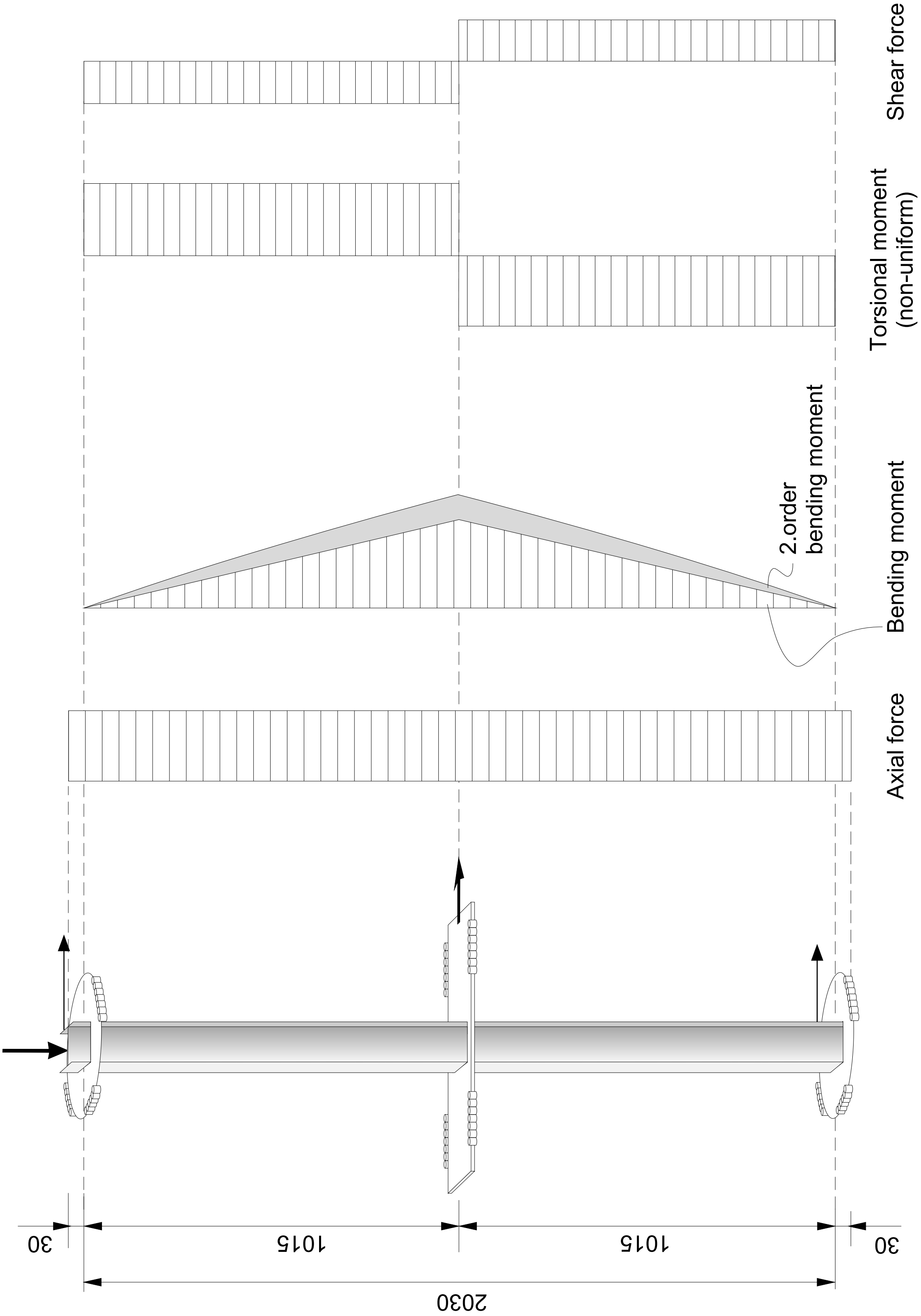

Figure 2.7: Force- and moment-diagrams.

the end fixture plates, and the forces are transmitted to the vertical loading frame through the large roller bearing at both end supports, see Figures 2.4 and 2.8. These bearings are designed to support large radial forces without preventing a simultaneous rotation due to torsional twisting of the test specimen.

The loading plate encloses the test specimen, and is mounted in a bracing frame that prevents its rotation and lateral displacement. In order to allow convenient insertion and removal of test specimens the opening in the loading plate is oversized and equipped with metal linings as shown in Figure 2.8. In addition to transmitting the transverse load, the loading plate has to balance the externally applied torsional moments for load combinations that include nonuniform torsion. The loading plate tends to rotate due to these moments, and at the same time the plate has to follow the displacement of the horizontal actuator without creating too much frictional resistance. This is achieved by a roller bearing where the loading plate and the adjacent part of the bracing frame have machined steel surfaces and are separated by cylindrical rollers. This is shown in Figure 2.5. Measurements of the friction force that can be developed are presented in Section 2.3.

Both the vertical and the horizontal actuator (Amsler) have hydrostatic bearings, are double-acting and have a maximum stroke of 200 mm. The actuator controllers are manufactured by Schenck, and provide ordinary actuator control, such as setting displacement limits and running tests by force or displacement control. The vertical and the horizontal actuator have a nominal dynamic capacity of 1000 kN and 400 kN, respectively. For static loading these limits can be exceeded by at least 20 %.

2.2.3 Torsional loading

Figure 2.4 shows the arrangement for the torsional loading. A hydraulic motor located at the level of each of the test specimen ends generates the torsional moment, and the moment is transferred to the test specimen by means of a roller chain. The force in the chain acts at a fixed distance from the specimen longitudinal axis. The torsional loading arrangement is symmetrically located at the ends of the test specimen, as shown in Figure 2.3.

Details of the rotating parts of the end supports are given in Figures 2.8 and 2.9. The end of the specimen is inserted into a quadratic steel plate located 30 mm from the end. This plate is 5 mm thick and has a rectangular opening that circumscribes the cross-section of the test specimen. The plate is again bolted to a 3 mm thick circular plate which is connected to a sprocket wheel. The sprocket wheel is engaged by a 1" roller chain driven by a smaller sprocket on the axle of the hydraulic motor. The sprocket wheel is an integrated part of the large roller bearing units at the end supports, and a cross-section of this bearing construction is shown in Figure 2.9. The bearing consists of machined steel surfaces separated by cylindrical rollers and balls. Under simultaneous torsion and transverse loading from a test specimen this bearing is subjected to an angular movement and a radial

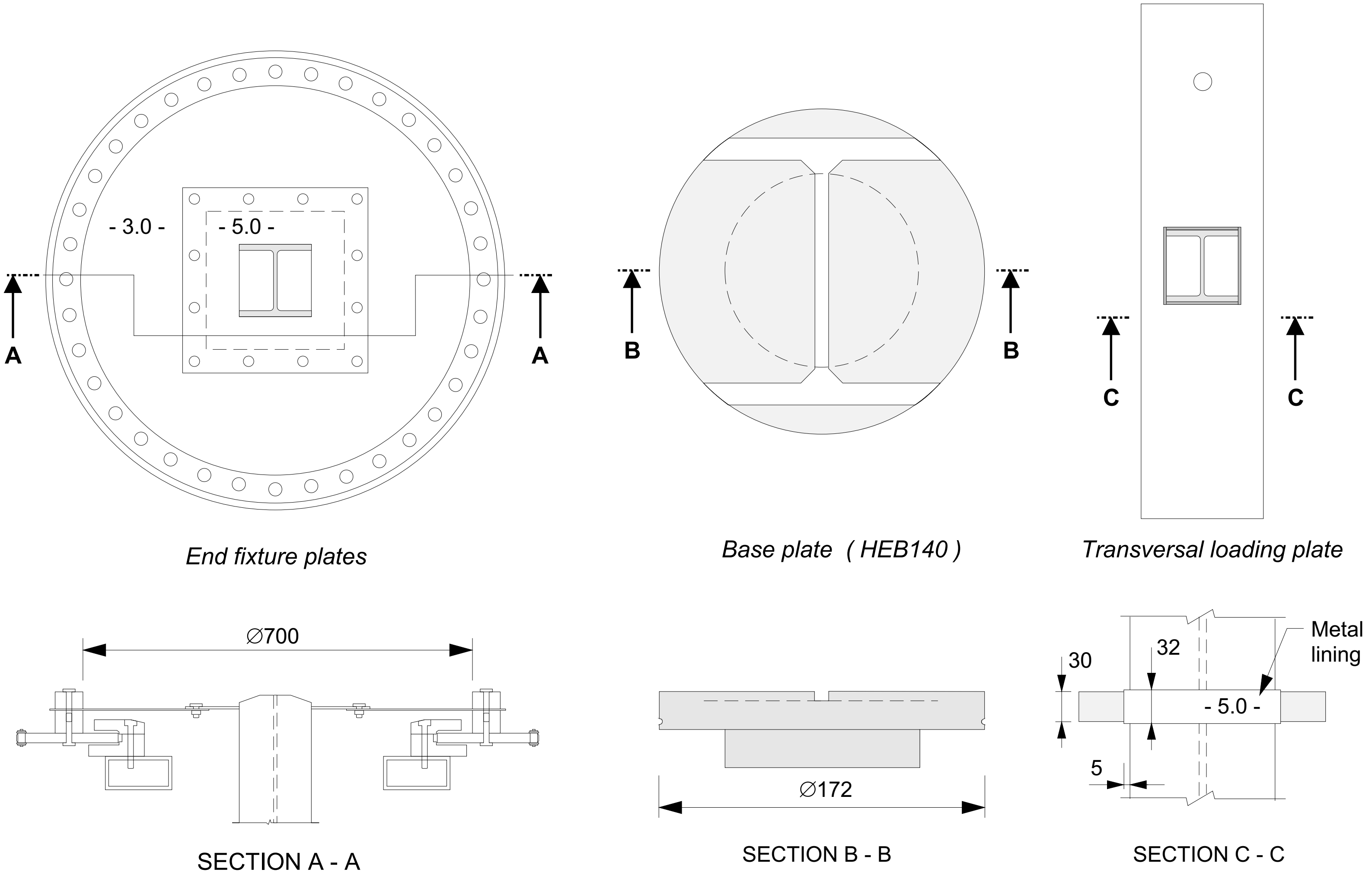

Figure 2.8: Details of end fixture plates, base plates and midspan loading plate.

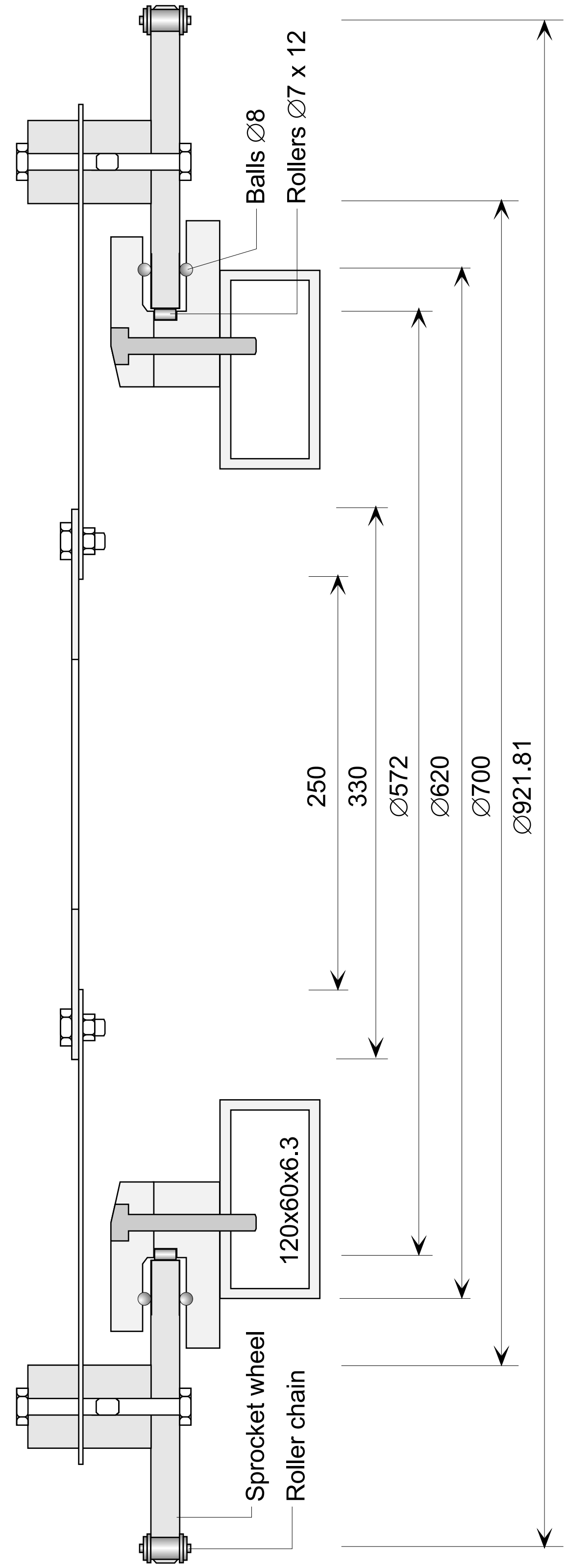

Figure 2.9: Cross-section of the bearing unit at the end supports.

force. A description of the bearing and a discussion of the resistance to rotation are provided in Section 2.3.

The torsional restraining arrangements at the specimen midspan, consisting of the loading plate for transverse load and the adjacent bracing frame, are shown in Figure 2.5.

Also when axial load is applied, the free rotation of the specimen ends about the longitudinal axis is ensured, by means of torsional bearings (or torsional "hinges") that give only a small torsional resistance. At the lower end of the test specimen this is obtained by a plane thrust bearing. This bearing is equipped with a center-alignment plate and a fixture bolt that keep the bearing assembled and centered, see Figure 2.6. At the upper end it is provided by the free rotation of the piston rod and the piston inside the hydraulic actuator. A discussion of the rotational resistance of these torsional bearings are presented in Section 2.3.

The hydraulic motors are manufactured by Riva Calzone, and are denoted MR300. The motor consists of five cylinders mounted in a star configuration on the motor axle, producing a smooth torque output and a high starting torque. The operation of the hydraulic motors is controlled by means of servo-valves, in the same manner as the linear (Amsler) actuators, feedback being provided by multiturn potentiometers on the motor axles or the load cells in the chains. The motors have separate RPD Howden controllers, in principle similar to the controllers connected to the actuators. The main elements of the controllers are; a servo amplifier, a ramp generator and a transducer amplifier. During the testing, one ramp generator is used to control both motors.

The hydraulic motors are originally not intended to be operated at the low speed range used in the present experiments. Due to the characteristics of the motors, they gave a slightly "stepwise" motion of the roller chains, and not as smooth motion as for instance provided by a linear actuator. The effect of this can be seen in the graphs for the test results, presented in Chapters 4 and 5. Taking Figure 5.10 as an example, it is seen that the curve for the measured/calculated torsional moment, $\overline{T}$-$\overline{\phi}$, has a somewhat oscillating behaviour.

The force from which the torsional moment is computed, is measured by the load cell in the roller chain (located near the motor). As the force is transmitted to the specimen through the chain, the large bearing unit and the end fixture plates, some of the measured oscillations in the force is hence due to inertia effects of these parts. For the tests with large axial loads, the oscillations are somewhat more pronounced, which is also due to the friction developed in the thrust bearings.

The observed oscillations are not believed to influence the obtained test results.

2.3 Bearing resistance

In order to calculate the forces acting on the test specimens information is needed about the frictional resistance in all bearings supporting the test specimen. A

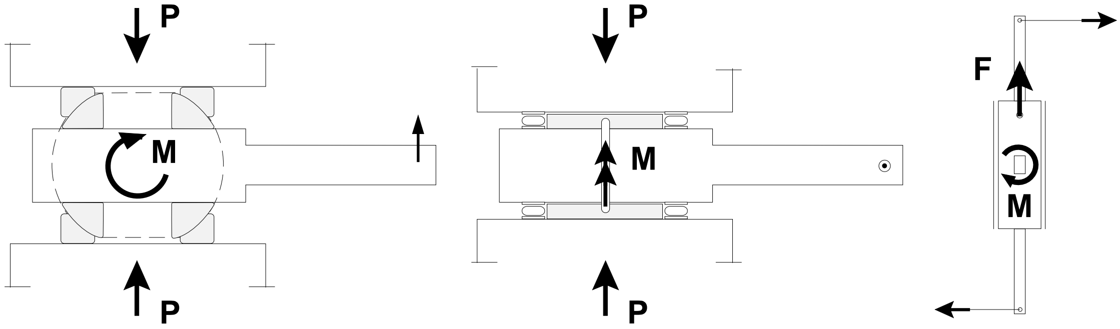

Figure 2.10: Test setup at frictional resistance tests

separate investigation was carried out in order to obtain required data for the resistance at various load levels. Figure 2.10 shows the principle of these tests.

Thrust bearings - bending moment "hinges"

These bearings are manufactured by SKF, and are denoted GX80F. They consist of a spherical cap and a ring-shaped casing, separated by a sliding surface. This sliding surface consists of a layer of glass fibre reinforced polyamide oiled with polytetrafluoroethylene. Prior to each test some extra lubricant was applied to the bearing surfaces.

The bearings were tested in a Losenhausen 3000 kN universal testing machine. As shown in Figure 2.10 the bearings were assembled to form a sphere, which was then subjected to compressive loading. The load required to rotate this sphere was measured, and the corresponding frictional moment was hence calculated. Maximum compressive load during testing was 800 kN. There was no significant difference between friction at rest and friction at motion. The frictional moment developed in each bearing was almost negligible, and can be taken as : $M_{Friction} = [0.2 + 0.001{\cdot}P(kN)]kNm$

Thrust bearing - lower torsional moment "hinge"

This was a SKF bearing denoted AXK160. It is a single-acting bearing consisting of two plain lipless stamped and hardened steel washers and a set of cylindrical needle rollers in star formation held together in a cage. The bearing was tested in the Losenhausen machine at load levels up to 800 kN, where two similar bearings were mounted as shown in Figure 2.10. The bearings showed a linearly increasing frictional moment when subjected to increasing compressive loads. The frictional moment in one bearing can be expressed as : $M_{Friction} = [0.000375 \cdot P(kN)]kNm$

Thrust bearing - upper torsional moment "hinge"

This torsion moment "hinge" consists of the piston rod and the piston rotating in the cylinder of the vertical actuator. The piston and the cylinder walls are separated by a thin layer of compressed oil creating a hydrostatic bearing. Such bearings are commonly considered to be almost without friction.

The frictional moment in this hydrostatic bearing was measured to be about 0.04 kNm for the unloaded actuator. The bearing was also tested using an ordinary test specimen mounted in the test rig. Axial load was applied, and the torsional moment required to rotate both the test specimen, the piston and the lower thrust bearing was measured. From this test, data for the total frictional moment in the Amsler actuator was calculated, and was found to be less than 0.2 kNm for the interesting levels of axial load.

Loading plate bearings

The midspan loading plate and the adjacent part of the bracing frame have machined steel surfaces and are separated by full-complemented rows of cylindrical steel rollers. Since the loading plate has to balance the external applied torsional moment and follow a movement of the horizontal actuator, the resisting transversal frictional force is of interest. A simplified friction resistance test was carried out in the test rig as shown in Figure 2.10. When subjected to a torsional moment of 6 kNm, approximately equal to the maximum moment during the experiments, the transverse frictional force F was less than 0.5 kN. A friction force of this magnitude has practically no influence on the experimental results.

End support bearings

The reaction forces due to transverse loading on the test specimen are absorbed by the large radial bearings at the end supports. The bearings were produced in the laboratory workshop from a structural steel St-52 and standard roller elements of bearing-steel grade. The large sprocket wheel constitutes the outer bearing ring, while the inner ring is fixed to the test rig. See Figure 2.9 for a detailed view of this bearing. The rotating parts are separated by a fully complemented ring of cylindrical rollers in the radial direction and balls in the axial direction. The bearing raceways are carefully machined and polished steel surfaces without hardening treatment. The rollers carry the main load and the balls guide the sprocket wheel.

The maximum applied radial force (R=H/2) results in relatively low local stresses at the contact points of the cylindrical rollers and the raceways. Calculations based on recommendations in Eschmann et al. (1985) shows that the loading is less than 50% of the admissible static rolling element loading, and the load dependent component of the frictional resistance can easily be calculated. The load independent part, i.e. the sliding resistance, was measured at the bearings. Due to an eccentricity of the radial load the balls have to balance a moment in the bearing, which might lead to a limited degree of misalignment of the raceways. Nevertheless, this should not cause any decisive increase in the total friction resistance. The expected total frictional resistance is small, and can be expressed as : $\mathrm{M}_{Friction} = [0.02 + 0.0003 \cdot \mathrm{R(kN)}]\mathrm{kNm}$

2.4 Instrumentation and measurement

Figure 2.11 shows a schematic view of the test setup and the types of, and locations of the instrumentation. All external loads are measured using load cells, displacements by means of inductive displacement transducers (IDTs) and rotations by potentiometers. All measurement devices were calibrated prior to the testing, and checked after the test program was finished.

2.4.1 Axial and transverse loads

The 1000 kN and the 400 kN actuators are provided with load cells having measurement ranges adapted to the nominal actuator capacity. Both load cells are exited by the 10 volt power supply within the Schenck actuator controllers. The largest load cell is a SENSOTEC 75, and the other is a BLH U3L, both with a load accuracy of about 0.2%.

2.4.2 Torsional load

As indicated in Figure 2.11, a load cell is placed at the tension side of the roller chains transmitting the torsional moment from the hydraulic motors. The other side of the chain loops is unloaded, but provided with a guide to keep the chain on the rail (Figure 2.4). The torsional moment applied to the test specimen ends is computed on basis of the force in these load cells and the constant eccentricity of the force. The geometry of the load cells is shown in Figure 2.12. They were manufactured in the laboratory workshop to meet loads in the range of 0-20 kN with a sufficient accuracy. They have a tension-coupon shape with a rectangular cross-section and foil strain gauges of type FLA-3 in a temperature compensated full bridge circuit. The load cells were individually calibrated and balanced while connected to their corresponding amplifiers. This was done in an Instron universal testing machine, where the load cells were attached to the grips using short pieces of the current roller chain.

2.4.3 Displacements

Transverse displacements

The transverse displacement of the test specimen is measured at the loading point at midspan, using an external IDT (inductive displacement transducer) mounted on a bar attached to the end support frames (Figures 2.11 and 2.1). A part of this measured displacement is hence due to deformations at the end supports. Due to the torsional rotation of the test specimen, the centroid of the cross-section was not accessible for direct displacement measurement at the end supports. Data on the flexibility of the end supports were obtained from control tests, where the physical

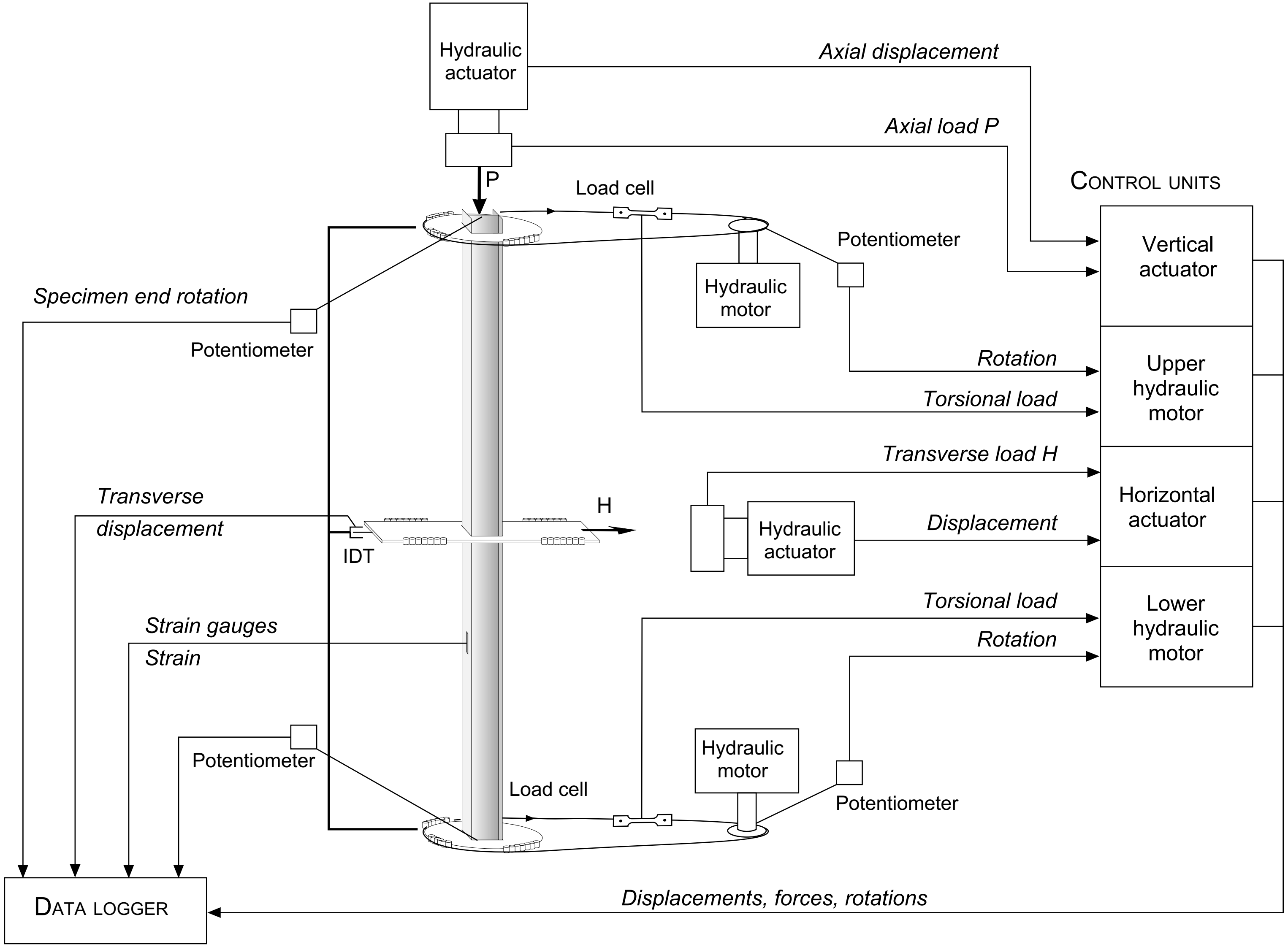

Figure 2.11: Instrumentation of test rig.

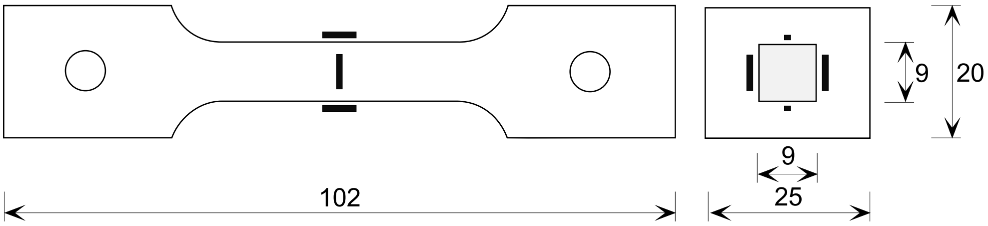

Figure 2.12: Load cell for torsional force.

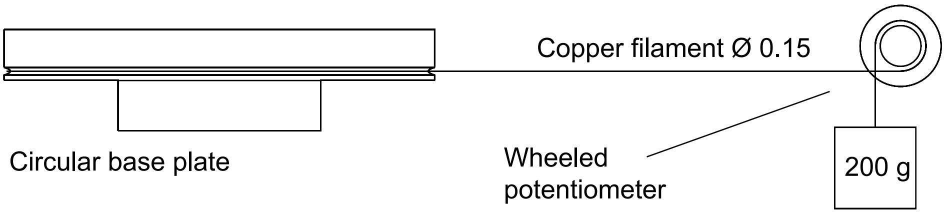

Figure 2.13: Rotation gauge for measurement of test specimen end rotations.

deflections were measured directly on a test specimen at various levels of transverse load.

An internal IDT in the horizontal actuator is used to monitor the position of the actuator piston. This provides duplicate measurements on the specimen displacements, even though significant elastical deformations of the loading and support arrangements are included in this displacement quantity. The operation of the actuator during the tests is based on the internal IDT.

Axial displacements
The axial shortening of the test specimen is measured by the displacement transducer in the vertical actuator. All tests are carried out with the axial load kept at a constant level, and the displacements measured in the actuator are hence equal to those of the specimen.

2.4.4 Rotations

The rotation about the longitudinal axis is measured directly at both ends of the test specimen using rotation gauges consisting of a grooved circular base plate, a copper filament and a multi-turn potentiometer with a pulley, see Figure 2.13. The rotation of the test specimen end is transferred to a rotation of the potentiometer, and the rotation angle can be read as an induced voltage difference. Calibration of these rotation gauges showed a linear and accurate behaviour. Potentiometers attached to the hydraulic motors provide duplicate measurements of the end rotations, and are used for the operation of the torsional motors.

The rotation flexibility of the loading plate and the bracing frame at the specimen midspan was measured in a control test.

2.4.5 Strain

Strains were measured in a conventional way by foil strain gauges glued to the test specimens at the relevant locations. TML electrical resistance foil gauges were used, both ordinary gauges and strain rosettes. Power was supplied to the strain gauges by the data logger.

2.4.6 Data acquisition

All electronic data were recorded using a Solatron datalogger. The system allowed a large number of channels to be scanned continuously, at a reading rate of 40 channels per second at the chosen resolution. All load cell, displacement transducer, rotation gauge and strain gauge measurements were recorded. In addition, the power supply for the strain gauges, the external IDT and the potentiometers were recorded to ensure that no considerable voltage fluctuation occurred. The recorded data were processed on a PC.

2.5 Test setup - load and support conditions

As mentioned above, there are two main objectives with these tests. The first is to obtain experimental data on the response of beam-columns when subjected to various combinations of axial load, bending and torsion. The second is to provide data for the cross-sectional resistance for two types of I-beam sections, limited to the load combination of axial force, torsional moment (warping) and a bending moment acting about the strong axis only.

The current test setup was chosen in order to give:

- A loading system without any limiting connections between the three load actions.
- Clearly defined loading and support conditions.
- One predefined section of the specimen with the largest load effect, and with clearly defined resulting forces.
- For that section, bending moment only about the strong axis.
- As few local disturbances as possible at the most heavily loaded section of the specimen, i.e. no welding or any other treatment.

Due to the chosen one-point transverse loading, there is a gradient in the bending moment along the test specimen, with a corresponding transverse shear force. Hence, when a plastic "hinge" is established, there is a gradient in the moment through the hinge. For the investigation of the pure bending part of the beam-column response, the commonly used two-point symmetrical transverse loading would be preferable, due to the advantages of the constant bending moment and less effect of strain hardening and local buckling (ASCE 1971). However, a two-point loading could not in practice be combined with the torsional loading.

When choosing the length of the specimens, both the bending moment gradient, the torsional conditions, the weak axis and the lateral-torsional buckling tendencies and the length to depth ratio of the beam-columns had to be considered. The chosen beam-column length of 2090 mm ensures that the tests can be carried out for the desired levels of the axial load and bending moment, and that plastification of the cross-section at midspan can be reached.

The effect of bending shear stresses are normally ignored in beam experiments. For the current tests, taking the case of pure bending loading as an example, the maximum value of the web shear stress is about 50% of the yield limit. For the tests with combined loading, this stress is considerably less and should not in any case affect the overall behaviour of the beam-columns significantly. In tests with torsion, the externally applied torsional moments are balanced by the restraining plate at midspan. The resulting compressive stresses at the contact points between the flanges of the test specimen and the linings in the restraining plate are very local, less than the yield stress and have a favourable direction, and are therefore considered to give no effect on the specimen response.

Chapter 3

Test specimens

3.1 Introductory remarks

This chapter describes the material and geometry of the test specimens, the cross-sectional dimensions and the mechanical properties of the materials. Most effort is spent to determine the stress-strain characteristics of the steel, focusing particularly on the yield strength and its variation over the cross-section.

3.2 Test specimens

The two shapes investigated in this study are the beam section IPE 160 and the wide flange section HEB 140. They are both hot-rolled sections made of semikilled mild structural steel, grade RSt 37-2 according to DIN 17100, Fe 360 BFN according to EN 10025 or similar to ASTM A283 Gr.D. The HEB 140 (denoted HEB in the following) is manufactured by a Norwegian steel mill (Fundia) and the IPE 160 (denoted IPE) is manufactured by Irish steel Ltd. Both shapes are cold-straightened in a standard rotorizing process after the hot rolling.

The steel was delivered in lengths of 12 meters, a total of 7 lengths of HEB and 5 lengths of IPE. The steel supplier provided steel materials with the lowest possible yield strength from the ordinary stock, in order to avoid limitations imposed by the test rig load capacity. Still, the measured mean yield stress was found to be about 25% above the specified minimum strength. The HEB lengths were all marked with the charge cast number while the IPE had no specific identification marks. Both the HEB and the IPE lengths were each declared positively to originate from one batch. The main elements of the chemical composition and the tensile properties of the steels are given in Table 3.1, based on information from the works certificate provided by the manufacturers. In this particular case the *upper* yield stress is given for the HEB section.

	C	Si	Mn	P	S	N	f_y/f_u
HEB 140	0.12%	0.23%	0.68%	0.025%	0.019%	0.006%	294 / 434 MPa
IPE 160	0.06%	0.21%	0.58%	0.021%	0.031%	-	302 / 410 MPa

Table 3.1: Chemical composition and tensile properties

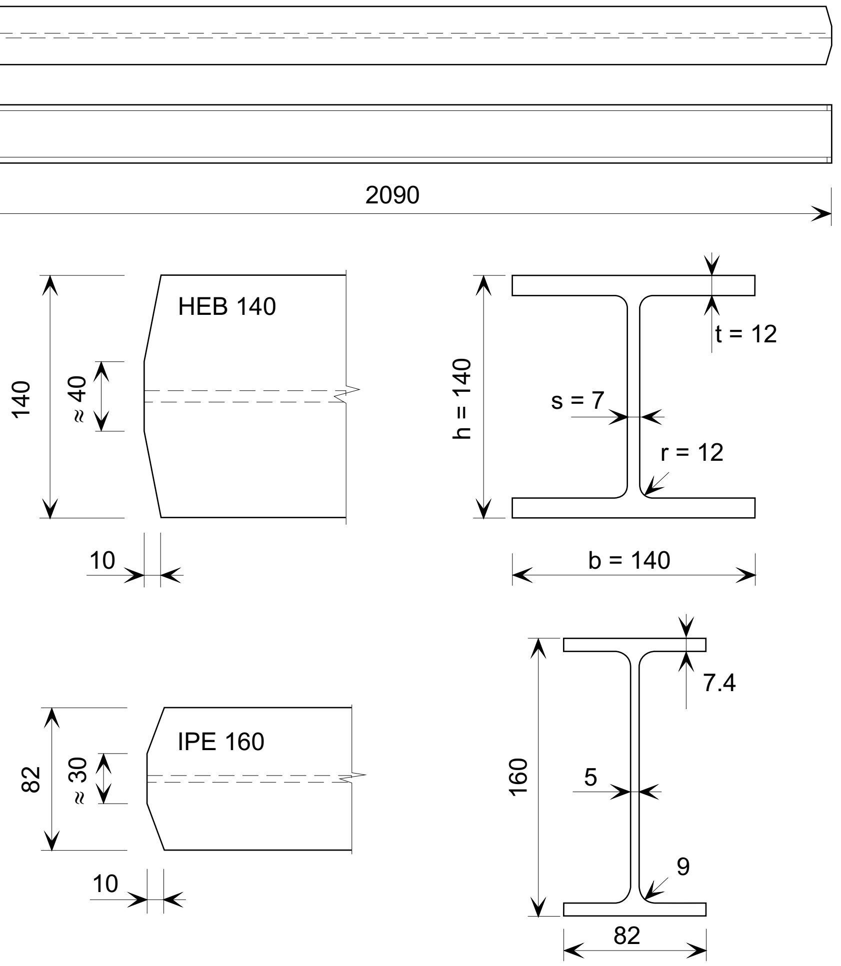

Figure 3.1: Test specimens HEB 140 and IPE 160, nominal cross-sectional dimensions.

Five test specimens were taken from each 12 meter unit, leaving shorter beam stubs for material testing. The preparation of the test specimens consisted of saw cutting and removal of the flange tips at each specimen end, and mill machining to provide plane ends. Except for this, the condition of the test specimen was as-rolled and rotorized. The test specimen geometry and the nominal cross-sectional dimensions are shown in Figure 3.1.

The cross-sectional dimensions of all 12 meter units were measured. The variation in flange and web thickness in the cross-section and the distortion of the sections were investigated. As usual (discussed in ECCS 1976), the flanges are thinner and the web is thicker than the nominal values, while the cross-section height and width deviate less from the nominal values. The torsional properties of the cross-section together with the weak axis properties such as the 2.moment

	b (mm)	h (mm)	t (mm)	s (mm)	A $(\mathrm{mm})^2$	$\frac{A}{A_n}$	$\frac{I_y}{I_{yn}}$	$\frac{I_z}{I_{zn}}$	$\frac{W_{py}}{W_{pyn}}$	$\frac{W_{pz}}{W_{pzn}}$
HEB 140	140.9	140.45	11.40	7.3	4190	0.98	0.98	0.97	0.97	0.96
IPE 160	83.2	160.2	6.83	5.6	2036	1.01	0.99	0.98	0.98	0.96

Table 3.2: Cross-sectional dimensions and properties

of area and the elastic and the plastic section modulus are most affected by this, while the corresponding strong axis properties and the cross-sectional area are closer to the nominal values. The measured dimensions and some of the cross-sectional properties for two representative cross-sections are given in Table 3.2. In the subsequent calculations and presentations of the beam-column test results the measured dimensions are used for each test specimen.

The initial longitudinal out-of-straightness of the members and the out-of-flatness of the sectional elements were measured for four units, each of 3.0 m length. Measurements were taken at both end sections and at three intermediate sections. The measured deviation from a straight line through the end sections was within 1.5 mm both for the section centroid and the flange tips. The initial longitudinal twist angle of the member axis was negligible.

3.3 Material tests

In the material tests, all load, strain and displacement measurements have an accuracy within 1% of the measured value.

3.3.1 Tension tests

The uniaxial tensile properties of the steels were determined from standard test coupons. Longitudinal test coupons were cut from various positions in the cross-sections and from some selected locations along the 12 meter units.

All coupons had a rectangular cross-section and were machined at all four sides at the reduced section, maintaining nearly the full thickness of the tested flange or web plate. The test coupons met the geometry specifications of a proportional test coupon, i.e. they had a machined parallel length L_C consisting of an *original gauge length* $L_0 = 5.65\sqrt{A_0}$ (minimum 25 mm) plus some additional transition length. The original gauge length was used only as a basis for calculating the percentage elongation after rupture ($\delta_{5.65}$). The dimensions of the tension coupons are given in Figure 3.2 and Table 3.3.

All tension tests were carried out on an Instron 250 kN universal testing machine using displacement control, with a preset deformation velocity. Strain, i.e.

Dimensions (mm)	L_C	L_0	B	b	t
HEB flange	125	95	35	26	11
HEB web	90	70	30	22	7
IPE flange	80	70	35	25	6
IPE web	70	55	30	20	5

Table 3.3: Geometry of tension test coupons

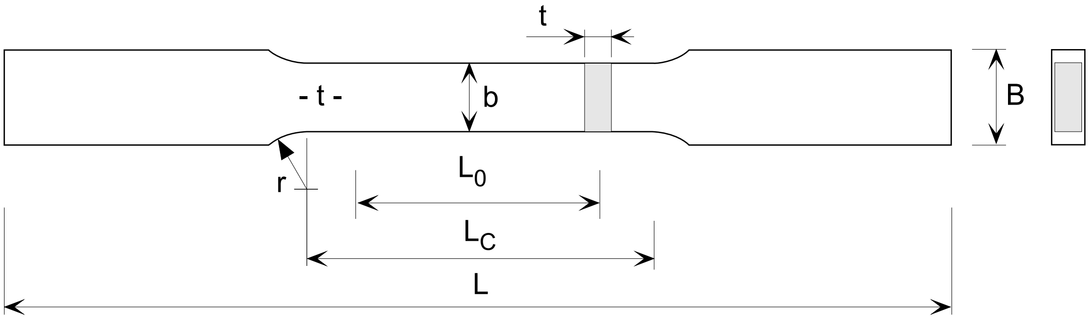

Figure 3.2: Test coupons for uniaxial tension tests

engineering strain, was measured by means of double-sided Instron extensometers. In the majority of the tests a 50 mm extensometer was used, but shorter extensometers were used for coupons with initial parallel length L_C less than 50 mm. Strain was measured with the extensometer up to a strain level 2%, beyond this level the Instron testing system determined the strain from the crosshead velocity setting, the time registrations and the initial length of the reduced parallel portion of the coupon. The coupons were tested at low strain rates in the elastic range and during the yielding of the material. At onset of strain-hardening, the strain rate was increased to reduce the time needed to complete the tests.

The strain rate in the beam-column tests was determined to vary mainly between $1 \cdot 10^{-5}/s$ and $1 \cdot 10^{-4}/s$ for the material involved in yielding. The majority of the tension coupons was therefore tested at a mean strain rate of $0.5 \cdot 10^{-4}/s$.

The cross-sectional position of the coupons is shown in Figure 3.3. A total of 40 coupons were taken from the HEB units and 20 coupons from the IPE units.

The HEB tests showed that the stress-strain curve differed significantly over the cross-section. The behaviour of the flange material was as expected for a mild structural steel, comprising a distinct yield-point elongation, while the web material near the web-flange junction showed no yield point in the stress-strain curve at all. This part also possessed an ultimate tensile strength as much as 25% higher than the remainder of the cross-section. The IPE tests showed that the flange and the web material had almost identical mechanical properties, with only a minor variation over the cross-section.

The yield strength varied consistently for the IPE and the HEB sections. Gen-

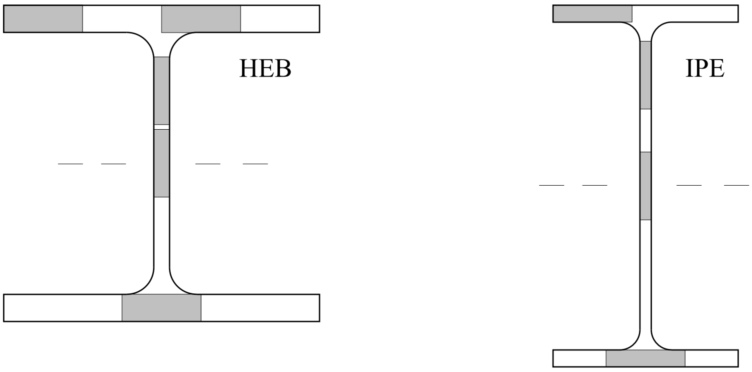

Figure 3.3: Location of tensile coupons on cross-section.

erally, the webs had a higher yield strength than the flanges, a difference of 3% was obtained for the IPE section. Furthermore, the yield strength of the flanges was highest at the flange tips. The measured yield strength at the flange tips of both sections was approximately 4% higher than the average for the flanges. These observations are consistent with similar investigations on semikilled steels (Alpsten 1970), and is explained from the difference in cooling rate, where the web and the flange tips cool faster than the rest of the section, resulting in a finer grain size and a higher yield strength. The rotorizing process did not seem to have affected the properties of the flange materials considerably, which was seen from practically constant elongation properties across the flanges of both sections ($\varepsilon_{yp}, \varepsilon_u, \delta_{5.65}$ in Figure 3.6).

Coupons taken from identical positions in the cross-sections showed only a small spread in the measured values. The values from 9 tested coupons taken at the flange tips of the HEB section can be taken as a representative example; mean yield strength 281 MPa, all measured values within a range of 17 MPa and a standard deviation of 5.8 MPa.

The mechanical properties obtained from the tests of the longitudinal coupons are summarized in Table 3.4. From the test, the yield strength f_y is taken as the mean stress in the yield plateau, neglecting any peak value at the start of yielding, and emphasizing the stress values in the first 2/3 of the yield plateau. The results in Table 3.4 are given as mean values for both flanges and for the web. The variation of the yield strength over the cross-section has to be considered when interpreting the beam-column test results in the following chapters.

Representative stress-strain curves for the flanges are shown for both sections in Figure 3.4, while the behaviour of the HEB web is depicted in Figure 3.5 (based on results from the following investigation). The central portion of the HEB web, position 4 in Figure 3.5, has a stress-strain curve similar to that of the flange material, while the behaviour of the rest of the web differs significantly. At web

	f_y (MPa)	f_u (MPa)	ε_{yp} (%)	ε_u (%)	$\delta_{5.65}$ (%)
HEB flange	279	438	1.6	20	34
HEB web, center	290	449	1.4	19	36
IPE flange	304	424	2.2	23	34
IPE web	314	425	2.6	21	34

Table 3.4: Mechanical properties of the HEB 140 and the IPE 160 beams.

positions 2 and 3 increased yield strength and decreased ductility are observed, both signs of cold-working during the rolling process. The lack of a yield point elongation for the web material closest to the web-flange junction, position 1, can be explained by a relatively higher extent of cold-work, whereas the large increase in ultimate strength might be a result from strain ageing caused by the lower cooling rate at this part of the section.

Variations in mechanical properties

The distribution of the strength and the ductility across the flange and the web plates was investigated in a separate test. To provide a higher resolution in the measured distributions, smaller test coupons were used than in the above investigation. Test coupons were taken from one HEB and one IPE stub as indicated in Figure 3.6, utilizing the entire actual part of the cross-sections. Proportional test coupons were used, the width was reduced with only 2 mm at the gauge length, and the coupons were the full thickness of the flange or web. The coupons were tested at identical strain rates. The measured mechanical properties are given in Figure 3.6.

Anisotropy tests

The hot-rolled beam sections are normally not expected to display anisotropy in the web and flange plates. However, a high extent of plastic work and severe deformation of the steel billets during the rolling process at improper temperatures may still lead to anisotropy in the tensile properties. The yield strength, and to a lesser extent the tensile strength, are most likely to display anisotropy (Dieter 1988), and the thinner web plate should be more affected than the flange if anisotropy exists.

A limited test programme was carried out to determine any possible anisotropy. Two tension coupons were taken from the beams at neighbouring positions, one coupon in the longitudinal direction of the beam and one coupon in the transverse direction, as indicated in Figure 3.7. The transverse coupons were much smaller than the standard tension coupons, and companion longitudinal coupons were hence given the identical geometry. Coupons were taken from the flange of both sections, from the center of both webs and from the part of the HEB-web next to the flange junction, as shown in Figure 3.7.

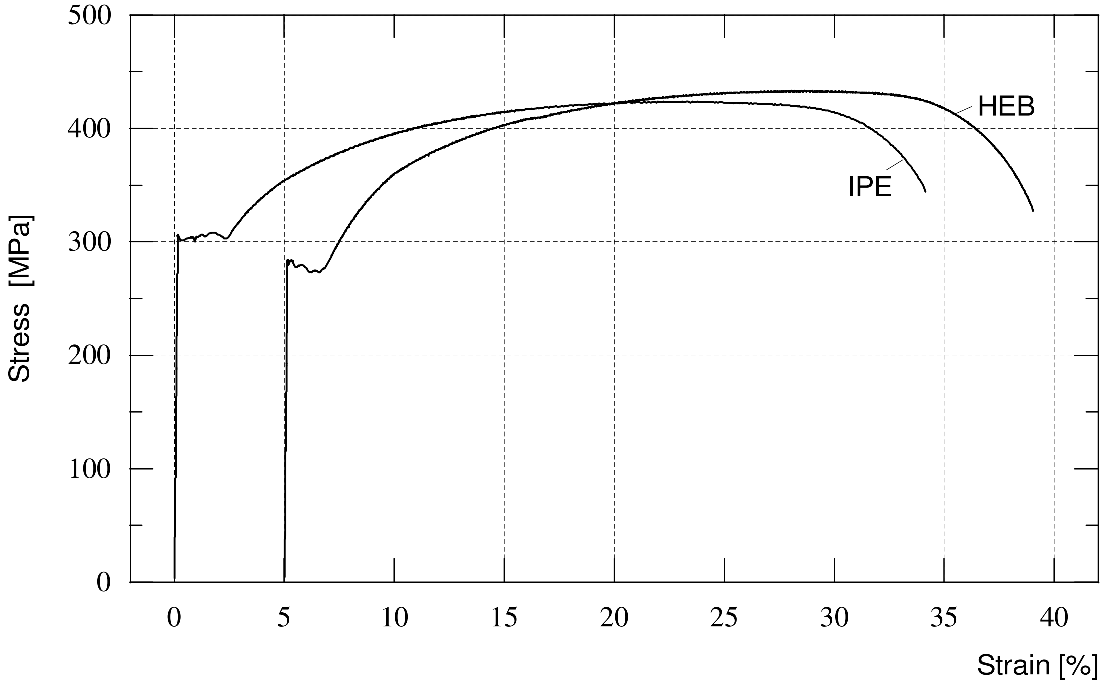

Figure 3.4: Typical stress-strain curves for IPE 160 and HEB 140 (flange coupon).

The tests showed no significant anisotropy in the stress-strain characteristics.

Modulus of elasticity

The modulus of elasticity (E) was determined from cylindrical tension specimens machined from the flange of the HEB and from the web-flange junction of the IPE section. The specimens had a parallel length $L_C = 80mm$ and a diameter equal to 8 mm, and were connected to the test machine by $12mm$ threaded grip ends. A double-sided extensometer was used, and care was taken to avoid possible effects due to curvature of the specimens.

Two companion test specimens from both sections were tested in a series of repeated loading and unloading up to load levels of 80% of the yield load. The two companion specimens gave practically identical results, and the modulus of elasticity was calculated to 210 GPa for the HEB and 207 GPa for the IPE steel.

3.3.2 Compression tests

Compression coupon tests

Compression coupon tests were carried out for the flange material of both sections. An Instron 100 kN servo-hydraulic testing machine was used, and the rectangular

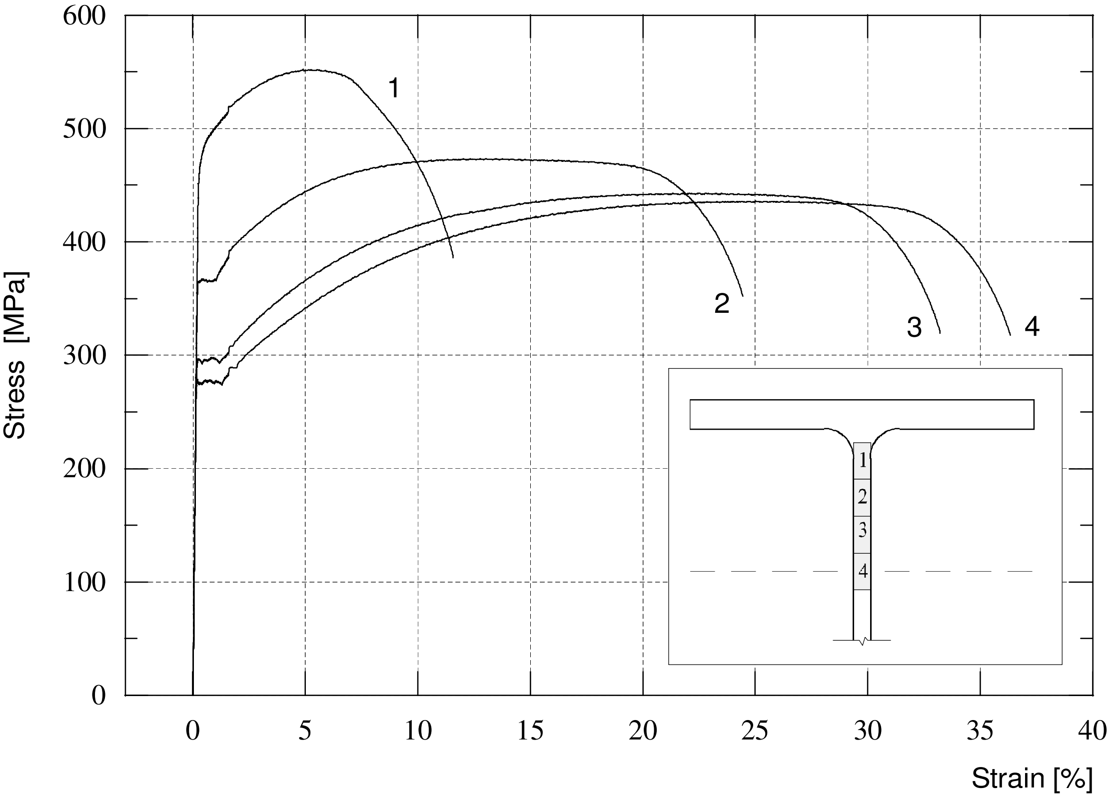

Figure 3.5: Stress-strain characteristics at different positions in web of HEB 140.

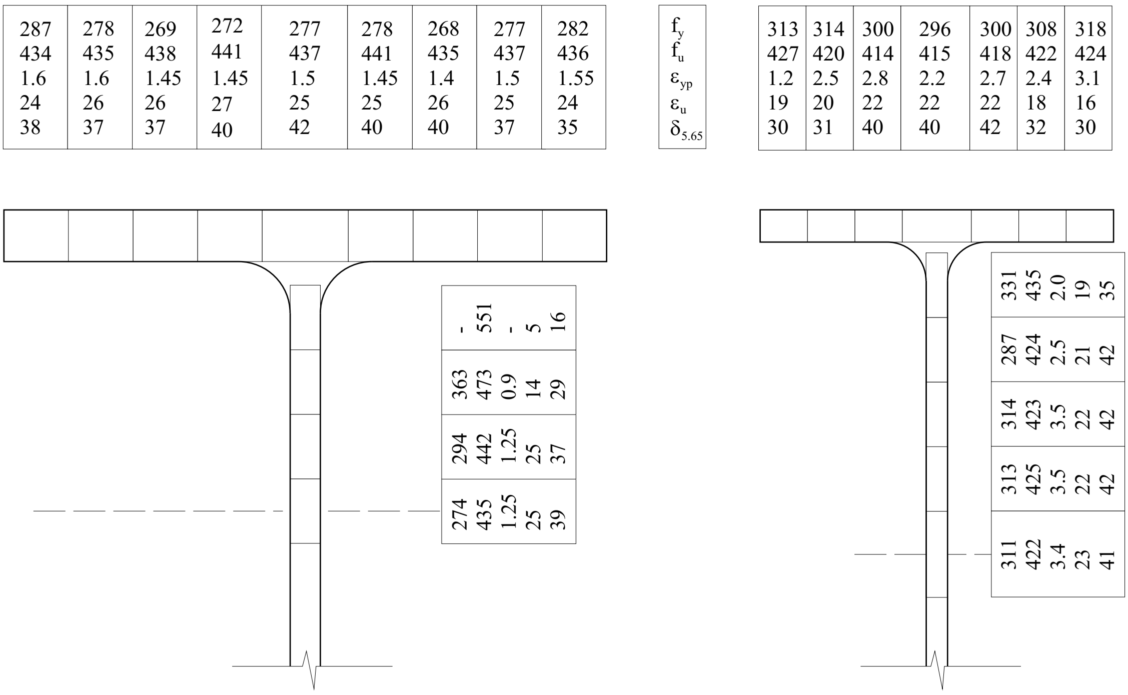

f_y	287	278	269	272	277	278	268	277	282
f_u	434	435	438	441	437	441	435	437	436
ε_{yp}	1.6	1.6	1.45	1.45	1.5	1.45	1.4	1.5	1.55
ε_u	24	26	26	27	25	25	26	25	24
$\delta_{5.65}$	38	37	37	40	42	40	40	37	35

f_y	-	363	294	274
f_u	551	473	442	435
ε_{yp}	-	0.9	1.25	1.25
ε_u	5	14	25	25
$\delta_{5.65}$	16	29	37	39

f_y	313	314	300	296	300	308	318
f_u	427	420	414	415	418	422	424
ε_{yp}	1.2	2.5	2.8	2.2	2.7	2.4	3.1
ε_u	19	20	22	22	22	18	16
$\delta_{5.65}$	30	31	40	40	42	32	30

f_y	331	287	314	313	311
f_u	435	424	423	425	422
ε_{yp}	2.0	2.5	3.5	3.5	3.4
ε_u	19	21	22	22	23
$\delta_{5.65}$	35	42	42	42	41

Figure 3.6: Variation of mechanical properties in HEB 140 and IPE 160.

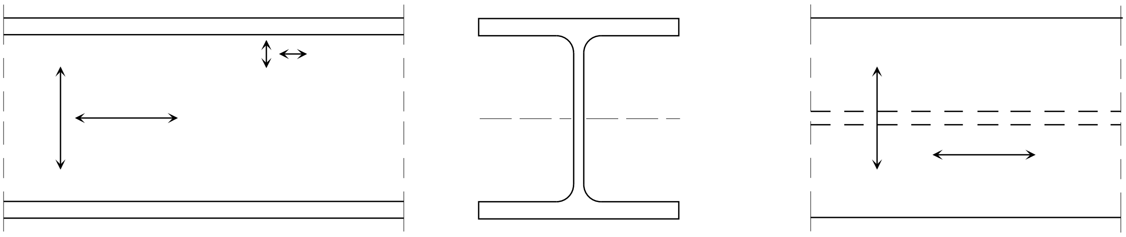

Figure 3.7: Location of coupons for anisotropy tests.

test coupons were attached to the machine by hydraulic grip-heads, i.e. clamped coupon ends. The coupons had a relatively short length L_C in order to avoid buckling, and were carefully machined and aligned before testing. Post yield strain gauges were attached to two opposite coupon surfaces for strain measurements, and the strain rate was the same as for the tension tests. Two coupons from the flange of both sections were tested. The measured yield strength based on these tests was as expected almost exactly the same as measured in the tension tests. The main difference from the tension test was the appearance of a sharp upper yield point about 10 to 15 percent higher than the average yield strength, which probably was caused by more careful machining and alignment of the test coupons and the use of a different and stiffer test machine.

Stub column tests

The mean yield strength in compression for the entire section was obtained by stub column tests, i.e. compressive loading of short columns into the inelastic range of the material. The length of the columns was chosen short enough to avoid buckling before reaching the yield load of the section, and sufficiently long to provide some information about the residual stress level of the section.

The tests were carried out on a Losenhausen 5000 kN servo-hydraulic testing machine, and load was imposed at a constant rate of deformation. A simplified view of the test setup is shown in Figure 3.8. The axial displacement, u, was measured by three inductive displacement transducers individually spaced 120 degrees along a circle, mounted on a collar enclosing the stub column. The stub column ends were carefully machined to give plane end sections, and base plates of hardened steel were used. The upper pressure platen of the test machine was equipped with a spherical thrust bearing, and the stub column was carefully centred. Any axial load eccentricities should therefore be minimized. The tests were performed at a deformation rate 0.03 mm/minute, which produced a mean strain rate somewhat lower than in the tension coupon tests. Data for the strain-rate sensitivity was obtained by varying the deformation rate in two of the tests (as described by Dieter 1988).

Representative curves from a total of 6 stub tests are shown in Figure 3.8. The load is made dimensionless by means of the measured cross-sectional area and the mean cross-sectional yield strength obtained from the tension coupon tests. Here, a yield strength of 286 MPa is used for the HEB section and 308 MPa for the IPE section. The test results are corrected to compensate for the strain rate effects, an increase of 3.8% is used for the HEB stub tests and 2.8% for the IPE stub tests.

The results from the compression stub tests agree very well with the results obtained from the tension coupon tests.

One of the HEB stubs was held at a constant deformation level for 5 minutes (strain rate zero) as shown in the figure. The load dropped to a level of about 95% of the yield load, which should be the *static yield load* of the cross-section. The 5% decrease in load illustrates the importance of using compatible strain rates when

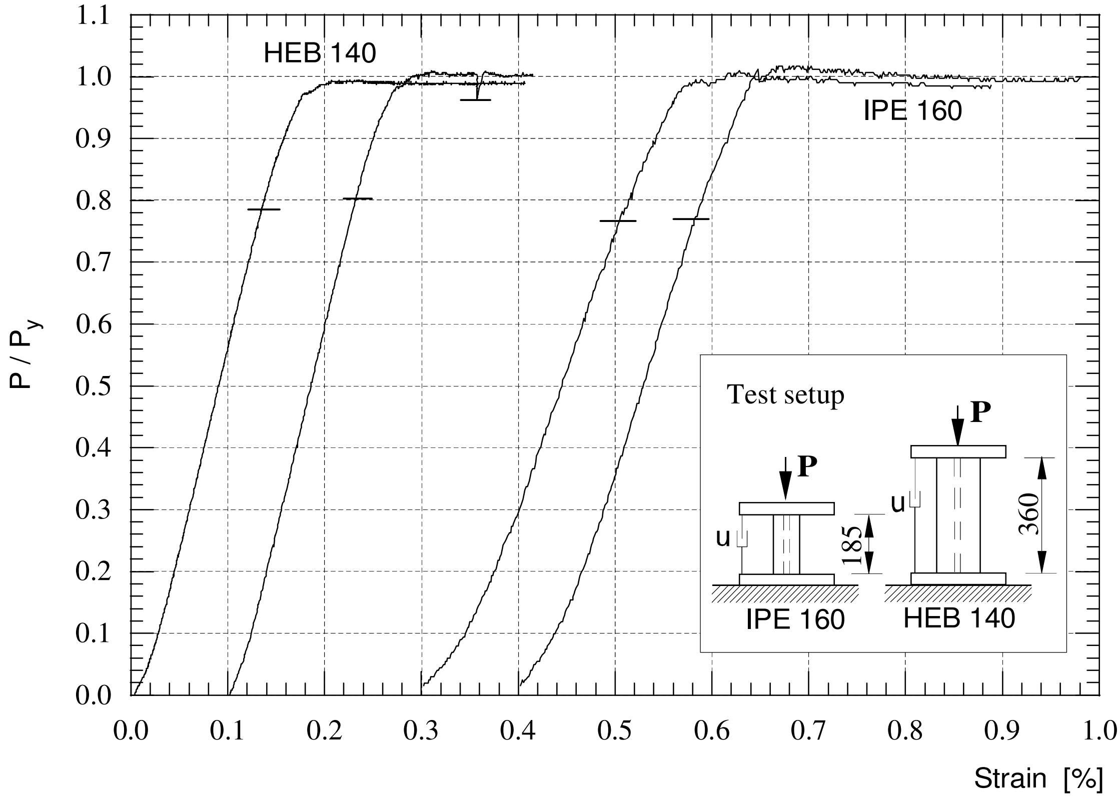

Figure 3.8: Stub column tests

comparing experimental results which involves material yielding.

3.4 Residual stresses

The typical residual stress distribution for the IPE and HEB sections is quite labour intensive to find, and hence only a limited study is carried out. A large number of measurements and studies has been made in the past, many references can be found in ECCS(1976) and Alpsten(1970).

The magnitude and distribution of *thermal* residual stresses in rolled shapes are mainly dependent on the geometry of the cross-section, and can to some accuracy be calculated from formulas found in the literature. The cold-straightening of the shapes after the rolling, the continuous rotorizing process, consists of controlled bending about the cross-section minor axis imposed by passing the shape through a series of rollers. In this operation *bending* stresses are superimposed on the *thermal* residual stresses and the flange residual stresses are redistributed for the whole profile length, except for a shorter part at the ends.

Alpsten (1970) has carried out an investigation concerning the mechanical properties and residual stresses in a shape of type HEA 200, whose geometry is quite similar to that of the HEB 140. His study of a normally-heavy cold-straightened HEA 200 shows a tooth-edged distribution of the residual stresses along the plates (i.e. flange and web) in the cross-section, and a considerable variation of the stresses through the thickness of the plates. Compared to residual stresses in as-rolled condition, the residual stresses are totally redistributed in the flanges of the straightened member, while the web shows a stress pattern more similar to that of as-rolled members. The average stresses in the flanges are very small, still with predominant compression stresses at the flange tips and tension at the flange middle, and the web has a local high stress peak near the fillets at the web-flange junctures. At this location the difference in stress level through the web thickness ranges from near yielding in tension at one side to yielding in compression at the other side.

Stub column tests

The magnitude of the longitudinal residual stresses in the present sections can to some extent be estimated from the stub column tests. The length of the stub column specimens was chosen equal to 10 times the minor axis radius of gyration ($\lambda = 10$), for shorter specimens the initial residual stress pattern may be disturbed (CRC 1961). A study of the load vs strain curves in Figure 3.8 shows a distinct deviation from a linear elastic response at points marked. This proportionality limit lies about 20-30% below the yield load for both sections, and this indicates that the residual stress value in substantial parts of the cross-section reaches 20-30% of the yield strength. This corresponds to residual stresses up to 90 MPa, which is considered to be low.

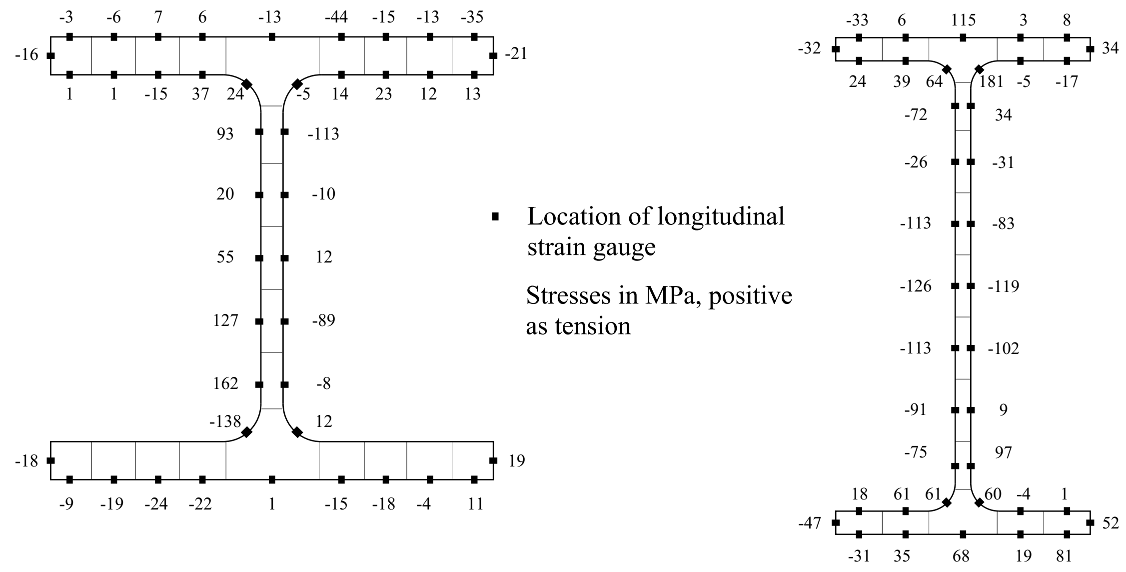

Figure 3.9: Measured residual stresses for HEB 140 and IPE 160

Sectioning

A limited investigation was carried out in order to obtain some data on the residual stress distribution over the cross-sections. Residual strains were measured using the plate sectioning technique. Foil strain gauges with a gauge length of 6 mm were bonded to opposite sides of the flange and web plates, and initial strain readings were taken. The plates, fitted with the strain gauges, were sliced into 14-20 mm wide and 40 mm long plate strips to release the residual strains, and the longitudinal stress was calculated from the measured strain. The results from one test on both sections are presented in Figure 3.9. Measurements on one of the other IPE-beams showed almost the same magnitude and distribution of the residual stresses in the web, and higher stress values in the flanges. It should be noted that due to the straightening process the residual stress distribution may vary considerably along the length of a beam.

Chapter 4

Torsion - experiments and analyses

4.1 Introductory remarks

As a special case of response of structural members subjected to load combinations consisting of torsion, bending and axial loading, there is a considerable interest in the response to single torsion loading.

Generally, the resistance of structural members to torsional loading can be considered to be the sum of two components. Consider an I-section beam, uniform in cross-section, subjected to opposed torsional moments at the ends. When there is no restraint against longitudinal displacement at any point along the beam, the warping of the cross-section is allowed to become uniform throughout the beam length, and the rate of change of the angle of twist becomes constant along the member. The resulting state of deformation is denoted *uniform torsion*. In this case, the torsional moment acting at any cross-section is resisted by a set of shear stresses distributed around the cross-section, with a constant distribution along the beam. In the elastic state, this case is also referred to as "St. Venant torsion".

If the longitudinal displacements are restrained or prevented at any location due to the support or loading conditions, the torsional loading results in twisting of the beam accompanied by warping that varies along the beam, and the result is *nonuniform torsion*. The torsional moment is then resisted by additional bending-shear stresses caused by the restrained warping, stresses which act in conjunction with those due to uniform torsion. If the resistance due to the restrained warping completely dominates the resistance due to uniform torsion, the member is in a limiting state of nonuniform torsion referred to as pure warping torsion (Trahair and Bradford 1988).

This chapter presents the results from torsion experiments on bars of three different cross-sections, the two I-beam sections used in the main experimental series and a rectangular bar section. The tests are carried out until the section is fully plastified, which involves large twisting deformations. The experiments with the I-beams include both an uniform torsion test and a nonuniform torsion test, whereas the flat bar was tested only in uniform torsion. The experimental results are compared with finite element (FE) simulations in order to investigate to what extent and accuracy the torsional response can be predicted by the use of an existing nonlinear FE program. Both a shell and a beam model of the I-beams are used in this investigation.

4.2 Torsional analysis

The analysis of torsional problems has a long history. The basic contributions are the study of uniform torsion of elastic beams by Saint-Venant, the membrane analogy introduced by Prandtl, the sand-heap analogy of Nadai and the engineering theories by Timoshenko and by Vlasov. These solutions of the torsion problem are based on simplifications regarding material behaviour and geometry effects, but provide valuable information about the elastic torsional stiffness of a member, the torsional moment at onset of yielding and estimates of the fully plastic moment. No analytical solutions for the torsional behaviour that takes both nonlinear material and geometry effects into account have been obtained.

The inelastic behaviour of I-shaped steel members subjected to torsion has been investigated experimentally only by a few authors. Uniform and nonuniform torsion tests on I-beams were carried out by Boulton (1962) on a rolled 3 in. by 1.5 in. cross-section, nonuniform torsion tests by Dinno and Gill (1964) on a 5/8 in. by 5/8 in. cross-section machined out from a solid bar, and by Farwell and Galambos (1969) on a 6 in. by 6 in. wide flange section.

Approximate methods to calculate the fully plastic torsional moment for an I-section beam with warping restraints were proposed by Boulton (1962), Dinno and Merchant (1965) and by Augusti (1966). A lower bound solution was presented by Boulton, while Dinno and Merchant presented an empirically based solution known as Merchants upper bound. Boulton also presented an interesting lower bound solution that describes the increase in torsional moment when an I-beam is subjected to large uniform torsional rotations. The solution is based on assumed tension and compression zones of the beam section that arise from the helical curvatures (i.e. nonlinear geometry effects).

Recently, a "mitre model" for the shear strain distribution in I-section beams in uniform torsion was presented by Billinghurst et al. (1992). This model gives an approximation for the complete inelastic torsional moment-twist relationship (elastic-perfect plastic material), with an accurate approximation for the elastic stiffness and a fully plastic moment similar to that given by the sand-heap analogy.

Both the geometrical and material nonlinearities due to torsion can, to some extent, be taken into account by the use of existing general purpose finite element formulations. The restrained warping of open section beams is often modelled by beam elements having an extra "warping" degree of freedom or "warping" springs. The geometrically linear and nonlinear torsion theories for beams in the elastic range are considered to be well developed, but the extension to the case of material nonlinearities is not as well advanced (Chen and Trahair 1992). One of the major problems is the modelling of the torsional shear stress distribution over the cross-sections, and how to account for these stresses in the elastic–plastic constitutive equations of the material. Some of the recent contributions on beam elements for nonlinear inelastic torsion are those of El-Khenfas and Nethercot (1989), Chen and Trahair (1992) and Pi and Trahair (1994a).

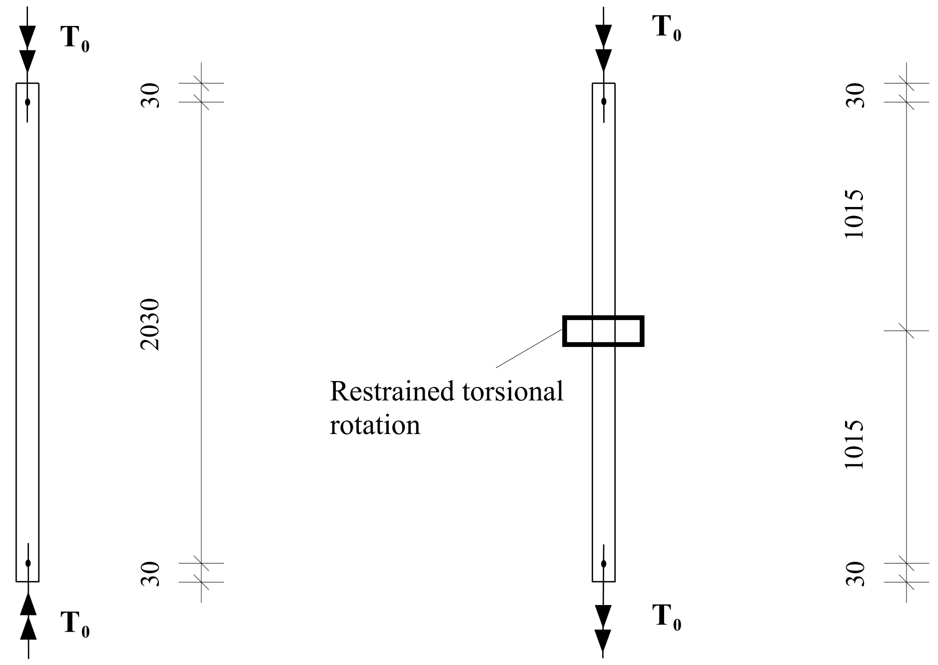

Figure 4.1: Uniform and nonuniform torsion tests.

4.3 Experimental investigation on torsional behaviour

The torsion tests of the present investigation were all conducted in the test rig described in Chapter 2. Only the torsional loading and supporting parts of the test rig were used. The load and support conditions of the torsion tests are shown in Figure 4.1. The total length of the specimens was 2090 mm, and concentrated torsional moments (T_0) were applied 30 mm from the free ends.

In the tests with uniform torsion, equal and opposite directed moments were applied to the specimens, resulting in a span of 2030 mm loaded with a constant torsional moment $T=T_0$.

In the nonuniform torsion tests the specimens were restrained against torsional rotation at midspan (please note the symbol), and the specimen ends were given equal rotations, both in direction and magnitude, about the longitudinal axis. In principle, this produced equal torsional moments $T=T_0$ in the upper and lower half of the test specimens. Hence, provided that the specimen ends are given exactly equal rotations, the chosen test setup models the torsionally simply supported beam (length L) subjected to a midpoint torsional moment of $2T_0$, or two torsionally fixed cantilevers (length L/2) that meet in the midpoint of this beam (see Appendix A).

Details of the bracing arrangement at midspan is shown in Figure 2.5. Briefly described, the bracing consisted of a 30 mm steel plate, fixed in space and with a

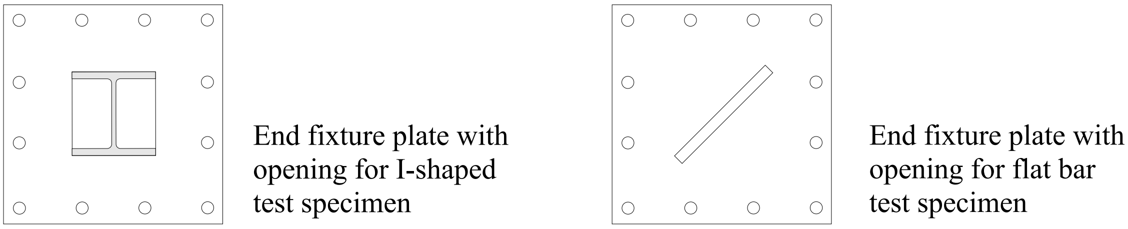

Figure 4.2: End fixture plates used in torsion tests.

rectangular opening that the specimen passed through.

The torsional deformations at the ends of the specimen were imposed by means of the circular and rectangular end plates shown in Figures 2.4 and 4.2. The end plates were not connected to the specimen. This lack of connection and the small lateral stiffness of the end plates result in a practically negligible restraint against axial or warping displacements of the test specimen at the loading points. Hence, no resultant axial force could be developed in the test specimens, even at large twists. A photograph from the test on a HEB 140 beam is given in Figure 4.3, showing the test setup and the large extent of twisting applied to the specimens.

The chosen loading arrangement transmits the torsional moments to the specimen by compressive contact stresses, resulting in a stress distribution in the test specimen near the loading point which differs from those in the cross-section some distance from the loading point. The size of the stress transition-zone is estimated to be about the size of the outer dimension of the actual section. For the HEB 140 beam tested in uniform torsion, this means that about 85 % of the specimen length has strictly uniform torsional conditions, i.e. perfect uniform twist and perfect uniform internal stress distribution, as assumed in the St.Venant torsion theory. A study of the stress distribution near the support and loading points of the specimens, obtained by the FE analyses, indicated that the actual length of the stress transition-zone is about 50% of the largest cross-sectional dimension of the specimen.

4.3.1 Experiments

A total of 10 specimens were tested. Four tests were carried out on the HEB 140 beam, namely one test with uniform and three tests with nonuniform torsion. For the IPE 160 two tests were performed, one in uniform and one in nonuniform torsion. In addition, four flat bar specimens with cross-sectional dimensions $15.3\text{mm} \cdot 200\text{mm}$ were tested in uniform torsion.

The material properties of the HEB and the IPE beams are as presented in Chapter 3, and cross-sectional dimensions as given in Table 3.2. However, note that the HEB 140 section had a measured web and flange thickness equal to 7.30 mm

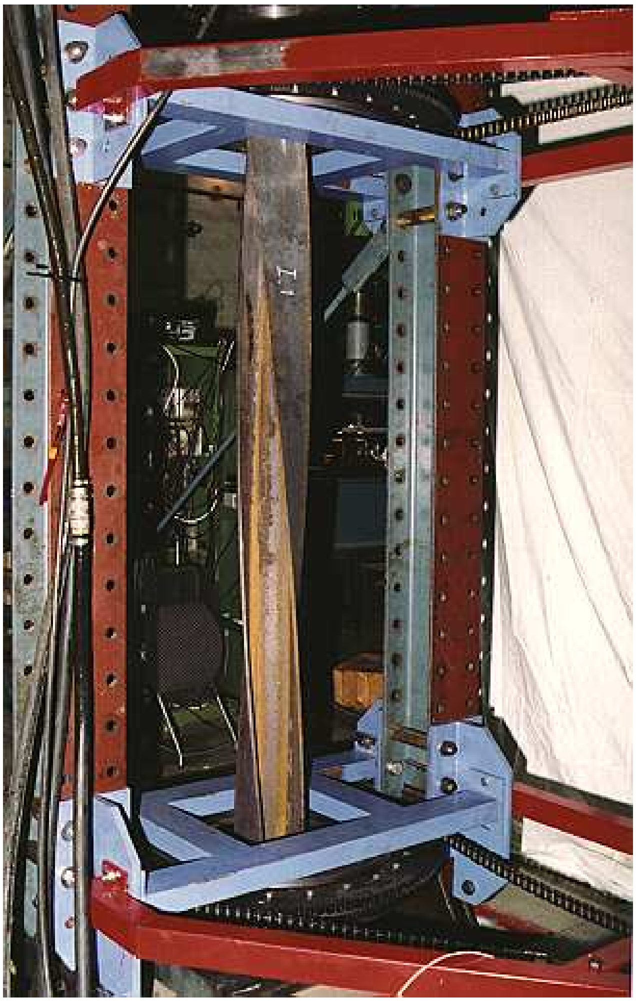

Figure 4.3: Uniform torsion test on a HEB 140 beam.

and 11.64 mm, respectively, for these specimens.

The tensile properties of the flat bar steel were determined by testing 10 tension coupons, 8 coupons taken parallel to the bar axis and 2 coupons in the transverse direction. The coupons were the full thickness of the bar section. The mean longitudinal yield stress of the bar steel was 275 MPa, and the mean yield point elongation (ε_{yp}) was 2.0 %. The yield strength at the edges of the bar section was about 4% higher than in the central part. No anisotropy was detected in these tests.

The torsion tests were run at a constant rate of twisting, applying a constant rate of rotation of the specimen ends, each test lasting about 30 minutes. The tests were carried out to large angles of twist, in the uniform torsion case up to more than 180°. For comparison it can be noted that the proportionality limit for rotation in uniform torsional loading is approximately 20° for the HEB beam. Consequently a large part of the sections was plastified during the tests. The angle of rotation was measured only at the end sections of the specimens.

4.3.2 Test results on uniform torsion

The results from the uniform torsion tests are presented in Figures 4.4, 4.5 and 4.6. The graphs depict the applied torsional moment ($T = T_0$) vs the total twist rotation measured over the full specimen length of 2090 mm. The experimental results are compared to the fully-plastic torsional moment given by Nadai's sand-heap analogy, the elastic response in uniform torsion

$$T = \phi_x \cdot \frac{GI_T}{L} \tag{4.1}$$

and the proportionality limit based on the first yielding (initial yielding) of the steel, using the von Mises yield criterion and the St.Venant shear stress distribution. The sand-heap capacity of the I-sections is computed neglecting the effect of the fillets (Equation 6.1). For the torsional rigidity, however, the effects of the fillets are included (El Darwish and Johnston 1965).

During the tests there were no indications that the boundary conditions differed from those assumed. Even at large twists there were no significant deflection or bending of the end fixture plates, indicating that the specimen was not subjected to any axial force or warping restraints.

The experimental results agree quite well with those from theory. The main exception is the 10% increase in the elastic stiffness in the HEB test and the almost linear elastic response that exceeds the proportionality limit by almost 20% in the test with the flat bar. It should be pointed out that the test on the HEB beam is a single test, while the results presented for the flat bar represents one of four identical tests with almost identical results.

When calculating the proportionality limit for the flat bar, the mean yield stress of the entire section is used as yield strength for the steel at the surface. As reported

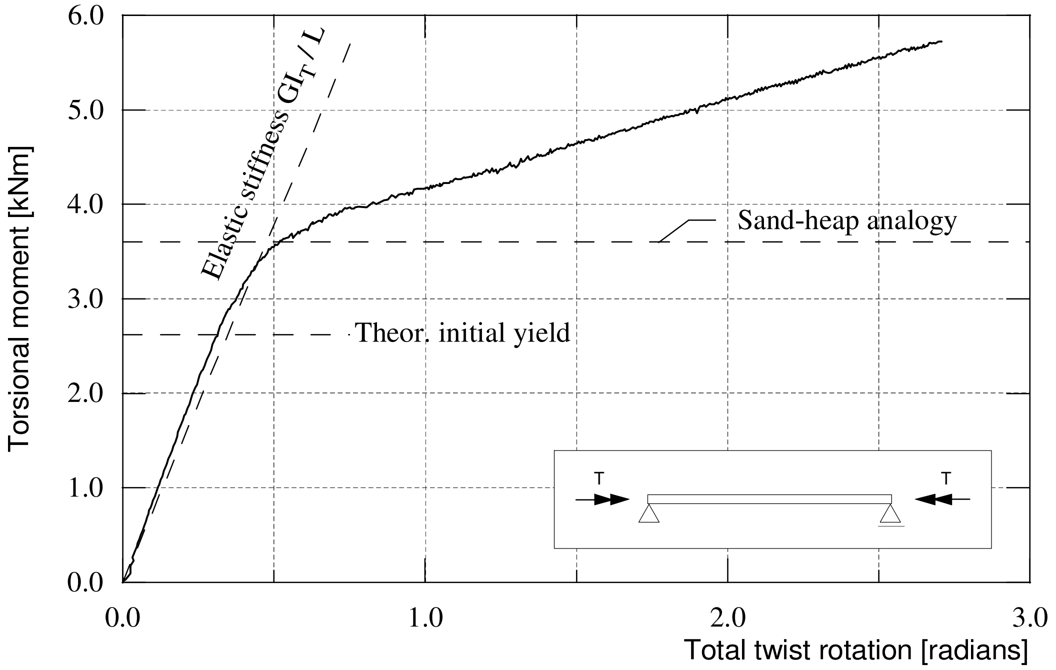

Figure 4.4: Uniform torsion test on HEB 140 beam.

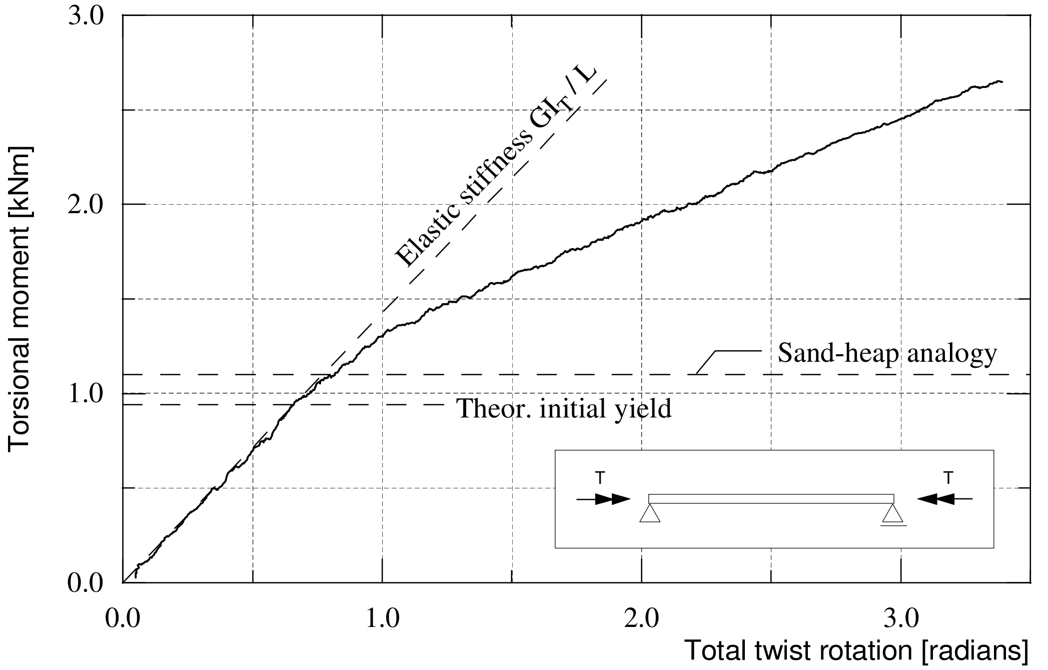

Figure 4.5: Uniform torsion test on IPE 160 beam.

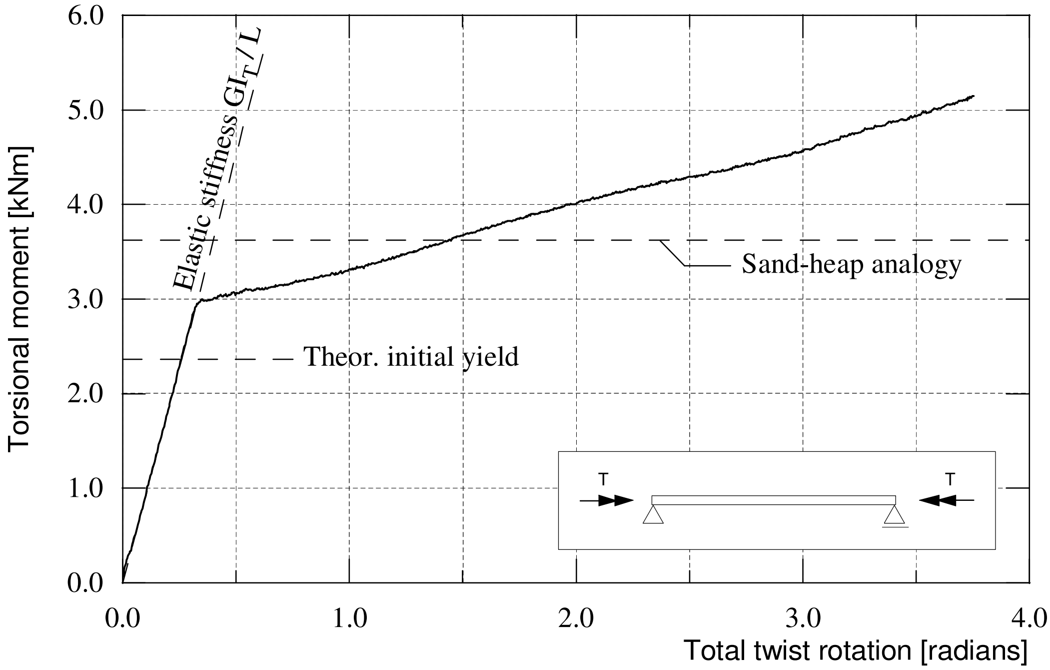

Figure 4.6: Uniform torsion test on flat bar section 15.3 mm * 200 mm.

by Alpsten (1967), the actual value of the yield stress at the surface of an element is commonly somewhat higher than the average stress, with a variation through the thickness of the same order as the variation across the width. According to his experimental data, a 4-9% higher yield stress can be expected at the surface, which for the flat bar should give a similar increase in the proportionality limit. However, this increase does not fully explain the overshoot of the theoretical value in Figure 4.6.

In the inelastic range, no distinct yield capacity or collapse moment can be defined for any of the tests. Instead, there is a steady and almost linear increase in the torsional moment with increasing twist, and the sand-heap capacity does not represent an upper limit for neither sections.

4.3.3 Tests results on nonuniform torsion

The experimental results from the nonuniform torsion tests are presented in Figures 4.7 and 4.8. Both specimen ends were given equal and linear increasing rotations, and the moments measured at the two ends did not differ significantly. The graphs show the applied torsional moment at one end plotted against the angle of twist measured at the same end section, i.e. due to the twist over the half length of the specimen. The theoretical elastic stiffness and the limit of proportionality are

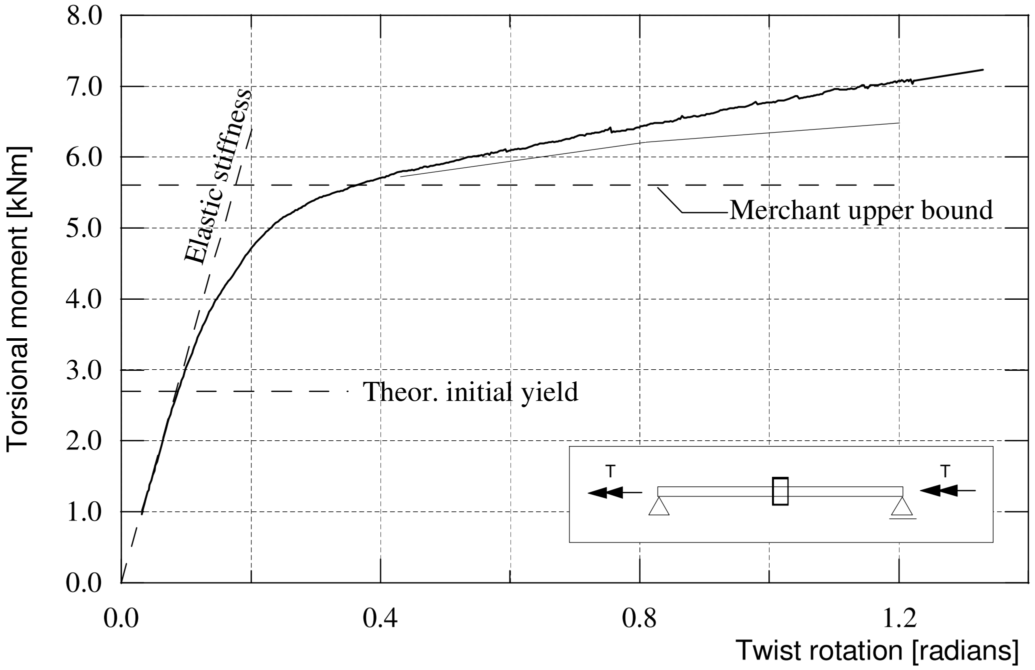

Figure 4.7: Nonuniform torsion test on HEB 140 beam.

calculated using the Timoshenko elastic analysis

$$T = -EI_w \frac{d^3\phi}{dx^3} + GI_T \frac{d\phi}{dx} \tag{4.2}$$

and the first yielding of the most highly stressed point, which is the flange tips at midspan. Please, refer to Appendix A for a discussion. Also shown is the torsional capacity given by Merchant's upper bound for the present case (discussed in Section 6.1).

In Figure 4.7, an extra curve is shown in the rotation range 0.4-1.2 radians, representing the lowest response curve obtained from the two other tests on this case.

The test on the IPE-beam (Figure 4.8) gives a response curve quite similar to that obtained in the test with uniform torsion on the same section. Obviously the two torsional cases have different member stiffness, but both have a steady increase in the torsional moment for increasing twist. In contrast, the response curve for the HEB levels off somewhat more than for the IPE in the plastic range. The different behaviour for the two beams can be understood from the rather significant difference in cross-sectional shape, where the flanges contribute more to the total torsional capacity for the HEB beam. Consequently, when the flanges of the HEB beam have yielded a lesser part of the cross-section is available to carry an increased torsional moment.

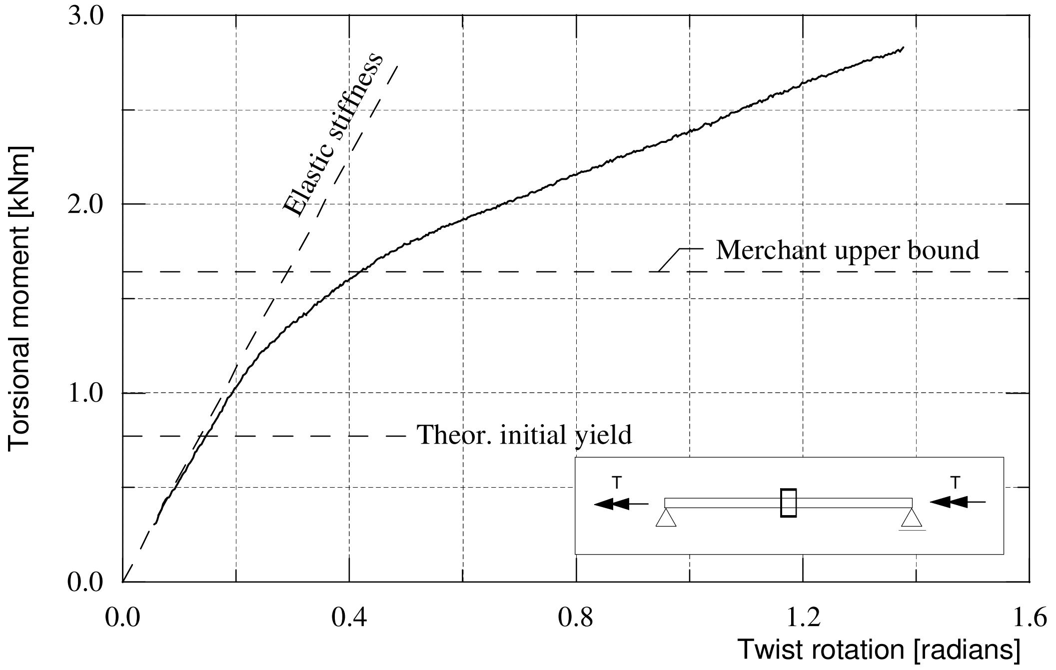

Figure 4.8: Nonuniform torsion test on IPE 160 section.

The experimental results from the tests on the I-beams, both for uniform and nonuniform torsion, agrees quite well with the previous tests (Boulton, Farwell and Galambos, Dinno and Gill), both regarding torsional resistance, shape of curves, and the different inelastic behaviour for the two kinds of beam sections.

None of the specimens developed any local buckles during the testing. Photographs of the deformed test specimens are given in Appendix B. It can be seen from the photographs that the specimens tested in uniform torsion developed perfectly uniform twist deformations along the bar axis, while, as expected, the deformations for the nonuniform torsion specimens were concentrated in the central part of the specimens. As shown, these specimens have developed a slope discontinuity in the flanges at the midpoint, due to localized cross-sectional plastification and bending of the flanges about their weak axis.

Measurements on the permanent twist rotations along the beams are given in Appendix C for the two specimens tested in nonuniform torsion. From similar experiments Dinno and Gill (1963) found inelastic twist distributions geometrically quite similar to that in the elastic range (obtained from Equation 4.2, see Appendix A). They pointed out that for their tests the twist rotation at any section and stage of loading could be deduced approximately from the knowledge of its value at a given section (in their case it was the center section) and from its ordinary elastic distribution along the beam. The main difference is that their tests were carried out for smaller and much more compact I-section specimens. As shown in Appendix C the permanent rotations for the beams of the present study are significantly more localized.

4.4 Finite element simulations

The FE program ABAQUS (Hibbitt et al. 1994) is used for the nonlinear static simulations of the torsion experiments. A model of the I-section beams was established using eight-node shell elements (S8R) and an element mesh as shown in Figure 4.9. The element mesh was chosen such that it could also be used for load combinations that include axial force and bending moment, and allow for a proper and practical representation of the support and loading conditions. The influence of the mesh density on the numerical results is discussed in Chapter 8, where the present mesh is found to give good results. Please, see also Figure 8.1 for a view of the model.

The warping torsional resistance of the beam, which mainly is constituted of the lateral bending of the flanges, should in any case be satisfactory modelled by using four element across the flanges. (Please, refer to Section 8.1 for a discussion of this).

For simulating the uniform torsional resistance, which is present in both the uniform and the nonuniform torsion case, the capability of the model to represent the *uniform* torsional shear stresses (τ_u) in a section is important. As known, these stresses "flow" in a "circular" pattern in the cross-section, similar to what is indicated for the plastic situation in Figure 6.1a. They are directed parallel to the web and flange planes except at the flange tips and at the web/flange intersections. In the elastic state, the stresses have a linear variation in the "through-thickness direction" of the cross-sectional plates, and have a value equal to zero in the mid-plane of the plates.

In the shell model, the actual distribution of the uniform torsional shear stresses is quite well represented by the S8R elements. Here, the membrane part of the element formulation allows a linearly varying shear strain distribution through the shell thickness, and hence also contain the desired in-plane shear stresses. If a reasonable number of section integration points through the thickness of the shell is used, the uniform torsional response of the beam is properly modelled even for the case of inelastic material.

However, there are uncertainties about the properties of the shell model with respect to, among others, the elastic uniform torsional stiffness due to local disturbances at the edges of the plates and at the web/flange junctures. Hence, a limited study was performed on this topic and the results are presented in Appendix D.1. The main conclusions are that no more than one shell element is needed to give a correct elastic torsional stiffness for a rectangular section, and that the modelling of the transverse shear flexibility of the shell is of no importance to the predicted elastic stiffness. The present mesh with four elements across the flanges and the

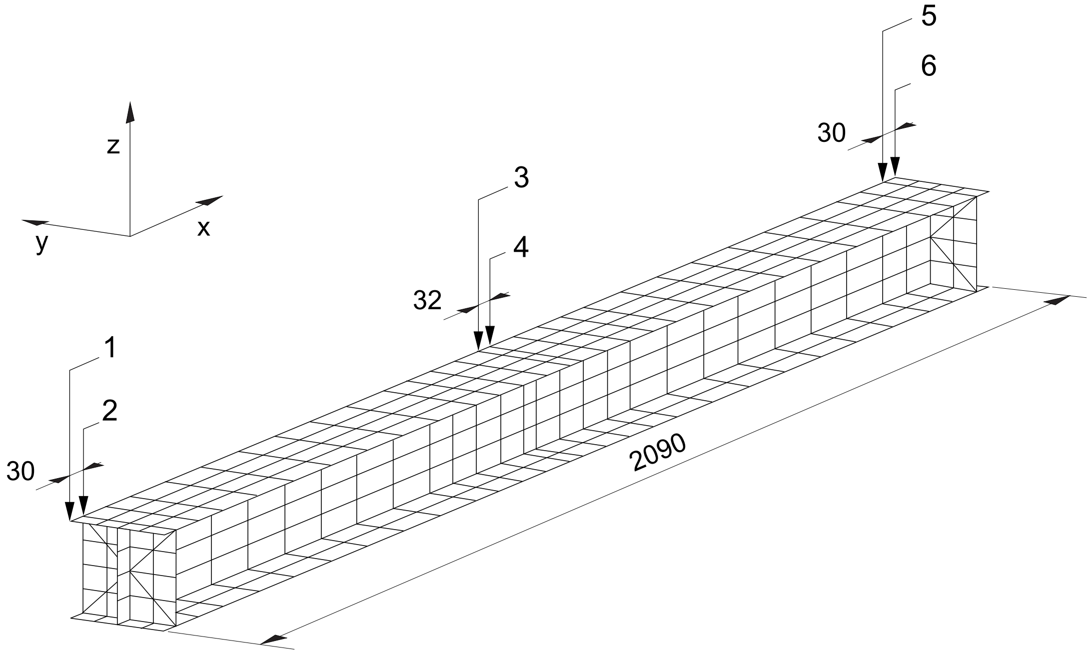

Figure 4.9: Shell model of I-section beam. Here: model of an HEB 140 specimen.

web is therefore expected to give satisfactory results also for the uniform torsion resistance.

The model was established as follows:

- The full I-beam specimen is modelled using four eight-node shell elements across the flanges and the web as depicted in Figure 4.9. The model consists of a total of 396 elements, giving 7242 degrees of freedom.
- Fictitious stiffener plates and diagonal beam stiffeners are added to the model at sections 2 and 5 to allow proper modelling of the concentrated loading.
- The shell element interpolates the rotation and displacement degrees of freedom independently, uses reduced ($2 \cdot 2$) surface integration, allows for transverse shear deformations and provides estimates for the transverse shear stresses. The kinematics in the element formulation allow large rotations and small strains. Five or more integration points are used through the shell thickness, two of which are located on the shell surfaces.
- The constitutive model uses a standard von Mises yield surface and the associated plastic flow theory with isotropic hardening. A piece-wise linear model is used for the stress-strain curve, with seven line-segments up to the ultimate strength level (f_u) of the material. The yield plateau is represented

by a single line segment with a hardening of 4 MPa over the plateau (ε_{yp}). Slightly different material properties were assigned for the elements in the web and in the flanges (see discussion in section 8.1).

- The uniform torsion case is analysed by applying oppositely directed torsional rotations to the nodes at the centroid of the cross-section, at beam sections 2 and 5 (Figure 4.9).
- In the case of nonuniform torsion, the torsional rotation of the beam at sections 3 and 4 was restrained by lateral supports (y-direction) at the flange tips, while the torsional rotations were applied at the centroid at sections 2 and 5, as above.

The fictitious stiffener arrangement at the loading points was required to ensure that the entire beam section followed the rotation of the node at the centroid. A linearly elastic model was used for the stiffeners, and the dimensions of the stiffeners were carefully chosen to prevent significant warping restraints for the beam. This was achieved using 5 mm thick plates and beams with cross-sectional dimensions of 0.5 mm · 100 mm orientated with their weak axis in the plane of the stiffener plates.

Both nonlinear geometry and nonlinear material behaviour were taken into account in the numerical simulations. Displacement control with automatic incrementation of the rotation was used, limiting the increments to not more than 1% of the total rotation. Default values were used for the convergence control.

Note that the fillets at the web-flange junctures are not represented in the shell model of the beam. The elastic torsional stiffness is strongly effected by this geometrical simplification, even though the resulting loss in cross-sectional area is more than balanced by the extra area introduced in the overlap of the shell elements at the web and flange junctures. The torsional constant I_T for the beam sections is built up with a contribution of as much as 18% and 30% from the juncture effect for the HEB and the IPE section, respectively. The underestimation of the torsional stiffness is expected to be most significant in the uniform torsion case. No attempts were made to model the residual stresses or any initial geometrical imperfections of the specimens.

The results from both FE analyses and experiments are given in Figures 4.10 to 4.13. The numerical response agrees quite well with the experimental one, and the best agreement is achieved for the cases of nonuniform torsion. This is as expected as the warping stresses in nonuniform torsion are quite well modelled by the shell elements.

In uniform torsion the numerical response is too soft in the elastic range. This may be explained by the omission of the fillets in the model, but calculations show that the stiffness reduction is somewhat less than what could be expected from the corresponding error in I_T. (See Appendix D.1 for a discussion). In nonuniform

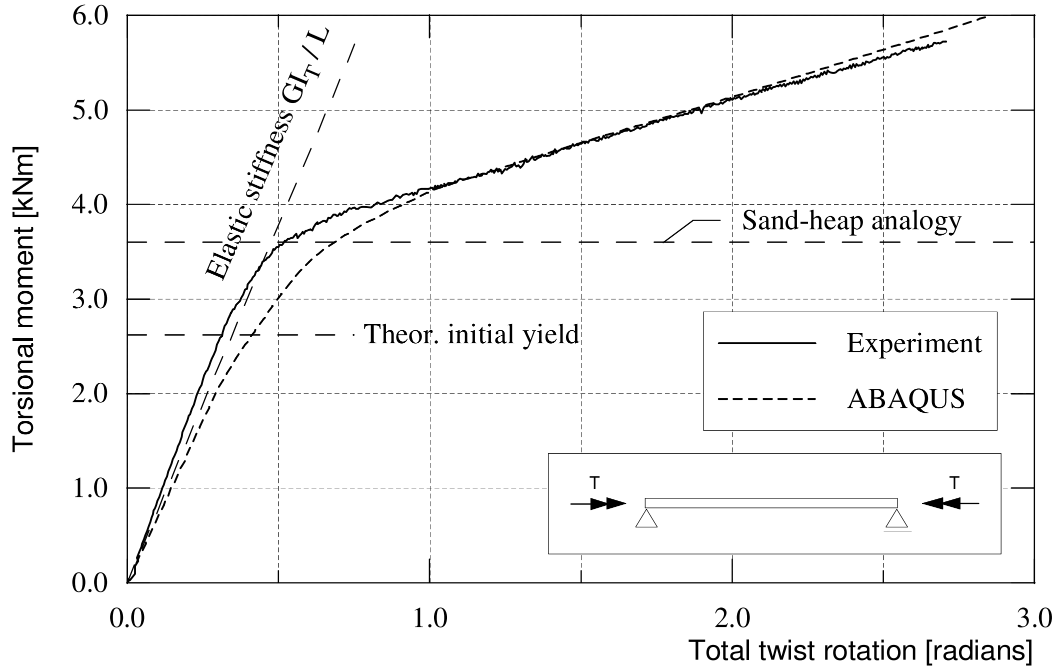

Figure 4.10: Uniform torsion on HEB 140, experiment and analysis.

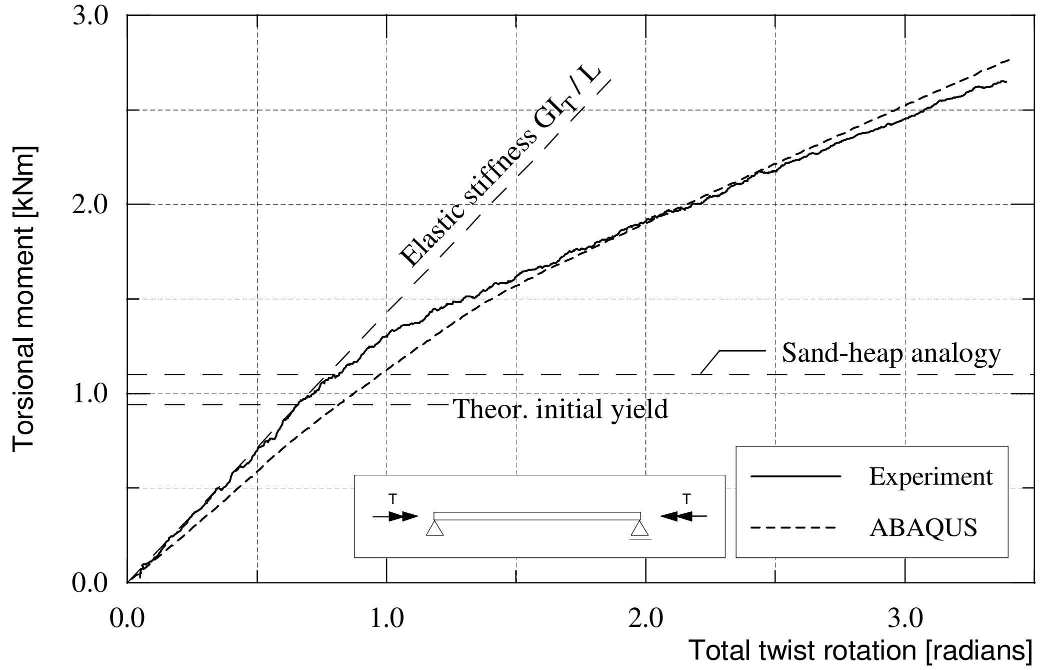

Figure 4.11: Uniform torsion on IPE 160, experiment and analysis.

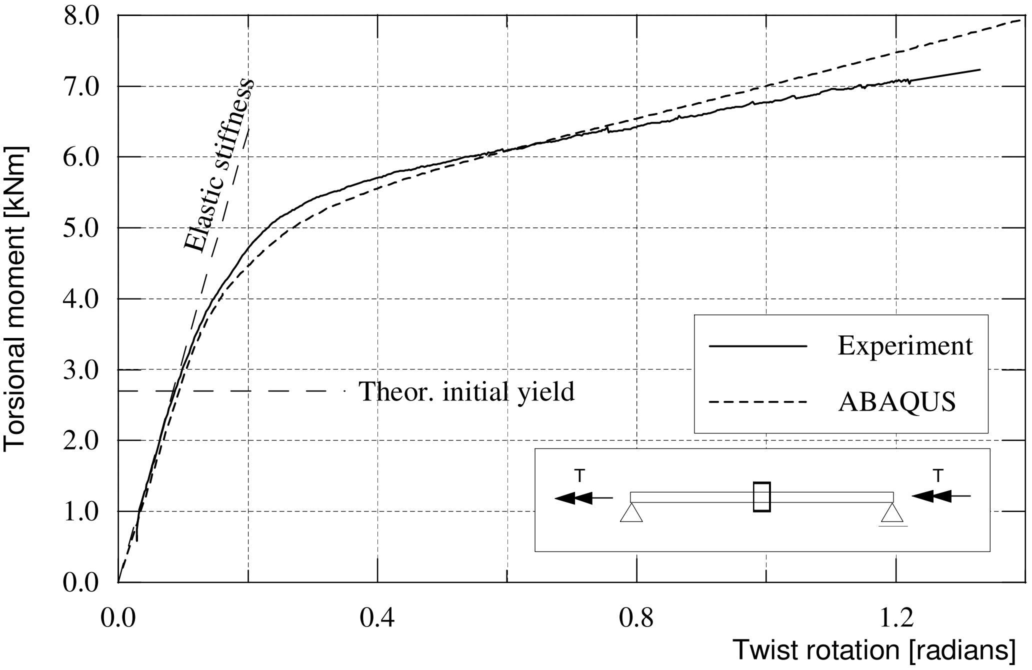

Figure 4.12: Nonuniform torsion on HEB 140, experiment and analysis.

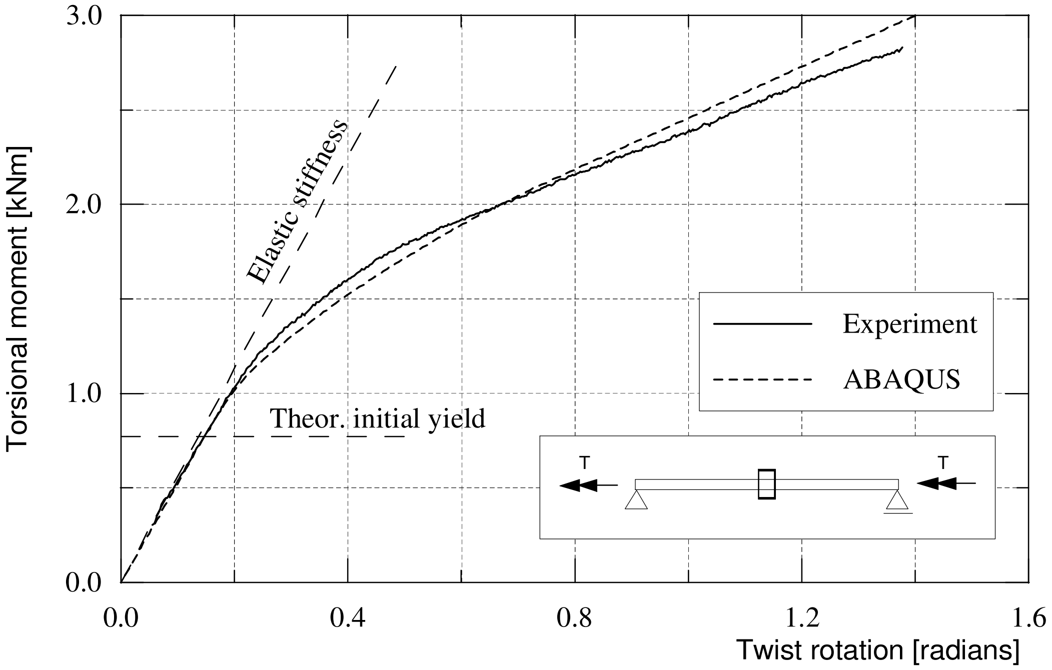

Figure 4.13: Nonuniform torsion on IPE 160, experiment and analysis.

torsion this deficiency of the model has less effect, because a larger part of the applied moment is carried by warping.

In the uniform torsion analyses the equivalent Mises stress does not exceed the yield stress at any material point, even for an applied rotation of more than 3 radians. For the HEB specimen, yielding has extended to the middle surface of the web for a rotation of 1.7 radians, but not the middle surface of the flanges. The yielding is, due to the helical deformation of the member, strongly influenced by axial tensile and compressive stresses that for this rotation vary from 150 MPa in tension at the flange tips to 210 MPa in compression in the center of the web, both given as values averaged through the thickness.

In nonuniform torsion the maximum equivalent Mises stress occurs in the flange tips at the midspan of the specimens, where the warping normal stresses (σ_w) are largest. For the HEB beam the onset of strain hardening occurs at a rotation of about 0.26 radians. At this stage, the flanges have developed extensive plastification at midspan due to the flange bending (warping). Yielding has also developed at the surface of the beam along the entire member, due to the uniform torsional shear stresses. At a rotation of 0.6 radians, the corresponding maximum equivalent Mises stress at the flange tips at midspan has a value of 340 MPa, or about 22 % higher than the yield plateau of the material.

In Appendix D.2, additional simulation results are shown for the HEB section. Here, the effects of strain hardening and nonlinear geometry are separated. It is shown that, for nonuniform torsion, the strain hardening contributes only slightly to the predicted torsional moment, and that the predicted response in uniform torsion agrees reasonably well with the sand-heap value of the torsional moment if the nonlinear geometry option is excluded in the simulation.

Simulations of the flat bar tested in uniform torsion

The flat bar was tested to provide experimental data for a specimen with simple geometry and shear stress distribution. The finite element discretization of the flat bar was easily done without omitting any part of the cross-sectional area.

The flat bar is modelled with both 8-node shell elements and with 20-node solid elements. Transverse stiffener beams at the loading point are included in the models in order to represent the actual loading conditions. The material model is the same as for the I-beams. The solid model is analysed primarily to evaluate the response predicted using the shell model.

- The shell model consists of 5 elements in the transverse direction and 52 elements along the bar axis, i.e. a total of 260 elements in a uniform mesh.

- The solid model has two layers of brick elements through the thickness, 6 elements in the transverse direction and 70 elements along the bar axis. This gives about 16000 DOFs.

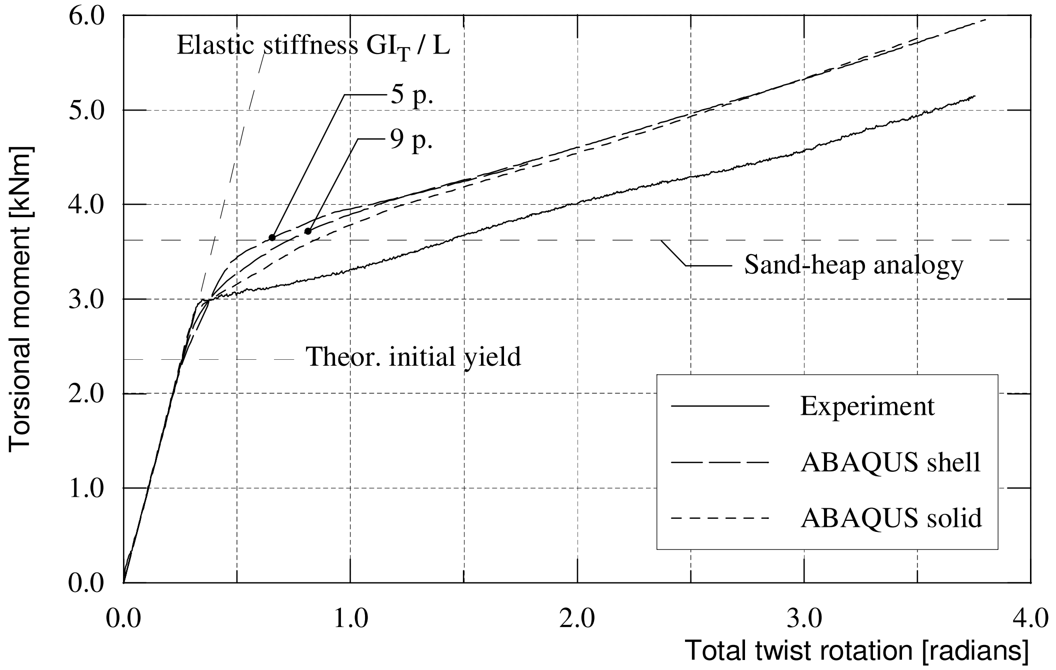

Figure 4.14: Uniform torsion on flat bar section 15.3 mm*200 mm.

The solid element uses quadratic interpolation of the displacements and reduced $(2 \cdot 2 \cdot 2)$ integration at the Gauss points for both internal forces and the element stiffness, which gives 4 integration points through the thickness of the model. The outermost integration points of the solid element are then located at a distance of approximately $t/10$ or 1.6 mm from the outer surface of the bar, while the shell element model has integration points on the surface.

The numerical results are compared with the experimental result in Figure 4.14. For the shell model two curves are depicted, based on respectively 5 and 9 integration points through the shell thickness. The numerical analyses predict the torsional response quite well, except that the torsional resistance in the plastic region is overestimated. The results from the shell and the solid models agree quite well, except in the elastic-plastic transition region. As shown, the use of more than 5 integration points in the shell elements improves the predicted response in this region. A closer view of this region is given in Appendix D.

The deformation caused by the transverse shear stresses in the shell elements is treated elastically at all stress levels by ABAQUS, and some of the overshoot in the plastic region may be caused by this. On the other hand, the solid elements should model this shear flexibility better, but give almost equal results.

Simulations of torsion of I-beam using beam elements

An open section beam element (ABAQUS:B32OS) with three-node quadratic interpolation was used to establish a simple 1-D model of the HEB 140 specimens.

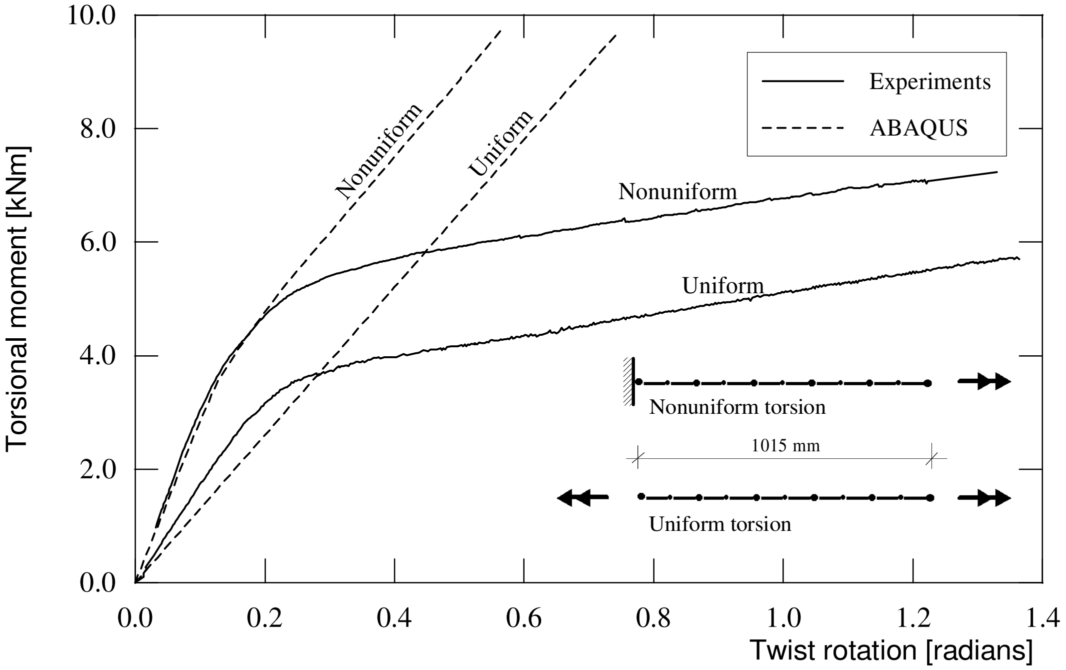

Figure 4.15: Torsional response of HEB 140 beam, modelled with beam elements.

Here, the 2030 mm length of the specimen between the loading points was modelled with 10 beam elements, which gives 5 beam elements to represent the half specimen length (Figure 4.15). The beam element has an additional "warping magnitude" degree of freedom at each node, and is intended for problems with restrained warping. The element formulation is based on Timoshenko beam theory and includes transverse shear deformation. Note however, that the behaviour in transverse shear and torsional shear always is assumed to be elastic. The strain formulation allows large axial strains and moderately large torsional strain. The cross-section is defined by a number of line segments, and ABAQUS obtains the beam section properties by numerical integration. Here, a total of 25 integration points were used, nine points in each flange and seven in the web. The element uses three Gauss integration points along the beam axis.

The numerical response is compared to the experiments in Figure 4.15. As expected from the element formulation, the response to uniform torsion is almost linear, and gives a poor representation of the torsional behaviour for large values of twist. The deviation in initial stiffness between the test and analysis is mainly caused by the simplified computation of the torsional constant I_T , which is taken as $\sum \frac{1}{3} bt^3$ by ABAQUS.

The prediction of the nonuniform torsional response is somewhat better, with a fairly accurate prediction of initial yielding and almost correct representation of the initial stiffness. For larger twist values the computed linear elastic response to uniform torsion again causes the model to grossly overestimate the behaviour.

From this limited study it can be concluded that the beam element with its "warping DOFs" is unsuited for analyses of structures subjected to large torsional twists and inelastic deformations. However, the element gives a correct representation of the increase in stiffness which results from warping restraints on a member, and the warping DOFs of the element are essentially for modelling stability problems where torsional deformations occur, like in lateral torsional buckling of beams and torsional buckling of columns. Thus, for elastic analysis the element may give adequate results.

Summary

The response of the specimens, to both uniform and nonuniform torsion, is predicted quite well when shell elements are used. For uniform torsion on the I-section beams, the largest source of error in the model is due to the representation of the fillets. If the elastic torsional stiffness could be computed correctly in the analyses, the experimental and the analysis response curves would follow even better.

The analyses of the flat bar specimens show that a shell model is able to predict uniform torsional response almost as accurately as a much larger model based on solid elements.

Torsional problems involving beams with constrained warping can also be properly modelled with beam elements having warping DOFs, as long as the application is restricted to problems where nonlinear material behaviour is not dominant.

Chapter 5

Beam-column tests

5.1 Introductory remarks

In this chapter the results from the beam-column experiments are presented. The response of the beam-columns is presented by means of curves that show the relationships between the applied resultant forces and the corresponding displacements.

Generally, the curves are drawn as straight lines between subsequent data points, based on approximately thousand points in each test. For some of the tests, the presented curves are based on a polynomial fit to the recorded response data, as will be pointed out in each case. The testing and the observed behaviour of each test specimen are briefly discussed in connection with the graphical presentation of the response.

5.2 About the tests and the presentation

5.2.1 Test conditions

Figure 5.1 shows the load and support conditions of the beam-columns. The beam-column specimens are subjected to a combination of the three applied loads N_0, H and T_0. At the ends, the specimens are simply supported with respect to the y and z axes (v=0 and w=0). They are supported with respect to the y axis (v=0) at midpoint, where also the torsional rotation is restrained (ϕ_x=0). Please note the symbol for the support conditions at midpoint, as it will be frequently used in the following. As shown in Figure b), the compressive axial load N_0 acts along a line through the cross-sectional centroids at the transverse end supports. The deflection w is also measured from this line.

The most heavily loaded part of the specimen is at midpoint, where the bending moment has its maximum. At this location the bending moment is balanced by strong axis bending of the cross-section only. The active stress resultants (internal forces) at the midsection are denoted N, M and T, and all experimental results presented in the following refer to these forces.

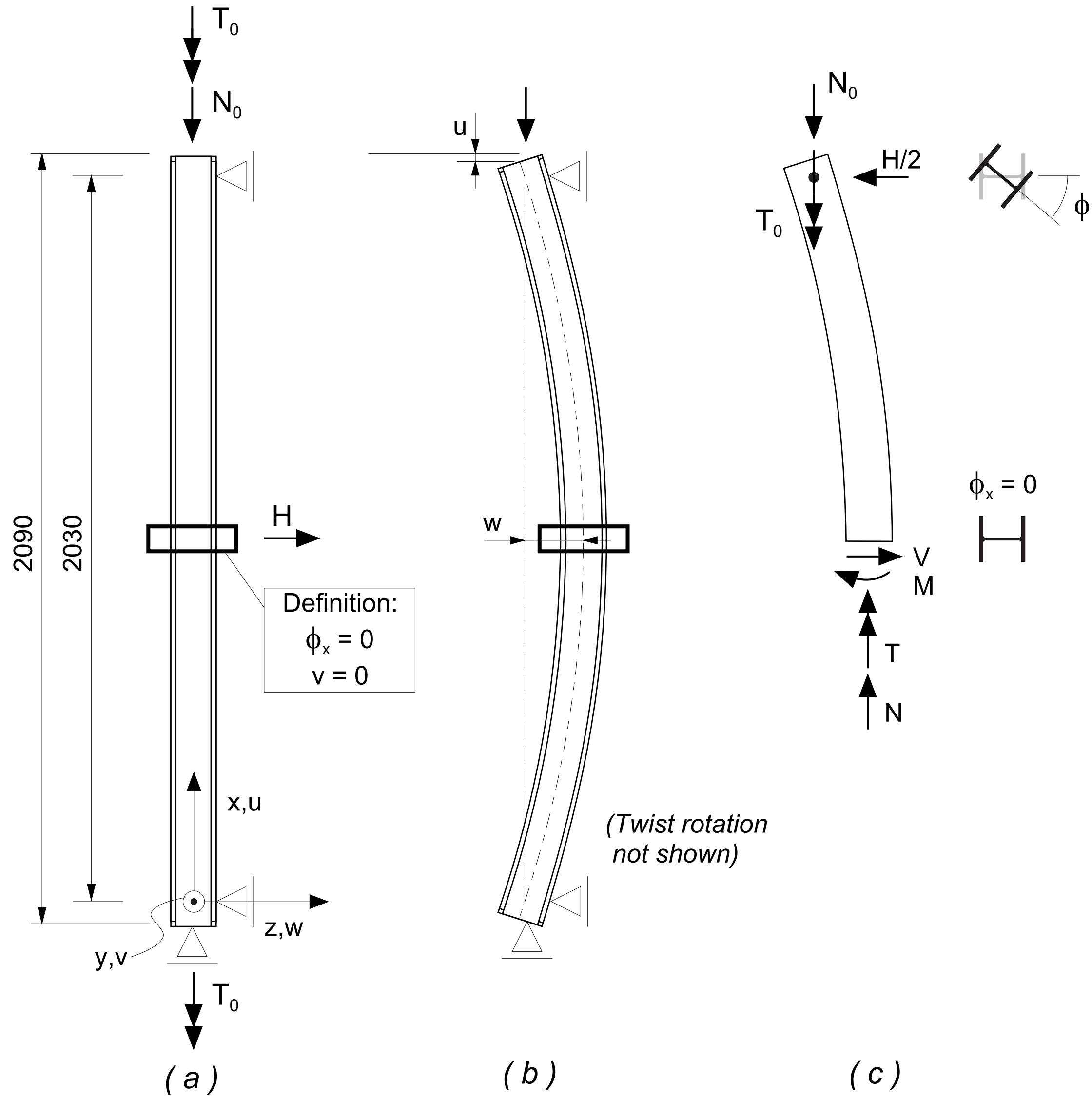

Figure 5.1: Beam-column tests, load and support conditions.

The internal forces are taken as:

$$\begin{aligned} N &= N_0 \\ M &= \frac{1}{4} \cdot H \cdot 2030mm + N_0 \cdot w \\ T &= T_0 \end{aligned} \tag{5.1}$$

Note that the internal torsional moment (T) at midsection is in fact influenced by the axial load. Reference is made to Section 6.2 for a discussion of the second order effect of N_0 on the internal torsional moment.

The displacements that are associated with the internal forces are the axial shortening u, the transverse displacement w at midsection and the twist rotation ϕ at the end sections as defined in Figure 5.1. The forces and the displacements point in the same direction in all tests and are taken positive as shown.

5.2.2 Normalization

The graphical presentation of the test results uses normalized (nondimensionalized) values for the measured forces and displacements. The internal forces N, M and T and the corresponding displacements u, w and ϕ are normalized by their yield values, viz.:

$$\begin{aligned} \overline{N} &= \frac{N}{N_Y} \quad , \quad \overline{u} = \frac{u}{u_Y} \\ \overline{M} &= \frac{M}{M_Y} \quad , \quad \overline{w} = \frac{w}{w_Y} \\ \overline{T} &= \frac{T}{T_Y} \quad , \quad \overline{\phi} = \frac{\phi}{\phi_Y} \end{aligned} \tag{5.2}$$

Here, the yield value means the value of the single force or the displacement that corresponds to initial yielding at the most stressed point in the beam-column. Both for the strong axis bending moment, M, and the torsional moment, T, this yielding occurs at the extreme fibres at the midsection. For bending, the displacement w is taken as the sum of the contributions from the axial strain ($w_b = 1/48 \cdot Hl^3/EI_y$) and the not insignificant contribution from the shear strain ($w_s = 1/4 \cdot Hl\kappa/GA$). Here, the value of κ is as given by Shames and Dym (1985). For torsion, the yield values T_Y and ϕ_Y are obtained from the differential equation for elastic torsion $T = -EI_W d^3\phi/dx^3 + GI_T d\phi/dx$, assuming full symmetry in torsional rotations about the midsection and initial yielding of the flange-tips at midsection caused by pure warping stresses. The yield value ϕ_Y is calculated at the position where the torsional moment is applied, i.e. 30 mm from the end sections where the rotations are actually measured (Figures 5.1a and c). Since the 30 mm long extensions at

	Axial loading			Strong axis bending			Torsion		
	f_y MPa	N_Y kN	u_Y mm	f_y MPa	M_Y kNm	w_Y mm	f_y MPa	T_Y kNm	ϕ_Y degrees
HEB 140	286	1198	2.85	279	58.9	7.3	290	2.65	4.95
IPE 160	308	626	3.11	304	32.4	6.8	316	0.772	7.84

Table 5.1: Yield values used for normalization of test data.

both ends of the specimen are not subjected to torsional loading, the rotations measured at the end sections are considered to be representative for the loading points. Appendix A.2 gives the formulas for the torsional moment - twist rotation relationships for the present load situation.

The normalization is based on measured cross-sectional dimensions, and takes the variation of the yield strength over the cross-section into account. Consequently, the value of the yield stress is different for the three internal forces (N,M,T). The mean yield strength of the flanges is used for the strong axis bending moment, the yield strength at the flange tips is used for the torsional moment while the squash load obtained from the stub column tests is used for the axial force.

Table 5.1 gives the force and displacement values that are used in the normalization. The values are given for the typical test specimen with cross-sectional dimensions as presented in Table 3.2. Only smaller adjustments of these values were needed for some of the test specimens.

5.2.3 Test procedure - chosen loading

In principle, the three loadings N, M and T could all be applied either by displacement/rotation control or by force control. However, many considerations influenced the choice of test procedure.

In order to provide full symmetry in displacements about the specimen midpoint, the torsional loading had to be imposed by applying equal rotations at the two ends, i.e. by rotation control.

As shown in Table 5.1, the axial shortening of the test specimens at squash load is small, approximately 3 mm. The shortening of a specimen due to simultaneously twist is of at least the same order as this, and it develops nonlinearly throughout the test (Figure 5.11). Due to this, the axial force in the specimen resulting from a prescribed linear displacement of the vertical actuator would develop quite unpredictable. Displacement control of the axial loading by means of the displacement-transducer in the vertical actuator was hence considered infeasible. On the other hand, a force controlled axial loading using a linearly increasing axial load was considered unsuitable due to instability at the load level when the specimens resistance no longer increases.

For all tests the axial load is hence kept constant throughout the test. This simplified both the testing and the subsequent presentation of the test data.

Furthermore, at least one of the displacement components w and/or ϕ were increased linearly in each test. This allowed the specimen response to be extended into the fully plastic state of the cross-section, also for decreasing values of the resistances.

At the beginning of each test, the loads were applied to the test specimen up to a limited level of force to establish contact in the parts of the loading arrangements. In torsion, the start-up of each test was quite troublesome due to the relatively low torsional resistance of the sections, with corresponding small start values of the torsional force, and the requirement of equal rotations at the two ends. The actual testing of a specimen to failure took about 30 minutes.

The actual load combinations were chosen in order to cover most of the force space, however, taking into consideration what combinations could be of practical interest. As the effect of combined bending moment and axial loading, including local and global buckling, is well known for the present sections, torsional loading was present for most tests. For the IPE beam-columns the magnitude of the axial load had to be restricted due to the possibility of weak axis buckling (see Appendix A.1 for capacities).

5.3 Test program

The loading situations for the beam-column tests are summarized in Table 5.2. The test program is subdivided into two main parts, tests on the HEB 140 section (identification H in Table 5.2) and tests on the IPE 160 section (identification I), with a total of 26 tests. Each test has its individual number, and the load conditions are indicated with the letters N, M and T. For all tests with axial load, the magnitude of the constant axial load is given. The expression "active" in Table 5.2 means that the force is applied gradually by increasing its corresponding displacement value.

The references (a) to (m) in Table 5.2 connect each test to one of the load paths in Figure 5.2, where each arrow represents one test. The arrows in the different $\overline{M}$-$\overline{T}$ planes indicate only the ratio between the load components $\overline{M}$ and $\overline{T}$ in the test, and not the obtained load values. In addition to the 26 beam-columns tested (and presented here in Sections 5.4 and 5.5), the two nonuniform torsion tests from Chapter 4 are also shown in Figure 5.2.

Figure 5.2 shows that the loading (M and T) was applied in two different ways. Figures 5.2(a)-(d) depict 11 tests on the HEB 140 section where the loading consisted of single M or T loading or proportional M-T loading at different levels of axial load. For the 5 other tests depicted in Figures 5.2(e)-(h) the bending moment (M) was first applied to a predetermined level, and then the torsional loading was imposed. Three out of the 5 tests were carried out at a constant bending moment, achieved by reducing the transverse load (H) as a function of the transverse displacement (w), i.e. compensating for the second order effect from the axial load

Test	$\overline{N}$	$\overline{M}$	$\overline{T}$	Load path (in Figure 5.2)
H-1-M	-	active	-	(a)
H-2-MT	-	active	active	(a)
H-3-MT	-	active	active	(a)
H-4-NM	0.334	active	-	(b)
H-5-NMT	0.334	active	active	(b)
H-6-NMT	0.334	active	active	(b)
H-7-NT	0.334	-	active	(b)
H-8-NMT	0.50	active	active	(c)
H-9-NT	0.50	-	active	(c)
H-10-NT	0.835	-	active	(d)
H-11-MT	-	0.77	active	(e)
H-12-NMT	0.25	0.93	active	(f)
H-13-NMT	0.334	0.55	active	(g)
H-14-NMT	0.50	0.62	active	(h)
H-15-NMT	0.50	0.155	active	(h)
I-1-M	-	active	-	(i)
I-2-MT	-	active	active	(i)
I-3-MT	-	active	active	(i)
I-4-NMT	0.14	active	active	(j)
I-5-NMT	0.14	active	active	(j)
I-6-NM	0.32	active	-	(k)
I-7-NMT	0.32	active	active	(k)
I-8-NT	0.32	-	active	(k)
I-9-NT	0.50	-	active	(l)
I-10-MT	-	0.71	active	(m)
I-11-MT	-	0.42	active	(m)

Table 5.2: Beam-column test program

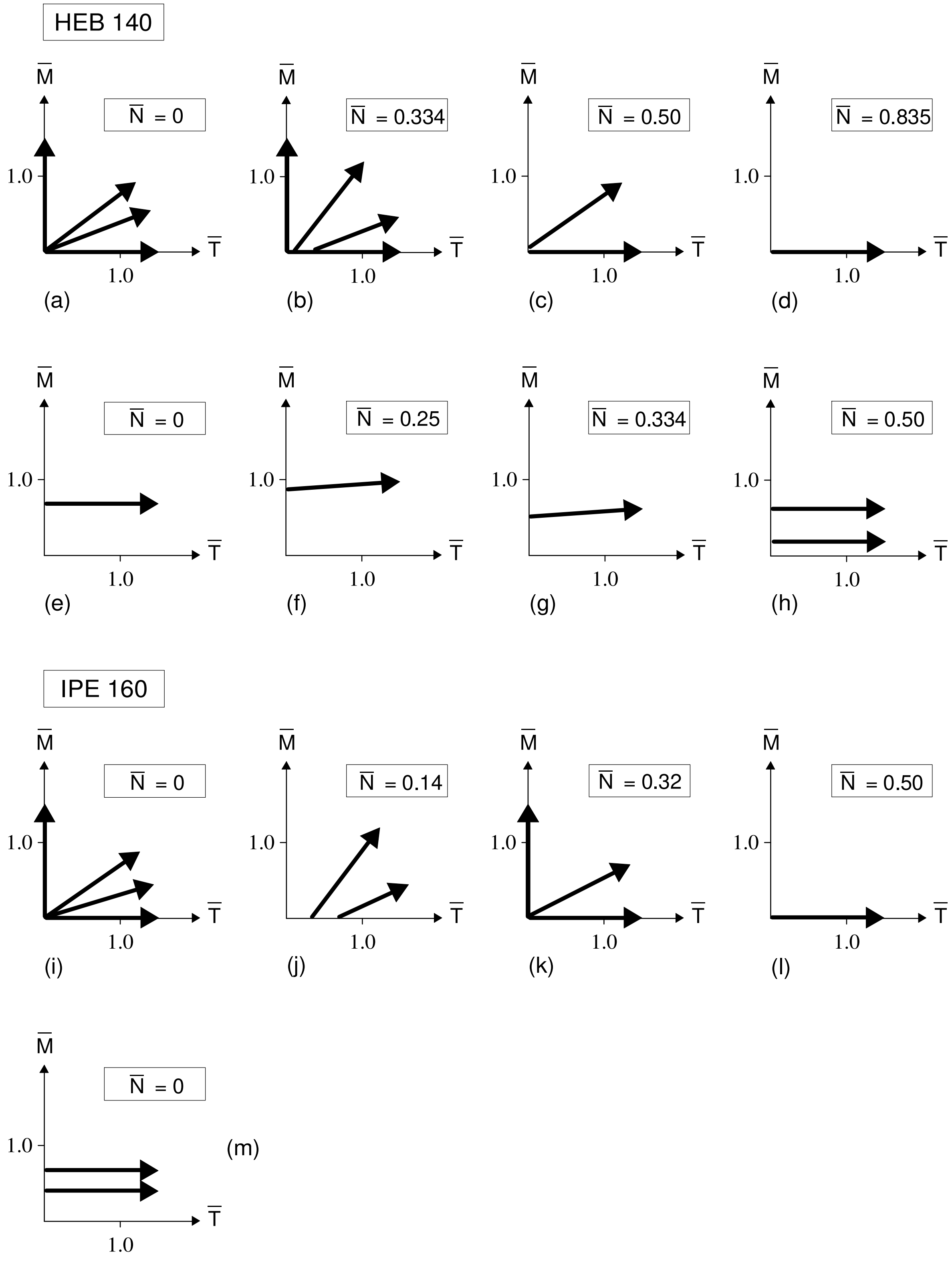

Figure 5.2: Load paths for beam-column tests.

(N·w). For the other two tests the bending moment increased somewhat during the test due to this effect. The main reason for two different test procedures, was that the last 5 tests mentioned (three tests at a constant bending moment and two at "near" constant moment) were considerably simpler to perform.

Table 5.2 gives the magnitude of only the first order bending moment (H·l/4). The tests on the IPE 160 section are organized in a similar manner.

As shown in Figure 5.2 both the HEB and the IPE sections are tested in strong axis bending. Together with the axial load tests presented in Chapter 3, i.e. the stub column tests, and the nonuniform torsion tests in Chapter 4, this means that the three basic load cases N, M, and T are all investigated.

In some of the tests with proportional M-T loading, Figures 5.2(b) and (j), the bending moment M is started with some delay. This was unintended, and was caused by inaccurate operation of the loading devices and slack in the loading parts.

5.4 Beam-column test results

The following presentation of the tests show all measured test parameters, i.e. the forces N, M, and T and the displacements u, w and ϕ. In all tests where torsion is applied, the torsional rotation ϕ is increased almost linearly throughout the test and can, in a sense, be interpreted as the "time" scale of the test. The graphs depict curves that connect all response parameters to this rotation, and this allows the simultaneous value of all test parameters to be presented within one single graph for each test.

Generally, the graphs use solid lines for the forces and dotted lines for the displacements, and for some of the tests two horizontal and two vertical axes are used in the diagrams. In all graphs the curves are labelled, and the labels use a y-axis versus x-axis convention, which means that a $\overline{M}$-$\overline{w}$ curve is shown with the value of the moment $\overline{M}$ along one of the y-axes and the deflection $\overline{w}$ along one of the x-axes.

As discussed above, the curves show the normalized values of the response parameters. The normalizing values are the theoretical limit for the elastic linear behaviour, and the first part of response curves for torsional moment ($\overline{T}$-$\overline{\phi}$) and bending moment ($\overline{M}$-$\overline{w}$) is therefore, for tests without axial load, expected to point against the (1.0,1.0)-coordinate in the graphs. The measured torsional response followed this quite well.

As discussed in Chapter 2, the deflection w due to bending is not measured directly on the specimens. A part of the measured displacement is hence due to elastic deformation at the end supports. This is taken care of by a small linear correction to the measured displacements, based on data from control tests where the physical deflections were measured directly at the specimens at various load levels. The correction to the measured deflection value is not more than 1.5 mm for any of the tests.

Due to different deformations of the loading devices for torsion and bending, the applied displacement histories (paths) do not follow a perfectly straight line in any of the proportional M-T tests. The $\overline{w}$-$\overline{\phi}$ curve in Figure 5.9 illustrates this. The deviation was not considered to be of significant importance for the test results. If so, it may have been avoided by controlling the testing by the displacements measured directly on the specimen (i.e. the rotation gauges at the specimen ends and the displacement transducer at midspan).

In the following presentation, similar tests on the HEB 140 and the IPE 160 are grouped together. Only the measured force and displacement relationships are given in the main text. Some measurements on the distribution of angle of twist along the specimens are given in Appendix C. Photographs of some of the deformed specimens are given in Appendix B.

5.4.1 Bending tests

Tests H-1-M and I-1-M, strong axis bending

Figures 5.3 and 5.4 show the behaviour of the specimens that were subjected to pure strong axis bending. The specimen ends were braced against torsional rotations in these tests.

The nominal plastic shape factor (α) for strong axis bending is 1.14 for both the HEB 140 and the IPE 160 section. However, as the web and the flanges have slightly different material properties, the fully plastic moment is computed to be M_p=1.145·M_Y for the HEB section and M_p=1.155·M_Y for the IPE section. The corresponding values for the normalized moments are, of course, $\overline{M}$=1.145 and $\overline{M}$=1.155, respectively.

The response curves show a distinct yield plateau at a moment value somewhat higher than the theoretical plastic moment resistance M_p for both sections. At a deflection of $\overline{w}$=2.0 the developed moment is 6% higher than M_p for the HEB beam, and 3% higher for the IPE beam. Most of the increased resistance can be explained from the effect of the localized plastic deformation and strain hardening at the loading point, as a result of the gradient in the moment. ASCE (1971) presents results for a similar test on a beam with almost identical geometry (h/l -ratio and cross-section shape) as the present IPE. Here, a moment plateau about 6% higher than M_p for a similar deflection level is obtained.

The first observed flange buckle appeared close to the loading point, and is marked on the curves. The bending tests demonstrate clearly that the moment resistance for these sections is almost unaffected by developed flange buckles until the resistance decreases (only observed for the IPE) due to lateral buckling between the braced points.

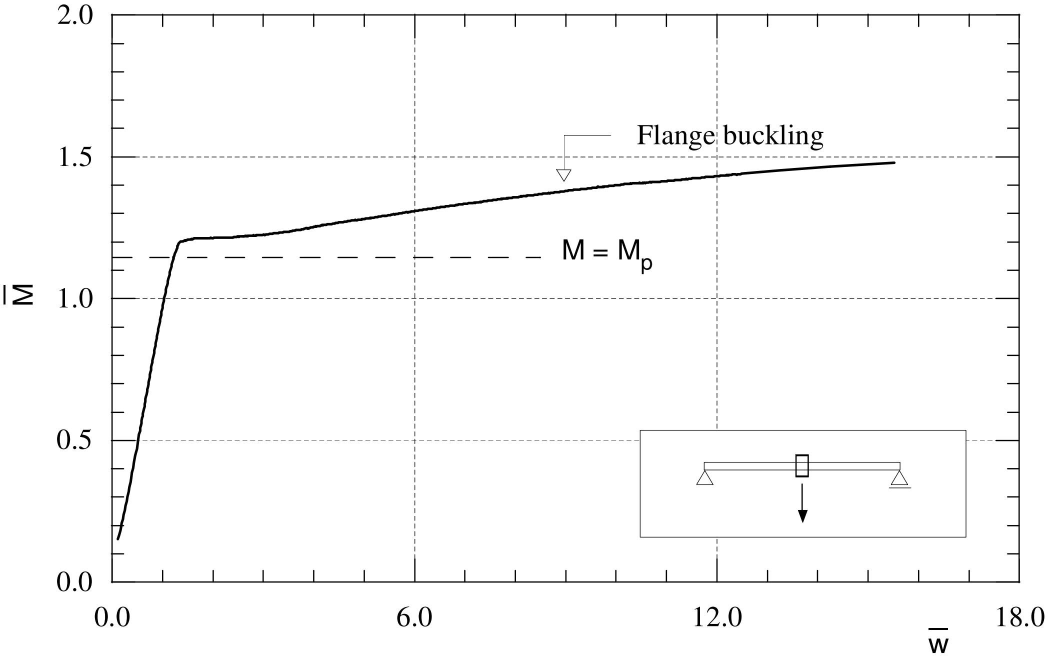

Figure 5.3: Test H-1-M, HEB 140 subjected to strong axis bending.

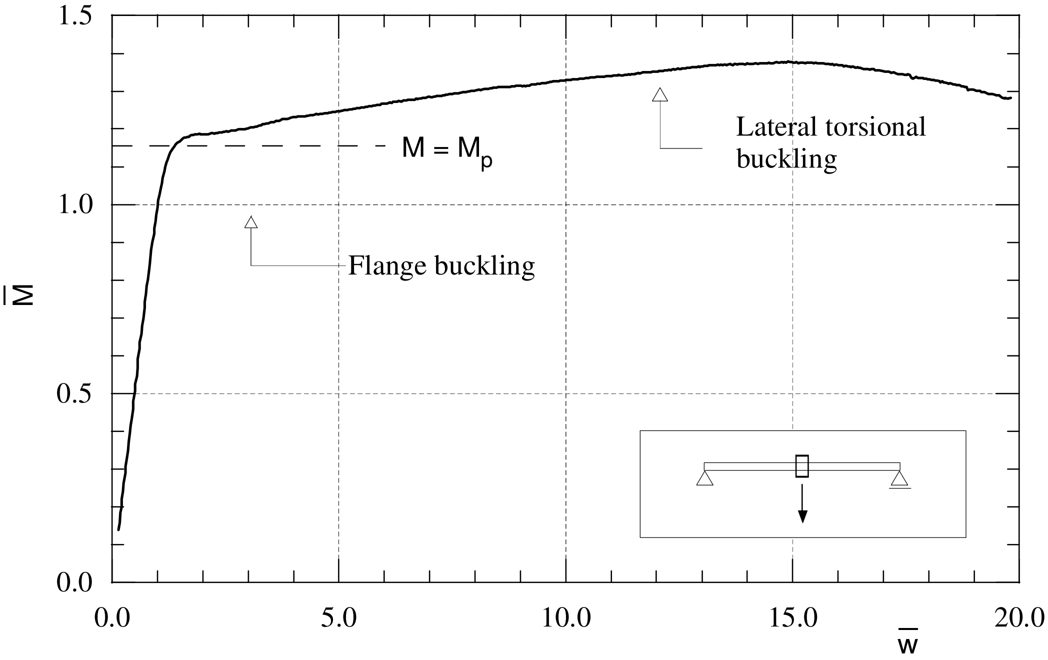

Figure 5.4: Test I-1-M, IPE 160 subjected to strong axis bending.

5.4.2 Load combination NM

Tests H-4-NM and I-6-NM, axial load and strong axis bending

Figures 5.5 and 5.6 show the results of the two NM tests that were carried out. Also for these tests the specimen ends were restrained against torsional rotations. The response curves for pure bending ($\overline{N}$=0) are shown for comparison. The graphs show how the axial load affects the behaviour in bending, and that the moment "capacity" becomes more difficult to define from tests.

The HEB test ($\overline{N}$=0.334) gave a nice and smooth curve, where the plastification starts as expected at a moment value about 30% lower than in the pure bending test. The first flange buckle appeared near the loading point at a deflection $\overline{w}$=5.2, and lateral buckling deformations started at a deflection about $\overline{w}$=12.0, as a S-shaped deformation of the compression flange.

The IPE test ($\overline{N}$=0.32) showed less effect of the axial load at the beginning of the plastic range, even though the inelastic response also for this test starts at the expected level. The resistance decreased when the flange buckled, and the test ended in a lateral buckling of the compressive parts of the section. The somewhat different behaviour in the start of the plastic range for the two sections may be explained from the difference in cross-section geometry. For the IPE section the web contributes with 25% to the total plastic bending capacity, while the corresponding value for the HEB section is 11%. Hence, most of the applied axial force can be carried by the web of the IPE without affecting the bending response as much as for the HEB.

5.4.3 Load combination MT

Tests H-2-MT, H-3-MT, I-2-MT and I-3-MT, bending and torsion

Figures 5.7 to 5.10 show the behaviour of the specimens that were subjected to proportional bending and torsional loading. As discussed previously the tests were carried out under displacement control, in this case by imposition of transverse displacement w and twist rotation ϕ. For each test the actual imposed displacement history (deformation path) is shown with the curve labelled $\overline{w}$-$\overline{\phi}$. It could have been desirable for this curve to be completely linear, but due to the flexibility in the load transfer systems it is somewhat nonlinear especially at the lower load levels and most marked for the IPE specimens, due to their extremely low torsional resistance. The bending response and the torsional response are shown with the $\overline{M}$-$\overline{w}$ and the $\overline{T}$-$\overline{\phi}$ curve, respectively. An additional curve $\overline{M}$-$\overline{\phi}$ connects the two single responses, and allows the simultaneous values of $\overline{M}$ and $\overline{T}$ to be read from the graphs as a function of $\overline{\phi}$ (or the "time"). Of course the latter curve could have been omitted, as the $\overline{M}$ and $\overline{T}$ responses are also connected through the $\overline{w}$-$\overline{\phi}$ curve.

The two specimens H-2-MT and I-2-MT were subjected to almost identical displacement histories, and the behaviour and measured resistance is quite similar in both bending and torsion. From Figures 5.7 and 5.9 it can be seen that the value

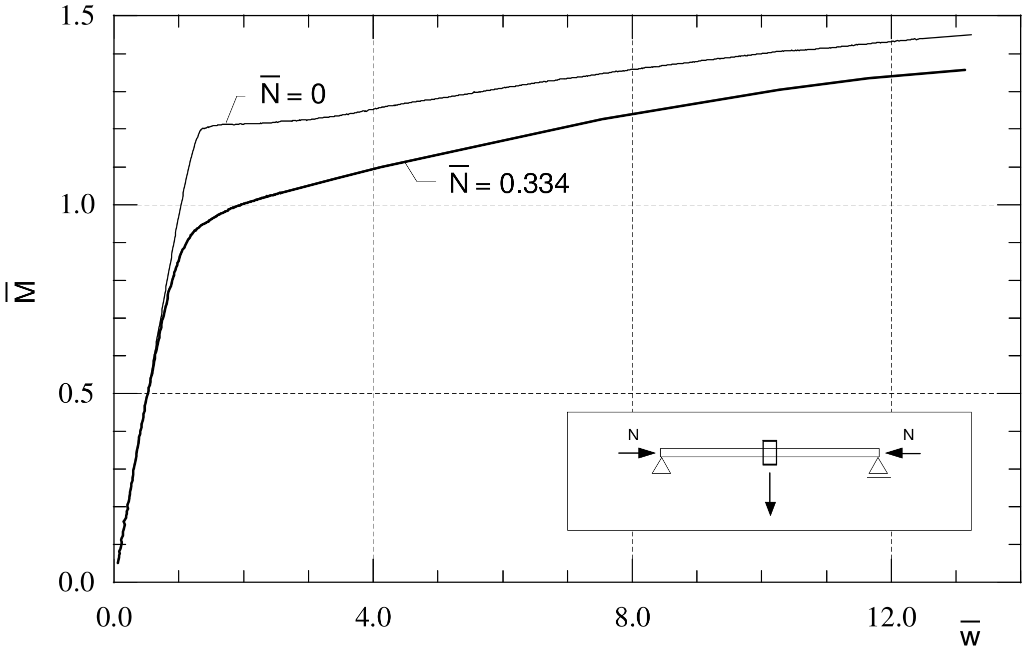

Figure 5.5: Test H-4-NM, HEB 140 with axial load and strong axis bending moment.

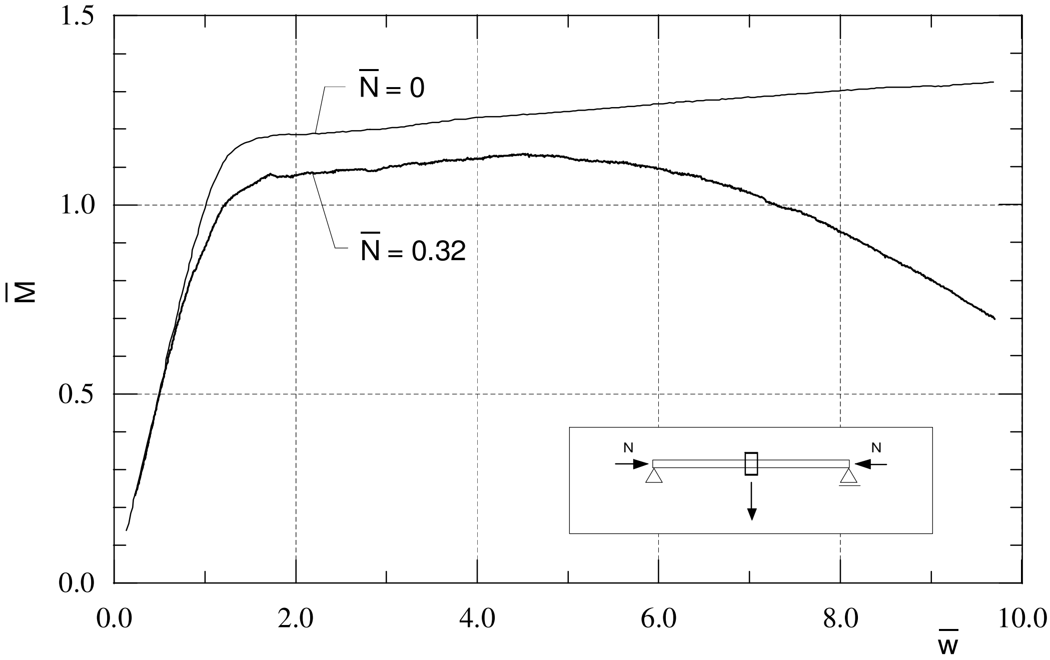

Figure 5.6: Test I-6-NM, IPE 160 with axial load and strong axis bending moment.

obtained for the moment is approximately $\overline{M}$=1.0 for both sections, while the maximum value for the torsional moment is $\overline{T}$=1.5 and $\overline{T}$=1.6 for the HEB and the IPE section, respectively. The levelling off of the response curves is due to plastification, as no local instabilities occurred. For both sections a significant reduction in the bending stiffness occurs at approximately $\overline{M}$=0.5, while the torsional stiffness remains relatively unchanged up to $\overline{T}$=0.7 to 0.8.

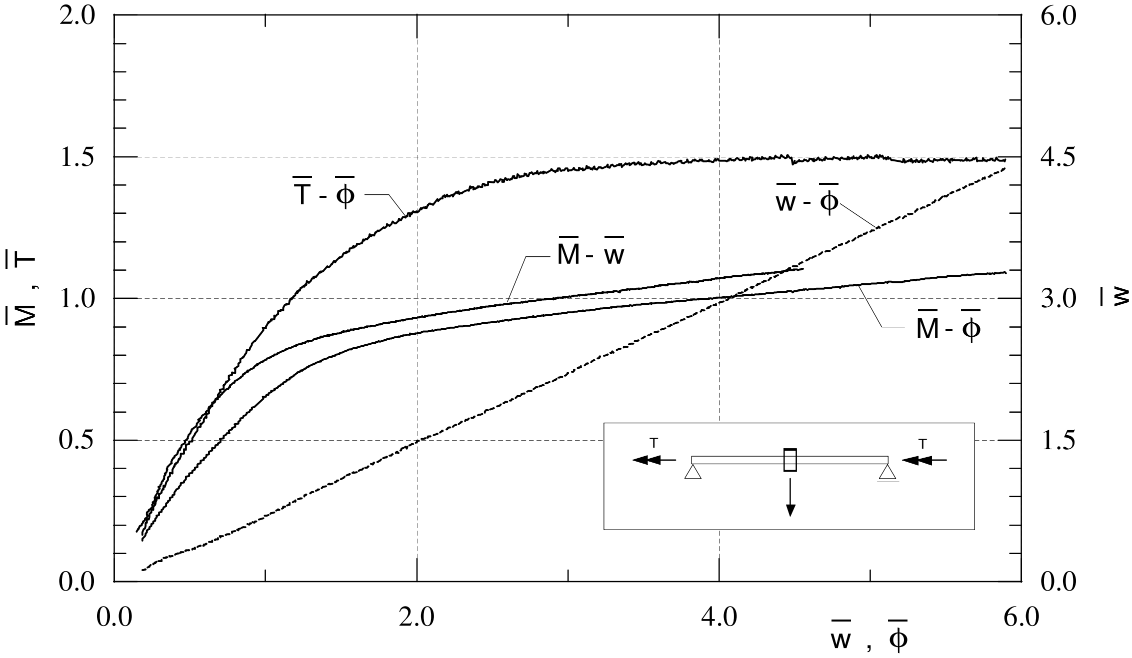

Figure 5.7: Test H-2-MT, HEB 140 with bending and torsion.

The plastic capacity in bending only, is about $\overline{M}$=1.15 for both sections. In torsion, the fully plastic warping torsional moment is $\overline{T}$=1.5 (discussed in Section 6.1), where the value 1.5 refers to the plastic shape factor for pure bending of a rectangular cross-section, in this case the flanges. When these fully plastic "capacities" are compared to the measured resistances for tests H-2-MT and I-2-MT, it can be seen that the values agree quite well. Note that this indicates a weak interaction between the forces for this particular load case.

The two specimens H-3-MT and I-3-MT were subjected to the same load combination, but were given a relatively larger torsion load than the two previous tests. Due to this the torsional deformations became larger, and a significant weak axis bending component arose, increasing from the midsection towards the end supports. For the I-3-MT specimen the response is shown to a twist rotation of approximately $\overline{\phi}$=12.0 or ϕ=12.0·7.84°= 94°, i.e. practically a state of pure weak axis bending near the support points at the end of the test. Figures 5.8 and 5.10

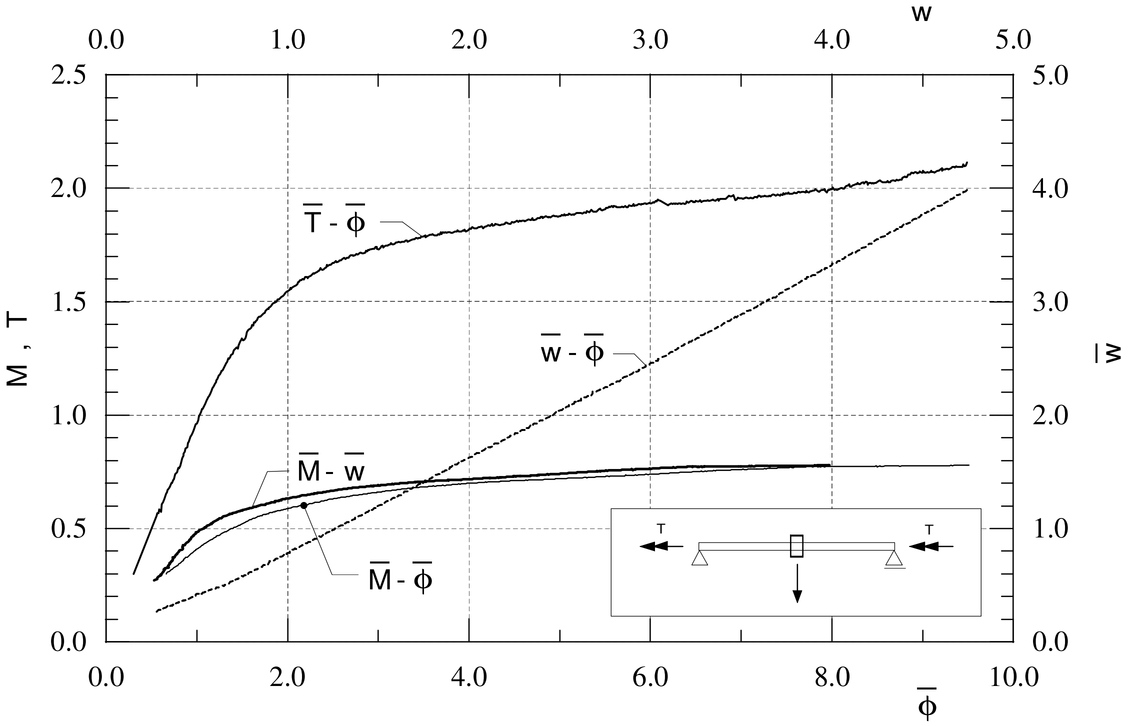

Figure 5.8: Test H-3-MT, HEB 140 with bending and torsion.

show the response, that for the torsional moment gives curves that have a steadily increase in the inelastic range for increasing twist, whereas the curves for bending moment level off. For the IPE section in particular, the bending resistance decreases for deformations $\overline{w}$ beyond approximately 5.0, probably due to the introduced weak axis bending. For the HEB section this is not observed, and this can be explained by the relatively smaller rotation of this specimen and hence less weak axis bending, and also by the smaller difference between weak and strong axis bending resistance for this section.

The torsional moments obtained are almost as large as for the specimens subjected to nonuniform torsion alone, see Figures 5.27 and 5.28. Also the shape of the curves is quite similar. For the bending moment, the maximum value obtained is $\overline{M}$=0.8 and $\overline{M}$=0.7 for the HEB and the IPE section, respectively. The interaction between the forces (M and T) is hence weak. Furthermore, it can also be seen that the response in torsion for these tests is quite similar to the response obtained in the MT-tests performed with a constant bending moment, see Figures 5.22 and 5.26. Hence the load path dependence seems to be small.

For all four MT tests the sum of the largest obtained torsional and bending moment greatly exceeds the capacity defined by initial yielding. Taking a rotation of $\overline{\phi}$=4.0 as reference in all tests, it is seen that the sum of the moments, $\overline{M} + \overline{T}$, results in values ranging from 2.5 to 3.0 times the capacity determined from linear interaction between the theoretical first yield values ($\overline{M} + \overline{T}$=1.0). All tests show a ductile behaviour, and a design based on the plastic capacities is conservative.

None of the specimens developed any significant local buckles during the testing. Like all the test specimens subjected to nonuniform torsional loading, and as depicted in Appendix B, the deformed specimens showed a smaller slope discontinuity in the flanges at the specimen midpoint, due to localized plastification.

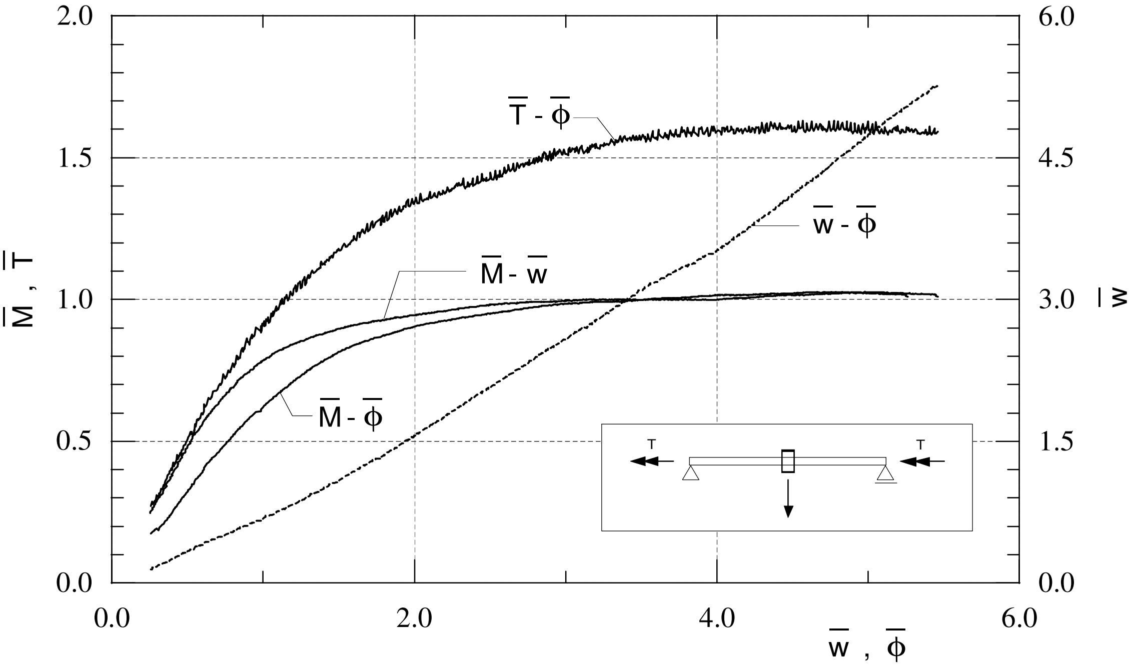

Figure 5.9: Test I-2-MT, IPE 160 with bending and torsion.

5.4.4 Load combination NT

Tests H-7-NT, H-9-NT and H-10-NT, axial load and torsion

Figures 5.11 to 5.13 show the behaviour of the HEB specimens that were subjected to axial load and nonuniform torsion. Both the torsional response ($\overline{T}$-$\overline{\phi}$) and the axial shortening $\overline{u}$-$\overline{\phi}$ during the tests are given. As indicated in the graphs, the displacement in w-direction was restrained at the specimen midpoint in these tests, to prevent the test specimens from buckling in that direction.

For the H-10-NT test ($\overline{N}$=0.835, Figure 5.13) the response-data for the torsional moment was significantly disturbed by friction effects and some problems with finding the appropriate amplification of the control signal for the torsional motors. A 10'th degree polynomial fit is therefore used for curve smoothing. The response curves for the tests at $\overline{N}$=0.334 and $\overline{N}$=0.50 are plotted directly from the recorded data.

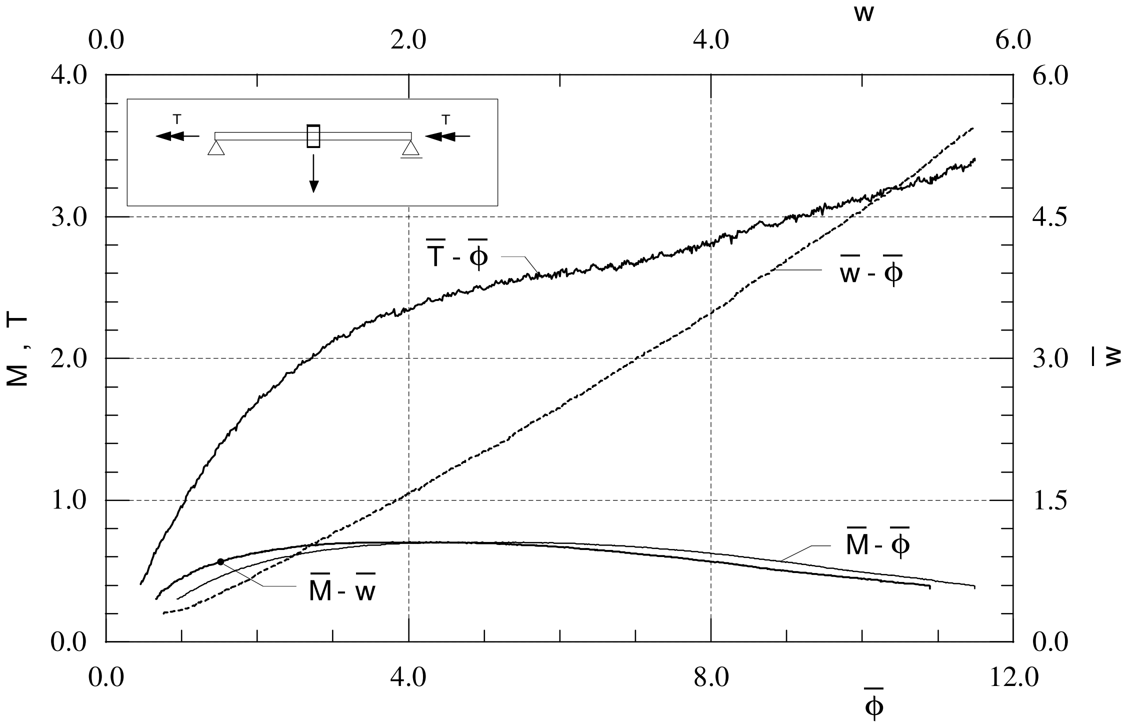

Figure 5.10: Test I-3-MT, IPE 160 with bending and torsion.

No local buckles were observed for the H-7-NT and the H-9-NT specimens. The distribution of the twist angle along the specimen H-7-NT was measured during the test, and the results are presented in Appendix C. The H-10-NT test specimen developed a smaller local buckle in one of the flanges at the $l/4$ point of the specimen after the maximum moment was well passed.

A repeat experiment was carried out for test H-9-NT, in order to study to what extent the axial load transfer at the specimen ends could influence the experimental results. The results from this repeat experiment are discussed in Section 8.2, and the experimental results are shown in Figure 8.6.

Tests I-8-NT and I-9-NT, axial load and torsion

The results from these tests are given in Figures 5.14 and 5.15. Both tests were carried out without observing any local buckling of the flanges, but at the end of test I-9-NT the web developed some large buckles which was followed by a deformation of the flanges. The curve for the torsional moment is smoothed for both tests.

5.4.5 Load combination NMT

Tests H-5-NMT and H-6-NMT

The test results are shown in Figures 5.16 and 5.17.

These tests were both carried out at an axial load level $\overline{N}$=0.344. For H-5-NMT the loading vector in the force space gives a larger moment component than for

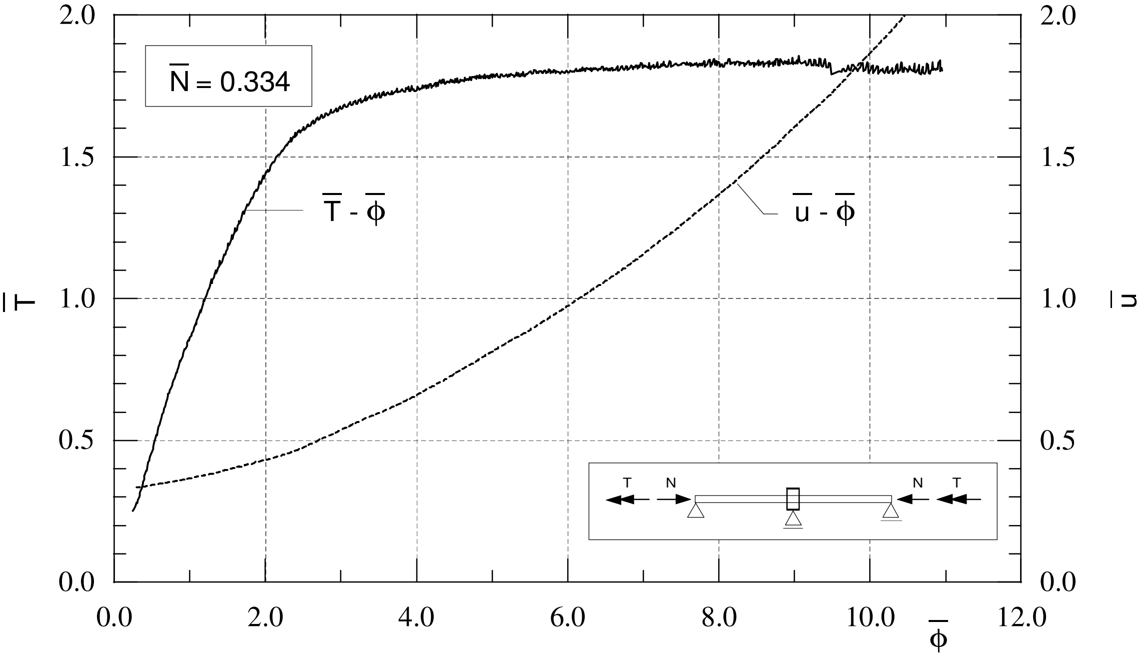

Figure 5.11: Test H-7-NT, HEB 140 with axial load and torsion.

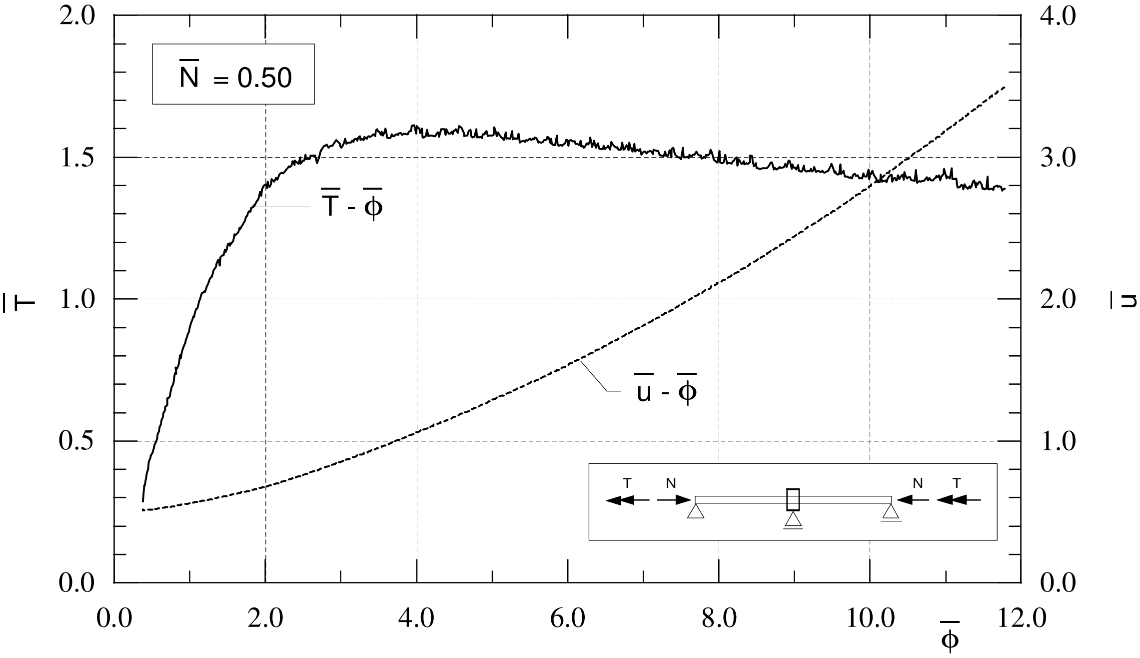

Figure 5.12: Test H-9-NT, HEB 140 with axial load and torsion.

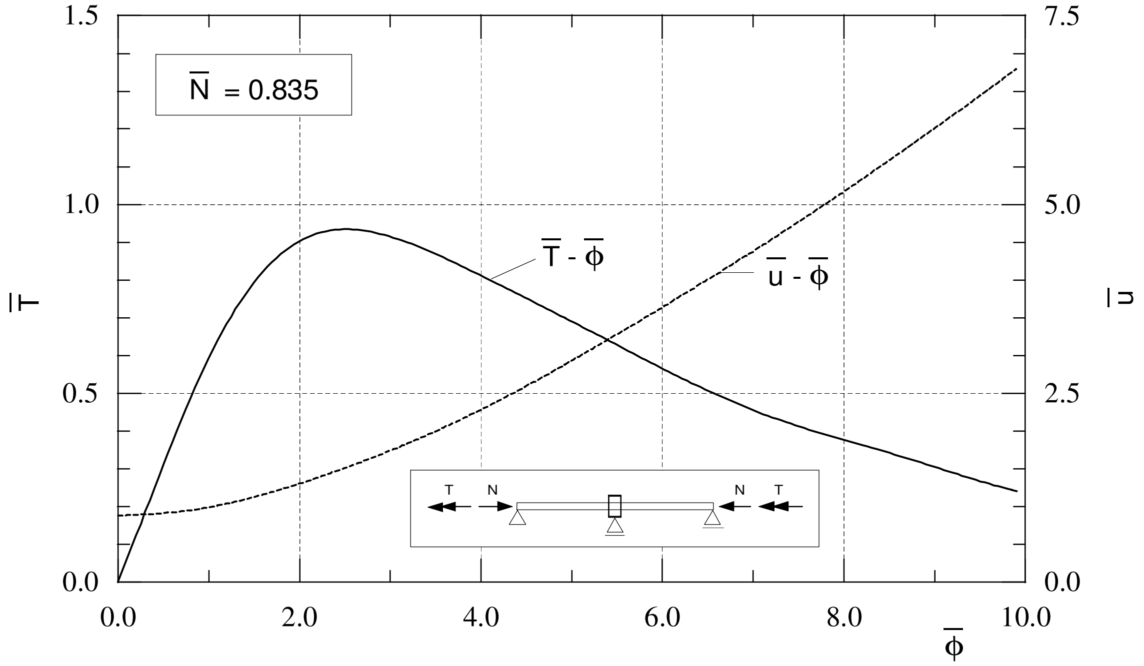

Figure 5.13: Test H-10-NT, HEB 140 with axial load and torsion.

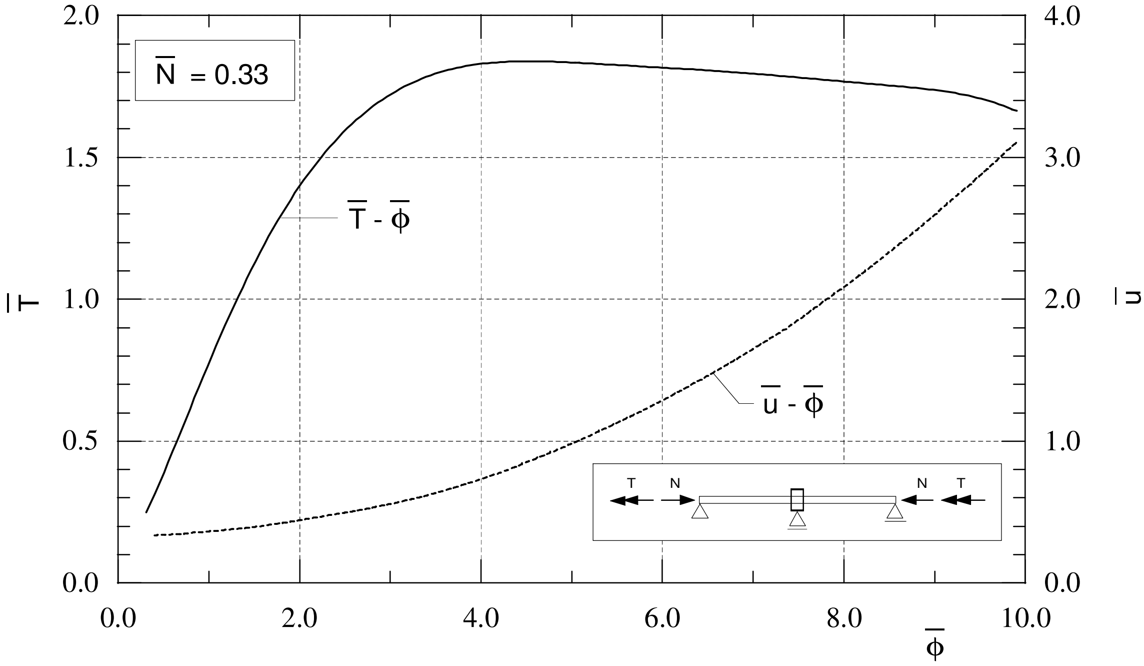

Figure 5.14: Test I-8-NT, IPE 160 with axial load and torsion.

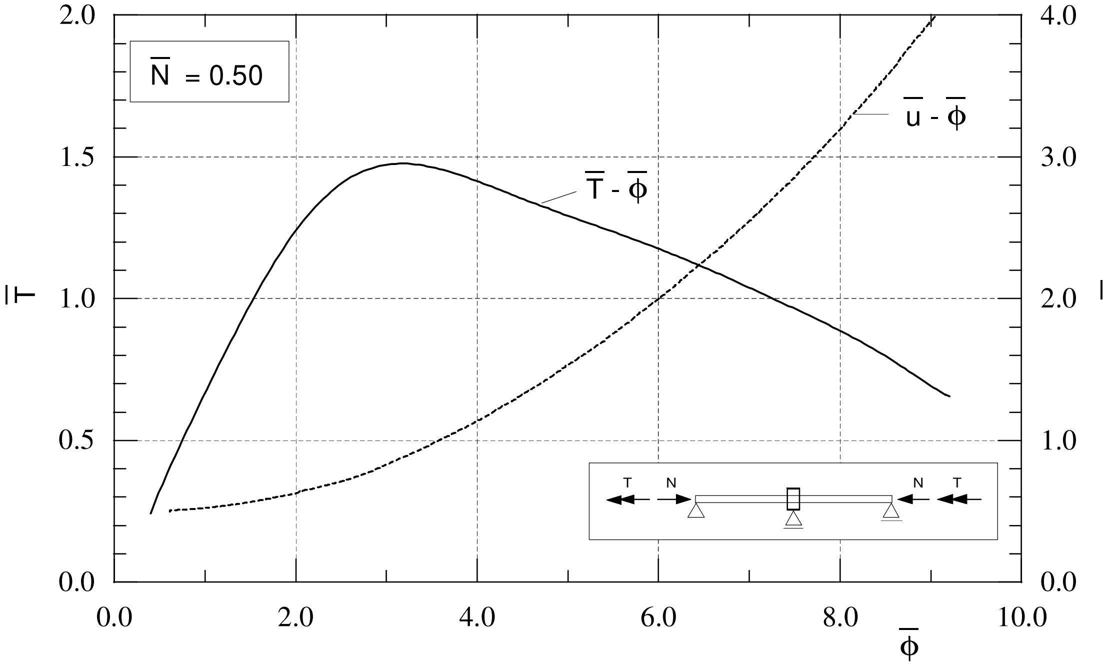

Figure 5.15: Test I-9-NT, IPE 160 with axial load and torsion.

H-6-NMT. The specimens showed only minor flange deformations, and no clear local buckles. For test H-6-NMT the deflection w was measured only by the IDT in the actuator, and the presented $\overline{w}$-$\overline{\phi}$ curve may be slightly misleading at low levels of the bending moment. In both tests, values of $\overline{N}$+$\overline{M}$+$\overline{T}$ in the range 2.4 to 2.7 are obtained.

Test H-8-NMT

Test H-8-NMT is shown in Figure 5.18. Two flange buckles appeared symmetrically about and close to the specimen midpoint in the most compressed flange part at the deflection level $\overline{w}$=3.4. The buckle amplitude was about 2 mm, but seemed to be straightened out towards the end of the test. Again, a value of $\overline{N}$+$\overline{M}$+$\overline{T}$ of approximately 2.5 is obtained, which indicates large inelastic reserves.

Tests I-4-NMT and I-5-NMT

The results from the tests at the axial load level $\overline{N}$=0.14 are shown in Figures 5.19 and 5.20, where the $\overline{T}$-$\overline{\phi}$ curve for test I-4-NMT is smoothed. At this low level of axial load both tests were carried out without significant local buckling before the response curves started to flatten out. In test I-5-NMT the transverse loading was started somewhat late, but still within the linear part of the torsional response. Both tests ended in a kind of lateral torsional / lateral buckling failure. Also for the IPE specimens the sum of the obtained values of $\overline{N}$, $\overline{M}$ and $\overline{T}$ exceeds 2.0.

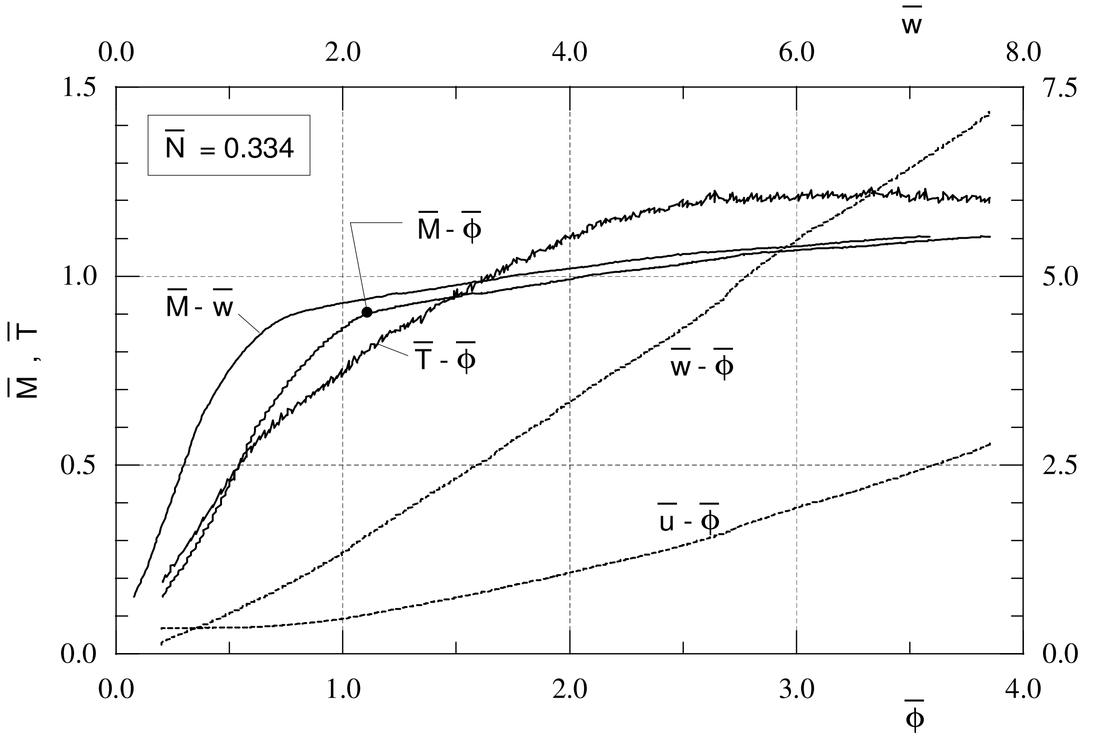

Figure 5.16: Test H-5-NMT, HEB 140 with axial load,bending and torsion.

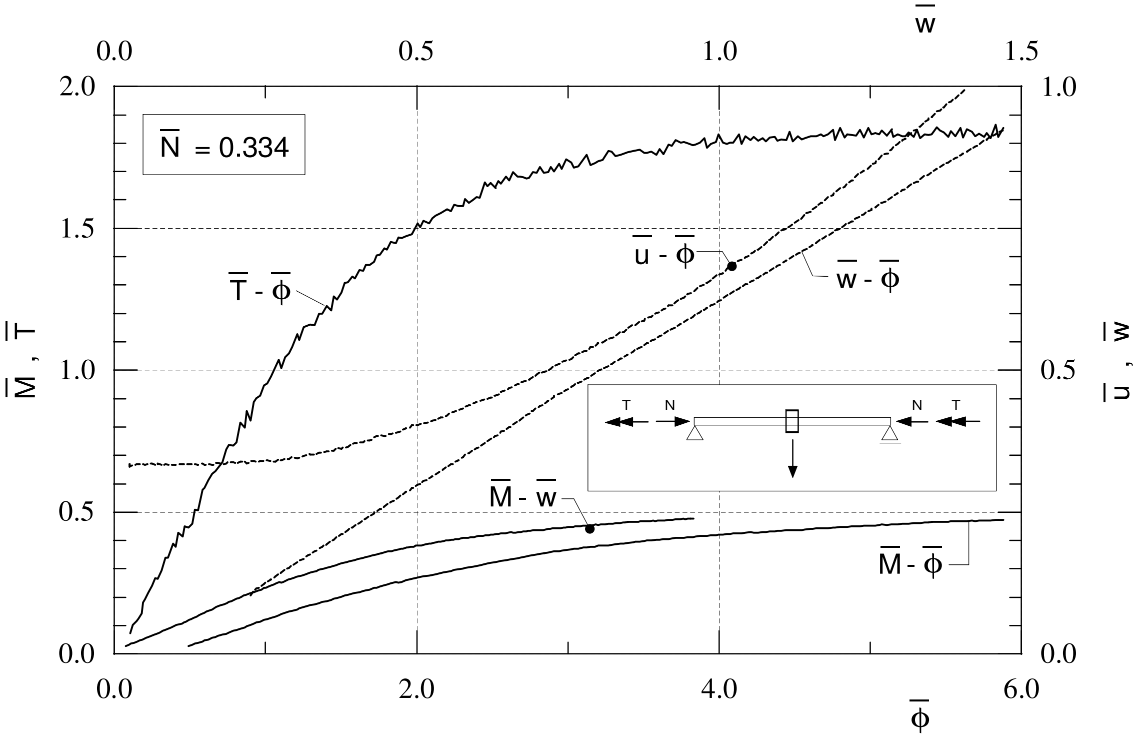

Figure 5.17: Test H-6-NMT, HEB 140 with axial load,bending and torsion.

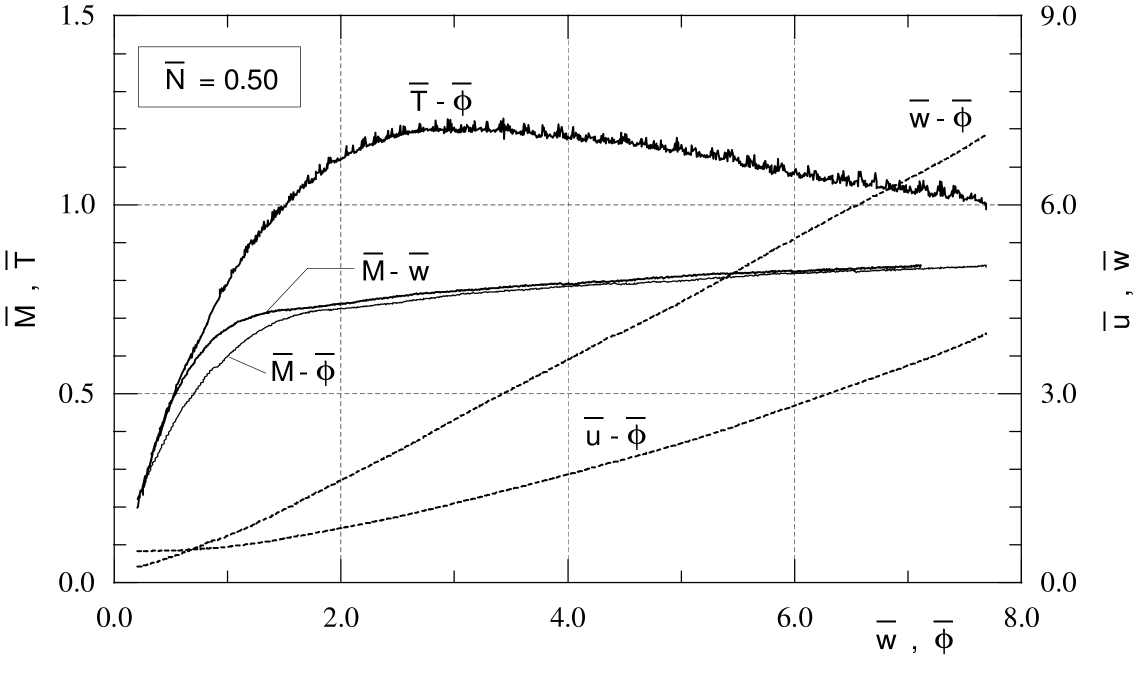

Figure 5.18: Test H-8-NMT, HEB 140 with axial load,bending and torsion.

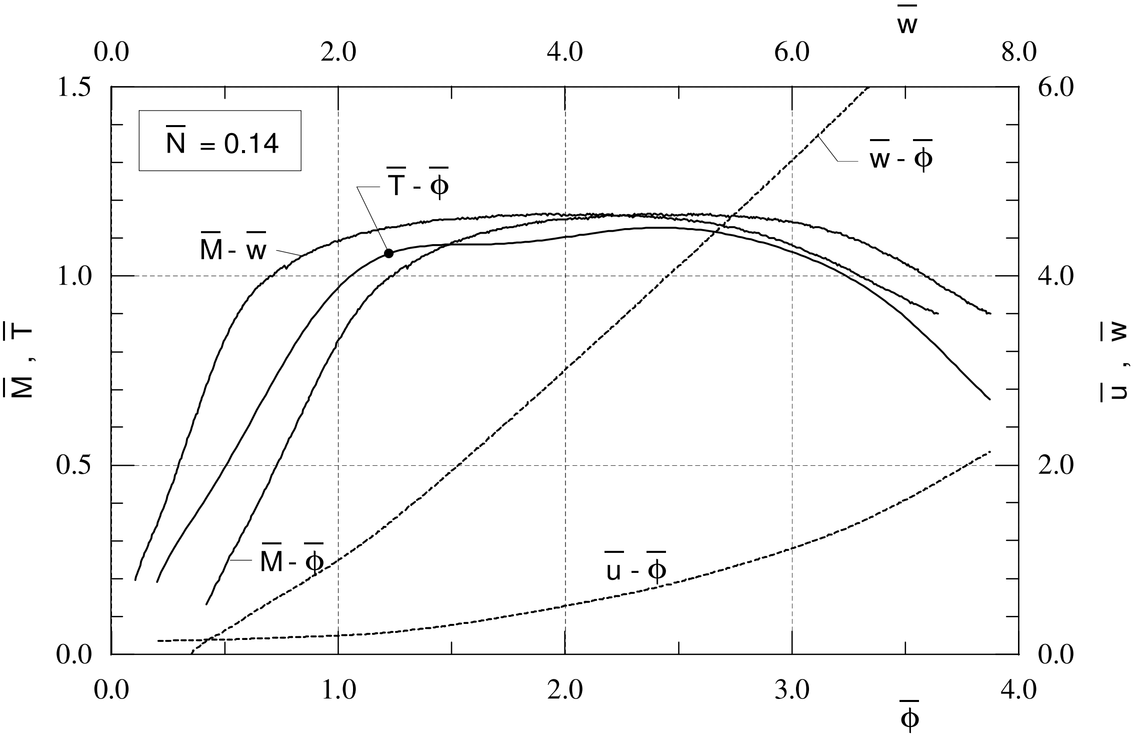

Figure 5.19: Test I-4-NMT, IPE 160 with axial load,bending and torsion.

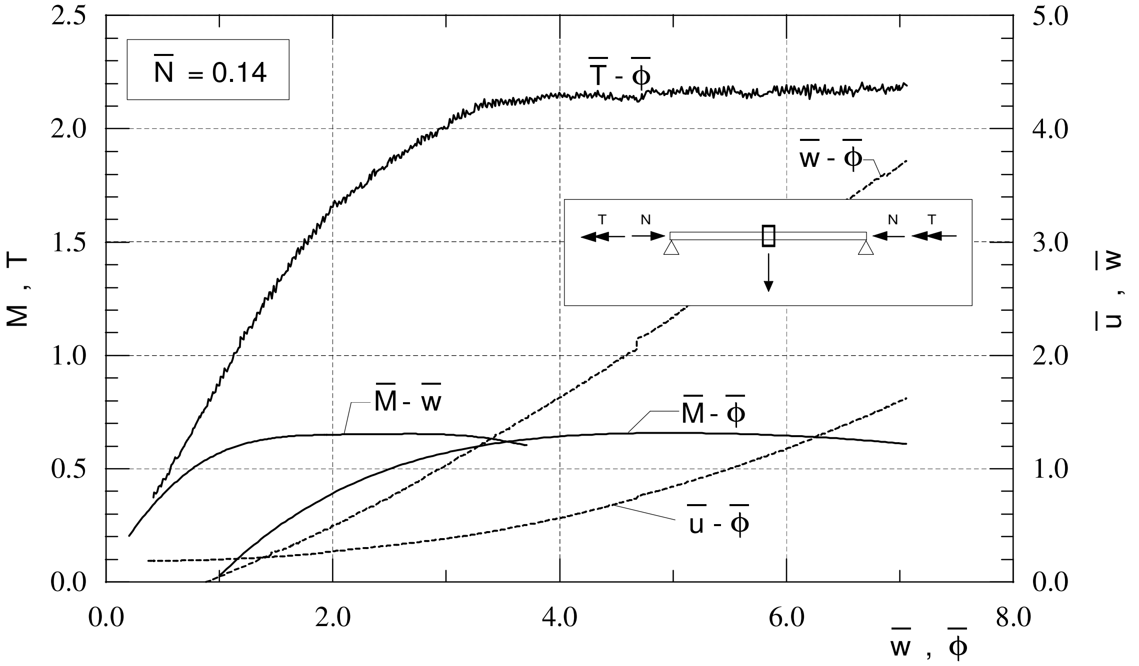

Figure 5.20: Test I-5-NMT, IPE 160 with axial load,bending and torsion.

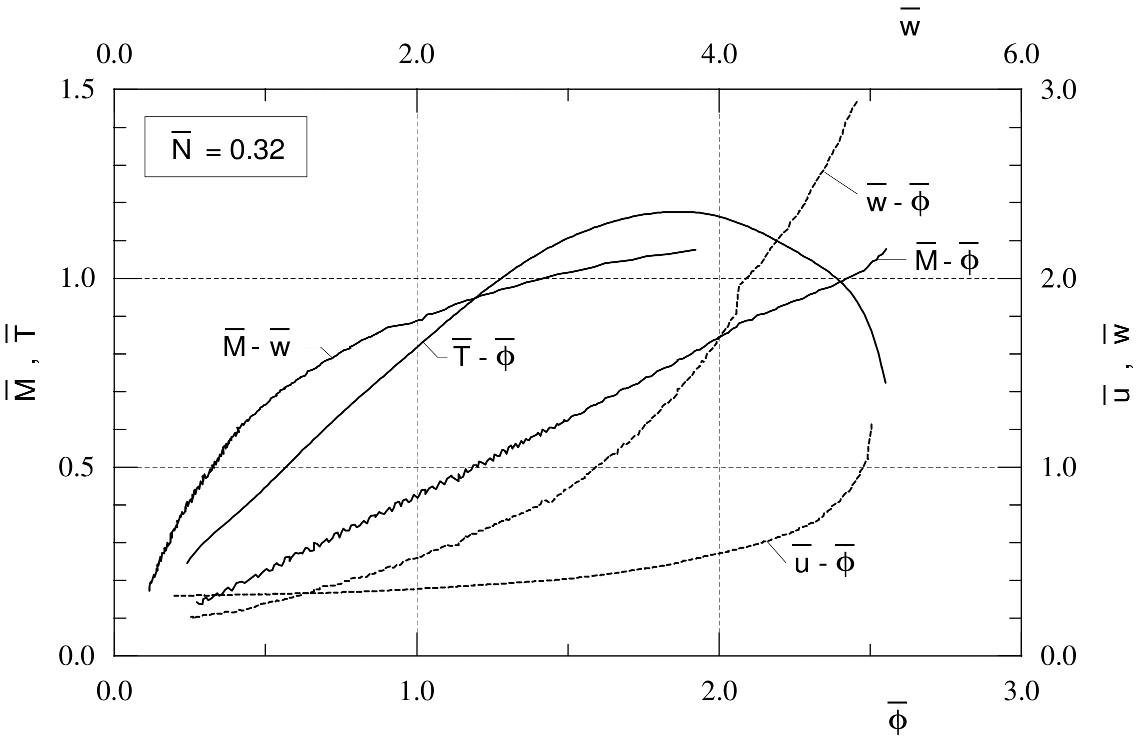

Figure 5.21: Test I-7-NMT, IPE 160 with axial load,bending and torsion.

Test I-7-NMT

This test was carried out at an axial load level $\overline{N}$=0.32, and the results are given in Figure 5.21. As clearly shown by the $\overline{u}$-$\overline{\phi}$ curve, the test ended in a sudden buckling, starting from local flange buckles which appeared about at the time of the maximum torsional moment. A cross-sectional capacity can hardly be determined from this test.

5.4.6 Load combinations with constant bending moment

In the following, the results from the tests with constant and near constant bending moment are presented.

Test H-11-MT

In this test, the bending moment ($\overline{M}$=0.77) was kept constant by means a constant transverse load H, and no axial load was applied. Figure 5.22 shows both the response in torsion, $\overline{T}$-$\overline{\phi}$, and the developed midspan deflection, $\overline{w}$-$\overline{\phi}$. Also shown is the response curve from the test with nonuniform torsion only ($\overline{M}$=0), presented in Chapter 4. It is seen that the applied bending moment reduces the torsional moment with approximately 20 %.

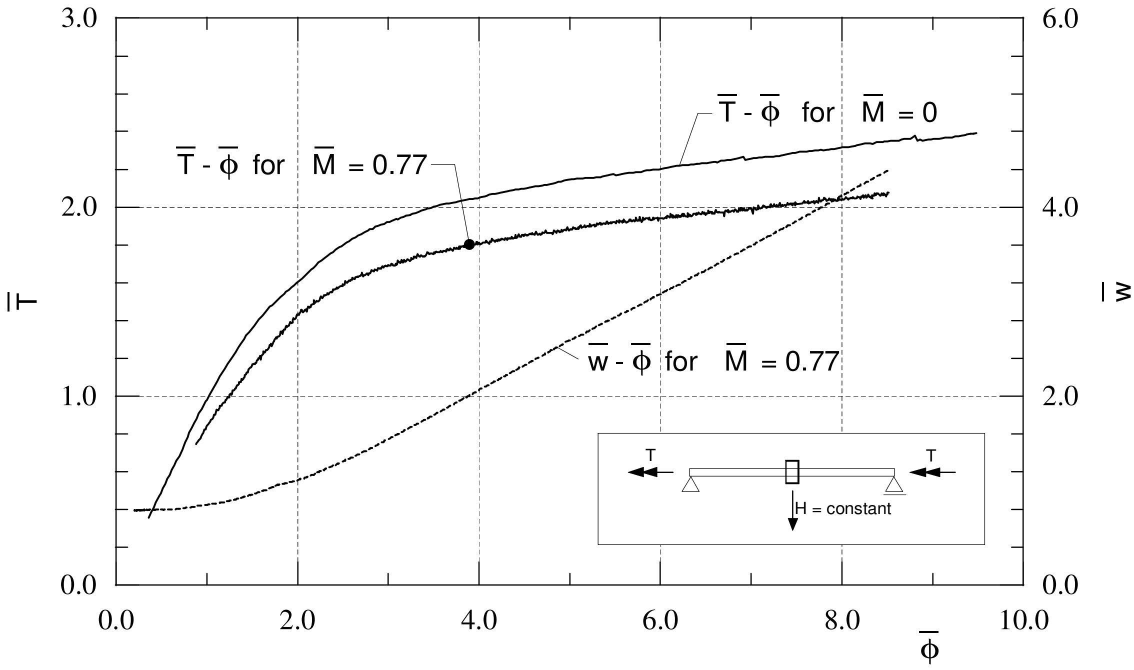

Figure 5.22: Test H-11-MT, HEB 140 with constant bending moment and torsion.

Tests H-12-NMT and H-13-NMT

In these two tests the axial load (N) was first applied, followed by the constant transverse load (H), and then the torsional loading was started (linearly increasing ϕ).

Figure 5.23 presents the results from test H-12-NMT, where an axial load of $\overline{N}$=0.25 was applied. As shown in the figure, the bending moment increases throughout the test due to the induced additional bending moment N·w.

Figure 5.24 shows the results for test H-13-NMT. Compared to test H-7-NT (Figure 5.11), which has the same axial load but no bending moment, it is seen that almost the same values are obtained for the torsional moment.

Tests H-14-NMT and H-15-NMT

These two tests were carried out with a constant axial load $\overline{N}$=0.50 and a constant bending moment.

The results from test H-14-NMT is presented in Figure 5.25. If the test is compared to test H-8-NMT (Figure 5.18, with a different loading procedure) it can be seen that almost the same capacities are achieved.

In test H-15-NMT a constant bending moment $\overline{M}$=0.155 was applied. The results obtained for the torsional moment were nearly identical to those given in Figure 5.12. No graph for this test is shown here, but the results are in used in

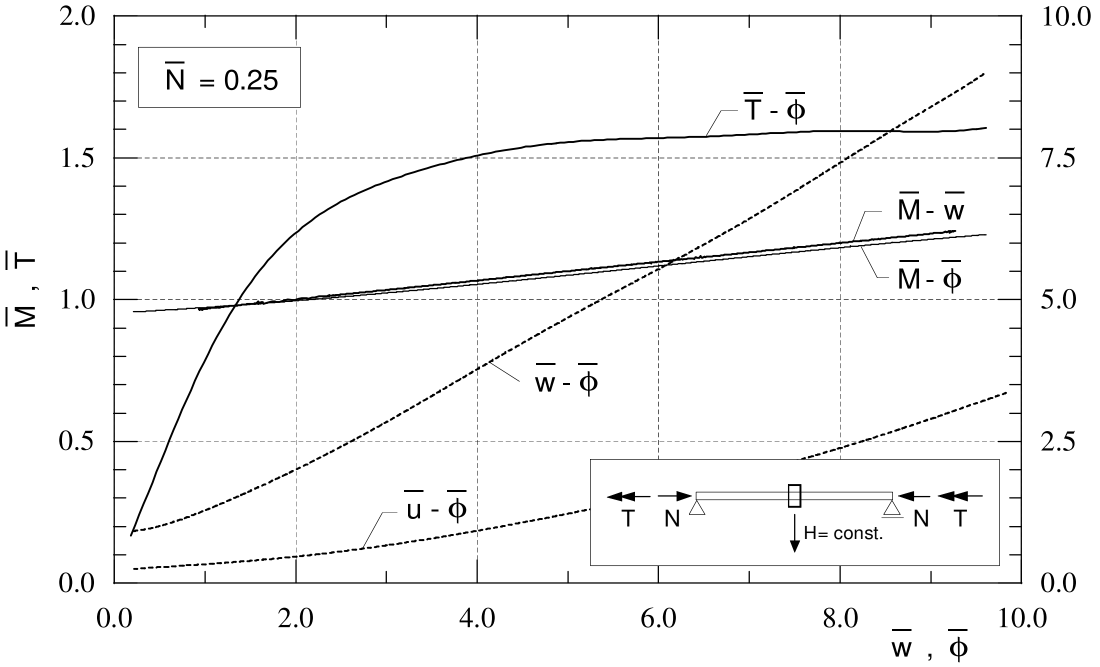

Figure 5.23: Test H-12-NMT, HEB 140 with axial load, bending and torsion.

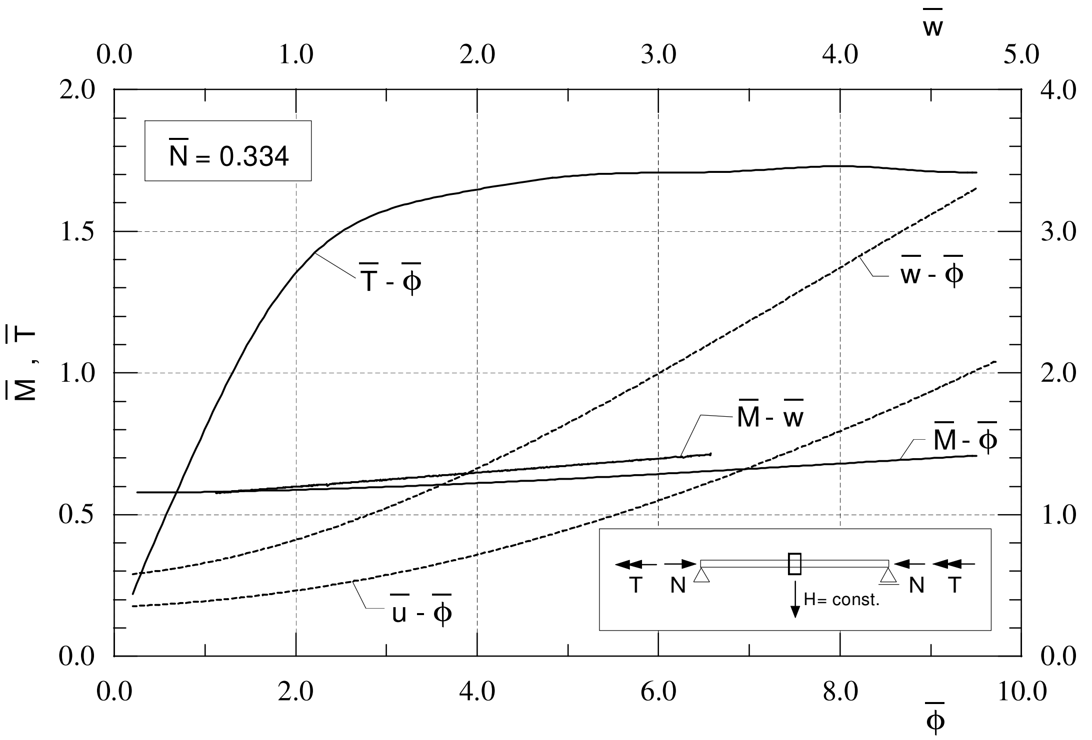

Figure 5.24: Test H-13-NMT, HEB 140 with axial load, bending and torsion.

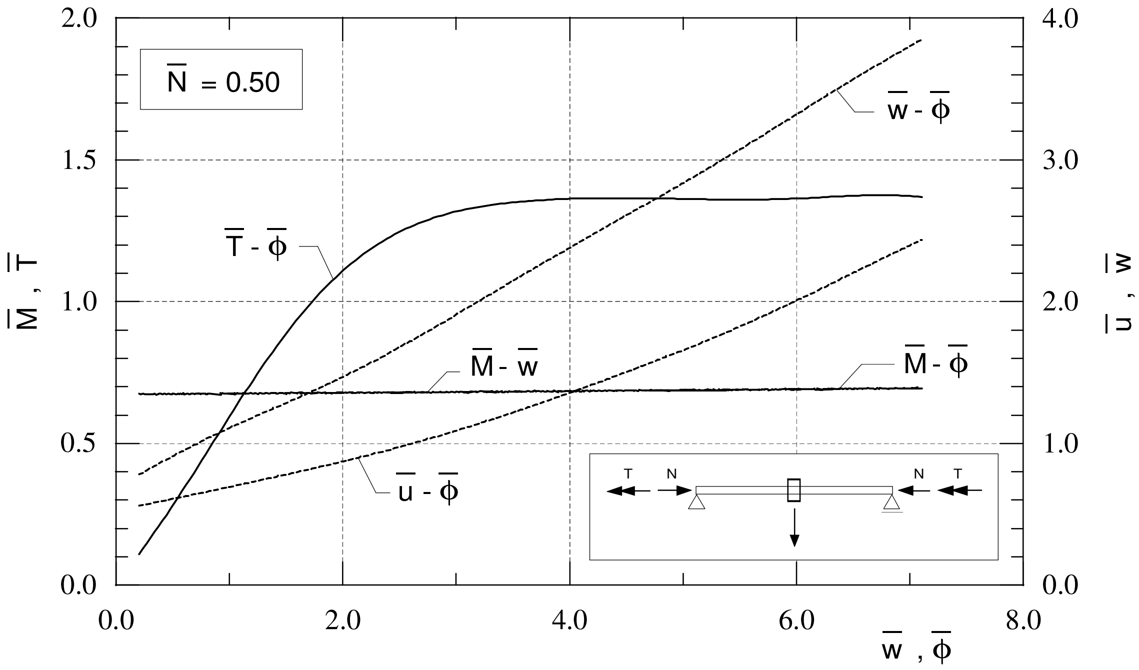

Figure 5.25: Test H-14-NMT, HEB 140 with axial load, bending and torsion.

Section 6.4 (Figure 6.15).

Tests I-10-MT and I-11-MT

The torsional response from these tests is shown in Figure 5.26 together with the response curve for pure nonuniform torsion, $\overline{M}$=0. The two curves from the present tests are smoothed, and are based on mean values of the torsional moment measured at the upper and lower end of the specimens. The rotation symmetry was not too good in the two tests, and the torsional moment differed about 10% at the specimen ends in both tests. Nevertheless, the presented curves give quite representative results.

As shown, the torsional resistance is not much affected by the bending moment. Still at an end rotation of 31 degrees ($\overline{\phi}$=4.0) the curves show almost identical values for the torsional moment. At twice this rotation, the torsional resistance is reduced with not more than 20% due to the bending moment $\overline{M}$=0.71. For the test with $\overline{M}$=0.71, it is seen that the sum $\overline{M}+\overline{T}$ is approximately 3.3 at the end of the test, i.e. a significant larger capacity than predicted by any existing design method. The total deflection w of the specimens was about 25 mm in these two tests.

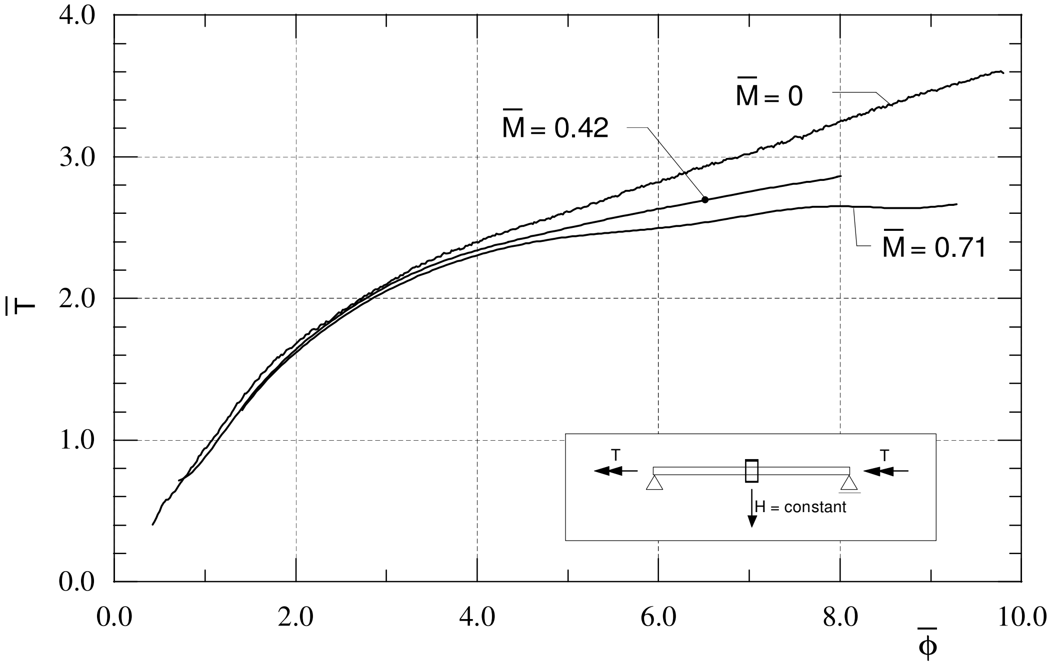

Figure 5.26: Tests I-10-MT and I-11-MT, IPE 160 with constant bending moment and torsion.

5.5 Compilation of tests with axial load and torsion

Figure 5.27 presents the results for all NT tests on the HEB section, i.e. the axial load levels $\overline{N}$=0, $\overline{N}$=0.334, $\overline{N}$=0.50 and $\overline{N}$=0.835. Here, the rotation $\overline{\phi}$=14.0 corresponds to a twist rotation of approximately 70 degrees. As shown, no global instability is reached for axial loads less than approximately $\overline{N}$=0.35. This is mainly due to the fact that the induced second order effects caused by N (discussed in Section 6.2) are balanced by the increased torsional resistance due to large rotations. Note that the initial torsional stiffness is dependent on the level of the axial load. Note also that even for an axial load equal to 83.5% of the section squash load, a torsional moment equal to 90% of the initial yield moment is reached.

Figure 5.28 shows the corresponding results for the IPE section. Here, the instable situation is reached already for the test at $\overline{N}$=0.33. Taking the $\overline{N}$=0.50 -test as an example, it is seen that the sum of $\overline{N}$ and $\overline{T}$ is about 2.0. This indicates that there are large inelastic reserves present also for this load combination. Compared to the tests on the HEB section, it is seen that the initial torsional stiffness for the IPE tests is relatively more affected by the applied axial load.

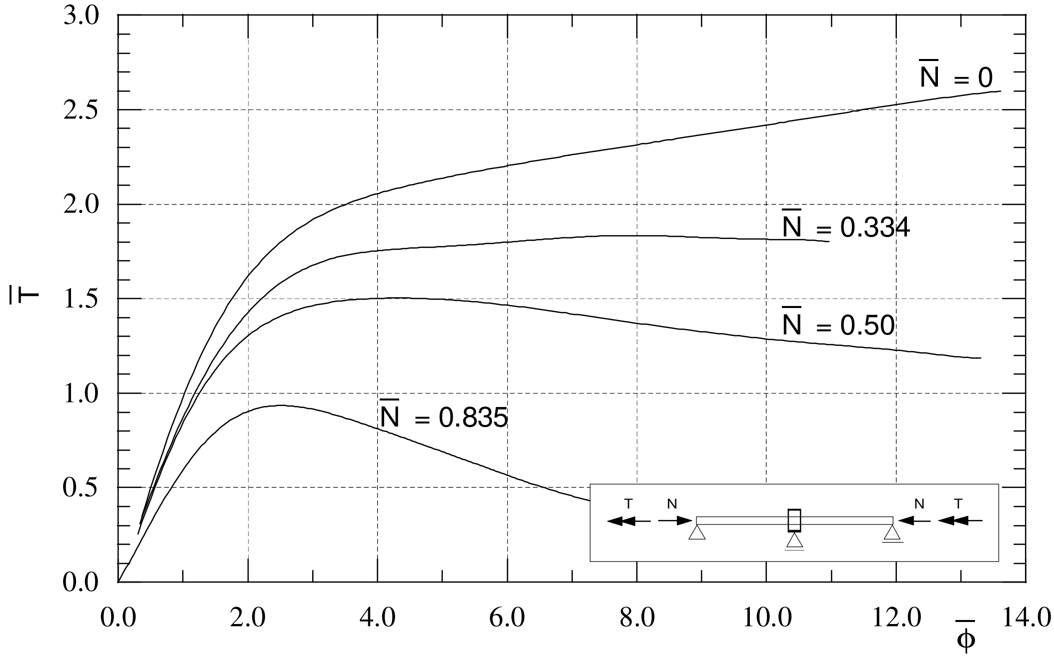

Figure 5.27: Tests with axial load and nonuniform torsion on HEB 140.

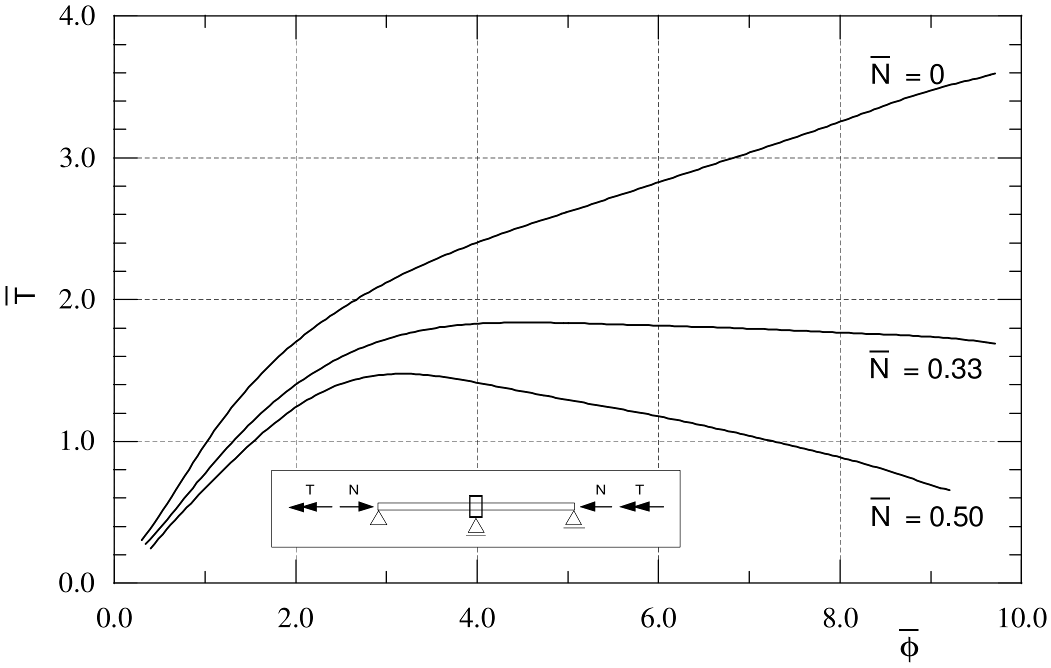

Figure 5.28: Tests with axial load and nonuniform torsion on IPE 160.

5.6 Tests with uniform torsion and axial load.

In addition to the beam-column tests presented in the previous, two tests were carried out for columns with axial load and *uniform* torsion. The loading conditions are shown in the inset of Figure 5.29. The axial load was applied and held at a constant level, and uniform twist rotations were applied linearly. The objective of these tests was to investigate how the axial force affects the behaviour in uniform torsion, and an axial load level of 50% and 34% was chosen for the HEB and the IPE, respectively. The IPE specimen ($\overline{N}$=0.34) was laterally braced (v=0) at the midpoint to prevent lateral buckling.

The uniform torsion was applied in the same manner as in the pure uniform torsion tests in Chapter 4, i.e. without warping restraints at the loading points or at the specimen midspan. For these two particular tests the specimen ends were given a special design, slightly different from that used for the beam-columns tested in nonuniform torsion. At the ends of these two specimens more of the flange material was removed, leaving only the web plate (h·s) in contact with the base plates. The axial load was then applied through the base plates without constraining the warping of the flanges.

The results from the tests are shown in Figures 5.29 and 5.30. The normalization of the torsional moments and the rotations is based on the first-yield values in single uniform torsion. Here, the values T_Y=2.62 kNm and ϕ_Y=19.9° are used for the

HEB and T$_Y$=0.938 kNm and ϕ_Y=37.1° for the IPE. Only the response curve for the HEB test ($\overline{N}$=0.50) is smoothed. The corresponding curves from the uniform torsion tests at $\overline{N}$=0 are shown for comparison.

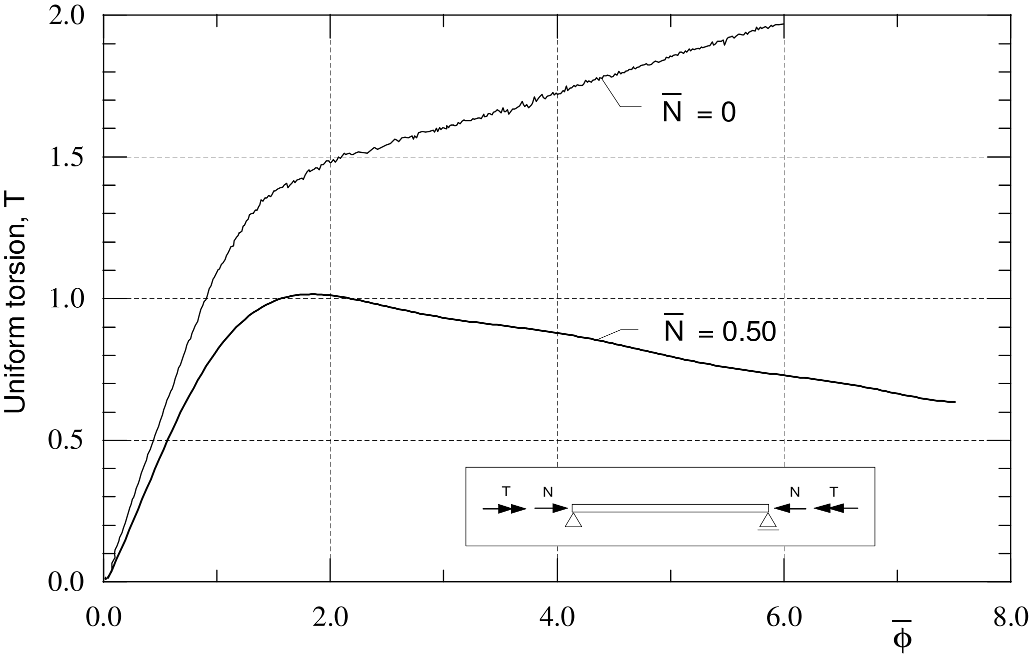

Figure 5.29: Tests on HEB 140, uniform torsion at constant axial load.

As pointed out in Chapter 4 the HEB test in single uniform torsion ($\overline{N}$=0) gave a somewhat large elastic torsional stiffness (compared to theory). Hence, some of the difference in elastic stiffness for the two HEB tests in Figure 5.29 may be caused by this. Nevertheless, as the applied axial load N is expected to reduce the torsional stiffness somewhat, the results seems quite reasonable.

Note that the initial yield moment ($\overline{T}$=1.0) is reached in the HEB test, even though the axial load level is as high as 50%.

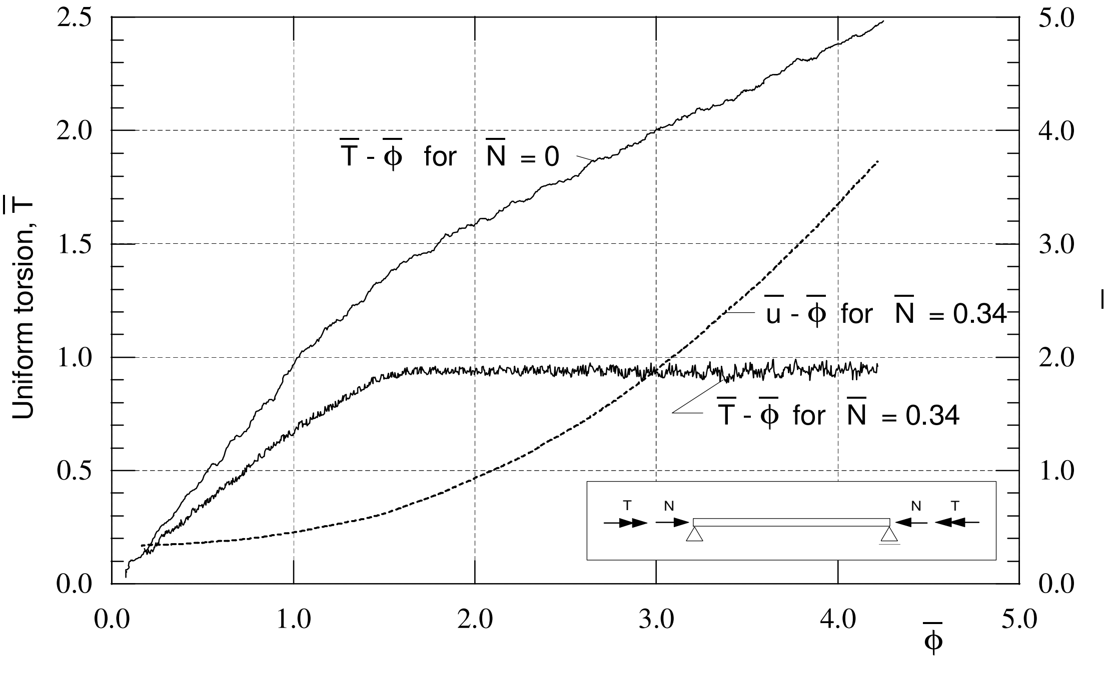

Figure 5.30: Tests on IPE 160, uniform torsion at constant axial load.

Chapter 6

Interpretation of results

This chapter presents results from the beam-column tests. The second order torsional effects arising from the axial force is discussed, and the interaction between bending and torsion is shown for different levels of the axial force.

6.1 Plastic torsional moment

As previously noted, the total internal resistance of a member to torsional loading is composed of the sum of the two components "uniform torsion" and "warping torsion". With the assumptions of the linear elastic torsion theory, these two components and their interdependence may be determined from the differential equation for torsion (Equation 4.2). Appendix A.2 gives the solution for the elastic distribution between uniform torsional moment (T_u) and warping torsional moment (T_w) for the beam-columns of the present study. As shown, the applied torsional moment is resisted 100% by warping torsional moment at the midspan section decreasing to about 30% at the free ends.

In the elastic state the shear stresses due to uniform torsion and the normal and shear stresses due to warping torsion may be determined at any point in a beam. For inelastic torsion, however, no theory exists for calculating the two components or the resulting stresses, but there exist some simple limits for the plastic resistance. For an I-section fully plastified in uniform shear, i.e. with a fully plastic shear stress distribution as shown in Figure 6.1a, the corresponding plastic moment T_{up} is given by the sand-heap analogy (Nadai 1950)

$$T_{up} = \frac{f_y}{\sqrt{3}} \left[bt^2 \left(1 - \frac{t}{3b} \right) + (h - 2t)\frac{s^2}{2} + \frac{s^3}{6} \right] \tag{6.1}$$

if the section is considered to be made up of three rectangular strips and the von Mises yield criterion is used. For a real rolled section, the contribution of the fillets to the capacity may increase T_{up} somewhat, but this is not taken into account in the following.

For pure elastic warping torsion on an I-shaped section the external torsional moment is resisted by warping shear stresses τ_w creating a flange shear couple V_f as shown in Figure 6.1b. The flanges are bent laterally, about their strong axis, resulting in equal and opposite directed flange bending moments M_f. These moments may also be expressed in form of the bimoment $B = h_t M_f$, to allow

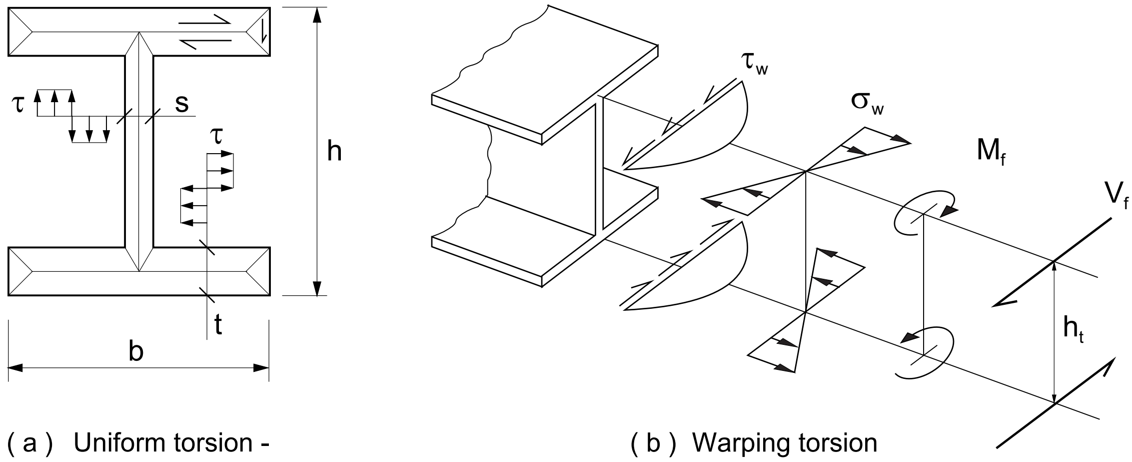

(a) Uniform torsion -
plastic shear stress distribution

(b) Warping torsion

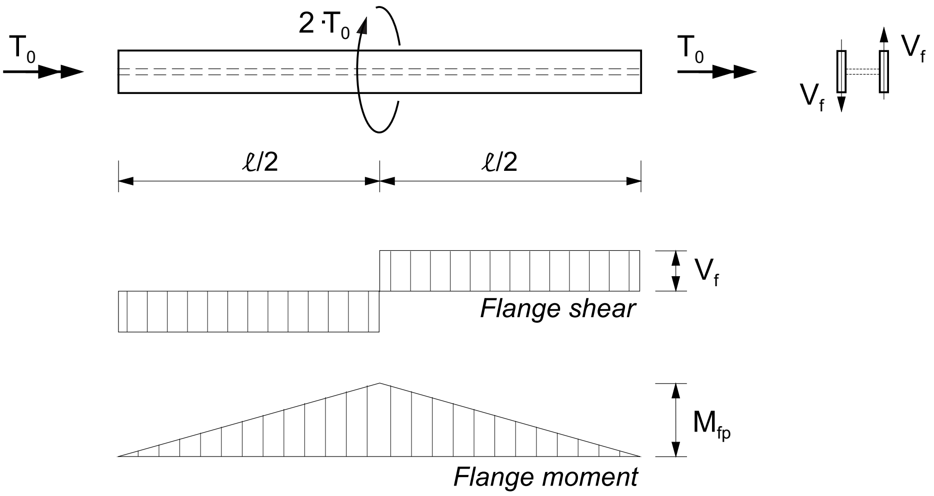

(c) Flange bending analogy

Figure 6.1: Torsion on an I-shaped section.

the warping stress - bimoment relationship to be expressed in the same form as for ordinary beam flexure. The warping normal stresses σ_w developed are usually much larger than the warping shear stresses τ_w, and the initial yield flange moment is hence governed by the normal stresses. As the plastic shape factor for pure bending of rectangular sections (the flanges) is equal to 1.5, the fully plastic warping flange moment is correspondingly equal to 1.5 times the initial yield flange moment. Even with this simple and well defined plastic limit in warping the plastic capacity for an I-shaped member cannot in general be determined. For a structural component the condition of pure warping torsion may not be realized due to plastic deformation as the boundary conditions that lead to zero St.Venant torsion in the elastic case may be violated.

However, when considering that in uniform torsion the ratio between the fully plastic moment T_{up} and the initial yield moment is also equal to 1.5 (for narrow rectangular section, Appendix A.3), it may seem reasonable to accept the shape factor 1.5 used also for computation of the plastic capacity of a member, regardless of the type of torsion. If so, the plastic capacity for nonuniform torsion should be taken as 1.5 times the torsional moment that produces initial yielding in torsion, based on an elastic member distribution between the two torsion types. Note that only the flanges of the I-section are utilized in this model for the case of warping torsion, and that the actual fully plastic uniform torsional moment T_{up} for an I-section with different thickness for web and flanges exceeds the first yield moment by a factor larger than 1.5. This is due to the fact that the thinner plate remains elastic when the thicker reaches yielding. For these reasons the use of a factor equal to 1.5 is expected to give a conservative estimate of the capacity.

Another possible limit for the plastic torsional moment may be determined from a bending analogy, where only the lateral bending resistance of the flanges is considered. As shown in Figure 6.1 the applied torsional moment is replaced by a shear force couple V_f acting on the flanges, and the flanges are treated as two separate rectangular beams bent in opposite directions about their strong axes. For a torsionally pinned beam with a concentrated torsional moment T_0 applied at both ends, similar to the situation for the beam-columns of the present study (see also Appendix A), the flange shear force and the flange moment are distributed as shown in Figure 6.1c. The plastic flange moment is

$$M_{fp} = f_y \frac{1}{4} t b^2 \tag{6.2}$$

and the corresponding flange shear force is

$$V_f = \frac{2M_{fp}}{l} \tag{6.3}$$

which gives a plastic torsional moment

$$T_{0p} = V_f \cdot h_t = f_y \frac{1}{2} t b^2 \frac{h_t}{l} \tag{6.4}$$

As the entire torsional moment is here assumed to be resisted by flange bending only, the in many cases significant uniform torsion resistance is neglected and the resulting bending actions and the normal stresses are over-estimated. When considering that for most cases the normal stresses are critical, rather than the uniform shear stresses, the bending analogy is expected to give quite conservative values for the plastic capacity. For the present HEB and the IPE beam this is clearly demonstrated, as the full plastic torsional moments predicted by the bending analogy are even less than the initial yielding torsional moments obtained from the elastic torsion equation (Equation 4.2).

For the nonuniform torsion tests presented in Chapter 4 the experimental results for the torsional moment are compared to a value denoted "Merchant upper bound". This "upper bound" was originally suggested by Dinno and Merchant (1965) as an empirically based limit for the plastic collapse torsional moment for an I-section cantilever beam subjected to a concentrated torsional moment at the free end. The method has been extended to other load and support conditions and used in several investigations. Dinno and Merchant assumed that the total torsional moment at plastic collapse of the cantilever could be taken as the sum of the plastic uniform torsional moment T_{up}, i.e. the full sand heap capacity of the section, plus a contribution T_{wp} from plastic bending (warping resistance) of the flanges similar to the bending analogy above. The "Merchant" value of the torsional moment for the beam in Figure 6.1c is then

$$T_{0,Merchant} = T_{up} + T_{wp} \quad = T_{up} + f_y \frac{1}{2} t b^2 \frac{h_t}{l} \tag{6.5}$$

where T_{up} is given in Equation 6.1.

Equation 6.5 is obviously not an upper bound according to the theory of plasticity. In that case it should have involved an assumed deformation field from which the stress resultants were deduced. Instead, full yielding over the cross-section and along the beam due to uniform shear stresses is assumed, with simultaneously occurring warping stresses in the flanges, which reaches full yielding at the critical section. In addition, as in the bending analogy, the normally less significant warping shear stresses τ_w are ignored. However, as the Merchant upper bound includes both torsional resistance components, and models the warping resistance's dependency of the beam length and boundary conditions, it seems to be a reasonable method for estimating the capacity for nonuniform torsion.

In all available experiments on I-section beams in nonuniform torsion, (Boulton 1965, Dinno and Merchant 1965, Farwell and Galambos 1969), higher values of the torsional moments are reached than those predicted by Equation 6.5. As shown in Figures 4.6 and 4.7 this is also the case for the tests in the present investigation, for which the ultimate value is predicted quite well for the HEB section while the resistance for the IPE exceeds the Merchant value considerably. This is of course due to nonlinear geometric and material strain hardening effects. It can also be seen from the experimental data in the literature that the Merchant value also gives a reasonable prediction of the values of the torsional moment at which a significant change in torsional stiffness occurs. At least the Merchant value gives no poorer information on this point than the alternatives do (sand-heap or initial yielding). The results obtained in the numerical studies by Baba et al. (1982), Bathe et al. (1983), May et al. (1989) and Pi and Trahair (1994c) all lend support to the acceptance of Merchant's upper bound as a reasonable accurate model for estimating the torsional moment at plastic collapse.

An alternative formula can easily be derived based on the same approach to the problem, but without the violation of the yield criterion. This is achieved simply by reducing the values for the plastic warping moment T_{wp} and for the plastic uniform torsional moment T_{up} (Equation 6.5) in the flanges such that the combination of the resulting stresses, still plastic distributed, at any material point satisfies the von Mises yield criterion

$$\sigma^2 + 3\tau^2 = f_y^2 \tag{6.6}$$

This has the effect of using a reduced (*) value for the yield stress

$$\sigma_Y^* = \sqrt{f_y^2 - 3\tau^2} \qquad \left(or \;\; \tau_Y^* = \frac{1}{\sqrt{3}}\sqrt{f_y^2 - \sigma^2} \right) \tag{6.7}$$

in the development of the formula. For a beam with a load situation as shown in Figure 6.1c the alternative capacity ($T_{0,alt}$) is hence obtained as the sum of the fully plastic uniform torsional moment for the web plus the two contributions from the flanges (combining Equations 6.1, 6.5 and 6.7)

$$T_{0,alt} = \frac{f_y}{\sqrt{3}}\left[(h-2t)\frac{s^2}{2} + \frac{s^3}{6}\right] + \tau\left[bt^2\left(1 - \frac{t}{3b}\right)\right] + \sqrt{f_y^2 - 3\tau^2}\left[\frac{1}{2}tb^2\frac{h_t}{l}\right] \tag{6.8}$$

Note, however, that interaction with the warping shear stresses τ_w in the flanges is neglected.

The largest value max($T_{0,alt}$) is obtained by maximizing Equation 6.8 with respect to τ, which gives the optimum ratio between the torsional moment carried by warping and by uniform torsion in the flanges. The solution for max($T_{0,alt}$) is

$$\begin{aligned} max(T_{0,alt}) &= \frac{f_{y,web}}{\sqrt{3}}\left(\frac{s^2}{2}(h-2t) + \frac{s^3}{6}\right) \\ &+ \frac{f_{y,flange}}{\sqrt{3}}\left(1 - \frac{t}{3b}\right)^2 t^3 b \sqrt{\frac{1}{t^2\left(1-\frac{t}{3b}\right)^2 + \frac{3}{4}\frac{b^2 h_t^2}{l^2}}} \\ &+ f_{y,flange}\frac{tb^2 h_t}{2l}\sqrt{1 - \frac{t^2\left(1-\frac{t}{3b}\right)^2}{t^2\left(1-\frac{t}{3b}\right)^2 + \frac{3}{4}\frac{b^2 h_t^2}{l^2}}} \end{aligned} \tag{6.9}$$

Note that Equation 6.8 is based on the interaction between internal forces due to two separate load carrying mechanisms. Due to the similarity with standard

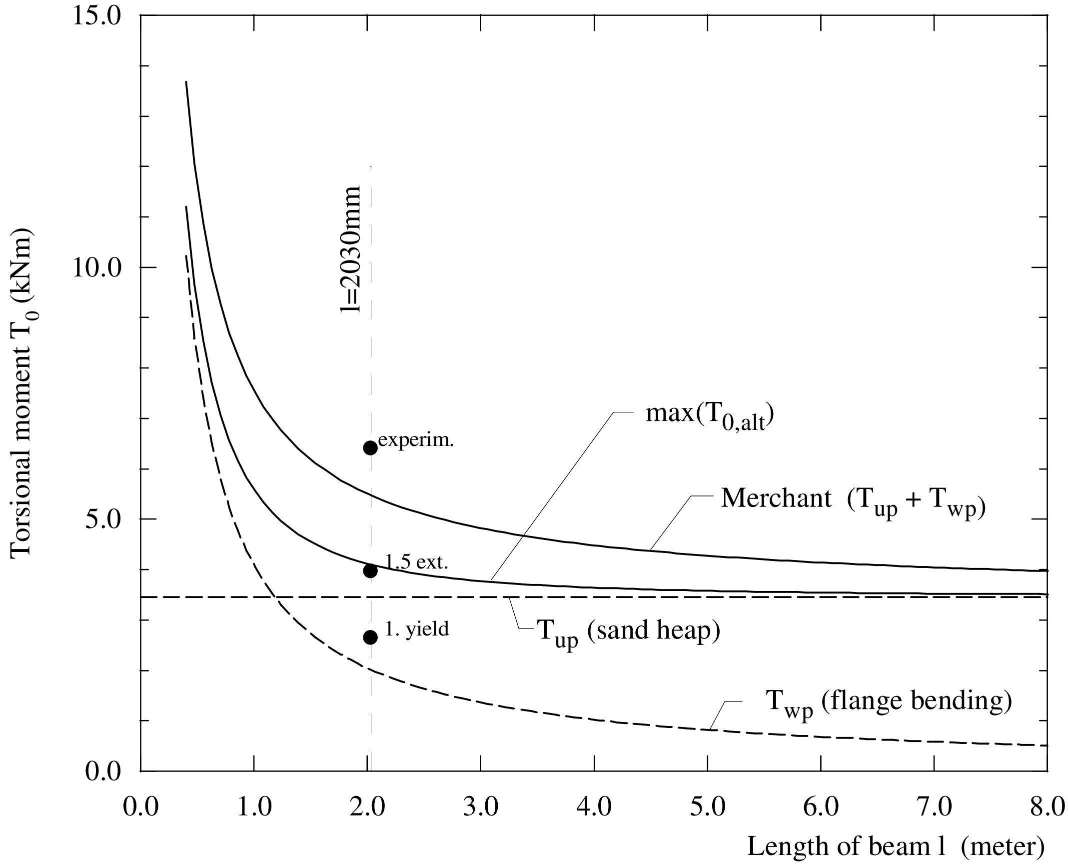

Figure 6.2: Methods for determining plastic collapse torsional moment.

solutions for interaction between sectional forces, it is assumed that also Equation 6.8 will give conservative results.

Figure 6.2 gives a comparison of some of the above methods for estimating the torsional moment at plastic collapse. The figure shows curves for the plastic torsional moment as a function of the beam length (l), calculated for the HEB 140 section with the load situation shown in Figure 6.1c. As the sand-heap moment T_{up} is a property of the section (for a given material) it is of course constant for all beam lengths, while the resistance caused by flange bending T_{wp} varies as a linear function of $1/l$. The capacity for a real beam will exceed the values given by T_{up} and T_{wp} since the sand-heap value T_{up} is exceeded in all experimental investigations and T_{wp} is a conservative solution. The figure clearly demonstrates that the Merchant upper bound predicts values for the torsional moment relatively close to T_{up} and T_{wp} for the limiting cases of very short and very long beams, with a maximum relative deviation for a beam length of approximately 1.2 meter. The solution max($T_{0,alt}$) predicts values close to T_{up} and T_{wp} for beam length less than 0.8 meter and larger than 2.5 meter respectively, but gives a significant increase for beam lengths of 0.8 to 2.5 meter.

The actual beam length 2030 mm used in the experiments of the present investigation is marked on the figure. Also marked is the value for the torsional moments corresponding to the computed first yield in elastic torsion, the value obtained by scaling this value by 1.5, and the real value measured in experiment. As shown, the torsional moment predicted by the Merchant upper bound is closest to the experimental value, and about 33% higher than the value predicted by max($T_{0,alt}$). As the scaled value of the elastic solution and the derived "lower bound" solution (max($T_{0,alt}$)) predict almost identical values for the torsional moment, these methods might be best suited for design purposes. Furthermore, this assumption is supported by studying the response curves from the nonuniform torsion tests, where the torsional stiffness remains almost unchanged for both the HEB and the IPE up to this level.

Nevertheless, due to the very simple form of the Merchant upper bound, and the good agreement with experimental and numerical tests, it seems to be the most obvious value to be used in discussions regarding full plastic torsional capacity.

6.2 Interaction effects

For a beam-column element subjected to loadings consisting of axial force, bending and torsion actions, there exist several types of interaction and amplification effects. The following discussion refers to components of I-shaped sections, but some of these effects are present for other cross-sections.

An extensive presentation of interaction and amplification effects for beam-columns in general is given by Chen and Atsuta (1977). They give a detailed description of the displacement/strain/sectional-force relationships for beam-columns of general cross-section, and of I-sections in particular. Some of these effects are discussed also by Pi and Trahair (1992) and (1994c) for the case of beams in bending and torsion.

The various interaction effects for beam-columns subjected to torsion as one of the actions, may be considered to be analogous to the situation in a member subjected to bending and compressive axial force, for which the lateral deflection induces additional moments, which in turn amplify the deflections. For torsion this "lateral deflection" is the deflection of the plate elements (web and flanges) that constitutes the cross-section, caused by the twist rotation of the member. The axial force that creates additional moments, or second order load actions, is the resultant of the compressive stresses in the particular parts of the cross-section. For an I-shaped cross-section, these effects are most prominent in the flanges.

The main effects related to torsional deformations for beam-columns are :

- Torsional buckling caused by a compressive axial force on the member.
- Torsional buckling caused by strong axis bending actions. This is only possible for beams which are continuously braced laterally, such that the lateral deflections (v) at the cross-sectional shear center remain at zero, and when prebuckling deflections are included.
- Lateral torsional buckling.
- Interaction between these buckling modes.
- Secondary weak axis bending moments that are induced when a beam originally subjected to strong axis bending is rotated/twisted about its longitudinal axis.

For a real beam-column not continuously braced, the actual failure will be a combination of those above, where also strong and weak axis flexural buckling and local buckling may contribute. As all member displacements are amplified by cross-sectional plastification, the behaviour is of course also strongly affected by this.

6.2.1 Uniform torsion - effects from axial load

Figure 6.3a shows the case of an I-section beam-column segment subjected to uniform torsion and a compressive axial load. Due to the applied uniform twist rotation, the longitudinal "fibers" of the segment form a helical shaped curve about the axis of rotation, while the cross-section sustains considerable warping deformation. The resulting warping of the flanges is illustrated in Figure 6.3a (no attempt is made to depict the actual twist). For the symmetric I-sections, the axis of rotation coincides with the member axis through the shear center/centroid of the cross-section. As the fibers outside the centroid form a helical curve, they are inclined relative to the member axis, with an angle that depends on the applied angle of twist and the distance from the centroid to the considered fiber.

The normal stresses σ caused by an axial load N can produce a second order contribution to the torsional moment due to the warping deformation that exists in the cross-section, i.e. due to the resulting inclination of the fibers and hence the normal stresses σ relative to the member axis. The component of these stresses in the plane normal to the member axis, indicated by the arrows in Figure 6.3b, contributes to this additional torsional moment. In the general case this contribution is called the "Wagner effect" (Chen and Atsuta 1977).

The importance of these effects may be demonstrated for the HEB section of the present study. For simplicity consider only the lateral rigid body motion

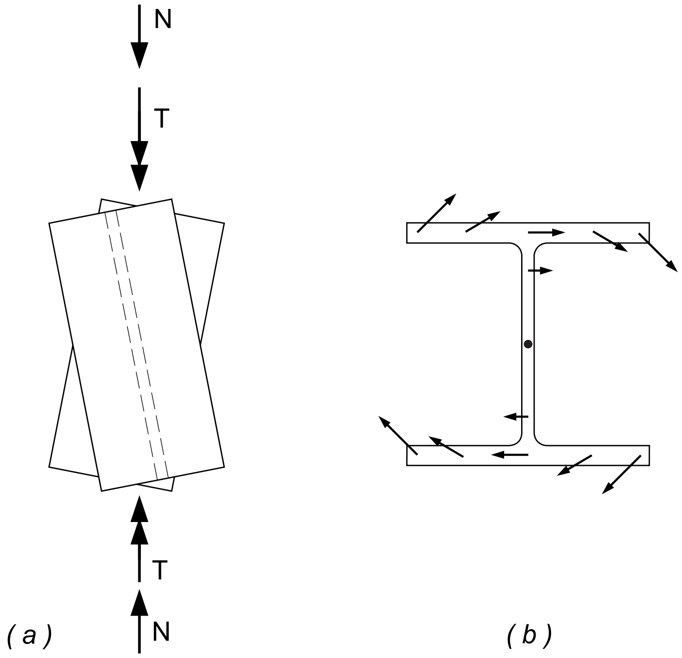

Figure 6.3: I-section beam-column in uniform torsion.

of the flanges (Figure 6.3a) and disregard the inclination normal to the flange element. Furthermore, assume the axial load to be carried by the flanges alone. For the beam-column of 2030 mm length subjected to an axial load of $\overline{N}$ =0.50 (600 kN) and a uniform twist rotation of $\overline{\phi}$=1.0 (19.9°), the resulting additional torsional moment equals approximately 16% of the initial yield moment. The full additional moment is obviously somewhat larger than this. Refer to Figure 5.27 for experimental results for the present example.

The critical value of the axial compressive load for the case of pure elastic torsional buckling with uniform twist deformations may be derived directly from a consideration of the force equilibrium. Consider the I-shaped member in Figure 6.4 which is subjected to an axial load N and is free to warp and to rotate about the longitudinal axis at the ends. The initial compressive stress is given by $\sigma = N/A$. A stub mn of this beam between two consecutive cross-sections, subjected to a small angle of twist ϕ, is shown in Figure 6.4b. By considering a strip in the flange as shown in figure b) of length dx and cross-sectional area dA, it is seen that the force $\sigma \cdot dA$ acting on the strip parallel to the member axis may be decomposed into a component $\sigma \cdot \beta \cdot dA$ directed perpendicular to the member axis (and $\perp$ to the radius-vector) and a component $\approx \sigma \cdot dA$ acting along the strip direction. Only the former component gives a contribution to a torsional moment as the force along the strip is balanced by an equal force at the opposite end. The inclination β of

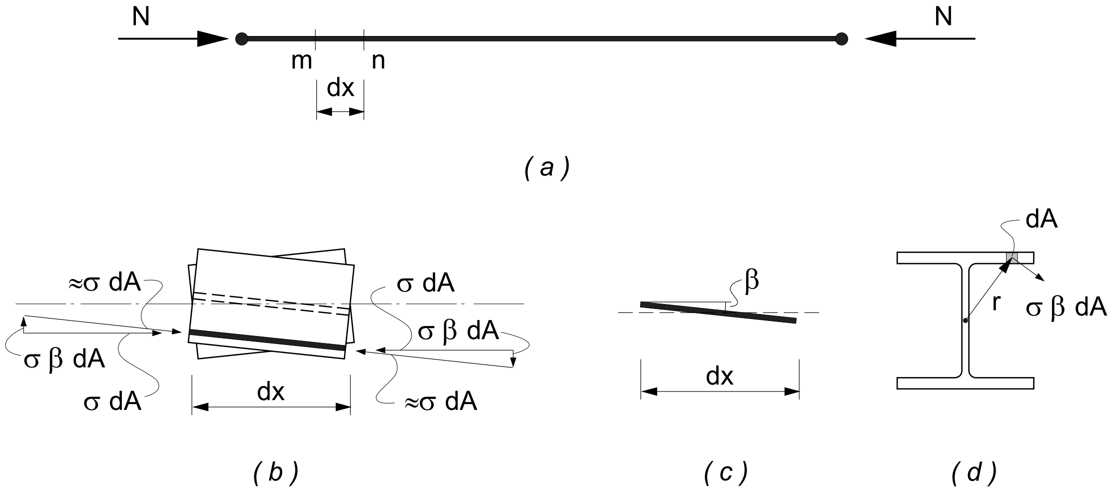

Figure 6.4: Uniform torsional buckling of an I-section beam.

the strip is given by

$$\beta = r\,\frac{d\phi}{dx} \tag{6.10}$$

By integrating the moment contributions for the entire section about the member axis the equilibrium equation describing torsional buckling is obtained

$$\int_A \sigma r \frac{d\phi}{dx} \cdot dA \cdot r - GI_T \frac{d\phi}{dx} = 0 \tag{6.11}$$

This gives a critical value (N_{ET}) for the axial force N

$$N_{ET} = \frac{A}{I_p} GI_T \tag{6.12}$$

Here, $I_p = \int_A r^2 dA$. Note that all the common assumptions of the linearized elastic buckling theory have been invoked.

The interaction effects between uniform torsion and a compressive axial load may be obtained by a similar approach. Let the beam-column element have an initial rotation ϕ_T and the strip have an initial inclination β_T caused by the externally applied torsional moment T on the beam-column. The application of the axial load N will produce an additional angle of twist ϕ_N and an additional inclination β_N. In terms of the total values $\phi_r = \phi_T + \phi_N$ and $\beta_r = \beta_T + \beta_N$, the equilibrium equation becomes

$$\int_A \sigma r \frac{d\phi_r}{dx} r dA - GI_T \frac{d\phi_N}{dx} = 0 \tag{6.13}$$

By using the value for N_{ET} from Equation 6.12, the additional twist angle caused by N is given by

$$\phi_N = \phi_T \, \frac{N/N_{ET}}{1 - N/N_{ET}} \tag{6.14}$$

and the total twist angle becomes

$$\phi_r = \phi_T \, \frac{1}{1 - N/N_{ET}} \tag{6.15}$$

The presence of the axial load N results in an amplification of the applied torsional moment T

$$T_r = T \, \frac{1}{1 - N/N_{ET}} \tag{6.16}$$

The amplification factor is similar to that obtained for beam-columns subjected to bending and compressive axial actions.

A simple design equation for beam-columns under uniform torsion and compressive axial load may be established based on the von Mises yield criterion $\sigma^2 + 3\tau^2 = f_y^2$. If the section modulus in uniform torsion is denoted W_T this reads

$$\left(\frac{N}{A}\right)^2 + 3\left(\frac{T}{W_T} \cdot \frac{1}{1 - N/N_{ET}}\right)^2 = {f_y}^2 \tag{6.17}$$

which may be rewritten as

$$\left(\frac{N}{N_d}\right)^2 + \left(\frac{T}{T_d} \cdot \frac{1}{1 - N/N_{ET}}\right)^2 = 1 \tag{6.18}$$

Here the yield stress f_y is replaced by a design stress f_d , and the capacities N_d and T_d are introduced. For a given value of the axial load N, the reduced capacity for a uniform torsional moment may be taken as

$$T^* = \sqrt{1 - \left(\frac{N}{N_d}\right)^2} \cdot (1 - N/N_{ET}) \cdot T_d \tag{6.19}$$

Figure 6.5 gives a comparison of the capacities predicted by Equation 6.18 (or 6.19) and the results obtained from numerical simulations for the HEB beam-column of the present study. The numerical results are obtained with the FE-program ABAQUS, using the shell element model of the beam-column as discussed in Chapter 8. Results are given for the torsional response at four values of the axial load, the largest being 80% of the yield load, i.e. $\overline{N}$=0.80. Experimental data for the case $\overline{N}$=0 and $\overline{N}$=0.50 are presented in Chapter 5, and the agreement between experiments and simulations is documented in Chapter 8. For the present purpose

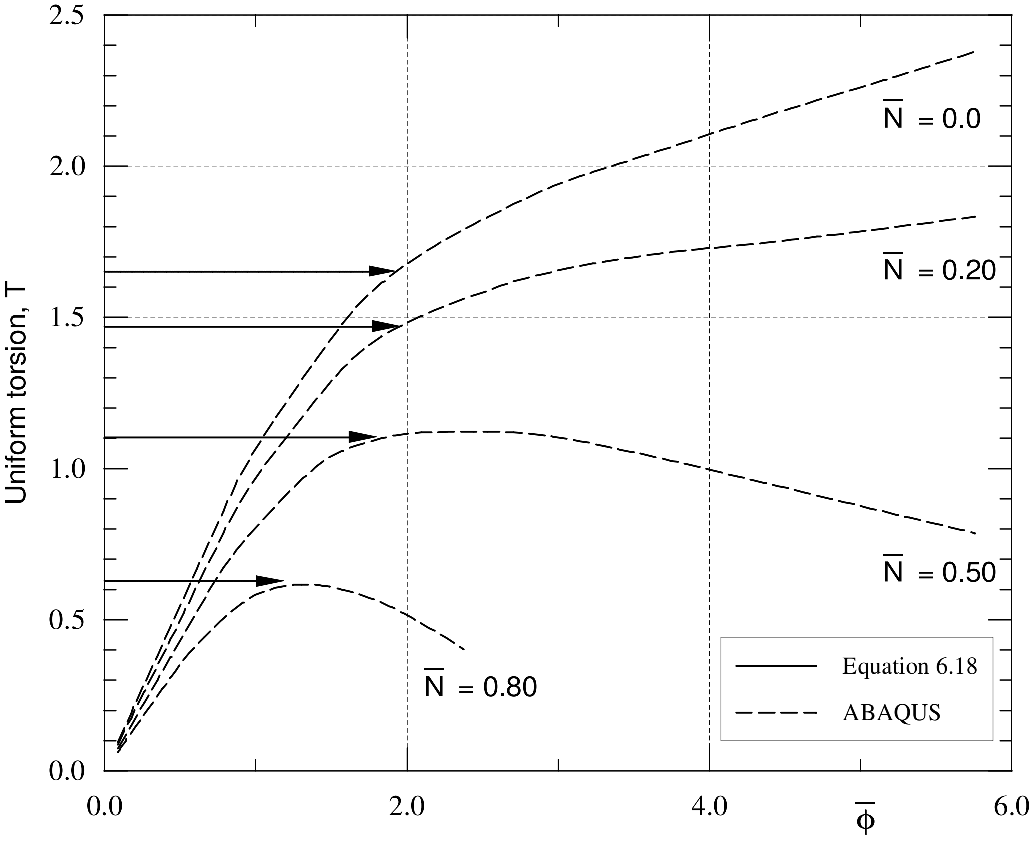

Figure 6.5: HEB 140 beam-column subjected to uniform torsion and axial load.

it was chosen to use simulations rather than the experiments for the comparison, as the latter contain data only for two values of N. In Figure 6.5 the fully plastic (sand-heap) value of T_d is used, and the torsional constant I_T which is used for calculation of N_{ET} is calculated without any contribution from the fillets. It may be noted that the torsional buckling load for the HEB specimen is approximately N_{ET}=2630 kN, while the axial yield load is N_Y=N_d=1198 kN. The results given in Figure 6.5 are normalized with respect to values at initial yielding, again based on a cross-section without fillets. For this reason, the experimental results given in Chapters 5 and 8 differ slightly from the results given in Figure 6.5, as the actual value of I_T is used for the interpretation of the tests.

Figure 6.5 shows that the capacity predicted by Equation 6.18 gives conservative results for axial loads up to $\overline{N}$ =0.80. As the beam-columns in real civil engineering structures normally are loaded far below this level, this seems to be acceptable. For the load cases $\overline{N}$ =0.50 and $\overline{N}$ =0.80, the largest value obtained for the torsional moment in the simulations is predicted with almost 100% accuracy. For the cases $\overline{N}$ =0 and $\overline{N}$ =0.20 no better agreement could be expected, as the plastic value for the torsional moment (sand-heap) used in Equation 6.18 is significantly exceeded for both simulations. Note that the torsional moments predicted by Equation 6.18 corresponds to a stage in the simulations where a significant reduction in the torsional stiffness has occurred, and that except for $\overline{N}$ =0.80 the deformations $\overline{\phi}$ are almost the same.

The values for the torsional moment for which the deviation from a perfect linear response occurs may be obtained from Figure 6.5 and the underlying response-data from the ABAQUS simulations. For the case $\overline{N}$ =0 this occurs for $\overline{T}$=1.0, while for $\overline{N}$=0.20, $\overline{N}$ =0.50 and $\overline{N}$=0.80 the corresponding values are $\overline{T}$=0.90, $\overline{T}$=0.70 and $\overline{T}$=0.39, respectively. The corresponding values of T derived from Equation 6.18, using the initial yield value for T_d, are $\overline{T}$=1.0, $\overline{T}$=0.89, $\overline{T}$=0.67 and $\overline{T}$=0.38, i.e. almost the identical values as above.

For the elastic torsional stiffness, the same good agreement is observed. Here, the simulations give values for the amplified rotations ϕ_r of 1.0, 1.10, 1.27 and 1.56 times the primary rotation ϕ_T, while the amplification factor $1/(1\text{-}N/N_{ET})$ according to Equation 6.15 should produce values of 1.0, 1.10, 1.26 and 1.58.

Both the suggested amplification factor for torsional actions and the design equation hence seem reasonable.

6.2.2 Nonuniform torsion - effects from axial load

Figure 6.6 shows the load situation for the beam-columns tested in nonuniform torsion and axial compression. Due to the symmetry in load and rotation in the tests, only one half of the specimen length needs to be considered. The fixed section shown in figure a) hence corresponds to the midsection of the beam-column, where the warping displacements are zero. The actual design of the specimen ends is shown in figure b).

The importance of the second order effects from an axial load N may also for this case be demonstrated by a simple approach. Consider the beam-column in Figure 6.6, subjected to a torsional moment T and an axial load N at the end. Mainly due to the torsional loading, the beam-column twists and the flanges deflects laterally as shown in figures a) and c). As discussed previously, initial yielding in torsion alone occurs in the flange tips at the fixed section due to the induced flange bending moment M_f. It can be seen from figure a) that the axial load contributes to an increase in this flange moment due to the load eccentricity e which develops when the free beam end is rotated.

If, for simplicity, the axial force is assumed to be carried by the flanges alone (flange forces N_f=N/2) and only the displacement of the flanges in y-direction is considered, the additional flange bending moment ($M_{f,N}$) at the fixed section may be taken as $M_{f,N} = N_f \cdot e$. Here, the displacement e caused by the rotation ϕ is given by $e = sin\phi \cdot (h - t)/2$. For the HEB specimen of the present study, subjected to an axial load of $\overline{N}$=0.50 and an end rotation of $\overline{\phi}$=1.0 (4.95°), this gives an additional flange moment of approximately 15% of the initial flange yield moment ($M_{fY} = f_y \cdot 1/6tb^2$). Note that this magnitude of the second order effect

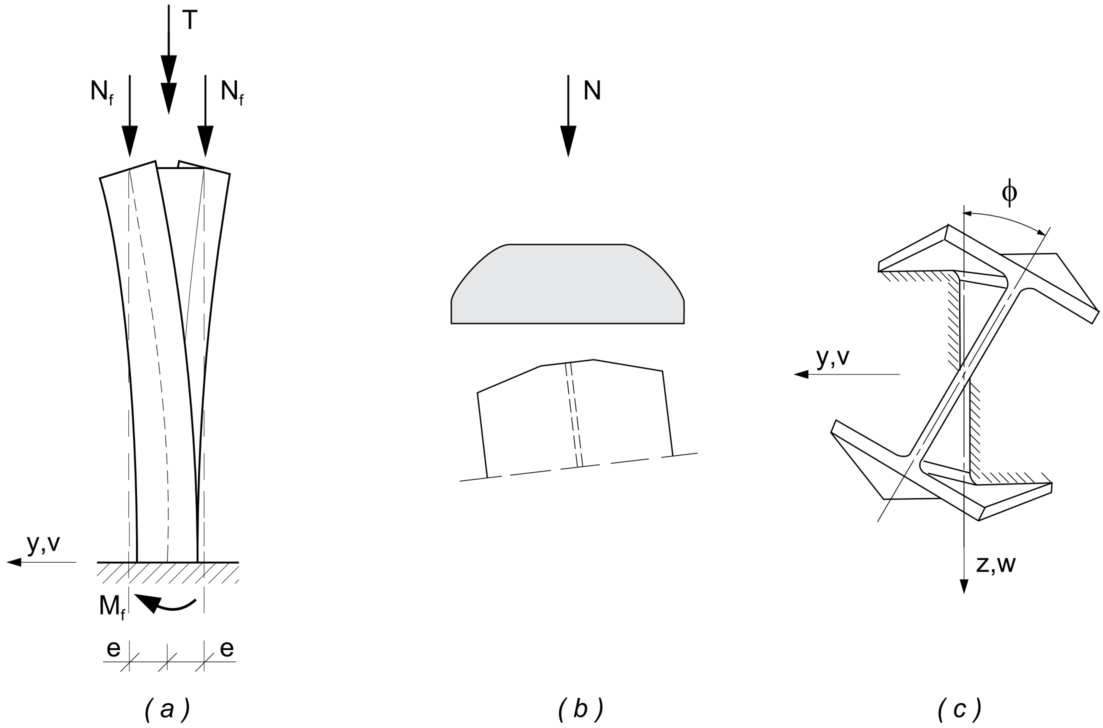

Figure 6.6: I-section beam-column in nonuniform torsion.

is somewhat smaller than that obtained for the uniform torsion case.

Experimental results for this example is given in Figure 5.26. By studying the response curves for the two tests $\overline{N}$=0 and $\overline{N}$=0.50, and also the corresponding numerical simulations presented later in this section (Figure 6.7), it can be seen that at the difference in torsional moment at $\overline{\phi}$=1.0 equals about 15%, as stipulated above.

The linear elastic torsional buckling load in nonuniform torsion is given by Timoshenko and Gere (1961). For the present case it is given by

$$N_{ET} = \frac{A}{I_p}\left(\frac{\pi^2 E I_w}{l^2} + G I_T\right) \tag{6.20}$$

where I_w is the section warping constant and l is the total length of the beam-column, i.e. twice the length of the "cantilever" depicted in Figure 6.6a.

The interaction effects between nonuniform torsion and a compressive axial load can not be derived analytically as easily as for the case of uniform torsion. The reason for this is that the hyperbolic solution of the torsion equation enters into the differential equation describing the torsional buckling problem. The resulting equation hence has no simple solution.

An amplification factor on the form

$$f = \frac{1}{1 - N/N_{ET}} \tag{6.21}$$

seems to be a reasonable choice also for the present case, as it is theoretically correct for cases where the uniform torsional resistance is dominant. It also reflects the behaviour in warping where the flange bending, as shown in Figure 6.6a, in principle is similar to the case of bending and compression for beams, where the amplification factor for the reference case is given by 1/(N-N_E). The torsional buckling load N_{ET} should then be based on Equation 6.20. The resulting amplified torsional moment T_r again becomes

$$T_r = T \ \frac{1}{1 - N/N_{ET}} \tag{6.22}$$

and the total twist angle

$$\phi_r = \phi_T \ \frac{1}{1 - N/N_{ET}} \tag{6.23}$$

Design equations for beam-columns under nonuniform torsion and compressive axial load may also for this case quite simply be established. If a first yield design is chosen as a basis for the development, the capacity is limited by the yielding in the flange tips at the fixed section (Figure 6.6a) due to the occurrence of the normal stresses σ_N from the axial loading N and the warping normal stresses σ_w from the induced flange bending moment M_f. These stresses then has to be limited by $\sigma_N + \sigma_w = f_y$. As the flange bending moment M_f consists of a contribution from the externally applied torsional moment T and a second order contribution due to the axial load N, the design equation becomes

$$\frac{N}{N_d} \ + \ \frac{T}{T_d} \cdot \frac{1}{1 - N/N_{ET}} \ = \ 1 \tag{6.24}$$

Again the design values N_d and T_d are introduced, as for Equation 6.18. For a given value of the axial load N, the reduced capacity now becomes

$$T^* = \left(1 - \frac{N}{N_d}\right) \cdot (1 - N/N_{ET}) \cdot T_d \tag{6.25}$$

If, on the other hand, a fully plastic distribution of the warping normal stresses is assumed, the capacity is limited by the plastic interaction between the axial force (N_f) and the bending moment (M_f) in the flanges at the fixed section. For this kind of loading, the capacity for a general rectangular shaped section (the flanges) with plastic capacities N_d and M_d is given by

$$\left(\frac{N}{N_d}\right)^2 \ + \ \frac{M}{M_d} \ = \ 1 \tag{6.26}$$

which is a standard solution according to the theory of plasticity for this combination. When the second order effect of the axial load is taken into account, the plastic design equation for the beam-column hence becomes

$$\left(\frac{N}{N_d}\right)^2 + \frac{T}{T_{pd}} \cdot \frac{1}{1 - N/N_{ET}} = 1 \tag{6.27}$$

which may be rewritten to express the reduced capacity in nonuniform torsion

$$T^* = \left[1 - \left(\frac{N}{N_d}\right)^2\right] \cdot (1 - N/N_{ET}) \cdot T_{pd} \tag{6.28}$$

Here, T_{pd} denotes that value of externally applied torsional moment T that corresponds to the fully plastic value (M_{fp}) for the flange bending moment M_f. As pointed out in Section 6.1, this plastic value of T has to be determined directly from an extension of the elastic solution of the nonuniform torsional problem, which previously was taken as T_{pd}=1.5·T_Y . However, as pointed out in Section 6.1, the stress situation for the beam-column is complex, and the stress distributions may only be determined analytically for the case of elastic behaviour. Hence, the model above may only be considered as a simple suggestion for a stress distribution for the inelastic situation, and it is known that the actual capacity in torsion alone at large rotations is considerably underestimated by this. It should also be pointed out that the capacity for other beam-columns, where the most heavily loaded part of the member is not necessarily dominated by pure warping actions, may be limited by the capacity in uniform torsion. In that case it may be more appropriate to use the elastic and the plastic capacity in uniform torsion to replace the capacities T_d and T_{pd} in Equations 6.24 and 6.27, respectively.

It should, however, be noted that Equation 6.27 may for instance be modified by assuming that the axial force N is primarily resisted by the web, and that only the excess axial force (N-N_{web}) enters into the square brackets of the equation.

Figure 6.7 gives a comparison of the capacities predicted by Equation 6.27 and the results obtained from ABAQUS simulations for the HEB beam-column. As shown, results are given for the torsional response at four values of the axial load N, $\overline{N}$=0, $\overline{N}$=0.334, $\overline{N}$=0.50 and $\overline{N}$=0.835, which corresponds to the experiments carried out for this load combination. A relatively good agreement between experiments and simulations is documented in Chapter 8, and it was chosen to use the simulations rather than the experiments for comparison. The results given in Figure 6.7 are normalized with respect to values at initial yielding. It can hence be seen that the plastic capacity in torsion alone ($\overline{N}$=0) according to Equation 6.27 corresponds to the value $\overline{T}$=1.5 in the figure. It may be noted that the torsional buckling load for this nonuniform torsional case is approximately N_{ET}=4950 kN, while the axial yield load remains at N_Y=N_d=1198 kN. As the torsional buckling load for this case is about twice the buckling load for the uniform torsion case, the destabilizing effects from the axial load are expected to be less prominent. However, as also the interaction equation is changed, a comparison of Figures 6.5 and 6.7

shows that the presence of an axial load gives the largest effect for the nonuniform torsion case.

As shown, the capacities predicted by Equation 6.27 give quite conservative results for the torsional moments $\overline{T}$ for all values of the axial load $\overline{N}$. As long as the actual observed capacity in nonuniform torsion is not properly represented by the plastic value used for T_{pd}, a better agreement could not be expected.

It can easily be shown that by using (N-N_{web}) as axial force in Equation 6.27, the predicted capacity in torsion can be increased, in particular for cases where N is large. If this is done for the case $\overline{N}$=0.835, the largest value obtained for the torsional moment in the simulation is predicted with good accuracy.

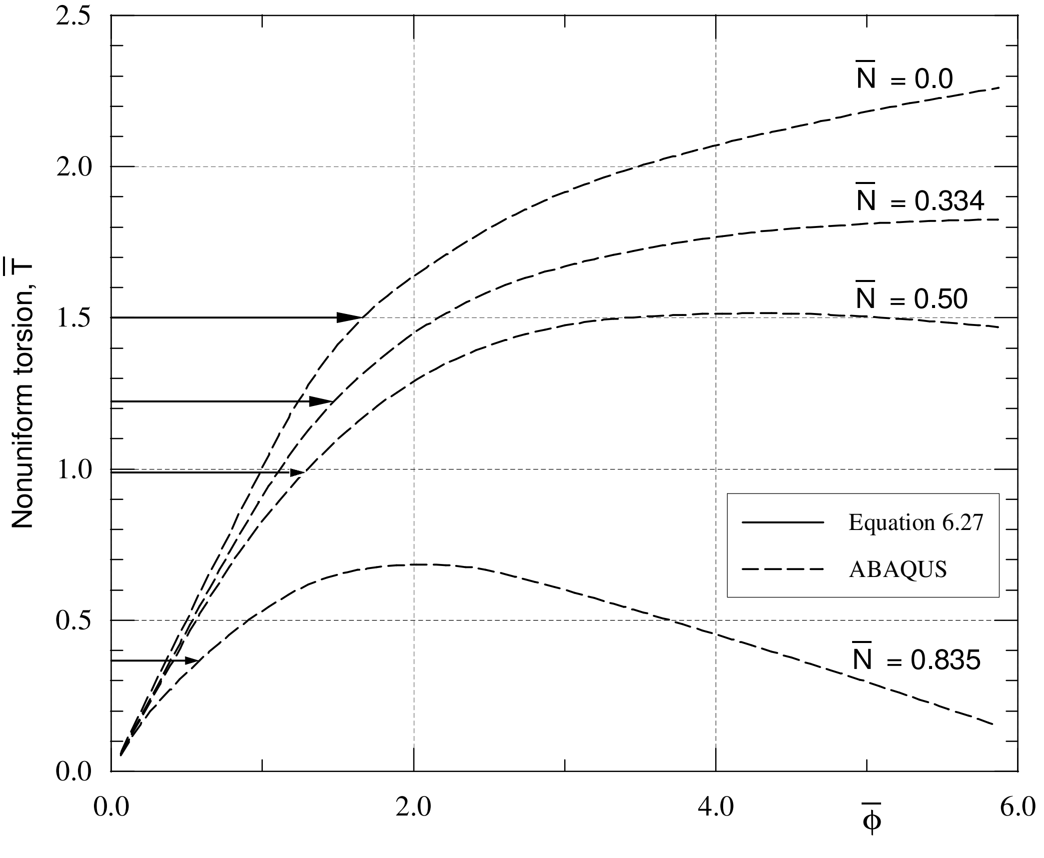

Figure 6.7: HEB 140 beam-column subjected to nonuniform torsion and axial load.

By studying the response curves in Figure 6.7, and the ABAQUS response-data from which they are derived, the torsional moments where the inelastic torsional behaviour starts can be obtained. For an axial load of $\overline{N}$=0 this occurs for $\overline{T}$=1.0, while for $\overline{N}$=0.334, $\overline{N}$=0.50 and $\overline{N}$=0.835 the corresponding values are $\overline{T}$=0.65, $\overline{T}$=0.51 and $\overline{T}$=0.13, respectively. The corresponding values derived from the "elastic" design equation, Equation 6.24, which uses the initial yield value T_Y

for the torsional capacity T$_d$, gives corresponding values $\overline{T}$=1.0, $\overline{T}$=0.61, $\overline{T}$=0.44 and $\overline{T}$=0.13. This means that the two methods give quite similar results.

The elastic torsional stiffness which can be read from the ABAQUS simulations gives values for the amplified rotations ϕ_r of 1.0, 1.08, 1.12 and 1.24 times the primary rotation ϕ_T. From Equation 6.23 the corresponding values are 1.0, 1.09, 1.14 and 1.25, i.e. as good as identical results.

It seems hence as if the suggested amplification factor also for the case of nonuniform torsion gives quite satisfactory results, and that the design equations are feasible. The observations presented here are supported by similar investigations/observations also for the IPE section.

6.3 Bending and torsion interaction

For the beams of this study the interaction between bending and torsion at a cross sectional level is discussed in the following. Results are given for the nonuniform torsion tests (T) presented in Chapter 4 and for the strong axis bending tests (M) and the combined bending and torsion tests (MT) in Chapter 5.

The advantage of the test setup of the present study, compared to many others, is that the cross-section at the critical midspan section of the beams maintains its orientation relative to the external transverse load (Figure 5.1). Independent of the torsional loading and the twist deformations, the beam specimens are bent solely about their strong axis at this section, and disturbing action from secondary weak axis bending is avoided. Consequently, the interaction effect between the pure sectional forces strong axis bending M and nonuniform torsion T may be studied, also for large inelastic deformations. Of course, at all sections outside the midspan section combined strong and weak axis bending takes place, which also affects the deformation measures used in the following. It should be remembered that the effect of the nonuniform torsion is strongly dependent on the actual load and boundary conditions, hence the conclusions presented in the following are closely related to the chosen specimens.

As shown with the graphs in Chapters 4 and 5, the torsional moment developed in the tests depends strongly on the extent of the torsional deformations. For most tests the torsional moment shows a steady increase with increasing twist, and no well defined value for the "capacity" or "yield" torsional moment is obtained. An ultimate limit resistance in torsion may hence only have meaning when referred to a specific value of the inelastic torsional deformations. For the pure strong axis bending tests some of the same deformation dependency may be observed, Figures 5.3 and 5.4, even though the response curves show a well defined yield plateau for the moment. It is hence necessary to choose a ductility requirement (i.e. amount of inelastic deformation) to serve as a basis for the definition of the capacity. This choice is discussed in the following.

Figures 6.8 and 6.9 depict the results in the MT-plane for the tests with proportional loading (Figures 5.2a) and i)). The results are given for the sectional forces M and T at midsection, as defined in Chapter 5. However, as the bending moment in this case is directly proportional with the applied transverse load H (M=H·l/4), the results presented in the following may also be interpreted as interaction effects for the external loads H and T.

The strong axis bending moment M is normalized with respect to the fully plastic bending moment

$$M_p = f_{y,flange}\left[bt\left(h-t\right)\right] + f_{y,web}\left[\frac{1}{4}s(h-2t)^2\right] \tag{6.29}$$

with an additional small contribution from the fillets. The torsional moment is normalized with respect to the Merchant upper bound value ($T_p = T_{0,Merchant}$). For the tests with both torsion and bending, simultaneous values for T and M are plotted. In the figures, the data points are identified by integer numbers that represent multiples of the deformation at initial yielding. For the tests with single torsion and combined torsion and bending points are given for $\overline{\phi}$=1, 2, 4, 6 and 8, while $\overline{w}$ is not used as a parameter. In bending, points are given for $\overline{w}$=1, 2, 4 and 6. Also shown is a circular interaction curve corresponding to a quadratic interaction between the sectional forces M and T :

$$\left(\frac{M}{M_p}\right)^2 + \left(\frac{T}{T_p}\right)^2 = 1 \tag{6.30}$$

Figures 6.8 and 6.9 show that the maximum values of M and T obtained in the tests significantly exceed the capacity given by the circular interaction, and that the choice of reference value for the inelastic deformations strongly influences the corresponding capacity. If curves are drawn through data points representing the same level of deformations, for instance through points where both $\overline{\phi}$ and $\overline{w}$ take on the value 4, it can be seen that the capacity may be approximately represented by curves of circular shape as given by Equation 6.30. The figures also show that for the HEB section the use of the Merchant upper bound value for the normalization of the torsional moment T gives good results, with respect to the possibility of using the quadratic interaction and the values for M_p and T_p without any modifications. For another value for T_p, the test results would not fit to a circle. When comparing the results for the HEB and the IPE sections, it should be remembered that equal values of $\overline{\phi}$ for the two sections do not represent equal physical rotations measured in degrees, as $\overline{\phi}$ is given as multiples of the rotation 4.95° for the HEB section and of 7.84° for the IPE section. Hence, the larger values obtained for the torsional moment T for the IPE section can be explained by larger contributions of the effects from large rotations and nonlinear geometry.

As shown in Figures 6.8 and 6.9, the loading path for the MT tests is changing direction when the inelastic deformations increase. This is a direct result of the test being run by displacement control, and the fact that the changes in the specimen stiffness in bending and torsion are not proportional for increasing proportional

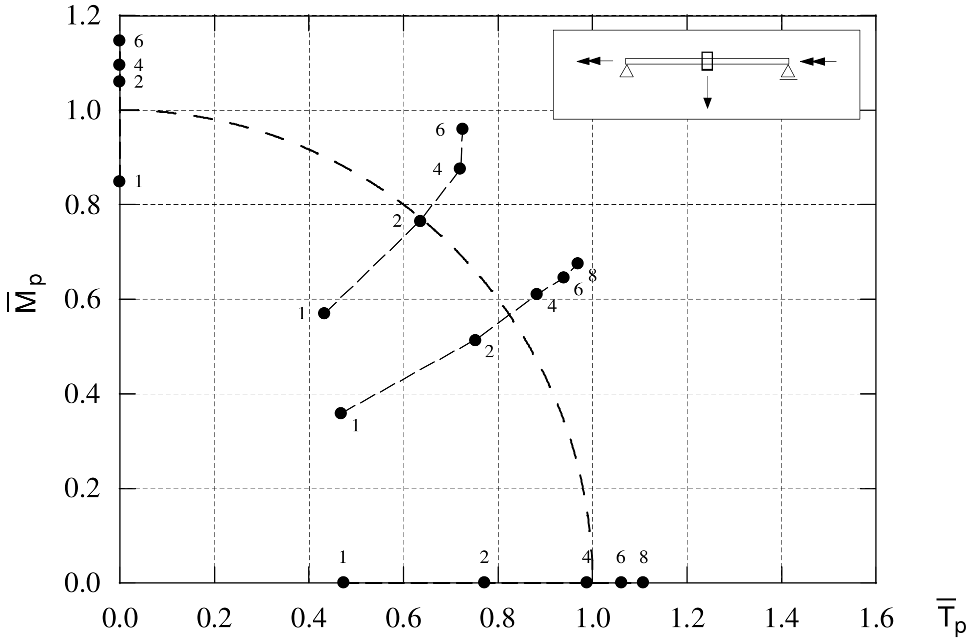

Figure 6.8: Interaction between bending and torsion for HEB 140 section.

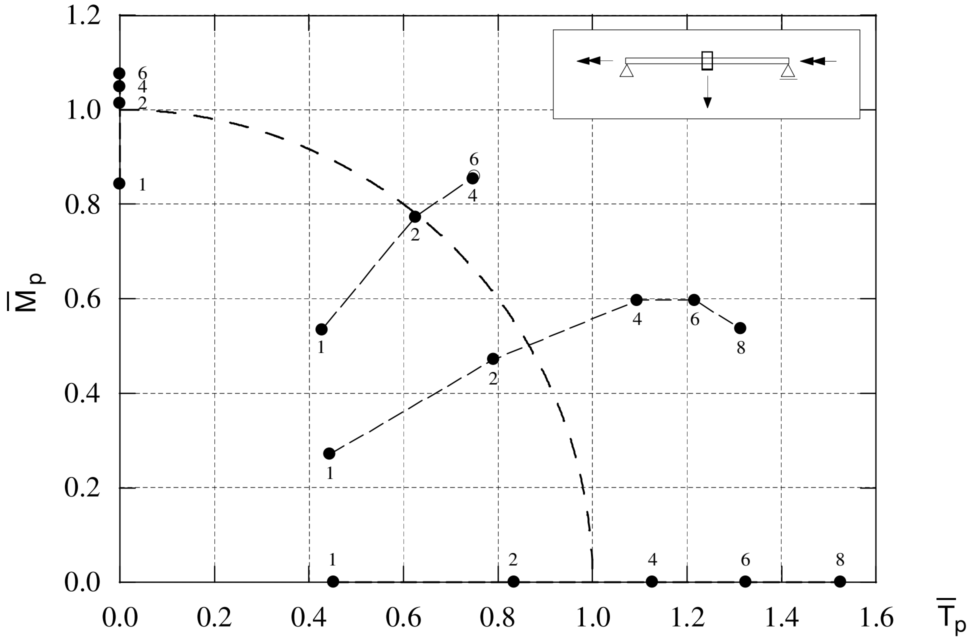

Figure 6.9: Interaction between bending and torsion for IPE 160 section.

deformations. For one of the IPE tests in particular, some of the reduction in the bending moment at large values of $\overline{\phi}$ is probably caused by stiffness reduction due to weak axis bending in parts of the specimen.

From separate FE-analyses (Chapters 4 and 8) it is found that, for the tests in pure bending and torsion only, the onset of strain hardening in the flanges takes place at a deformation of approximately $\overline{w}$=3.0 and $\overline{\phi}$=4.4 for the HEB and $\overline{w}$=3.9 and $\overline{\phi}$=4.6 for the IPE section. It may be noted that a rotation of, for instance, $\overline{\phi}$=4 corresponds to an end rotation of approximately 20° and 31° for the HEB and IPE specimens, respectively. Based on the results at hand it seems reasonable to choose values of $\overline{\phi}$ and $\overline{w}$ in the range 3 to 6. This choice is based on the fact that material strain hardening effects are commonly neglected in member design, and that limits are imposed on what twist rotations can be obtained in a real civil engineering structure. It does not seem appropriate to use values for the rotation $\overline{\phi}$ less than 3 in this context, as a "plastic" response in torsion depends on, at least, deformations of this size. The effect of rotations within this range may be illustrated with a beam originally loaded in strong axis bending. When the cross-section is given a rotation about the member axis of about 20 degrees ($\overline{\phi}$=4 for the HEB section), bending still takes place mainly about the strong axis of the section, even though a significant secondary weak axis bending moment is developed. The strong and the weak axis components of the bending moment M are $M \cdot \cos\phi$ and $M \cdot \sin\phi$, respectively for this case, or 94% and 34 % of M.

Considering both shape and values, Figures 6.8 and 6.9 show that reasonable agreement between test results and the circular curve is obtained for deformations $\overline{\phi}$ and $\overline{w}$ in the range 3 to 6. Figures 6.10 and 6.11 contain more closely spaced data points for $\overline{\phi}$, and lend support for a choice of the deformations $\overline{\phi}$ and $\overline{w}$ equal to 4 for the HEB section and $\overline{\phi}$ and $\overline{w}$ equal to 3 for the IPE section. In fact, this corresponds to almost equal twist rotation for the two sections, measured in degrees. For these levels of deformation, the tests in bending and in torsion only, show good agreement, while the deviation between test results and the circular curve is larger for the tests with combined bending and torsion (MT). It should, however, be noted that the given value of $\overline{\phi}$ does not give a true picture of the cross-sectional deformation in the MT tests, as the additional deformation due to $\overline{w}$ is not given. For this reason it is to be expected that the data points lie somewhat outside the quadratic interaction curve for these tests.

The effect of taking also the transverse displacement $\overline{w}$ into account, i.e. by using a deformation norm that includes both $\overline{w}$ and $\overline{\phi}$, is shown for the HEB section in Section 6.4. The use of such a deformation norm does not alter the conclusions presented here.

The circular interaction curve, Equation 6.30, was suggested by Hodge (1959) as a lower bound for the cross-sectional capacity for the interaction between bending and uniform torsion for various sections. The equation is based on interaction between uniform shear stresses and bending normal stresses with plastic distributions, and is hence theoretically valid only for beams of solid or closed cross-sections where the warping stresses are negligible. The equation was also used by Imegwu (1960) for circular, square and triangular sections subjected to the same type of loading.

Gill and Boucher (1964) and Dinno and Merchant (1965) investigated experimentally the interaction between torsion and in-plane bending for respectively beams of solid square and rectangular sections and for beams of a compact I-shaped section. The two investigations were concerned with the plastic capacity at a component level, and did not include the problem of lateral torsional buckling. The beams were subjected to combinations of a centrically applied torsional moment and a varying bending moment produced by a concentrated load at midspan. The I-section investigated by Dinno and Merchant had outer dimensions 5/8 in. by 5/8 in., and flange and web thickness of 1/8 in. and 3/32 in. respectively, i.e. it was quite thick-walled and had a relatively large lateral bending stiffness (I_z/I_y-ratio of 1/2). As a consequence of their choice of cross-sections, Gill and Boucher really studied a problem with uniform torsion while Dinno and Merchant studied nonuniform torsion.

In both investigations the experimental results were found to lie outside the circular interaction curve, Equation 6.30. Only Gill and Boucher discussed how they defined the plastic capacity on the basis of test results, which in this case was relatively simple due to the shape of the response curves. Dinno and Merchant reported only data points for the plastic values of M and T, but it is assumed that the response curves for their section also showed a well defined plastic capacity.

The interaction between bending, flexural-torsional buckling and torsion actions for I-beams with various types of lateral bracing was investigated numerically by Pi and Trahair (1994c). Based on finite element results obtained with a special beam element (Pi and Trahair 1994a), they proposed two equations for design of beams as a function of lateral slenderness. Here, Equation 6.30 was used as a basis with modifications made to the exponents only. Their investigation showed that the capacity for beams with significant secondary weak axis bending effects or with a significant tendency for lateral (and pure) torsional buckling was significantly overestimated by Equation 6.30. However, the interaction effects between bending and torsional buckling, as demonstrated by Pi and Trahair (1992) and (1994c), are not deemed important for the specimens of the present study.

Figures 6.10 and 6.11 show test results from all tests with load combinations M and T, i.e. both the tests with proportional loading in M and T as presented previously and additional tests where the bending moment was kept constant while the torsional moment increased. Figure 6.10 shows the test results for the HEB section, and includes also the data points given by Dinno and Merchant (1965) for their thick-walled I-section beam. It is seen that the Dinno and Merchant data points agree quite well with the present test results. It should, however, be noted that the tests of Dinno and Merchant included a smaller secondary weak axis bending component, but due to the shape of their section this is not believed to be important.

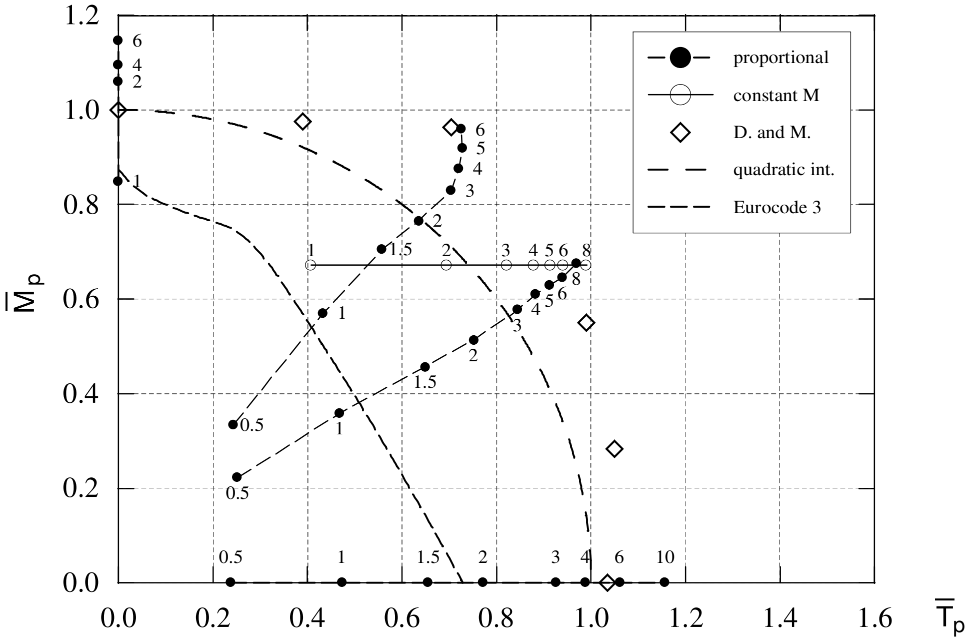

Figure 6.10: Interaction between bending and torsion for HEB 140 section, all tests.

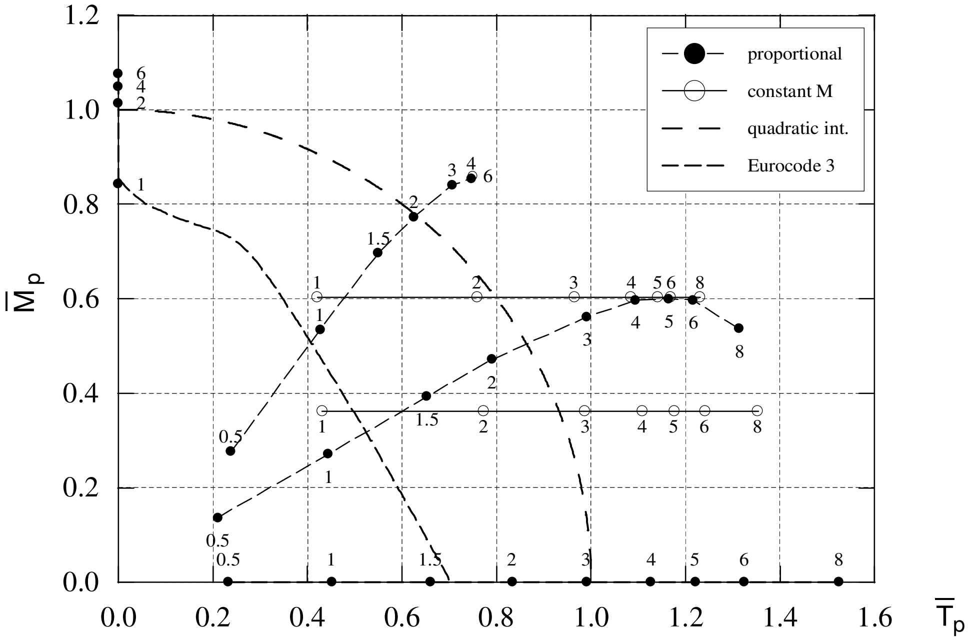

Figure 6.11: Interaction between bending and torsion for IPE 160 section, all tests

When comparing the results from the tests with proportional loading with those from the tests with constant bending moment, it can be seen that almost equal values for M and T are obtained for equal values of the deformation $\overline{\phi}$. Hence, the loading path; proportional loading or constant bending moment, has little effect on the test results for these specimens. As both the bending and the warping torsion actions produce mainly longitudinal uniaxial stresses in the specimens, the observed load-path independency at the cross-sectional level is not entirely unexpected.

Also shown in Figures 6.10 and 6.11 is the interaction curve based on the "linear" interaction equation given by Equation 7.1 of Eurocode 3. For the present I-sections, this interaction curve corresponds to full plastification of the flanges due to bending and warping stresses. Due to the nonlinear variation of the factor K in Equation 7.1 (Eurocode 3), caused by the variation in the ratio between M and T, the resulting interaction curve in the M_pT_p-plane is also somewhat nonlinear. The figures clearly demonstrate that Eurocode 3 underestimates the observed capacity.

6.4 Axial force, bending and torsion interaction

The interaction between torsion/torsional deformations and a compressive axial load was discussed in Section 6.2 for the I-section beam-columns. Based on the assumptions of elastic behaviour and linear geometry, the amplification of the torsional moments and of the torsional rotations was found to be dependent on the elastic torsional buckling load through the amplification factor $1/(1-N/N_{ET})$. This factor was then applied when deriving the design equations on member level for the load combination of axial load and torsional moment.

For determining the actual load effect on the beam-columns in the inelastic state, the above method surely represents a very simplified approach, as it does not take the magnitude and the distribution of the actual deformations into account. This situation is similar to that of a beam-column subjected to axial force and bending, where the amplification factor with same mathematical form is applicable for elastic behaviour only, and is exact only for some special cases of transverse loading. For the latter case the actual value of the internal bending moment at the critical section may easily be determined (Figure 5.1) by the well-known relationship

$$M = 1/4 \cdot H \cdot l + N \cdot w \qquad (6.31)$$

In torsion there is no such simple expression available to represent the second order effect. A discussion of the tests under combined axial loading, bending and torsion (NMT tests) in terms of the calculated/measured values for the cross-sectional forces does hence not seem feasible. Instead, the observed behaviour for the NMT tests is presented on member level, based on the values for the external loads applied to the beam-columns. The results for the beam-columns are hence given in terms of the applied torsional moment T ($=T_0$) and the applied transverse midspan load H, for the different levels of the axial force.

The value of the transverse load H is normalized with respect to its value corresponding to full yielding in bending at midspan, i.e. by using

$$H_p = M_p \cdot \frac{4}{l} \tag{6.32}$$

As the test results in Chapter 5 present values for the resulting bending moment, and not directly for the transverse load H, the values for H have to be determined from the test data by using Equation 6.31 for the tests where an axial load N is present. For the tests at zero axial load, however, the normalized value $\overline{H}_p$ is identical with $\overline{M}_p$.

For the tests presented in the following, it was found more appropriate to refer the observed capacity to a deformation norm that accounts for the amount of deformation in both bending and torsion. This norm (a) was taken as the mean square root of the normalized deformations

$$a = \sqrt{\overline{w}^2 + \overline{\phi}^2} \tag{6.33}$$

i.e. both terms weighted equally. Note that the normalized axial deformation is not included in a, which is motivated by a wish of treating the bending/torsion interaction as in the previous section, and by including the effect of a simultaneous axial load only by making modifications to the quadratic interaction equation, Equation 6.30.

Figures 6.12 to 6.15 depict the test results for the HEB 140 section. Figure 6.12 shows the results at zero axial load ($\overline{N}$=0), i.e. the same tests (MT) as presented in Figure 6.8, but now with data points for the observed capacities referred to the deformation norm a. Obviously, the data points for the test in bending only and for the test in torsion only (along H and T axes) remain unchanged, while a close comparison shows that the data points for the tests with combined bending and torsion are only slightly shifted due to the new deformation norm. Figures 6.13 and 6.14 allow a comparison of the two alternative ways of presenting the test results; Figure 6.13 shows the obtained values for the midspan internal bending moment and the externally applied torsional moment, while Figure 6.14 shows the results for the external loads. As expected, it is seen that only for load vectors were bending dominates will the two presentations differ. Note that even though the bending moment (M) increases as a function of increasing deformation norm, this is associated with a decreasing transverse force (H). For this reason, data points beyond the value a=3 are not present along the H-axis in Figure 6.14.

Based on the previous discussion and conclusions reached in Chapter 6.3 a simple interaction formula that takes also the axial load N into account is suggested on the form

$$\left(\frac{H}{H_p}\right)^2 + \left(\frac{T}{T_p}\right)^2 = \left(1 - \frac{N}{N_Y}\right)^2 \tag{6.34}$$

i.e. a uniform reduction of the circular (quadratic) interaction curve presented previously. Here, N$_Y$ is the squash load of the cross-section. Note that only the

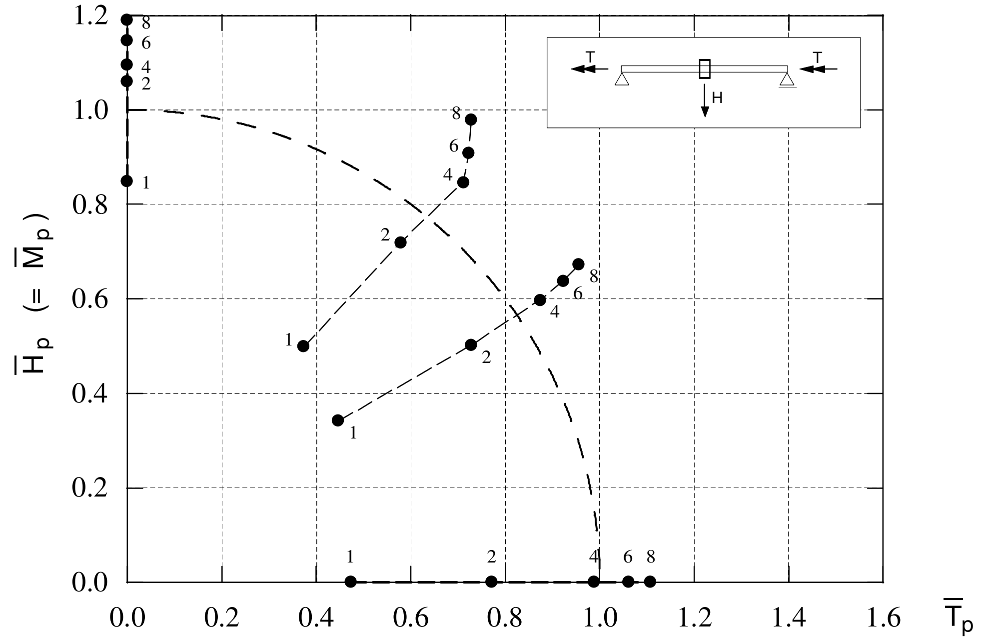

Figure 6.12: Interaction between a transverse load H and torsion for HEB 140 section for $\overline{N} = 0$.

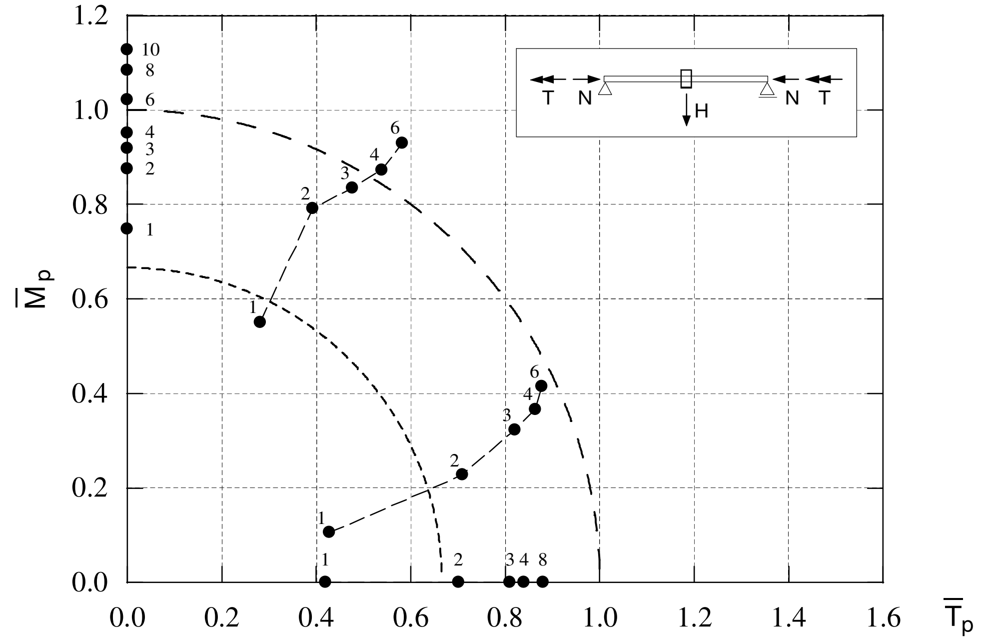

Figure 6.13: Interaction at axial load level $\overline{N}$=0.334 for HEB 140 beam-column, in terms of the bending moment and the torsional moment.

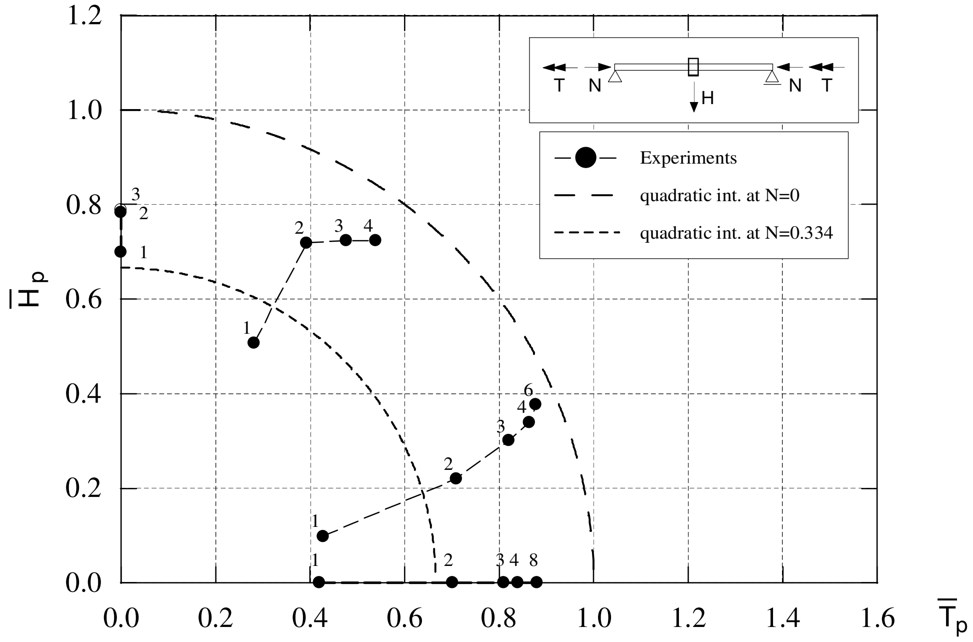

Figure 6.14: Interaction at axial load level $\overline{N}$=0.334 for HEB 140 beam-column.

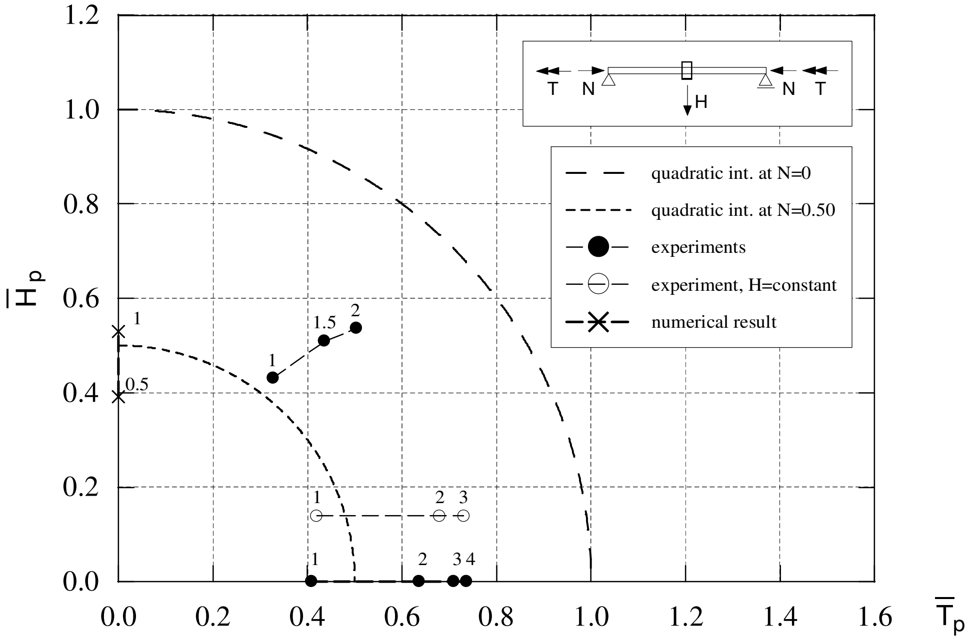

Figure 6.15: Interaction at axial load level $\overline{N}$=0.50 for HEB 140 beam-column.

increased stress level due to N is considered here, whereas the additional second order bending moment and the additional second order torsional moment produced by N are neglected.

Figures 6.14 and 6.15 show the test results at the axial load levels $\overline{N}$=0.334 and $\overline{N}$=0.50. Note that for $\overline{N}$=0.334 the data points for one load case are established by means of a *numerical simulation*, using the ABAQUS shell model presented in Chapter 8. Data points are given for values of the torsional moment T and the transverse load H up to the level where the moment/load no longer increased. As shown, the maximum values of T and H significantly exceed the capacity given by Equation 6.34 for all tests. This implies that the increase in bending and torsional capacities compensate for the increased load effect due to the second order effects as the deformations increase.

It is also seen that the agreement with the circular interaction curve is maintained both for $\overline{N}$=0.334 and $\overline{N}$=0.50. This may be due to the fact that the second order effects give an almost equal reduction of the capacity for both bending and torsion. It is seen (Figure 6.15) that the response in torsion reaches a higher value of inelastic deformations than in bending. This indicates the importance of the deformation norm in the definition of the member (component) capacity.

For other specimens, and particularly for specimens with larger slenderness in torsion and bending, the second order load effects are expected to be more significant. (For the present HEB 140 beam-column specimen the capacity in all buckling modes is close to the squash load, see Appendix A.1). For such cases it may be more appropriate to use the inelastic buckling load to replace the squash load N_Y in Equation 6.34. Furthermore, only further studies can verify if it is appropriate to neglect the second order effect of N in this equation.

Chapter 7

Design formats

The members of steel structures are occasionally subjected to torsional actions in addition to the primary axial and bending actions. The torsional actions often arises from secondary effects, resulting from various kinds of load eccentricities on members or connections, or from differential member deformation in space frames.

Steel design standards in general provide little guidance for the strength design of members subjected to torsion; in most cases the standards simply ignore the effects from torsion (Trahair and Bridge, AS4100 Supplement). This is not surprising as the literature in this field gives only a few very simple procedures for designing against torsion. Obviously, this is due to the fact that torsional response is inherently more complex than the simple axial force and bending response, and has a correspondingly more complex elastic theory which automatically limits the possibilities for direct application of theory to design. A need for design provisions for determining the ultimate capacity in torsion has been addressed by many authors (Driver and Kennedy 1987, Pi and Trahair 1994c).

7.1 Design based on codes

For the design of beam-columns subjected to torsion, it seems reasonable to follow the same requirements as for beam-columns in general, i.e. the structural analysis and the member design have to take into account :

- relevant material properties and their variations over the component
- residual stresses
- initial imperfections and erection eccentricities
- second-order effects from the design loads acting on the displaced structure
- second-order effects due to plastification, such as shift of gravity center and shift of shear center
- possible reduction in cross-sectional resistance due to local buckling

There are almost no field data for the imperfections that can be expected in real structures with relevance to the torsion problem, and only a few very simple analytical methods for determining second order effects on torsional response exists. In addition, the existing system for determining the classification of cross-sections with respect to for instance b/t -ratio is only based on the bending and axial actions.

The provisions for torsion given in two of the most recent design standards will be presented in the following. This is the Australian Standard AS 4100 - Steel structures - published in 1990, and Eurocode 3 - Design of steel structures - from 1992.

The Australian Standard (AS 4100) gives no specific rules or requirements for design against torsion. Nevertheless, this topic is treated in a Commentary to the standard - AS 4100, Supplement 1-1990. The Commentary discusses the occurrence and the significance of torsion in steel structures, and defines the types of torsion and the different torsional mechanisms that can be present in structures and components.

For the analysis of torsion only, the Commentary gives references for determining the cross-sectional properties, for the analysis of member distribution of uniform and warping torsion and for the distribution of the stresses caused by the torsion.

For the analysis of combined bending and torsion, three methods are outlined. The first is a common first-order analysis, where the bending and torsional responses are treated independently, followed by a superposition of the separate results. The second is an approximate second order analysis where the most significant second order contributions are added to the first-order bending- and torsional moments. Specifically, for a 3-D beam (beam in space), these contributions are the linearized minor and major axis bending component $\mathrm{M}_y \cdot \phi$ and $\mathrm{M}_z \cdot \phi$ respectively that arise from the first-order bending actions working through the first-order twist rotations ϕ, and the linearized second order torsional moments $\mathrm{M}_y \cdot v'$ and $\mathrm{M}_z \cdot w'$ that arise from the bending moments working through the deflections. It is pointed out that this approximated method is of reasonable accuracy only for laterally stable members. Hence, for beams with larger major bending moments M_y where the tendency for lateral torsional instability is significant, a third analysis method is suggested. This method consists of an amplification of the first-order deflections, the twist rotations, and of the minor axis bending moments and torsional moments. The suggested amplification takes the form of the conventional amplification factor $1/(1 - M_y/M_C)$, in which M_c is the elastic lateral torsional buckling moment.

For the design against torsion only, the stresses predicted by an elastic analysis are used in the design check. Both for the shearing stresses from pure uniform torsion and for the normal stresses from warping torsion the limiting design stresses are based on the respective yield values ($0.6 \cdot \mathrm{f}_y$ and f_y) reduced with a capacity factor 0.9. Due to the considerable capacity reserves of compact (Class 1 and 2) I-sections, that for both uniform torsion and for warping torsion (flange bending) have plastic shape factors equal to 1.5, an increase of 25% in the limiting design stresses is suggested. Interaction with the flange shear stresses is considered unimportant and is neglected. For the interaction between uniform shear stresses and warping normal stresses, as in the case of nonuniform torsion, a standard von Mises interaction equation is suggested, allowing a 25% exceeding of the yield values.

In the case of combined bending moment and warping torsional moment, the suggested strength design check incorporates the effect of the warping moment by using an increased value ($M_{incr.}$) for the design (action) bending moment (M): $M_{incr.} = M + \sigma_w M_s / 1.25 f_y$, where M_s is the nominal section moment capacity. For combined bending and uniform torsion, the interaction effects between the bending shear and the torsional shear stresses are treated similarly, i.e. by using an increased value for the design bending shear force. For both these cases the 25% increase is used only for Class 1 and 2 I-sections.

No guidance is given for the design against combined torsion, bending and axial actions in the Commentary. However, AS 4100 opens for design by means of "advanced structural analyses" for laterally braced frames, i.e. inelastic analysis/design, provided that the actual method takes into account all the significant in plane effects listed in the beginning of this section. This opens for the use of for instance nonlinear inelastic FE analyses. Obviously, several questions arise if this approach is chosen; how to model relevant imperfections and how to define a failure/capacity criterion. The provisions given for amplification and design checks in the Commentary are similar to those given by Nethercot et al. (1989), Trahair and Bradford (1988) and British Standard BS 5950.

Eurocode 3 (EC3) has an informative Annex G - Design for torsional resistance - that gives the application rules for the design of members subjected to torsion. The Annex summarizes the basic formulas for determination of the elastic torsional properties for members of open and box types of sections, as they also can be found in various text-books. The same information is also given in Part 2 of Eurocode 3 - Design of bridges. For the analysis of bending and torsion, also EC3 suggests an amplification of the first order twist rotations ϕ and the torsional moments due to the presence of the bending moment, and points attention to the additional minor axis moments which are caused by the twisting of a beam originally loaded in major axis bending.

For the design against torsion, EC3 suggests in essence a design check based on the stresses obtained from an elastic analysis. As an approximation it is suggested to neglect the uniform torsion resistance for open sections (as the bending analogy presented in Section 6.1) and to neglect the warping resistance for closed hollow sections. As a design criterion for open cross-sections, the first yield ($f_y/\sqrt{3}$) is suggested as the limit for the uniform shearing stresses without considering the interaction with any bending shear stresses or normal stresses, whereas this interaction is to be considered for closed hollow sections. The resistance of I-sections to warping torsion is to be limited by the capacity based on the plastic bending resistance of the flanges. For open sections this approach may lead to a significant larger calculated capacity than that obtained with the 25% increase used in the Australian rules. The latter uses a factor 1.25 with shear interaction while EC3 uses 1.5 without shear interaction.

For the interaction between axial force, bending moments and warping moments, second order effects included, EC3 gives an interesting linear interaction formula for the capacity of the cross-section in terms of the internal forces and moments :

$$\frac{N}{N_R} + \frac{M_y}{M_{yR}} + \frac{M_z}{M_{zR}} + \frac{M_w}{M_{wR}} \leq K \tag{7.1}$$

Here, the subscript R refers to the resistance for each particular action (N,M_y,M_z,M_w) based on elastic stress distribution within the cross-section and yielding at the most stressed point of the cross-section, and K is a factor that accounts for the degree of plastification. The interaction formula can be used for all classes of open sections. The plastification of the cross-sections cannot proceed beyond the full plastification of the most stressed plate element in the cross-section. This has to be interpreted as the plate element which has a stress distribution closest to full plastification, and not the element with the highest elastic stresses. Hence the value of K ranges from 1.5 for the case of a compact (Class 1 and 2) section where this particular plate element has a stress distribution that corresponds to pure bending to 1.0 for the case of uniform compression or tension or for Class 3 and 4 sections. The background for this formula is not known to the author, and compared to the recommendations in AS 4100 it leads to a higher utilization of the cross-section. It should be noted that the formula neglects the possibility of interaction with the shear stresses.

Similar to the Australian standard, EC3 allows the use of advanced methods of analysis. For inelastic torsion in particular, EC3 states that the full plastic capacity of the entire section can be utilized, as long as all the relevant effects are included in the analysis. In practice this implies the use of numerical simulations such as FE analyses, and in principle this is relatively simple as the second order effects are accounted for in the analyses. However, at the present stage this requires that the beam is modelled by shell elements as in Chapter 8, as no satisfactory formulation is available on the beam element level. For that reason this approach is not feasible at the design stage.

7.2 Other design procedures

As previously noted, the literature contains only a few and simple procedures for design against torsion. For the design against nonuniform torsion, an example is the bending analogy which assumes the torsional moment to be resisted only by the lateral bending of the flanges (Equations 6.2 to 6.4).

Based on experiments on an I-section cantilevered beam, Driver and Kennedy (1989) present a suggestion for an ultimate limit state design procedure for the case of combined strong axis bending and torsion. Their interaction model is based on assumed stress blocks in the cross-section (similar to Equation 6.26), where the web and the central portion of the flanges resist the bending moment, and warping normal stresses (σ_w) in the flange tips resist the torsional moment. Here, the yield strength (f_y) is used for the bending normal stresses, while the stresses σ_w are assumed to reach the ultimate strength (f_u) of the material. In addition, the cross-section is assumed to be able to carry the full sand-heap moment, again based on the ultimate stress ($f_u/\sqrt{3}$). Even with their somewhat non-conservative assumptions, good agreement with test results is obtained.

Kollbrunner et al. (1978) (referred by Driver and Kennedy) describe the behaviour of both a cantilever and a fixed end beam. For the combination of strong axis bending and torsion, they propose the interaction equation

$$\frac{(M - M_{p,web})^2}{(M_{p,flange})^2} + \frac{M_f}{M_{fp}} = 1 \tag{7.2}$$

to predict the full plastification of the section. $M_{p,web}$ and $M_{p,flange}$ are the plastic bending moments of the web and the flanges, respectively, and M_f and M_{fp} are the flange bending moment (warping) and the plastic flange moment. Again, Equation 6.26 is used as a basis. The ratio M/M_f is assumed to remain constant during loading from the elastic and into the plastic region. Here, M_f is to be derived from the differential equation for nonuniform torsion.

The two above methods have been compared to test results for the HEB 140 (test H-2-MT, initial $\overline{M}/\overline{T}$ ratio approx. 3/4). Here, the largest value obtained for the bending moment and the torsional moment in the test is $\overline{M}$=1.0 and $\overline{T}$=1.5, respectively. Compared to the Driver and Kennedy method which implies the construction of an interaction diagram, the tests results fall well inside the interaction curve, i.e. an non-conservative result. This is not surprising, as the extent of deformation for the test specimen can not in any case justify the use of ultimate values for the stresses. The results obtained using the Kollbrunner method (Equation 7.2) are better. Here, a capacity of $\overline{M}$=0.73 and $\overline{T}$=0.97 is reached, which is considered quite good, as the method does not take advantage of the section's resistance to uniform torsion beyond the fact that M_f is computed from the elastic differential equation.

7.3 Design by analysis

In Chapters 4 and 8, the experimental beam-column response is simulated by means of FE-analyses based on a shell-model for the I-section specimens. For the purpose of verification of test results and for the development of simple design models, this approach is well suited. For the analysis of real structures, of course, this is not a feasible approach.

For the analysis of structural problems where the modelling of torsion is needed, several element formulations based on beam elements have been developed. As discussed in Chapter 4, the beam-element provided by ABAQUS has inherent limitations, as the uniform shear stresses within the cross-section do not affect the yielding of the material. The same simplification is made by El-Khenfas and Nethercot (1989) in their beam-element formulation suitable for problems with large torsional rotations.

In a recent work, Pi and Trahair (1994a) have developed a beam element that allows a reasonable representation of the uniform shear stresses. Here, the "mitre" model developed by Billinghurst et al. (1991) is used to approximate the variations of the uniform shear strains around the cross-section (using a distribution similar to the distribution of the shear stresses in the sand-heap analogy, Figure 6.1). An elastic stiffness correction factor is used to give correct torsional stiffness for the beam element, and the numerical integration over the cross-section also takes the stress-variation through the web and flange plates into account. It is shown by Pi and Trahair (1995) that this formulation gives an accurate description of the behaviour of I-section beams in nonuniform torsion.

Several attempts have been made to model torsional effects also in FE programs that use the concept of concentrated plastic hinges, and where the inelastic behaviour of the members is treated at a cross-sectional level in terms of stress resultants. One of the contributions here is the work of Yang and Fan (1988), which describes a yield surface model for I-shaped sections, where the full combination of axial force, biaxial bending moments, warping moment (bimoment) and the uniform torsional moment are included. In most existing programs the torsional effects are, however, treated somewhat simplified. An example here is the FE program USFOS (Søreide et al. 1993), which is intended for ultimate strength and collapse analysis of framed structures. The program contains models both for members of tubular and I-shaped sections (and others), but does not have a warping degree of freedom to represent the restrained warping of members of open sections. The uniform torsional stresses are, however, accounted for quite well, as USFOS incorporates the effect of these stresses by reducing the available yield stress, which again gives a reduction of the bending and axial force capacities.

Chapter 8

Numerical simulations

In this chapter numerical simulations of some typical beam-column experiments are presented. The objective here is to study to what accuracy the beam-column behaviour under combined load actions can be predicted. The general finite element program ABAQUS is used, and the beam-column specimens are modelled using shell elements. In Chapter 4, the same shell model was used to analyse the experiments with torsion only.

Simulations are carried out for experiments on both the HEB 140 and the IPE 160 section. Only the results for the HEB are presented in the main text, while the corresponding results for the IPE are given in Appendix D.

8.1 Shell element model

The shell model of the beam-columns is discussed in detail in Chapter 4, and the element mesh is depicted in Figure 8.1. As shown, the entire test specimen is modelled, using four elements both across the width of the flanges and over the depth of the web, while 29 elements are used along the length of the specimen. Fictitious stiffener plates and diagonal beam stiffeners are added at the "support" points near the specimen ends, to allow the torsional loading to be applied to the model.

The choice of four elements across the web and the flanges was primarily governed by practical considerations. With the chosen eight-node shell element (Figure 8.1) this gives nine nodes across the web and the flange plates, and correspondingly eight element integration points across the plates. The outermost integration points at the flange tips are located a distance of 7.4 mm and 4.4 mm from the tip for the HEB and the IPE, respectively. For the flange bending (warping) caused by the nonuniform torsion this element mesh is expected to give reasonable results, while it for the beam-bending should give quite satisfactory results. As known from Chapter 4, the response in pure uniform torsion is quite well modelled also with fewer elements. The problem of local buckling was not considered when choosing the mesh, nor did it occur to any significant extent in the tests. Both the HEB and the IPE section are of cross-section Class 1.

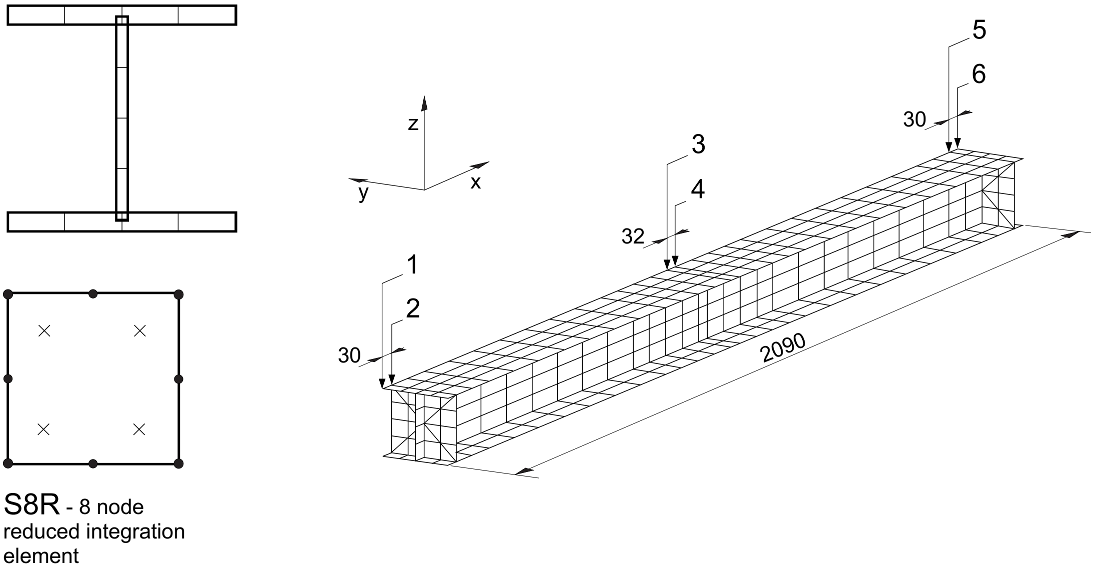

Figure 8.1: Shell model of HEB 140 beam-column.

The effect of several modelling choices was investigated.

- The influence of the mesh density was investigated for the case of pure strong axis bending and for the case of nonuniform torsion. Simulations were carried out using both the standard mesh of Figure 8.1 and a refined model where each shell element of the standard model was divided into four new elements of equal size. In torsion, the difference in the predicted torsional moment was less than 1% for the two models, and in bending the predicted moment was almost identical.

- By varying the number of section integration points through the shell thickness for some typical simulations with nonuniform torsion and/or bending, the chosen number of points (5) was found to be sufficient. Correspondingly, for the simulations with uniform torsion, the use of more than 7 integration points did not improve the results.

- The material of the specimens was modelled (See Chapter 4) with a piecewise linear representation of the actual stress-strain curve. For the IPE 160 one material curve was used for the shell elements in the web, and a slightly different material curve for the elements in the flanges. For the HEB 140, however, the material has a large variation across the web (Figure 3.5), and different material properties were assigned for the elements in the web. The two exterior and the two interior elements were modelled identically.

> Simulations showed that variations of this material modelling for the exterior elements of the web had a noticeable effect only for the predicted bending response. By using the same material for all elements in the web (the lower material curve in Figure 3.5), and comparing with the results obtained using the strongest material in Figure 3.5 for the exterior elements, a difference in the predicted bending moment of 2-3% was found. Mean values of the material properties are used in the following for the exterior elements.
>
> It should be noted that the size of the "exterior" web elements could have been reduced in order to reduce the variation in material properties within the element, but this was deemed unnecessary in view of the obtained results. For the same reason no attempt was made to model the slightly higher yield stress at the tips of the flanges.

The bending tests are analysed by imposing equal displacement (z-direction) to all nodes located in the compression flange of the cross-section at midspan, i.e. at beam sections 3 and 4 in Figure 8.1. The tests with torsion are analysed as previously discussed, by applying torsional rotations to the nodes at the centroid of the cross-section at beam sections 2 and 5. Here, for the case of nonuniform torsion, the torsional rotation at midspan is restrained by lateral supports (y-direction) at the flange tips. The axial loading is applied to all nodes at beam sections 2 and 5.

8.2 Numerical results

In the following, the response obtained in the numerical simulations (ABAQUS) is compared with the experimental (measured) response. Results are given for the case of pure strong axis bending (M), axial force and bending (NM), bending and nonuniform torsion (MT), axial force and nonuniform torsion (NT), and the full load combination of axial force, bending and torsion (NMT). Finally, results are given for the case of uniform torsion combined with axial loading. Simulations of the pure torsion tests, both for the case of uniform and the case of nonuniform torsion, is thoroughly discussed in Chapter 4, and are repeated here for the sake of completeness.

Both the initial residual stresses and the initial geometrical imperfections are ignored in the modelling. As discussed in Chapter 3, the measured residual stresses are, in average, quite small. For the flanges of the HEB section, stress values (Figure 3.9) average about 10 % of the yield strength, while in the web the residual stresses were somewhat higher. Due to the seemingly random variation of the stresses, both in the cross-section, through the thickness of the plates and along the members, a typical distribution of the stresses could not be defined. Further, as residual stresses are expected only to affect the behaviour slightly at the level of initial yielding, and not the obtained inelastic load capacities, no attempt was made to model these stresses. The initial imperfections are, as discussed in Chapter 3, also small for the present specimens, and compared to the deformations applied in the tests of no significance.

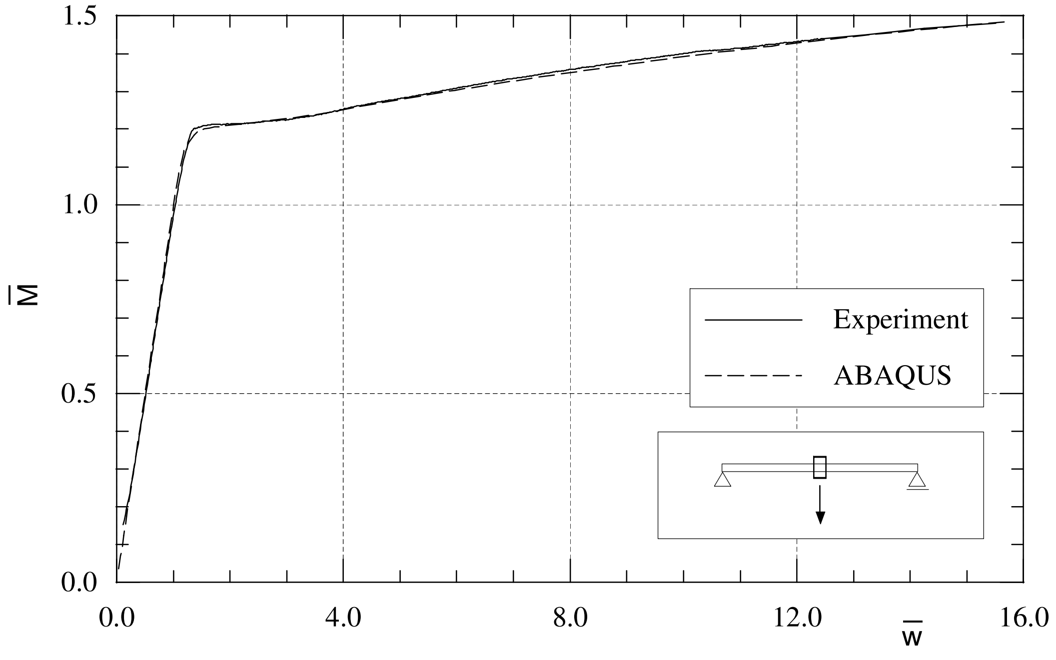

Figure 8.2: HEB 140 beam in pure strong axis bending (test H-1-M).

Figure 8.2 shows the results from the simulation of the strong axis bending test (M) on the HEB 140 section. As shown, the simulation gives a response curve practically identical to the experimental one. As both the bending and the shearing stresses in this case are modelled quite well with the chosen shell elements, and as the geometry and the material properties are well represented, this agreement is expected. It should, however, be noted that for large values of $\overline{w}$ the deformation for the specimen predicted by the simulation differs somewhat from the experimentally observed. Here, the simulation shows a stronger tendency for local flange buckling near the mid-section. This is partly due to the omission of the fillets of the section in the numerical model, where the flange restraint due to the support from the stiff web/flange juncture is not accounted for. In a simulation carried out with the refined model with four times as many elements, a sudden drop in the bending moment at about $\overline{w}$=14.0 was caused by flange buckling. This illustrates what is seen in many of the simulations; a somewhat "too" large tendency towards local flange buckling, even though the effect on the predicted response not necessarily is noticeable. This overestimation of local buckling increases with the mesh refinement.

The same good agreement is achieved also for the IPE 160 specimen for this load case, see Appendix D for further details.

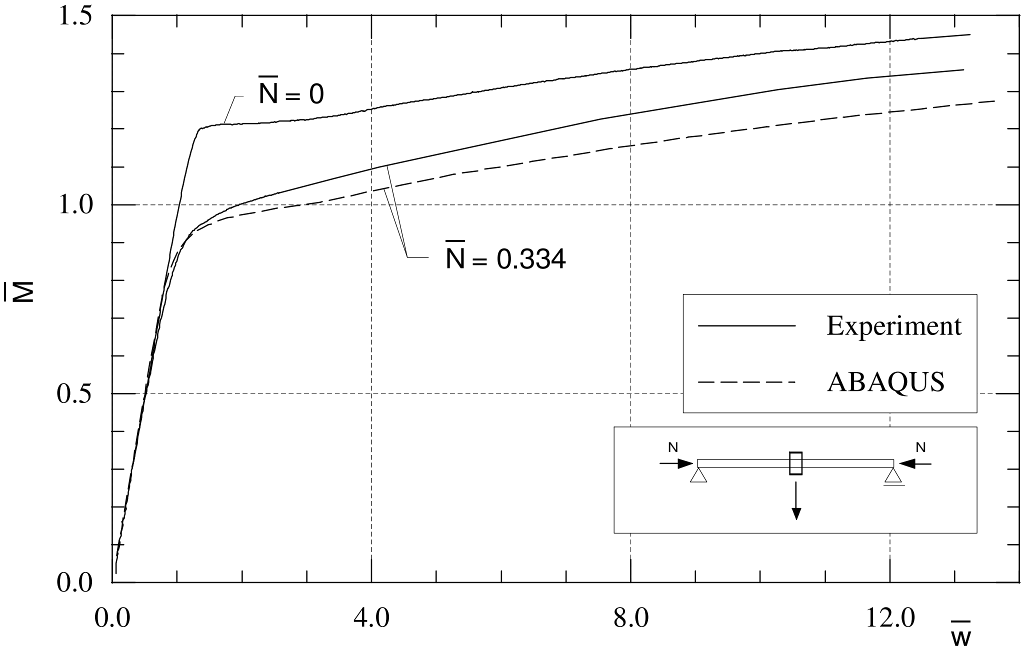

Figure 8.3: HEB 140 beam-column subjected to axial force and strong axis bending (test H-4-NM).

Figure 8.3 depicts the results for the axial force and bending case (NM). The ABAQUS simulation is carried out as in the experiment; by first applying the constant axial load ($\overline{N}$=0.334), and then imposing the linear increasing displacement (w) at midspan. The response in pure bending ($\overline{N}$=0) is given for comparison. The numerical response gives a reasonable prediction of the experimental response, although the curves do not follow as well as for the pure bending case. As seen, the deviation between predicted and experimental response is within 10%, even for large values of the displacement, w. A new modified simulation for this case, in which the flanges were given a larger thickness and a smaller width (i.e. maintaining the plastic bending capacity of the section), proved that the deviation between experiment and simulation is not caused by a relative larger tendency of local flange buckling in the simulation.

Figure 8.4 shows the numerical results of one of the bending and torsion interaction tests (MT) for the HEB section. The simulation is carried out by imposing the experimental displacement history given by the $\overline{w}$–$\overline{\phi}$ curve. As shown, the simulation gives in general a quite well prediction of both the response in torsion ($\overline{T}$-$\overline{\phi}$) and in bending ($\overline{M}$-$\overline{w}$). As in the previous case, the simulated bending moment is slightly underestimated for large values of the displacement w. In torsion, the predicted response becomes somewhat too stiff for large values of the rotation ϕ, which is also observed for the simulation of the case of torsion alone (Chapter 4

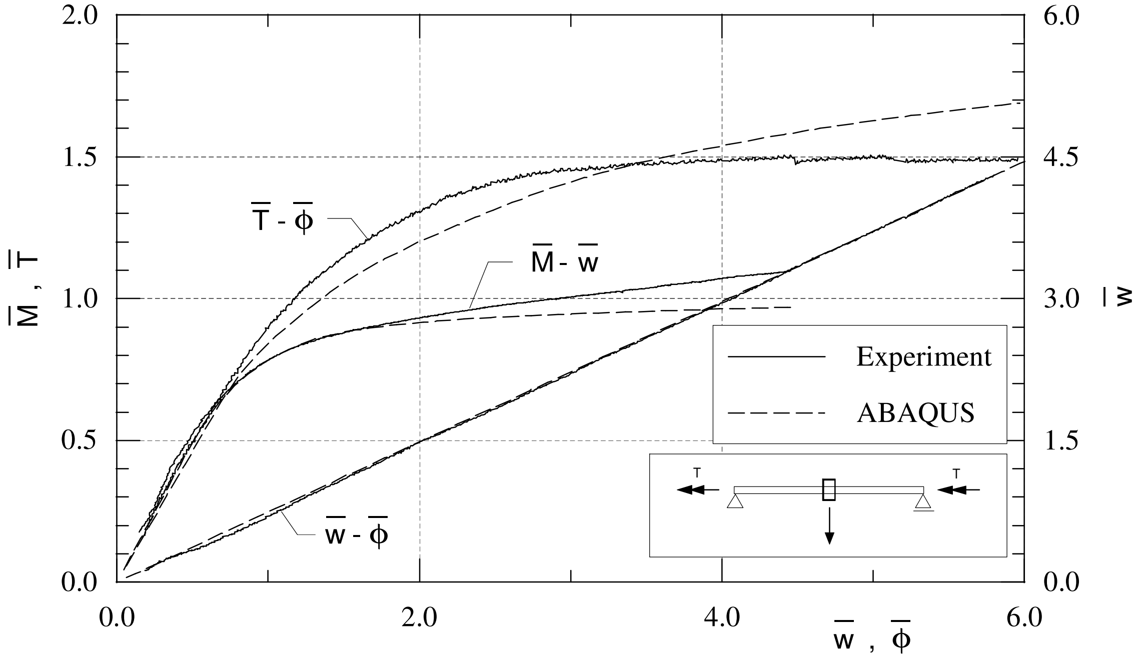

Figure 8.4: HEB 140 beam in bending and nonuniform torsion (test H-2-MT).

and Figure 8.7). Further, it can be seen that for the most relevant range of ϕ, which in Chapter 6.3 is defined as $\overline{\phi} \leq 4$, the deviation for the moments M and T is within 10%.

Figure 8.5 presents a simulation of one of the tests with axial load and nonuniform torsion (NT). The simulation is performed in two steps, by first applying the constant axial load $\overline{N}$=0.50, and subsequently the twist rotation ϕ at the specimen ends. Results are given for the response in torsion ($\overline{T}$-$\overline{\phi}$) and for the axial shortening of the specimen ($\overline{u}$-$\overline{\phi}$).

As shown, simulation and experiment agree reasonably well. The difference in the values for the maximum torsional moment is less than 7%. When considering the results for this case, it should be remembered that due to the axial load present ($\overline{N}$=0.50), only 50% of f_y is available for resisting the torsional moment, which implies a significant sensitivity of T to differences between model and experiment.

In this case, a small disagreement is observed already for low values of ϕ, and the initial torsional stiffness seems to be somewhat underestimated. This may be caused by the modelling of the geometry of the specimen ends. In the tests, the axial load is applied through the web and the 35-40 mm wide central part of the flanges (Figure 3.1). Primarily, this design was chosen to allow large axial loads to be applied without any local stress redistribution, and still allowing a warping free condition to be retained. When the flanges of the specimen warp due to the torsional loading, the present design causes a small shift in the application point

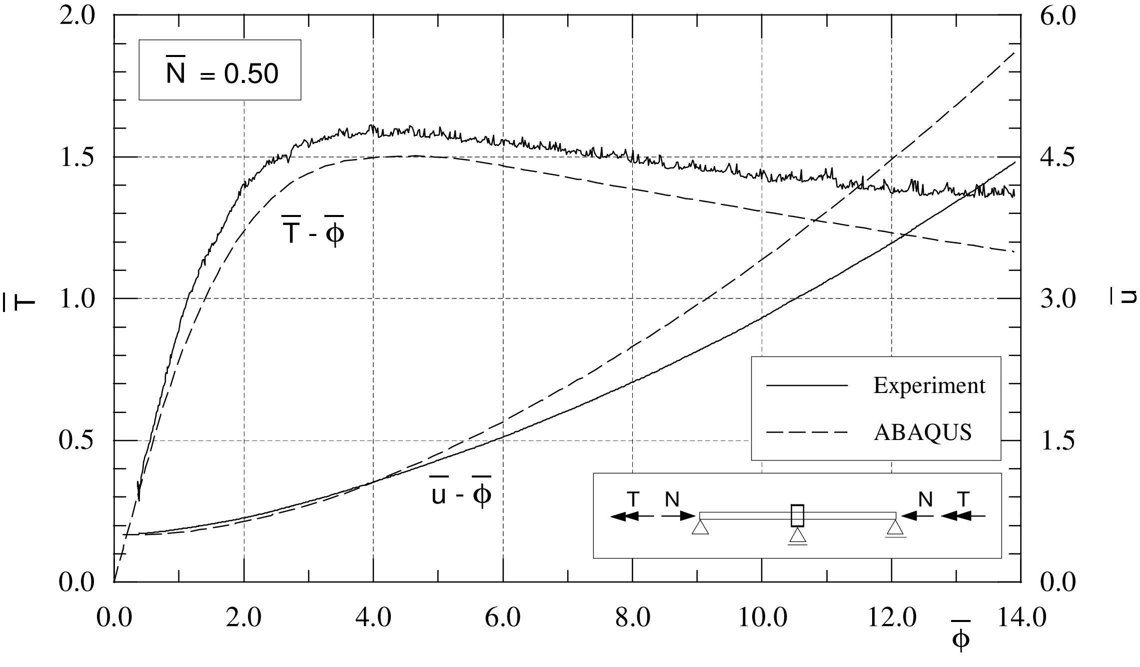

Figure 8.5: HEB 140 with axial load and nonuniform torsion (test H-9-NT).

of N, see Figure 6.6b. As this shift contributes to a reduction of the warping flange bending moment M_f (Section 6.2.2), the experimental response becomes stiffer and causes a higher specimen capacity. Later experience has, however, shown that for all actual values of N the web has sufficient capacity to transfer the axial load, and this problem could have been avoided.

No attempt is made to model the above situation as a contact problem in the simulations. Instead, a repeat experiment was carried out where the axial load ($\overline{N}$=0.50) was applied to the web only, leaving the flanges completely free to warp, and hence avoiding the contact problem. The simulation of this repeat test is shown in Figure 8.6, and it can be seen that the curves for the simulation and the experiment almost coincide. It should be noted that this study is included for the sake of completeness only, and that this inaccuracy in the modelling of the end conditions has significance only for the experiments with large values of N. The problem is primarily of academic interest, as such well defined boundary conditions will not be obtained in real structures.

Figure 8.7 presents the results for all NT tests, i.e. the axial load levels $\overline{N}$=0, $\overline{N}$=0.334, $\overline{N}$=0.50 and $\overline{N}$=0.835. For $\overline{N}$=0, the results are previously discussed in Chapter 4, while the test at $\overline{N}$=0.50 is already given in Figure 8.6. As shown, the numerical simulations give in essence a very accurate prediction of the experimental response. The deviation for the case $\overline{N}$=0.835 can be understood in view of the previous discussion. Considering that only 16.5% of f_y is available for resisting the

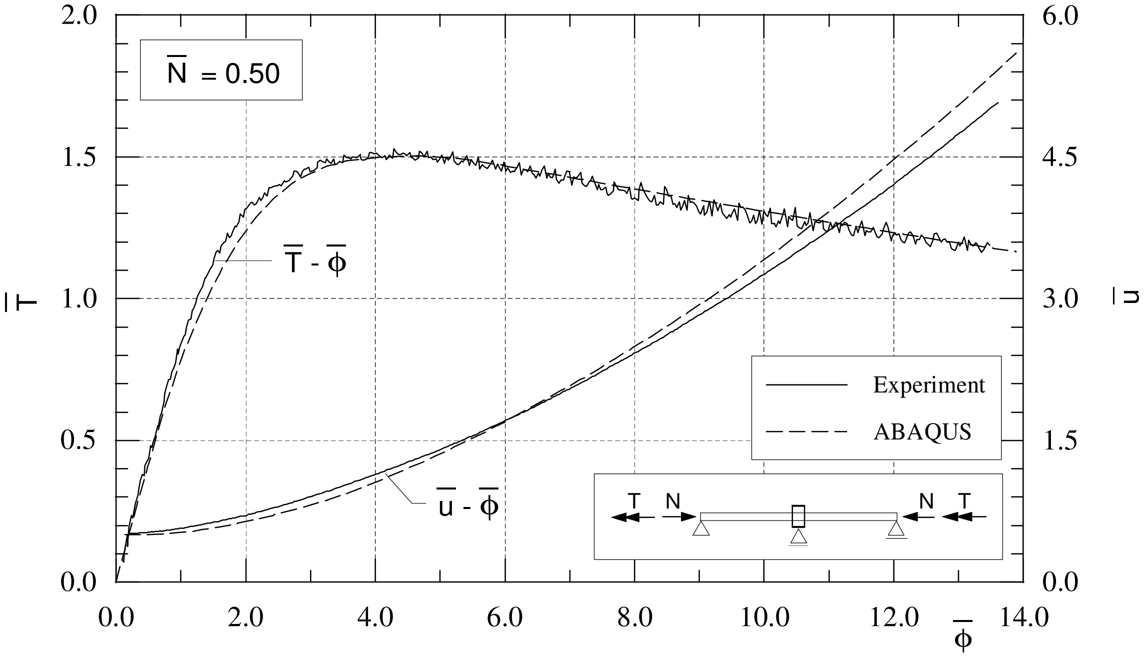

Figure 8.6: HEB 140 with axial load and nonuniform torsion (repeat test H-9-NT). Axial load applied to the specimen only through the web.

torsional moment for this case, the results may be considered acceptable. For all four simulations the stiffness in the elastic range is somewhat low, which is due to the omission of the web/flange fillets in the numerical model.

Figure 8.8 depicts the simulation for a case with a full load combination, consisting of an axial load of $\overline{N}$=0.50, bending moment and torsional moment. Again the axial load is applied first and kept constant, followed by the displacement history given by the almost bilinear $\overline{w}$-$\overline{\phi}$ curve. Also for this complex load case the numerical response is a quite good approximation to the experimental one. As for the previous cases the response in bending is somewhat underestimated for large values of the displacement, w, while the response in torsion is similar to that shown in Figure 8.5. Considering the discrepancies in N, T and M, a mean discrepancy of about 10% is present for the beam-column.

The simulations for the cases of *uniform* torsion combined with axial load for the HEB section are shown in Figure 8.9. Results are given for the two tests that were carried out for this somewhat special load situation. For the case of $\overline{N}$=0.50 the axial load was applied by contact at the web only, and hence no modelling problem occurs with respect to the warping deformation of the flanges. As shown, the numerical simulation underestimates the elastic torsional stiffness considerably in both cases, which is caused by the underestimation of I_T in the numerical model. This deficiency of course also affects the values for the predicted torsional moments

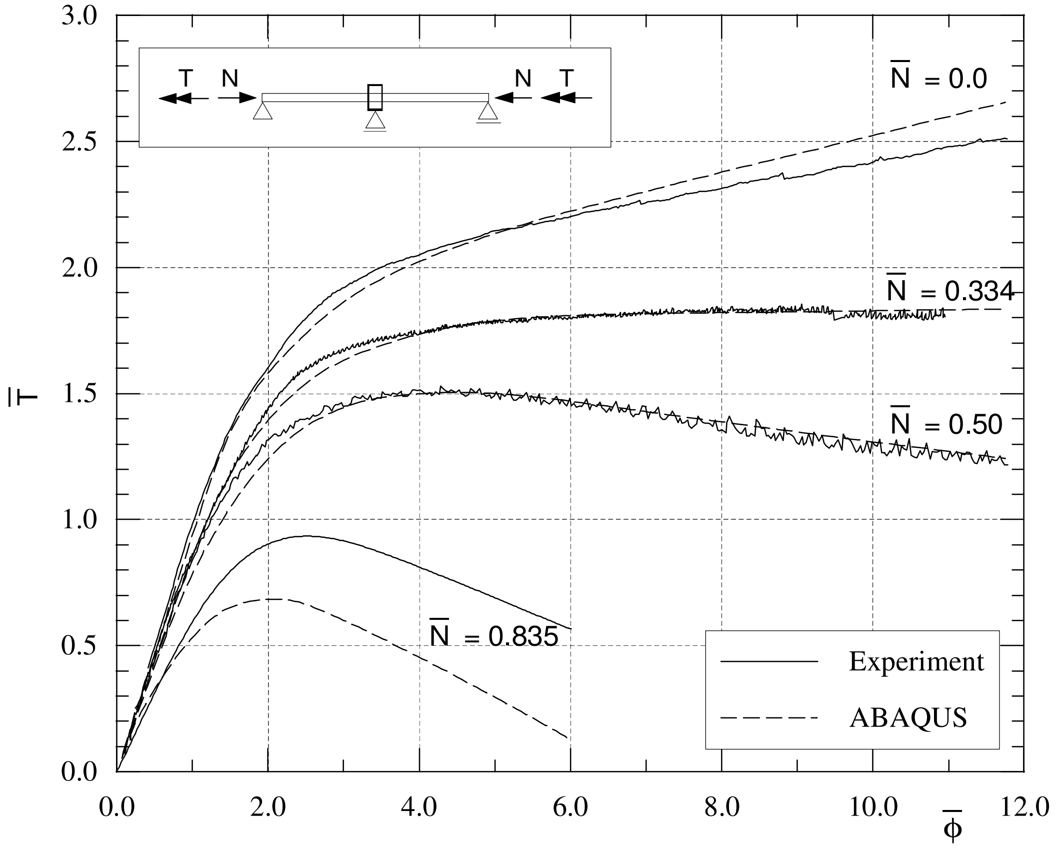

Figure 8.7: HEB 140 beam-column subjected to axial load and nonuniform torsion.

somewhat.

Note, however, that the difference in initial stiffness for the two simulations ($\overline{N}$=0.0 and $\overline{N}$=0.50) is of the same magnitude as the difference in stiffness for the two experiments. This shows that the simulations also for the uniform torsion case give a satisfactory prediction of the beam-column behaviour, and only the error in I_T causes the curves to differ.

8.3 Conclusions

In the previous section, a very good agreement between experiments and numerical simulations is shown for tests on HEB specimens. This is the case for the whole range of load combinations which is treated in the present study. Almost the same good agreement is obtained for typical tests on the IPE section (Appendix D). In general, the simulations are shown capable to predict the actual beam-column behaviour with an error of less than 10% with respect to the experimental load capacities.

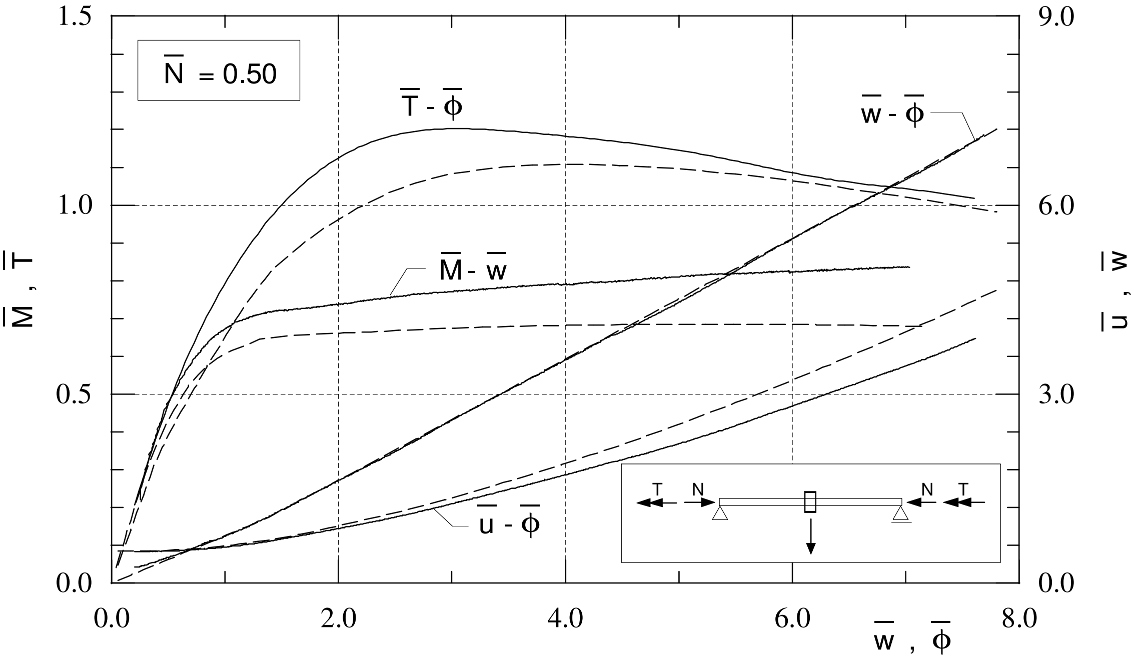

Figure 8.8: HEB 140 beam-column subjected combined axial load, bending and torsion (test H-8-NMT).

This means that numerical simulations can be used to replace experiments for similar load situations. For a further study of the problem at hand, the data basis may hence easily be augmented, both for the present specimen geometry and for beam-columns with different slenderness.

The present experimental and numerical data may serve as a basis both for the development of simple interaction formulas for design of beam-column components, and for the future development of more efficient beam elements capable of handling load combinations that include torsion. An initial attempt has been made to describe possible design models in Chapter 6, even though further studies must be made in order to extend the range of applicability of the models presented. A deficiency of some of the recent work on new beam elements, El-Khenfas and Nethercot (1989) and Pi and Trahair (1994b), is that the elements have been compared with classical analytical solutions. The present beam-column data may hence serve as a benchmark for further development of such elements.

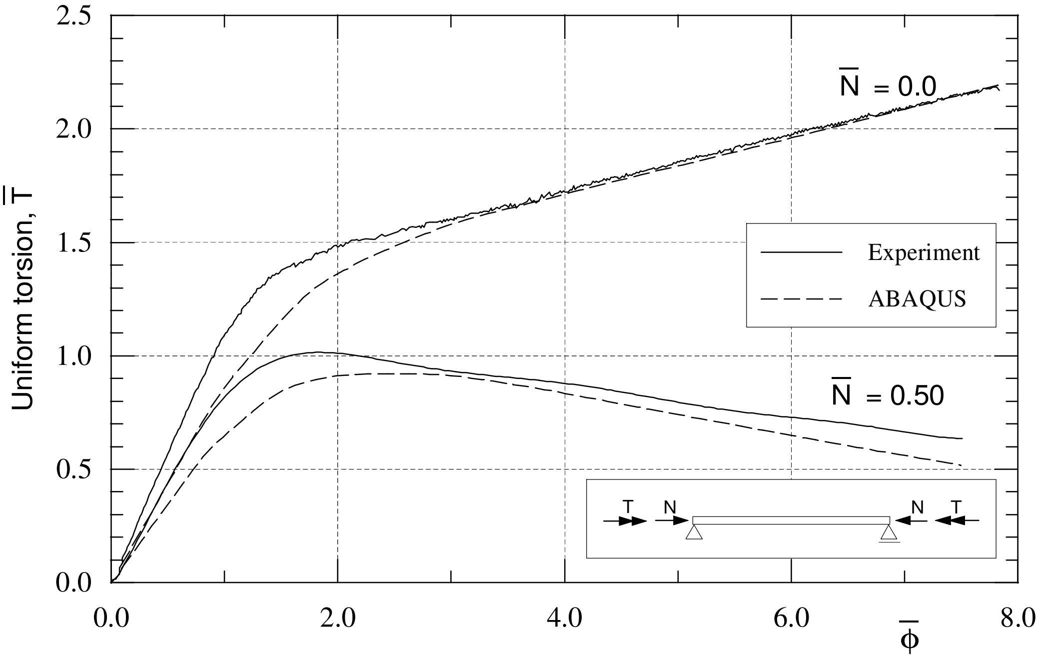

Figure 8.9: HEB 140 beam-column in uniform torsion and axial loading.

Chapter 9

Conclusions and suggestions

9.1 Conclusions

From the various experiments described in this report the following conclusions can be drawn:

1. The test facility is well suited for studies of beam-columns subjected to the load combinations investigated.

2. The test program for the beam-columns was carried out without significant problems. However, due to the low torsional stiffness of the members, and in particular for the IPE section, the initial part of the tests required special attention. A number of tests are not presented in the report due to lack of symmetry in the response and other minor deficiencies.

3. From the tests with single torsional loading (both uniform and nonuniform torsion), it is seen that there exists large inelastic reserves beyond the capacity defined by initial yielding. In the tests, no ultimate value is observed for the torsional moment, as the response curves show a steadily increasing torsional moment with increasing twist. It is hence necessary to define the capacity in torsion with reference to a given value of the inelastic rotations.

4. Also for the tests in combined strong axis bending and nonuniform torsion, large inelastic load capacities are observed, and a ductile behaviour is obtained. Again, the capacity must be referred to the extent of deformations. Assuming a direct summation of the obtained values for the bending and the torsional moments, a total capacity of about 2 to 3 times that given by initial yielding is observed.

5. For the beam-column tests at load combinations consisting of axial load and nonuniform torsion, no global instability is reached for axial loads up to 35% of the section squash load. This is mainly due to the fact that the induced second order effects caused by the axial load are balanced by the increased torsional resistance, again due to the large rotations (i.e. nonlinear geometry). Even for an axial load equal to 50% of the squash load, a torsional moment equal to 150% of the initial yield moment is reached (HEB section).

6. For the beam-column tests with a full load combination of axial load, bending moment and torsional moment, similar large inelastic load capacities are found. Again, the linear interaction gives a capacity that exceeds initial yielding by a factor of about 2.5.

7. Numerical simulations performed by means of the finite element program ABAQUS, using shell elements to model the beam-column specimens, show that the behaviour in torsion is very well modelled. Simulations of the beam-column tests, for the whole range of load combinations treated in this report, show a very good agreement between the numerical and the experimental response.

8. For the interaction between bending moment and nonuniform torsional moment, a commonly used quadratic interaction equation is found to give reasonable results for present tests. Here, Merchant's value for the fully plastic nonuniform torsional moment is used.

9. Interaction equations are suggested for the axial load and torsion interaction. An elastic amplification factor is used to represent the second order effects of the axial load, and gives good results.

9.2 Suggestions for further study

In the present study emphasis is put on the design and construction of a test facility for testing of beam-columns under the combined load actions, and to obtain a set of experimental data for such structural components.

The effect of the nonuniform torsion depends strongly on the specimen length, both with respect to the distribution between warping torsion and uniform torsion within the member, and the additional load action that results from the interaction with the axial load. Hence it is suggested that additional tests should be made with specimens of other lengths in order to investigate the applicability of the observations made. FE simulations using shell models are in general proved to be capable of simulating the beam-column response for the present specimens. Therefore, it should be sufficient to carry out only a limited number of experiments, and to augment these by simulations.

For members with larger slenderness than the present specimens, the member behaviour and the capacity will be influenced by effects from both flexural and lateral torsional buckling. For members of other cross-sections local buckling may introduce additional problems. Further tests and simulations should therefore be made to investigate if the present formulas can be extended to such situations.

In recent years new beam elements have been developed that model both uniform and nonuniform torsion. In order to increase the efficiency of such elements, material models should be formulated that can describe the inelastic behaviour on a cross-sectional level in terms of stress resultants (concentrated plastic hinges).

References

Alpsten G. A. (1967): *Residual stresses in hot-rolled steel profiles*, Inst.of Struc. Eng. and Bridge Building, Roy. Inst. of Techn., Stockholm.

Alpsten G. A. (1970): *Residual stresses and mechanical properties of cold-straightened H-shapes,* Jernkontorets Annaler, SBI Stockholm, Vol 154, pp 255-283.

ASCE (1971): *Plastic design in steel - A guide and commentary*, ASCE manuals and reports on engineering practice, No 41.

Attard M. M. (1986): *Nonlinear theory of non-uniform torsion of thin-walled open beams*, Thin-Walled Structures, Vol 4, pp 101-134.

Augusti G. (1966): *Full plastic torque of I-beams*, Int J Mech Sci, Pergamon Press Ltd, Vol 8, pp 641-649.

Australian Standard 4100 (1990): AS 4100-1990 *Steel structures* and AS 4100 Supplement 1-1990 *Steel structures - Commentary*, Standards Australia North Sydney NSW.

Bathe K. and Wiener P. M. (1983): *On elastic-plastic analysis of I-beams in bending and torsion*, Computers & Structures, Vol 17, No 5-6, pp 711-718.

Bild S., Chen G. and Trahair N. S. (1992): *Out-of-plane strengths of steel beams*, J of Structural Engineering, Vol 118, No 8.

Billingshurst A., Williams J. R. L., Chen G. and Trahair N. S. (1991): *Inelastic uniform torsion of steel members*, Computers & Struct., Vol 42, No 6, pp 887-894.

Boulton N. S. (1962): *Plastic twisting and bending of an I-beam in which the warp is restricted*, Int J Mech Sci, Pergamon Press Ltd, Vol 4, pp 491-502.

Chen G. and Trahair N. S. (1992): *Inelastic nonuniform torsion of steel I-beams*, J Construct Steel Research, Elsevier Science Publishers Ltd, Vol 23, pp 189-207.

Chen W. F. and Atsuta T. (1977): *Theory of beam-columns*, Vol 2, McGraw-Hill.

Chu K. and Johnson R. B. (1974): *Torsion in beams with open sections*, Journal of the Structural Division, Vol 100, No ST7.

CRC (1961): *Stub column test procedure*, Technical memorandum No. 3, SSRC.

Daddazio R. P., Bieniek M. P. and DiMaggio F. L. (1983): *Yield surface for thin bars with warping restraint*, Journal of Engineering Mechanics, Vol 109, No 2.

Dieter G. E. (1988): *Mechanical metallurgy*, McGraw-Hill.

Dinno K. S. and Gill, S. S. (1964): *The plastic torsion of I-sections with warping restraint*, Int J Mech Sci, Pergamon Press Ltd, Vol 6, pp 27-43.

Dinno K. S. and Merchant W. (1965): *A procedure for calculating the plastic collapse of I-sections under bending and torsion*, The Structural Engineer, Vol 43, No 7.

Driver R. G. and Kennedy D. J. L. (1989): *Combined flexure and torsion of I-shaped steel beams*, Canadian Journal of Civil Engineering, Vol 16, pp 124-139. Also: *Structural engineering report 144*, Department of Civil Engineering, University of Alberta, Edmonton (1987).

Duan L. and Chen W. (1990): *A yield surface equation for doubly symmetrical sections*, Eng Struct, Vol 12, April.

ECCS (1976): *Manual on stability of steel structures*, ECCS Committee 8 - Stability 1976, European Convention for Constructural Steelwork.

El-Khenfas M. A. and Nethercot D. A. (1989): *Ultimate strength analysis of steel beam-columns subject to biaxial bending and torsion*, Res Mechanica, Vol 28, pp 307-360.

El Darwish I. A. and Johnston B. G. (1965): *Torsion of structural shapes*, Journal of the Structural Division, Proceedings of the American Society of Civil Engineers, Vol 91, No ST1.

Eschmann, Hasbargen and Weigand (1985): *Ball and roller bearings*; *Theory, design and application*, John Wiley & Sons Ltd.

Eurocode 3 (1992): DD-ENV 1993-1-1:1992 *Design of steel structures part 1.1: General rules and rules for buildings*, European Committee for Standardization (CEN).

Farwell C. R. and Galambos T. V. (1969): *Nonuniform torsion of steel beams in inelastic range*, Journal of the Structural Division, Proceedings of the American Society of Civil Engineers, Vol 95, ST12.

Gaydon F. A. and Nuttall H. (1957): *On the combined bending and twisting of beams of various sections*, Journal of the Mechanics and Physics of Solids, Pergamon Press Ltd, Vol 6, pp 17-26.

Gill S. S. and Boucher J. K. G. (1964): *An experimental investigation of plastic collapse of structural members under combined bending and torsion*, The Structural Engineer, No 12, Vol 42.

Hibbitt et al. (1994): *ABAQUS Version 5.4*, User's manual and theory manual, Hibbitt, Carlsson & Sorensen, Inc.

Hill R. and Siebel M. P. L. (1952): *On the plastic distortion of solid bars by combined bending and twisting*, J of the Mechanics and Physics of Solids, Pergamon Press Ltd, Vol 1, pp 207-214.

Hodge P. G. (1959): *Plastic Analysis of Structures*, McGraw-Hill.

Imegwu E. O. (1960): *Plastic flexure and torsion*, J Mech Phys Solids, Vol 8, pp 141-146.

Kollbrunner C. F. and Basler K. (1969): *Torsion in structures,* Springer-Verlag.

Kollbrunner C. F., Hajdin N. and Coric (1979): *Elastic-plastic fixed ended beam of I-section subjected to bending and torsion,* Institut für bauwissenschaftliche forschung publikations, No 43.

May I. M. and Al-Shaarbaf I. A. S. (1988): *Elasto-plastic analysis of torsion using a three-dimensional finite element model*, Computers & Structures, Vol 33, No 3 pp 667-678.

Nadai A. (1950): *Theory of flow and fracture of solids*, McGraw-Hill.

Neal B. G. (1977): *The plastic methods of structural analysis*, Chapman and Hall.

Nethercot D. A., Salter P. R. and Malik A. S. (1989): *Design of members subjected to combined bending and torsion*, The Steel Construction Institute, Ascot, Berkshire, SCI publication 057.

Orbison J. G., McGuire W. and Abel J. F. (1982): *Yield surface applications in nonlinear steel frame analysis*, Computer Methods in Applied Mechanics and Engineering, Vol 33, pp 557-573.

Pastor T. P. and DeWolf J. T. (1979): *Beams with torsional and flexural loads*, Journal of the Structural Division, Vol 105, No St3.

Pi Y. L. and Trahair N. S. (1992): *Prebuckling deflections and lateral buckling - theory.* Journal of Structural Engineering, Vol 118, No 11.

Pi Y. L. and Trahair N. S. (1994a): *Nonlinear inelastic analysis of steel beam-columns. I: Theory*, Journal of Structural Engineering, Vol 120, No 7.

Pi Y. L. and Trahair N. S. (1994b): *Nonlinear inelastic analysis of steel beam-columns. II: Applications*, Journal of Structural Engineering, Vol 120, No 7.

Pi Y. L. and Trahair N. S. (1994c): *Inelastic bending and torsion of steel I-beams, ASCE,* Journal of Structural Engineering, Vol 120, No 12.

Pi Y. L. and Trahair N. S. (1995): *Inelastic torsion of steel I-beams.* Journal of Structural Engineering, Vol 121, No 4.

Razzaq Z. and Galambos T. V. (1980): *Biaxial bending tests with or without torsion*, Journal of the Structural Division, Proceedings of the American Society of Civil Engineers, Vol 105, No ST11.

Shames I. H. and Dym H. L. (1985): *Energy and finite element methods in structural analysis*, Hemisphere publishing corporation.

SKF (1989): *Main catalogue, Bearings and bearing parts 1989.*

Søreide, Amdahl, Eberg, Holmås, Helland (1993): *USFOS - Theory manual*, SINTEF report STF71 F88038, Trondheim.

Timoshenko S. P. (1936): *Theory of elastic stability*, McGraw-Hill.

Timoshenko S. P. and Gere J. M. (1961): *Theory of elastic stability*, McGraw-Hill.

Timoshenko S. and Goodier J. N. (1951): *Theory of elasticity*, McGraw-Hill.

Trahair N. S. and Bradford M. A. (1988): *The behaviour and design of steel structures*, second edition, Champman and Hall.

Vlassov V. Z. (1961): *Thin-walled elastic beams*, Israel Program for Scientific Translations, Jerusalem 1961.

Yang Y. and Fan H. (1988): *Yield surface modeling of I-sections with nonuniform torsion*, Journal of Engineering Mechanics, Vol 114, No 6.

Yang Y. and McGuire W. (1984): *A procedure for analysing space frames with partial warping restraints*, International Journal for Numerical Methods in Engineering, Vol 20, pp 1377-1398.

Appendix A

Characteristic data

A.1 Beam-column capacities

Load capacities for the beam-columns are given in Table A.1. Please, refer to Figures 3.1 and 5.1 for specimen geometry and load/support conditions. The buckling length for strong and weak axis flexural buckling is 2030 mm and 1015mm, respectively. For lateral torsional buckling, the buckling length is 1015 mm. The value denoted "torsional buckling" in the table refers to torsional buckling for the torsionally pin-ended beam-column of 2030 mm, i.e buckling between the two ends of the beam-column. "Torsional buckling (Uniform)" refers to a situation where the beam-column buckles with uniform twist deformations along the member axis, i.e. where the end sections are allowed to rotate relative to each other. For the uniform buckling case, the torsional buckling load is independent of the beam-column length. It can be seen from Table A.1 that only the IPE section has any significant buckling tendency.

Note that the HEB 140 and the IPE 160 sections are both of cross-section Class 1 according to the requirements given in Eurocode 3, both in pure bending and for the case of compressive axial force.

	HEB 140 Elastic / Inelastic	IPE 160 Elastic / Inelastic
Squash load ($= N_Y$)	- / 1198 kN	- / 626 kN
Strong axis buckling ($l = 2030mm$)	7450 kN / 0.93 N_Y	4288 kN / 0.96 N_Y
Weak axis buckling ($l = 1015mm$)	11000 kN / 0.94 N_Y	1341 kN / 0.80 N_Y
Torsional buckling ($l = 2030mm$)	5600 kN / 0.97 N_Y	1060 kN / 0.86 N_Y
Torsional buckling (Uniform)	3200 kN / 0.93 N_Y	649 kN / 0.71 N_Y
Lateral tors. buckl. ($l = 1015mm$)	1411 kNm / 1.0 M_Y	217 kNm / 0.99 M_Y

Table A.1: Beam-column capacities, based on NS 3472 - The Norwegian steel design standard.

A.2 Elastic nonuniform torsion

The differential equation describing the general case of elastic nonuniform torsion of a beam is given by Timoshenko (1930) and Kollbrunner and Basler (1969). The total resistance of a beam to torsional loading is given as the sum of the warping resistance T_w and the uniform torsional resistance T_u (also denoted St.Venant torsion, $T_{St.V}$) :

$$T = T_w + T_u = -EI_w \frac{d^3\phi}{dx^3} + GI_T \frac{d\phi}{dx} \tag{A.1}$$

The general solution of this equation, with respect to the twist rotation $\phi(x)$ along a beam is for the case of an applied constant torsional moment T_0

$$\phi(x) = \left[C_1 + C_2 x + C_3 cosh\frac{x}{\alpha} + C_4 sinh\frac{x}{\alpha}\right]\frac{T_0}{GI_T} \quad , \ \alpha = \sqrt{\frac{EI_w}{GI_T}} \tag{A.2}$$

For the beams of the present study, as shown in Figure A.1, concentrated torsional moments T_0 are applied at the free ends and a moment of $2T_0$ is resisted at midspan. It is easily seen that this is identical with the case of a simply supported beam, torsionally pinned at the ends, subjected to a concentrated torsional moment of $2T_0$ at midspan. From considerations of symmetry, the cross-section at midspan must remain plane during twisting. The present loading case may hence also be considered as two separate cantilevered beams connected at the midspan.

If the coordinate x and the rotation ϕ are measured from the midpoint of the beam as shown in the figure, the solution of Equation A.2 is given by

$$\phi(x) = \alpha\frac{T_0}{GI_T}\left[tanh\frac{l/2}{\alpha}\left(cosh\frac{x}{\alpha} - 1\right) - sinh\frac{x}{\alpha} + \frac{x}{\alpha}\right] \tag{A.3}$$

The elastic first-order twist rotation of the beam ends may hence be calculated by

$$\phi_{end} = \phi(x = l/2) \tag{A.4}$$

The distribution between warping torsional moment T_w and uniform torsional moment T_u along the beam is obtained using Equations A.1 and A.3, and is given by respectively

$$T_w = -EI_w\frac{d^3\phi}{dx^3} = \left[cosh\frac{x}{\alpha} - tanh\frac{l/2}{\alpha}\cdot sinh\frac{x}{\alpha}\right]T_0 \tag{A.5}$$

and

$$T_u = GI_T\frac{d\phi}{dx} = \left[1 + tanh\frac{l/2}{\alpha}\cdot sinh\frac{x}{\alpha} - cosh\frac{x}{\alpha}\right]T_0 \tag{A.6}$$

The resulting distribution along the beam is shown in Figure A.1, calculated for the HEB 140 section. The distribution for the IPE 160 section is almost identical. As shown, the external applied torsional moment T_0 is fully resisted by warping at midspan, decreasing towards the free ends where 32% and 28% are resisted by warping for the HEB and the IPE, respectively.

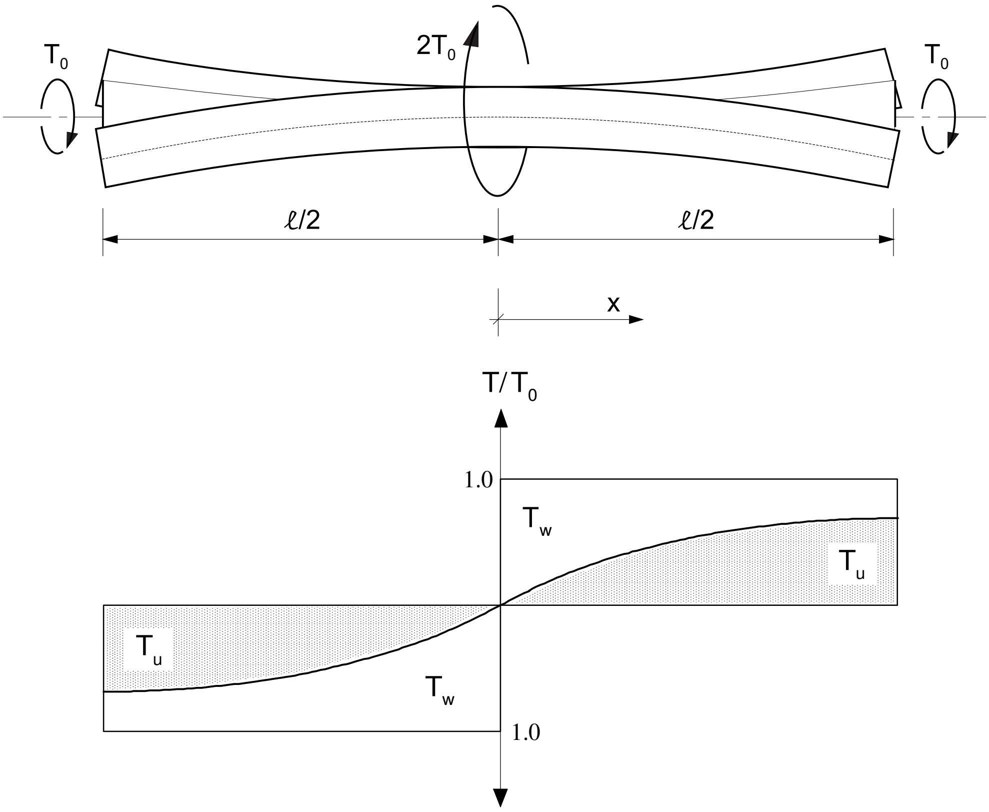

Figure A.1: Nonuniform torsion on I-section beam.

A.3 Uniform torsion - Elastic/Plastic

For a narrow rectangular section (b·t) in uniform torsion, the torsional moment at nominal initial yield is given by

$$T_Y = \frac{f_y}{\sqrt{3}} \cdot \frac{1}{3} b t^2 \tag{A.7}$$

if an elastic shear stress distribution is assumed (Timoshenko 1951).

Based on a fully plastic distribution of the shear stresses, obtained by using the sand-heap analogy of Prandtl (Nadai 1950), the torsional moment is correspondingly

$$T_{up} = \frac{f_y}{\sqrt{3}} \left(1 - \frac{t}{3b}\right) \frac{1}{2} b t^2 \;\approx\; \frac{f_y}{\sqrt{3}} \frac{1}{2} b t^2 \tag{A.8}$$

Hence, the ratio between the fully plastic torsional moment to the initial yield moment is

$$T_{up}/T_Y \;=\; 3/2 \quad or \; 1.5 \tag{A.9}$$

Appendix B

Photographs

Test rig

The Figures B.1 and B.2 show details from the test rig. Figure B.1 shows the upper end of an HEB 140 test specimen after testing, extending about 30 mm beyond the end fixture / torsional loading plates at the end support. Note the design of the test specimen end, where part of the flanges are removed to minimize the warping restraints resulting from the contact with the axial loading parts, i.e. the base plate. This particular specimen has been tested in bending and torsion (MT), and it can be seen that the flanges have sustained significant warping deformations.

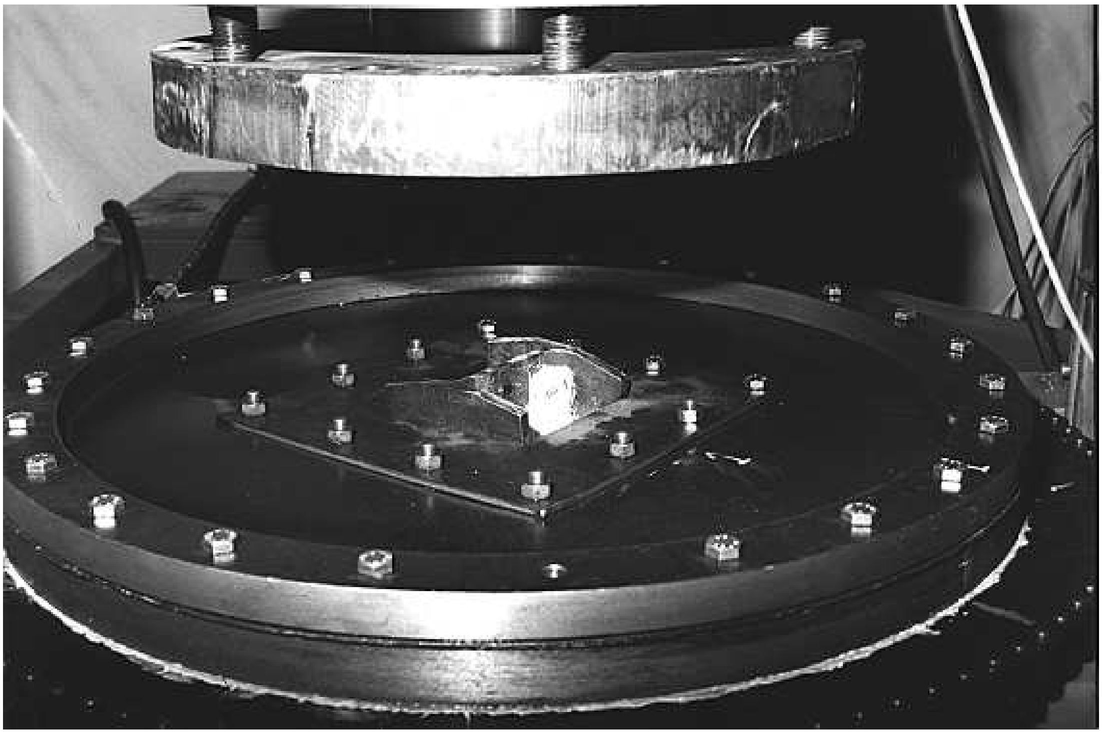

Figure B.1: End supports of test specimen, with circular and quadratic end fixture plate.

Figure B.2 shows the loading plate / torsional restraining plate at midspan, with a IPE 160 test specimen mounted in the test rig. The specimen extends through the opening in the 30 mm thick loading plate, where the opening is equipped with 32 mm metal linings. Also shown is some of the equipment used to measure the transverse displacement (w) at midspan; a displacement transducer attached to the loading plate by means of a magnetic foot, connected to a bar attached to the end support frames.

Figures B.3 and B.4 show details of the thrust bearings and the base plates.

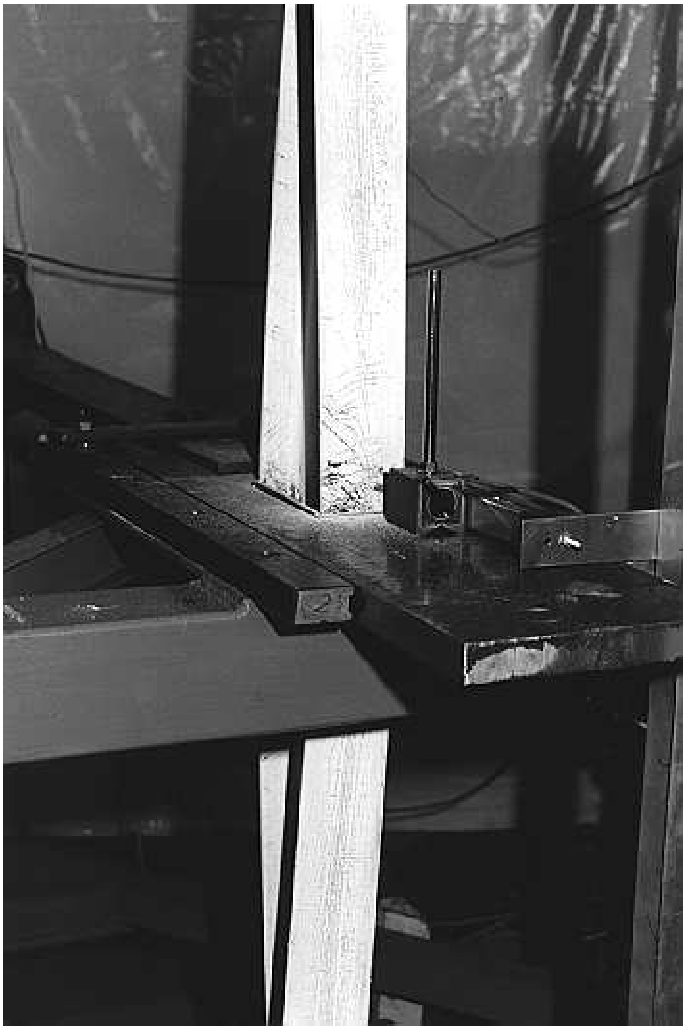

Figure B.2: Loading plate at midspan, and deformed test specimen.

Specimens tested in torsion

Figures B.5 and B.6 show photographs of the specimens tested in torsion only (Chapter 4). For the case of uniform torsion, only the IPE and the flat bar is shown.

Note the perfect uniform twist rotation along the specimens tested in uniform

Figure B.3: Spherical thrust bearing (bending moment "hinge") and plane thrust bearing (torsional moment "hinge").

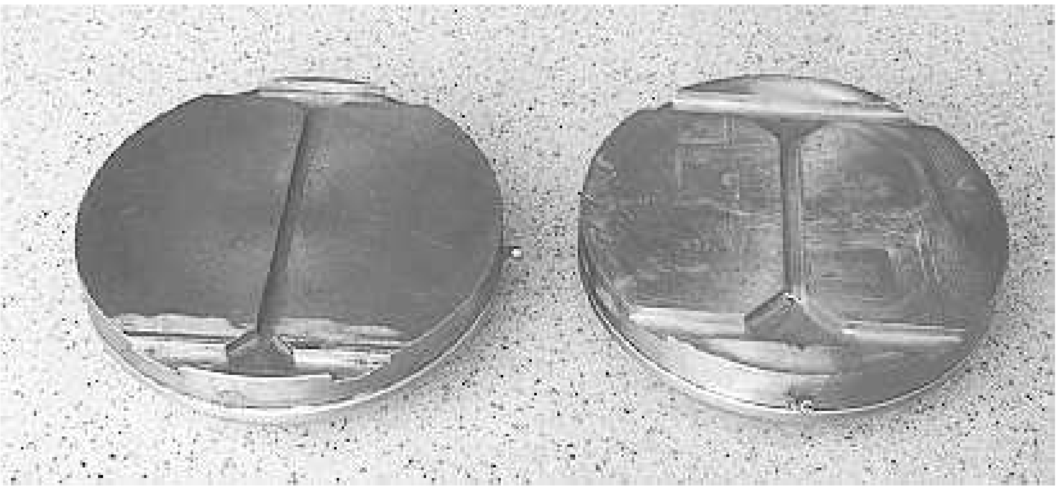

Figure B.4: Base plates fitted to the cross-section of the test specimens.

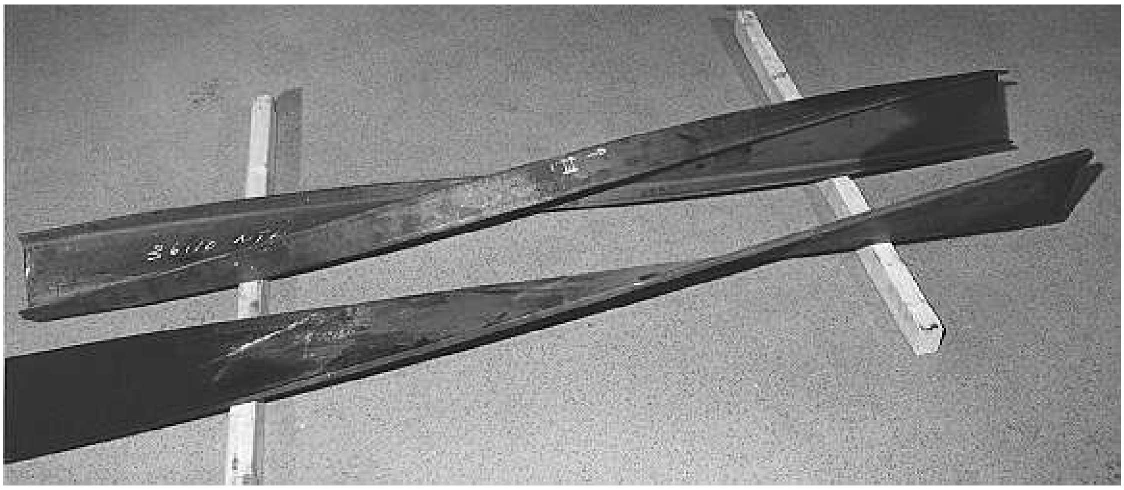

Figure B.5: IPE 160 section and flat bar section (15.3x200) tested in uniform torsion.

torsion, and the slope discontinuity in the flange of the specimens tested in nonuniform torsion.

Beam-column specimens

Figures B.7 to B.9 show photographs of some of the beam-column specimens, and illustrate the extent of deformation in the tests.

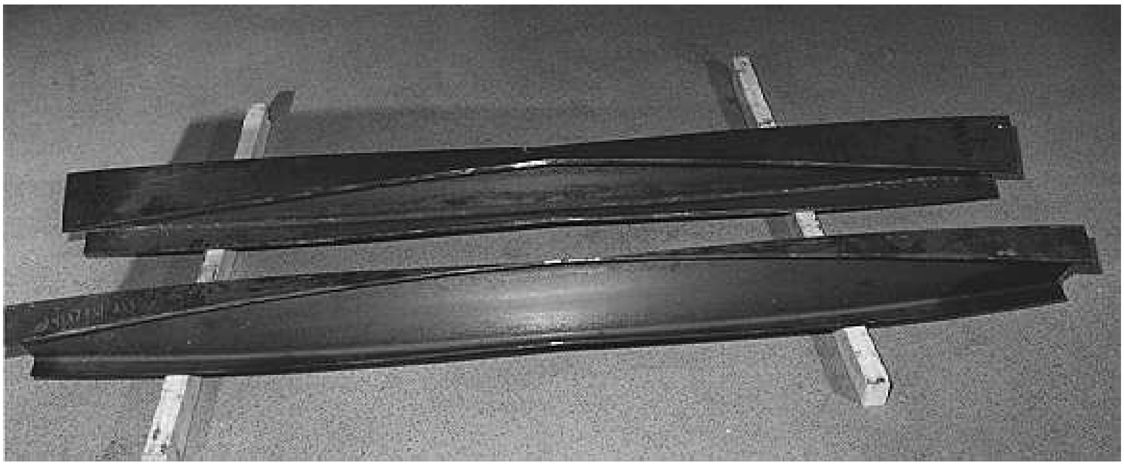

Figure B.6: HEB 140 and IPE 160 sections tested in nonuniform torsion.

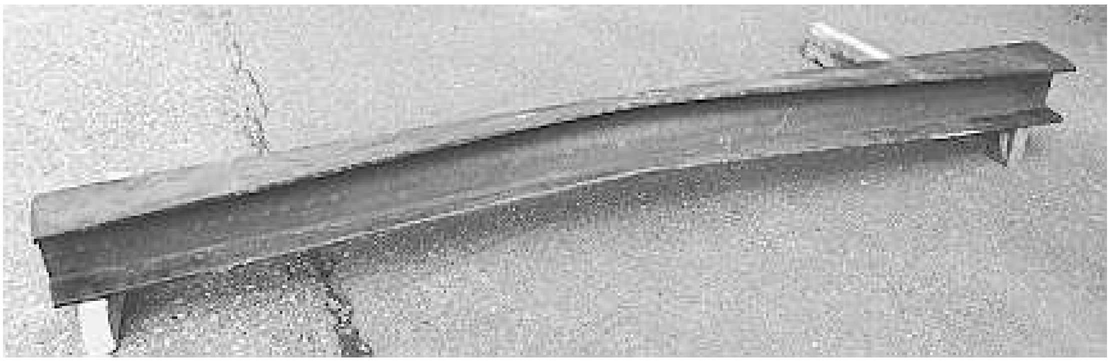

Figure B.7: Test specimen H-2-MT, HEB 140 tested in bending and nonuniform torsion.

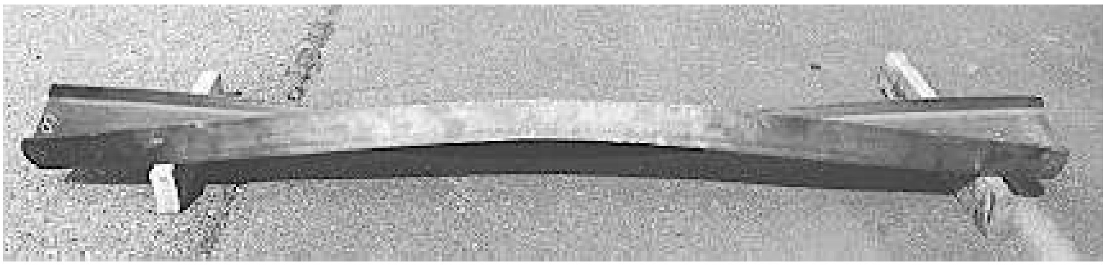

Figure B.8: Test specimen I-9-NT, IPE 160 tested in axial load and nonuniform torsion.

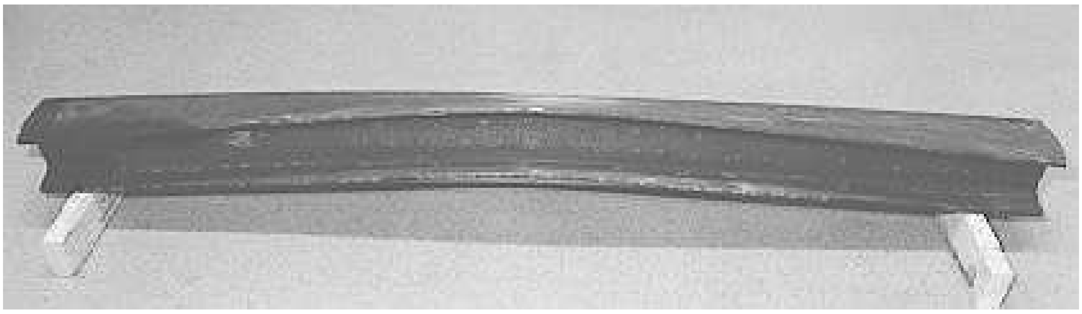

Figure B.9: Test specimen H-8-NMT, HEB 140 tested in axial load, bending and nonuniform torsion.

Appendix C

Twist rotations

Measurements of twist rotations along the specimens

The distribution of the permanent twist rotations was measured directly on the deformed, unloaded specimens using an adjustable angle measuring device, with the specimens mounted on a plane table.

During testing, the rotations were measured at different positions along the specimen (positions marked on the curves), by means of a simple arrangement with long sticks attached to the specimen, and a manually reading of their displacements.

Due to symmetry only half the specimen length is considered. The theoretical elastic distribution of the rotations, obtained from Equation A.3, is given for comparison. This distribution is practically identical for the two cross-sections. The rotations along the specimens are made dimensionless by means of the value of the rotation ϕ measured at the specimen end.

Figure C.1 shows the distribution of the permanent rotations for the specimens tested in nonuniform torsion (Chapter 4). In the figure, 0 mm corresponds to the midpoint of the specimen, and 1045 mm is at the specimen end.

Figure C.2 shows the twist rotations for one of the HEB 140 specimens tested with axial load and nonuniform torsion. Both the permanent rotations and the rotations measured during testing are given. As shown, the theoretical elastic distribution and the experienced (plastic) distribution differ significantly at the end of the test, due to localized plastification.

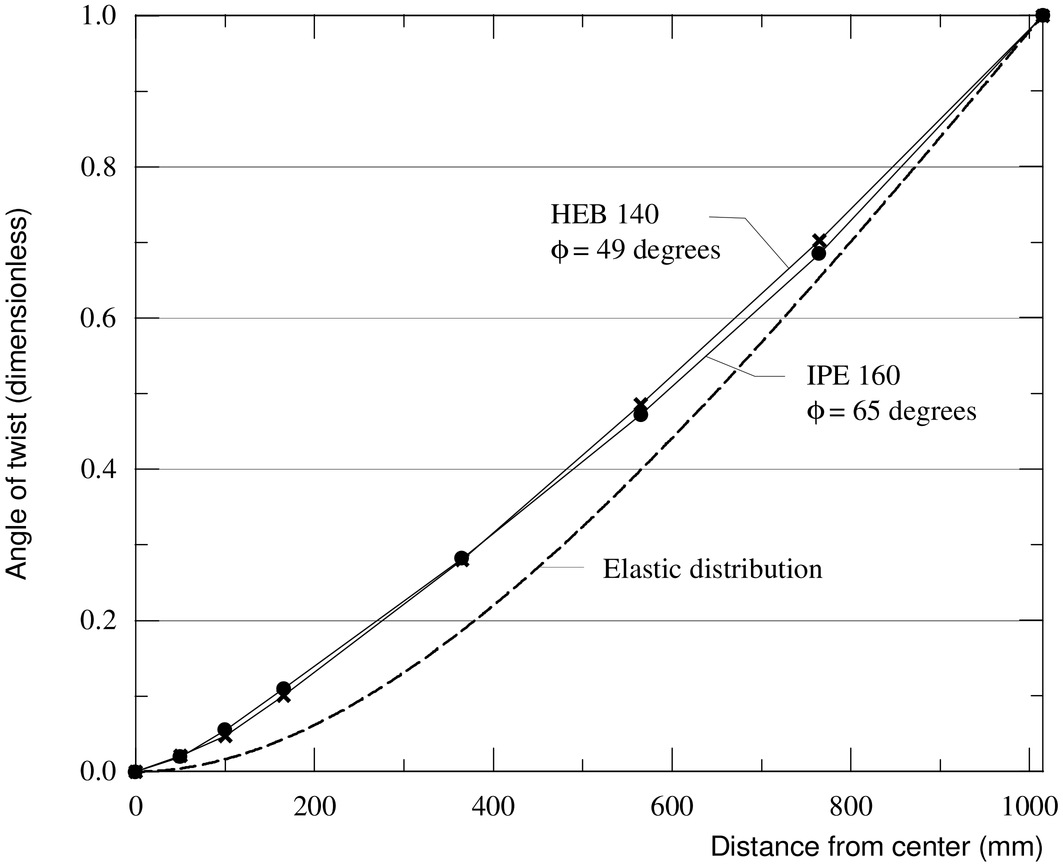

Figure C.1: HEB 140 and IPE 160 specimens tested in nonuniform torsion - distribution of permanent twist rotation.

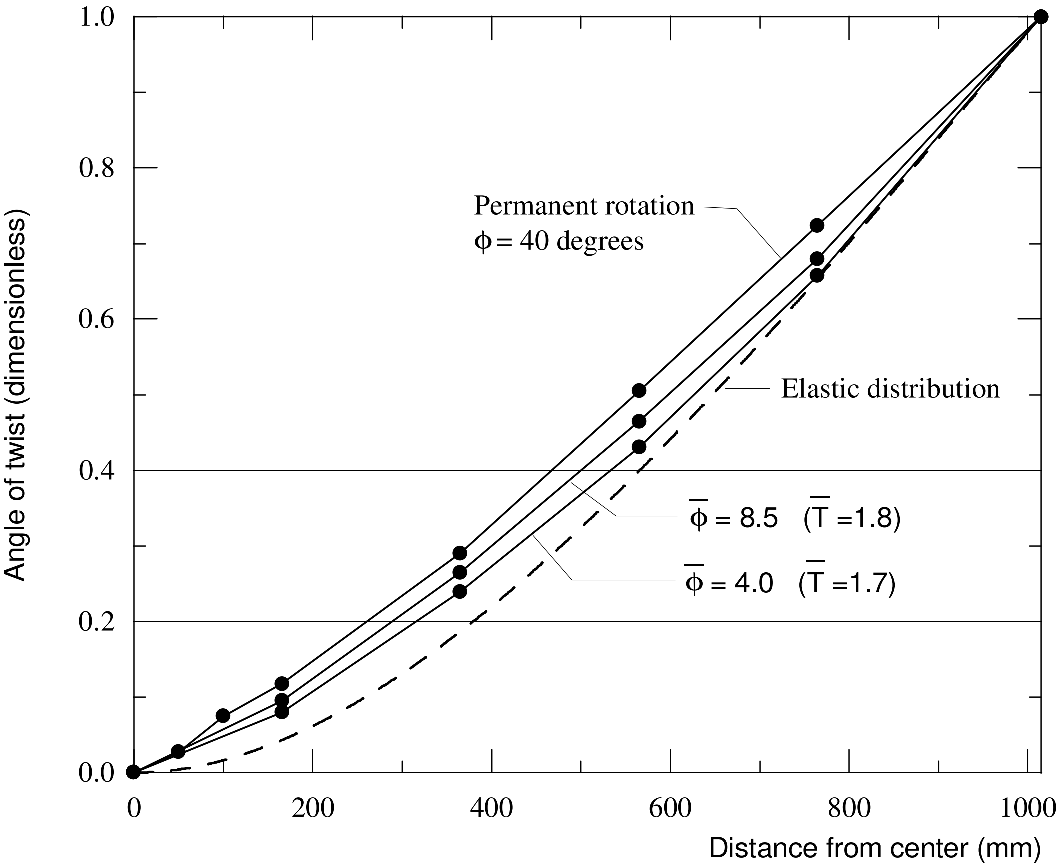

Figure C.2: Beam-column specimen H-7-NT, twist rotations.

Appendix D

Results from numerical simulations

D.1 Shell model - properties in uniform torsion

A limited numerical study was carried out in order to investigate how well the uniform torsional properties of the I-beams are represented by the present shell model (Figure 4.9). To reduce the complexity of the problem, pure uniform torsion on a rectangular cross-section was modelled. Several simulations were performed using the shell model of the $15.3 \cdot 200mm^2$ flat bar of length 2090 mm, presented in Section 4.4.

Simulations were performed using the transverse shear flexible shell element S8R, taking only linear geometry into account. Two alternatives were studied :

1. An element mesh consisting of 1 element in the width direction (200 mm) and 12 elements along the bar (2090 mm), i.e. quadratic shape.

2. An element mesh consisting of 5 elements in the width direction and 52 elements along the bar, i.e. quadratic shape.

Theoretical values for the elastic torsional stiffness and the torsional shear stresses are calculated from the formulas provided by Timoshenko and Goodier (1951). The elastic torsional stiffness predicted by alternatives 1.) and 2.) was 1.043 and 1.000 times the theoretical stiffness, respectively. For the shear stresses τ_{xy} at the bar surface, the simulations gave practically identical values, about 95% of the theoretical value. This shows that no more than one shell element is needed to give a reasonable prediction of the behaviour for this case, which seems reasonable as one element gives a quite good description of the actual displacement field.

Simulations similar to the alternatives 1.) and 2.) above were also performed using the ABAQUS element S8R5. This shell element does not have the transverse shear flexibility which is present for the S8R element. The results obtained with this shell element were practically identical to those above, both with respect to the predicted stiffness and the shear stresses. As the transverse shear stresses (τ_{xz}) contained in the S8R element give only an insignificant contribution to the total energy of the plate when twisted, this seems reasonable.

Simulations were also carried out for a quadratic cross-section with dimensions $100 \cdot 100mm^2$, still using shell elements. Here, the mesh with 1×12 elements predicted an elastic stiffness equal to 1.07 times the theoretical value, both for the simulation with the S8R element and the simulation with the S8R5 element. The predicted values for the stresses τ_{xy} were also almost identical for the two simulations. However, and not unexpected, the predicted stresses were in this case only 62% of the theoretical value. The interesting part here is to note that both elements give a almost correct value for the elastic torsional stiffness.

With reference to the shell model of the I-section beams, the above simulations show that the behaviour of the individual web and flange plates can be expected to be properly modelled by the chosen discretization. Of course, this does not automatically mean that I-section model gives the correct value for the stiffness of the beam. In fact, it is quite difficult a priori to give an estimate for the stiffness.

Here, the IPE 160 section can be taken as an example. The stiffness of the beam is directly proportional to the value of the torsional constant I_T. The theoretical value of I_T for the actual beam, including the effect of juncture and fillets (El Darwish and Jonhston 1965), is calculated to be 36370 mm^4. For a section without fillets, as in the shell model, the value of I_T may be calculated as the sum of I_T for the three sectional plates, which gives a value of 25470 mm^4 if corrections for end effects are made for the flange plates only. The value of I_T deduced from the ABAQUS simulation for the beam is correspondingly 28560 mm^4, which hence lies somewhere between the values above.

D.2 Torsion simulations

Uniform and nonuniform torsion on HEB 140

Figures D.1 and D.2 show simulations for the HEB section in uniform torsion and nonuniform torsion, respectively. For simplicity, the material data for the flange material is used for the entire beam.

For the uniform torsion case, the upper curve in Figure D.1 shows the numerical results when both nonlinear geometry and nonlinear material behaviour are taken into account. The lower curve shows the results from a linear analysis, i.e. where the nonlinear terms in the strain-displacement relationships are suppressed. It was seen from the simulations that strain hardening of the material not was reached within the given rotation range. Hence, the difference between the two curves is purely due to the effect of large rotations/deformations. As strain hardening not takes place, the linear analysis may also be considered to represent a linear elastic/perfect-plastic analysis. As shown, the torsional moment obtained in this linear analysis agrees reasonable well with the sand-heap value of the moment.

For the nonuniform torsion case, Figure D.2 shows simulations where the effects from nonlinear geometry and material strain hardening are separated. As shown by the two uppermost curves, strain hardening affects the behaviour only for rotations

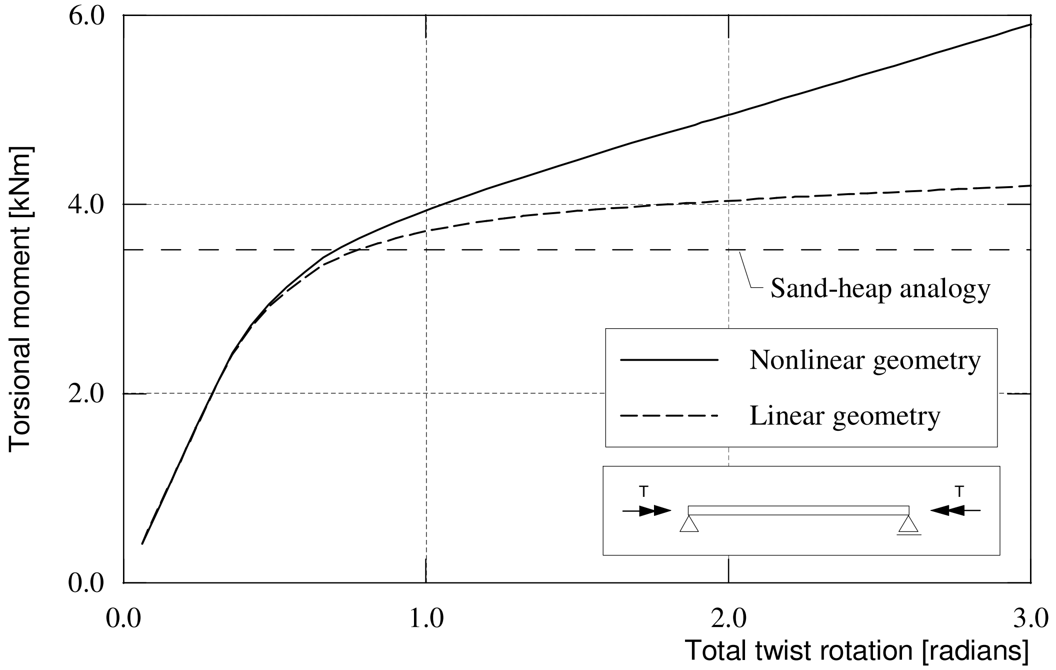

Figure D.1: Simulations for HEB 140 in uniform torsion.

larger than 0.6 radians.

Uniform torsion on flat bar steel

Figure D.3 shows a closer view of the torsional response in the elastic-plastic transition region for the flat bar steel (Figure 4.14). Of the three numerically predicted curves, the curve for the solid model shows better agreement with the experimental curve at the point where the experimental curve levels off.

D.3 Numerical results for IPE beam-columns

Beam-column tests on IPE 160 (Chapter 8).

In the following, numerical simulations of some typical beam-column experiments for the IPE 160 section are presented. The simulations are similar to those presented in Chapter 8 for the HEB 140 section.

Figure D.4 shows the results for the strong axis bending test (M). A very good agreement between experiment and simulation is achieved. While the actual specimen failed due to a combination of smaller local flange buckles combined with a significant extent of lateral torsional (S-shaped) buckling, the numerical model failed due to local flange and web buckling at midspan.

Figure D.5 shows the numerical results of one of the combined bending and torsion tests (MT) for the IPE section. The simulation is carried out by imposing

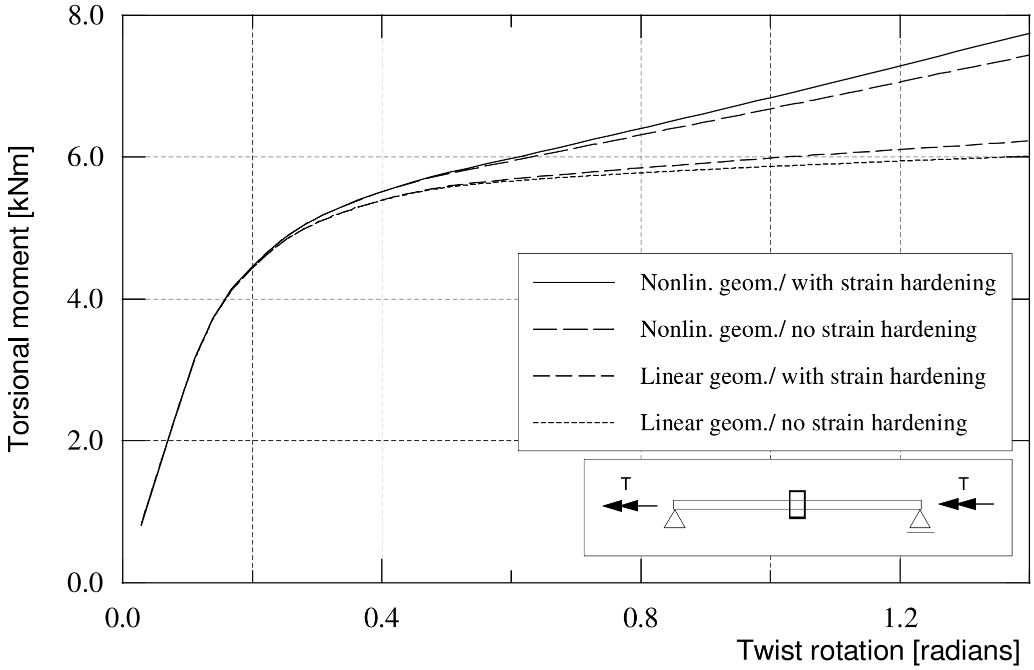

Figure D.2: Simulations for HEB 140 in nonuniform torsion.

the experimental displacement history given by the $\overline{w}$-$\overline{\phi}$ curve. In bending ($\overline{M}$-$\overline{w}$), the response curves are practically identical, while in torsion ($\overline{T}$-$\overline{\phi}$) the simulation underestimates the response somewhat. Considering the discrepancies in both M and T, a mean discrepancy of about 10% is present for the test.

Figure D.6 presents the results for all NT tests carried out for the IPE section. Results are shown for the axial load levels $\overline{N}$=0, $\overline{N}$=0.33 and $\overline{N}$=0.50. For $\overline{N}$=0, the results are discussed in Chapter 4. The simulations give in essence a reasonable prediction of the experimental responses, as the deviation between experiment and simulation for all three tests may be explained by the error in I_T. The actual design of the specimen ends may also contribute somewhat to the deviation for the tests at $\overline{N}$=0.33 and $\overline{N}$=0.50 (see discussion in Section 8.2)

Simulations for the case of *uniform torsion* combined with axial load are shown in Figure D.7. Also here the numerical simulations underestimate the torsional stiffness, due to the underestimation of I_T. Despite this, the torsional moment also for the test at $\overline{N}$=0.34 is predicted reasonably well. For the initial torsional stiffness, the two simulations show a stiffness reduction quite similar to that obtained in the experiments. It can be shown that this stiffness reduction agrees quite well with that predicted by using Equation 6.15 (based on the amplification factor).

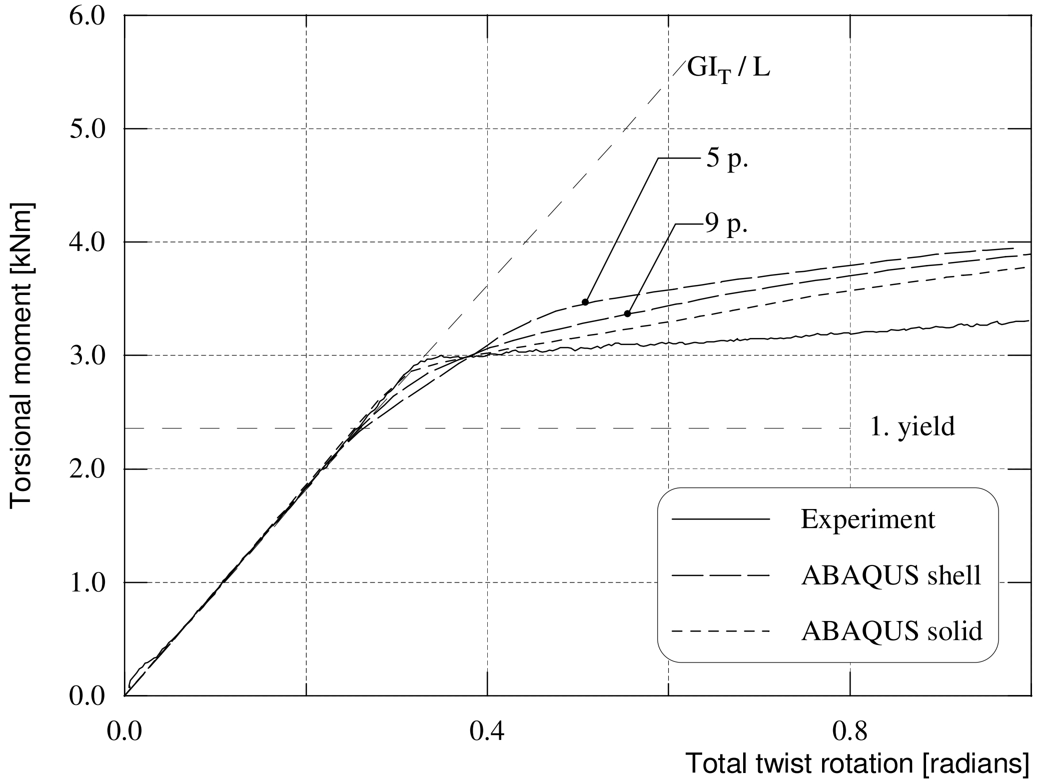

Figure D.3: Details of analyses on flat bar tested in uniform torsion.

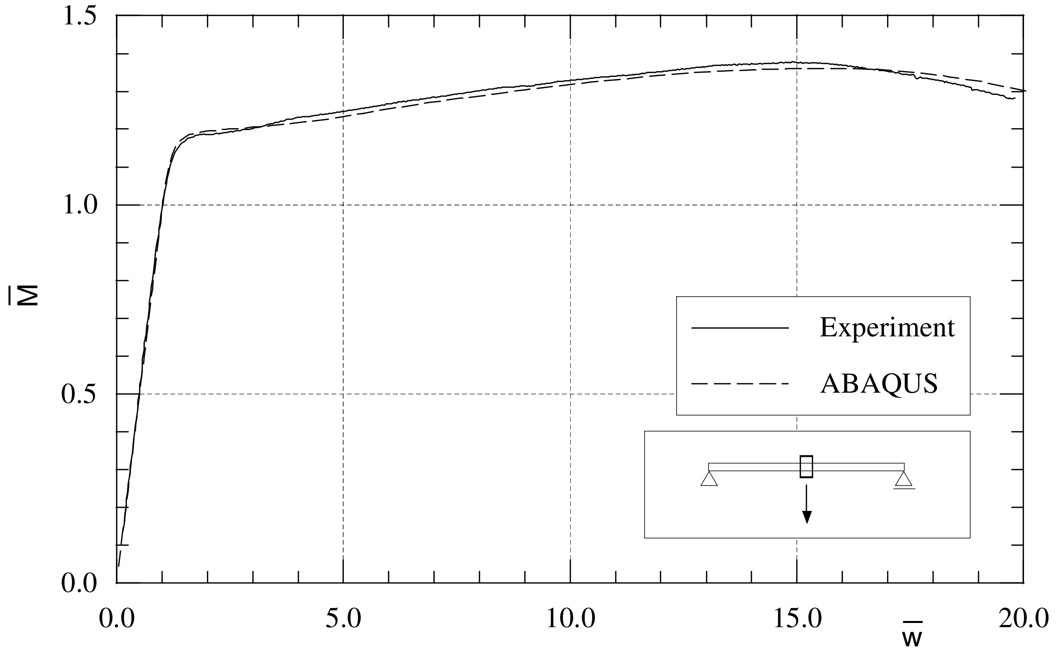

Figure D.4: IPE 160 beam in pure strong axis bending (test I-1-M).

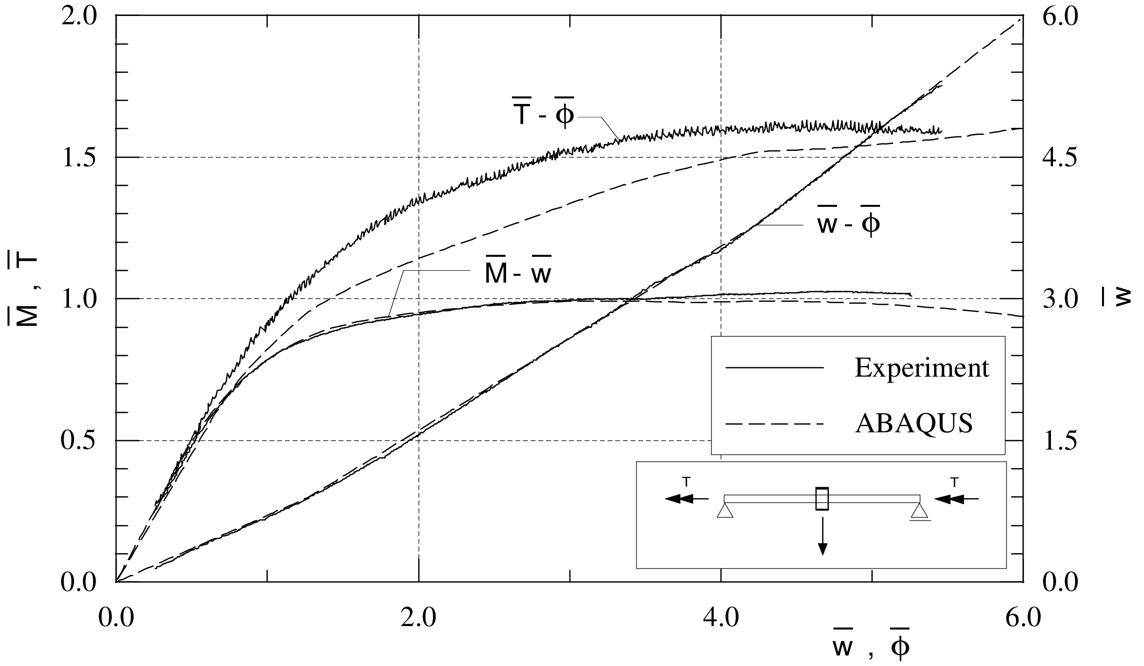

Figure D.5: IPE 160 beam in bending and nonuniform torsion (test I-2-MT)

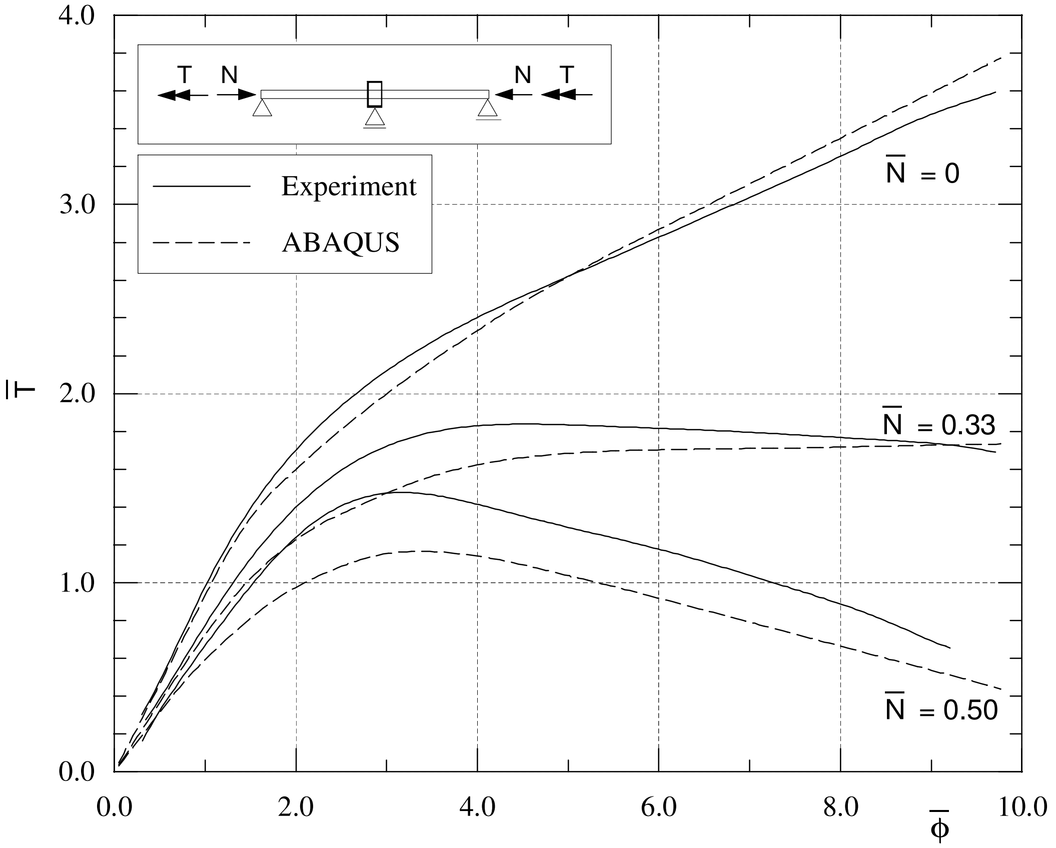

Figure D.6: IPE 160 beam-column subjected to axial load and nonuniform torsion.

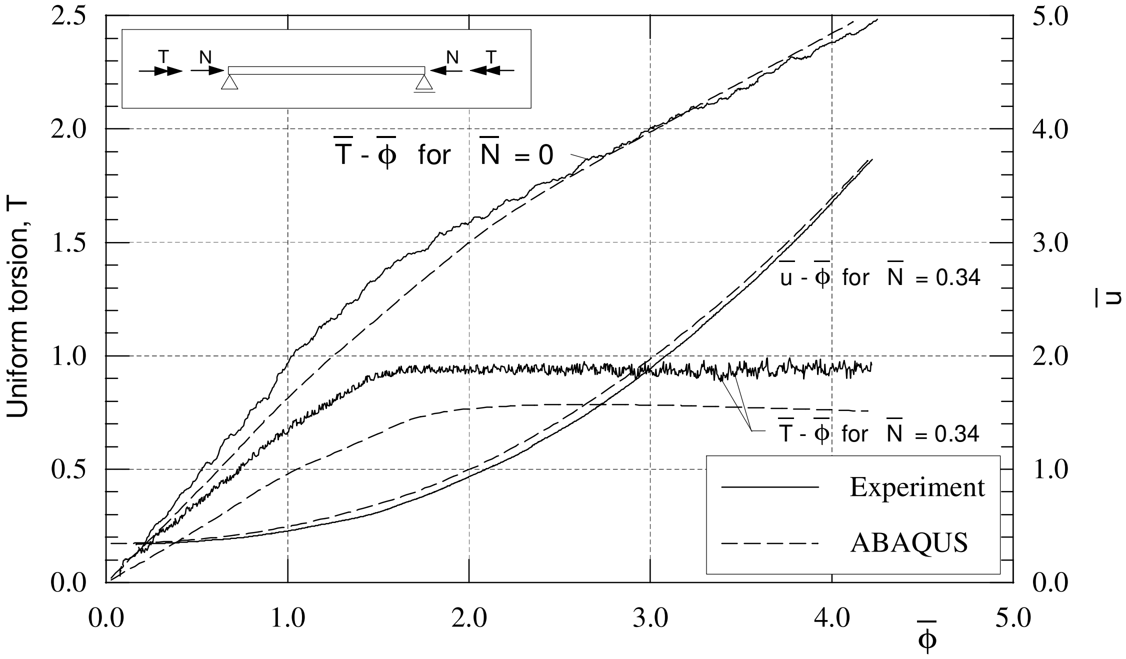

Figure D.7: IPE 160 beam-column subjected to uniform torsion and axial load.